DÉVELOPPEMENT D'UNE MÉTHODE DE CALIBRATION DE LA RUGOSITÉ DE SURFACE POUR LES SIMULATIONS DE GIVRAGE AÉRONAUTIQUE

par

Kevin IGNATOWICZ

THÈSE PAR ARTICLES PRÉSENTÉE À L'ÉCOLE DE TECHNOLOGIE SUPÉRIEURE COMME EXIGENCE PARTIELLE À L'OBTENTION DE DU DOCTORAT EN GÉNIE
Ph. D.

MONTRÉAL, LE 19 AVRIL 2024

ÉCOLE DE TECHNOLOGIE SUPÉRIEURE
UNIVERSITÉ DU QUÉBEC

©Tous droits réservés, Kevin Ignatowicz, 2024

©Tous droits réservés
Cette licence signifie qu'il est interdit de reproduire, d'enregistrer ou de diffuser en tout ou en partie, le présent document. Le lecteur qui désire imprimer ou conserver sur un autre media une partie importante de ce document, doit obligatoirement en demander l'autorisation à l'auteur.

PRÉSENTATION DU JURY

CETTE THÈSE A ÉTÉ ÉVALUÉE

PAR UN JURY COMPOSÉ DE :

M. François Morency, directeur de thèse
Département de Génie Mécanique à l'École de technologie supérieure

Mme Héloïse Beaugendre, codirectrice de thèse
INRIA, Université de Bordeaux

Mme Annie Poulin, présidente du jury
Département de Génie de la Construction à l'École de technologie supérieure

M. Patrice Seers, membre du jury
Département de Génie Mécanique à l'École de technologie supérieure

M. Bruno Blais, jury externe
École Polytechnique de Montréal

ELLE A FAIT L'OBJET D'UNE SOUTENANCE DEVANT JURY ET PUBLIC

LE 28 MARS 2024

À L'ÉCOLE DE TECHNOLOGIE SUPÉRIEURE

REMERCIEMENTS

Ce long travail de thèse n'aurait pas été aussi agréable sans la contribution de personnes importantes dans mon entourage. Je tiens tout particulièrement à remercier mon Directeur de thèse, le Professeur François Morency, qui de par son éthique de travail, sa discipline et son perfectionnisme m'ont permis de développer des compétences et un savoir-faire hors normes. Après huit années de collaboration en incluant ma Maîtrise, cela fait un sacré bout de chemin de parcouru ensemble. Nos interactions hebdomadaires dans le groupe de recherche et nos escapades mondiales lors de conférences en France ou en Autriche resteront des souvenirs inoubliables pour moi. Très grand merci également à ma codirectrice de thèse, la Professeure Héloïse Beaugendre, pour sa supervision bienveillante et efficace depuis la France tout au long de ces années de recherche. Les efforts combinés de mes deux superviseurs ont permis d'accomplir un travail de qualité sans la moindre pression. Merci à mes camarades de l'ÉTS, et particulièrement les autres membres du groupe de recherche pour votre agréable compagnie et la collaboration technique. Certains d'entre vous sont devenus de très grands amis ! Merci également à l'association Le TOMATO de l'Aéroclub de France, le FRQNT et l'ÉTS pour le soutien durant ce Doctorat. Pour finir, mille mercis à ma maman, mon papa et mon petit frère pour leur soutien indéfectible et inébranlable durant toutes ces années. Maman, tu m'as accompagné lors de ma première journée de maternelle en septembre 1996, et maintenant je termine enfin ma scolarité à rallonge, tu dois être fière de tout cet accomplissement ! Je suis sûr que ton billet d'avion est déjà prêt pour la cérémonie de graduation.

DÉVELOPPEMENT D'UNE MÉTHODE DE CALIBRATION DE LA RUGOSITÉ DE SURFACE POUR LES SIMULATIONS DE GIVRAGE AÉRONAUTIQUE

Kevin IGNATOWICZ

RÉSUMÉ

Le givrage en vol des aéronefs est une menace météorologique sérieuse pouvant mener à des accidents graves. L'anticipation des effets du givrage peut être faite par simulation numérique. Ce moyen d'investigation fait appel à un couplage entre l'écoulement d'air autour de l'avion, souvent modélisé par une approche RANS (Reynolds Averaged Navier-Stokes) et la solidification des gouttelettes d'eau atmosphériques sur l'appareil. Les observations expérimentales montrent que les premiers instants de givrage créent de la rugosité de surface, souvent incertaine et irrégulière. La rugosité jouant un rôle important dans la forme de glace finale, ces incertitudes nuisent à la qualité des prédictions numériques. Des modèles semi-empiriques de rugosité sont alors employés dans la littérature, mais très peu de travaux publiés abordent la calibration fine de la rugosité pour des conditions atmosphériques données. Les accrétions expérimentales publiées montrent la forme de glace finale, mais la rugosité de surface initiale est souvent inconnue. Ainsi, l'objectif de la thèse est de proposer, développer et valider une méthodologie permettant d'estimer les paramètres de rugosité à imposer dans une simulation RANS à la simple connaissance de la forme de glace expérimentale dans un contexte de givrage aéronautique. La méthodologie employée consiste à simuler l'écoulement d'air à l'aide d'un solveur RANS compressible avec rugosité de surface. Par la suite, l'accrétion de glace est obtenue avec un solveur de givrage basé sur le ruissellement d'un film liquide se solidifiant, inspiré du shallow water icing model (SWIM). L'impact des gouttelettes fait appel à des solutions manufacturées propres à la géométrie de profil d'aile employée, ici un profil NACA0012. La variation de la rugosité entrée dans le solveur RANS produit à la fin une variation de l'accrétion de glace. Plus particulièrement, le projet débute par une étude de sensibilité via les indices de Sobol et la création de métamodèles de type chaos polynomial pour quantifier la sensibilité d'une accrétion de glace 2D aux paramètres de rugosité de surface. La deuxième étape est la calibration de la rugosité par inversion Bayésienne pour déterminer les paramètres de rugosité menant à une prédiction de transferts de chaleur en adéquation avec les observations expérimentales. L'implémentation d'un solveur de givrage 3D dans SU2-CFD permet par la suite d'appliquer la méthodologie aux accrétions en 3D. Finalement, la méthode est étendue aux distributions de rugosité non constantes pour affiner les prédictions d'accrétions de glace et démontrer la flexibilité de la méthode. Les paramètres de rugosité calibrés obtenus avec la méthode donnent des accrétions de glace avec moins de 1.5 mm d'erreur quadratique moyenne par rapport aux accrétions expérimentales, ce qui représente 0.2% de la longueur de corde. Les formes de glace obtenues permettent par ailleurs de montrer l'intérêt de passer à une distribution de rugosité non constante, puisque les résultats sont améliorés. Sur les quatre cas de givrage avec film liquide ruisselant étudiés, les accrétions obtenues après calibrations sont très proches des formes expérimentales et parfois plus fidèles que les prédictions numériques publiés dans la littérature. La retombée principale de ce travail est de permettre de s'affranchir des corrélations semi-empiriques habituellement employées dans la littérature en estimant une rugosité sur-mesure pour un cas test déterminé. Une

recommandation future serait de calibrer davantage de cas, de façon à extraire une corrélation de rugosité spécifique pour les modèles utilisés et ainsi ne plus avoir à calibrer systématiquement chaque cas.

Mots-clés : simulation numérique, givrage aéronautique, calibration, rugosité, inversion Bayésienne, SU2-CFD, métamodèle chaos polynomial, sensibilité

DEVELOPMENT OF A SURFACE ROUGHNESS CALIBRATION METHOD FOR AIRCRAFT ICE ACCRETION SIMULATION

Kevin IGNATOWICZ

ABSTRACT

Aircraft in-flight icing is a serious meteorological threat that can lead to serious accidents. Anticipation of the effects of icing can be achieved by numerical simulation. This means of investigation uses a coupling between the air flow around the aircraft, often modeled by a RANS (Reynolds Averaged Navier-Stokes) approach and the solidification of atmospheric water droplets on the aircraft. Experimental observations show that the first moments of icing create surface roughness, often uncertain and irregular. Since roughness plays an important role in heat transfer, these uncertainties harm the quality of numerical predictions. Semi-empirical roughness models are then used in the literature, but very few published works address the fine calibration of roughness for given atmospheric conditions. Published experimental accretions show the final ice shape, but the initial surface roughness is often unknown. Thus, the objective of the thesis is to suggest, develop and validate a methodology allowing the estimation of the roughness parameters to be entered into a RANS simulation by simply knowing the experimental ice shape. The methodology used consists of simulating the air flow with a compressible RANS solver with surface roughness. Subsequently, ice accretion is obtained with an icing solver based on the solidification of a runback liquid film, inspired by the shallow water icing model (SWIM). The droplets impingement relies on manufactured solutions specific to the wing geometry used, here a NACA0012 profile. The variation in roughness entered into the RANS solver ultimately produces a variation in ice accretion. More specifically, the project begins with a sensitivity study via Sobol indices and the creation of polynomial chaos metamodels to quantify the sensitivity of a 2D ice accretion to surface roughness parameters. The second step is the roughness calibration by Bayesian inversion to determine the roughness parameters leading to a prediction of heat transfers in line with the experimental observations. The implementation of a 3D ice accretion solver in SU2-CFD subsequently allows the methodology to be applied to 3D accretions. Finally, the method is extended to non-constant roughness distributions to refine ice accretion predictions and demonstrate the flexibility of the method. The calibrated roughness parameters obtained with the method yield ice accretions with less than 1.5 mm root mean square error compared to the experimental accretions, which represents 0.2% of the chord length. The ice shapes obtained also make it possible to show the interest of moving to a non-constant roughness distribution, since the results are greatly improved. In the four cases of icing with runback liquid film studied, the accretions obtained after calibrations are very close to the experimental shapes and sometimes more faithful than the numerical predictions published in the literature. The main outcome of this work is to make it possible to overcome the semi-empirical correlations usually used in the literature by estimating a tailor-made roughness for a specific test case. A future recommendation would be to calibrate more cases, in order to extract a specific roughness correlation for the models used and thus no longer have to systematically calibrate each case.

X

Keywords: numerical simulation, aircraft icing, calibration, roughness, Bayesian inversion, SU2-CFD, polynomial chaos expansion metamodel, sensitivity

TABLE DES MATIÈRES

LISTE DES TABLEAUX

Page

LISTE DES FIGURES

Page

LISTE DES ABRÉVIATIONS, SIGLES ET ACRONYMES

2D	Bidimensionnel
2.5D	Tridimensionnel avec une seule cellule dans l'envergure
3D	Tridimensionnel
3AF	Association Aéronautique et Astronautique de France
AIES	Affine Invariant Ensemble Algorithm
CASI	Canadian Aeronautics and Space Institute
CFD	Computational Fluid Dynamics
CFL	Nombre de Courant-Friedrichs-Lewy
CFDSC	Computational Fluid Dynamics Society of Canada
CIFQE	Colloque International Franco-Québécois en Énergie
CIRA	Centre de Recherche Aerospatial Italien
DERM	Discrete Element Roughness Method
DNS	Direct Numerical Simulation
DOE	Design of Experiments
DRA	Defense Research Agency
ESGR	Equivalent Sand Grain Roughness
CGI	Grid Convergence Index
HAPS	High Altitude Pseudo Satellite
HAX	Correction thermique Aupoix
ISO	International Organization for Standardization
JST	Schéma de Jameson-Schmidt-Turkel

LES	Large Eddy Simulation
LHS	Latin Hypercube Sampling
LOO	Erreur Leave-One-Out
LWC	Liquid Water Content
MAP	Maximum A Posteriori
MCMC	Markov Chain Monte-Carlo
MH	Algorithme Metropolis Hastings
MUSCL	Monotonic Upstream-Centered Scheme for Conservation Laws
MVD	Median Volume Diameter
NASA	National Aeronautics and Space Administration
NIPCE	Non-Intrusive Polynomial Chaos Expansion
ONERA	Office National d'Études et de Recherche Aérospatiales
PCE	Polynomial Chaos Expansion
PDE	Partial Differential Equations
PDF	Probability Distribution Function
QOI	Quantity Of Interest
RANS	Reynolds Averaged Navier-Stokes
RBF	Radial Basis Function
RMS	Root Mean Square
SA	Modèle de turbulence Spalart-Allmaras
SAE	Society of Automotive Engineers
SGR	Sand Grain Roughness
SST	Modèle de turbulence Menter Shear Stress Transport

SU2	Stanford University Unstructured
SU2-CFD	Module CFD de SU2
SU2-ICE	Code de givrage implémenté dans SU2
SWIM	Shallow Water Icing Model
UQ	Uncertainty Quantification
UQLab	Uncertainty Quantification Laboratory
2PP	Correction thermique 2-Parameter Prandtl

LISTE DES SYMBOLES ET UNITÉS DE MESURE

SYMBOLES LATINS		UNITÉ
a, b	Paramètres de distribution de rugosité	Variable
$\boldsymbol{A_e}$	Matrice de Roe pour l'arête e	[m/s; J/kg/m/s]
A_f	Surface frontale d'un élément de rugosité	m²
A_s	Surface mouillée d'un élément de rugosité	m²
c	Longueur de corde	m
Ckc	Paramètre de la correction thermique 2PP	-
CFL	Nombre de Courant-Friedrichs-Lewy	-
C_p	Capacité thermique	J/kg·K
d	Distance à la paroi (lisse)	m
d_k	Espacement entre les éléments de rugosité	m
d_{rough}	Distance à la paroi (rugueuse)	m
e_a^{ij}	Erreur relative entre les maillages i et j	-
$E\big(V(Y\|X_i)\big)$	Moyenne de la variance conditionnelle à X_i fixe	-
$E\left(V\big(Y\big\|X_i, X_j\big)\right)$	Moyenne de la variance conditionnelle à X_i et X_j fixes	-
$\boldsymbol{F}$	Vecteur des flux convectifs (SU2-ICE)	[kg/m/s; J/m/s]
f	Fraction de givrage	-
$\boldsymbol{F_e}$	Vecteur des flux convectifs à travers l'arête e (SU2-ICE)	[kg/m/s; J/m/s]
f_s	Facteur de sur-échantillonnage	-
g	Fonction d'amortissement de la correction thermique 2PP	-
GCI^{ij}	Indice de convergence entre les maillages i et j	-
g_z	Constante de gravitation	m/s²
h	Épaisseur	m
h_c	Coefficient convectif de transfert de chaleur	W/m²·K
k	Hauteur de rugosité	m
k_0	Hauteur de rugosité maximale	m
k_s	Rugosité équivalent grain de sable	m
Ku	Aplatissement de rugosité	m
L	Longueur	m

l	Longueur caractéristique d'un maillage	m
L_e	Chaleur latente d'évaporation	J/kg
L_{fus}	Chaleur latente de fusion	J/kg
L_s	Chaleur latente de sublimation	J/kg
LWC	Contenu en eau liquide dans l'air	kg/m^3
$\dot{m}$	Débit massique surfacique	kg/m²/s
m	Nombre de paramètres à calibrer	-
M	Nombre de Mach	-
$M_i(\boldsymbol{X})$	Fonction métamodèle numéro *i* d'entrée $\boldsymbol{X}$	-
$\vec{\boldsymbol{n}}, n$	Vecteur normal, direction normale	-
N	Nombre de points dans une sommation	-
N_M	Nombre de monômes dans la décomposition polynomiale	-
N_{out}	Nombre de sorties	-
N_{points}	Nombre de points de maillage	-
N_s	Nombre d'échantillons	-
p	Degré du métamodèle/ordre de convergence	-
Pr	Nombre de Prandtl (air)	-
P_v	Pression de vapeur d'eau dans l'air	Pa
$\dot{Q}$	Débit d'énergie surfacique	J/m²/s
QOI	Quantité d'intérêt	-
q_{wall}	Flux de chaleur surfacique au mur	W/m²
R^2	Coefficient de régression	-
Ra	Élévation moyenne arithmétique de rugosité	m
Re_S	Nombre de Reynolds de rugosité	-
$Re_{S,smooth}$	Reynolds de rugosité minorant le régime transitionnel	-
$Re_{S,rough}$	Reynolds de rugosité majorant le régime transitionnel	-
Res_{energy}	Résidu en température de la glace/film	K
Res_{mass}	Résidu de masse de la glace	kg/s
r_{ij}	Raffinement entre les maillages *i* et *j*	-
Rp	Élévation de pic maximale de rugosité	m
Rq	Élévation uadratique moyenne de rugosité	m

Rv	Profondeur de vallée maximale de rugosité	m
Rz	Dénivelé maximal entre une vallée et un pic de rugosité	m
$\boldsymbol{S}$	Vecteur des termes sources (SU2-ICE)	[kg/m²/s; J/m²/s]
S	Surface totale lisse	m²
s	Abscisse curviligne	m
S_{corr}	Facteur de correction (correction thermique Aupoix)	-
S_{elem}	Surface d'un élément de maillage tridimensionnel	m²
S_f	Surface frontale totale de tous les éléments de rugosité	m²
S_i	Indice de Sobol de premier ordre	-
$S_{i,j}$	Indice de Sobol du second ordre	-
S_i^{TOT}	Indice de Sobol total du i^{ème} paramètre	-
Sk	Asymétrie de rugosité	-
S_r	Facteur de correction rugueuse pour le modèle k-ω	-
S_s	Surface mouillée totale de tous les éléments de rugosité	m²
s_0	Abscisse curviligne du point de stagnation	m
T	Température	K
t	Temps	s
T_0	Température de fusion de la glace	K
T^+	Température adimensionnelle	-
$\bar{T}$	Température	°C
T_{rec}	Température de récupération	K
$\boldsymbol{u}$	Vecteur vitesse	m/s
u	Composante de vitesse axiale (direction x)	m/s
u_τ	Vitesse de friction	m/s
U^+	Vitesse adimensionnelle	-
$U(y)$	Champ de vitesse dépendant de la distance à la paroi	m/s
$\bar{\boldsymbol{u}}$	Vitesse moyenne (vecteur) du film liquide	m/s
V	Vitesse d'écoulement en amont	m/s
v	Composante de vitesse transversale (direction y)	m/s
$V(Y)$	Variance de la quantité Y	-
$\boldsymbol{W}$	Vecteur des variables conservatives (SU2-ICE)	[kg/m²; J/m²]

w	Composante de vitesse verticale (direction z)	m/s
$\boldsymbol{X}$	Vecteur d'entrées d'une fonction générique	Variable
$\boldsymbol{x}$	Vecteur des coordonnées spatiales	m
x	Première coordonnée spatiale	m
y	Seconde coordonnée spatiale	m
y^+	Distance adimensionnelle à la paroi	-
y_α	Composante de la décomposition polynomiale	-
Y_i	Sortie numéro i d'une fonction	Variable
y_i	Élévation du point i	m
z	Troisième coordonnée spatiale	m

SYMBOLES GRECS		**UNITÉ**
α	Multi-index d'un polynôme multi-variables	-
α_p, β_p	Paramètres de la correction thermique 2PP	-
β	Efficacité de captation des gouttelettes	-
γ	Indice adiabatique de l'air	-
ΔPr_t	Correction au nombre de Prandtl turbulent	-
Δt	Pas de temps	s
ΔT^+	Décalage de la température adimensionnelle	-
ΔU^+	Décalage de la vitesse adimensionnelle	-
ε	Émissivité	-
ε_r	Erreur relative moyenne	-
ε_{RMS}	Erreur quadratique moyenne	m
ε_s	Énergie cinétique turbulente à la hauteur k_s	J
ε_y	Énergie cinétique turbulente à la distance y de la paroi	J
κ	Constante de von Kármán	-
Λ	Paramètre de forme de rugosité	-
λ	Conductivité thermique	W/m·K
μ	Viscosité dynamique	Pa·s
μ, σ	Moyenne et écart-type	Variable
ν	Viscosité cinématique	m²/s

$\tilde{\nu}$	Variable de turbulence (Spalart-Allmaras)	m²/s
$\pi(\theta)$	Distribution a priori (inversion Bayésienne)	-
$\pi(\theta\|X_i)$	Distribution a postériori (inversion Bayésienne)	-
$\pi(X_i\|\theta)$	Fonction de probabilité (inversion Bayésienne)	-
$\pi(X_i)$	Fonction de normalisation (inversion Bayésienne)	-
ρ	Masse volumique	kg/m^3
σ	Constante de Boltzmann	-
$\boldsymbol{\tau_{wall}}$	Cisaillement à la paroi (vecteur)	Pa
ϕ	Flux de chaleur surfacique au mur (solution air)	W/m²
φ_{α_i}	Polynôme élémentaire uni-variable	-
ψ_α	Polynôme multi-variables	-
Ω	Surface de la cellule	m²
ω	Paramètre du modèle de turbulence *k*-ω	-

INDICES		**UNITÉ**
A, B, C, …	Du point A, B, C, …	-
a	De l'air	-
CFD/RANS	Obtenu par simulation CFD	-
conv	Convectif	-
drop	Des gouttelettes	-
e	Sur l'arête *e*	-
es	Évaporation/sublimation	-
EXP	Mesure expérimentale	-
g	De la glace	-
i, j,…	Au point *i,* au point *j,*…/composante *i, j*…	-
ice	Changement de phase eau/glace	-
imp	Impact des gouttelettes	-
in	Ruissellement entrant	-
kin	De l'énergie cinétique	-
L, R, LR	État gauche, droite, moyenne (discrétisation Roe)	-
lam	Laminaire	-

n	À l'instant *n*	-
neigh	Cellules adjacentes	-
out	Ruissellement sortant	-
(NI)PCE	Obtenu par estimation du métamodèle	-
rad	Radiation	-
rough	Rugueux	-
t	Turbulent	-
total	Quantité totale (statique + dynamique)	-
w	De l'eau liquide	-
wall	À la paroi	-
∞	De l'écoulement libre	-

EXPOSANTS		**UNITÉ**
n	À l'instant *n*	-

INTRODUCTION

0.1 Mise en Contexte et Problématique

Le givrage en vol des avions est un phénomène météorologique présentant une menace pour la sécurité. Connu depuis les débuts de l'aviation, le givrage intervient lorsque l'appareil rencontre des conditions atmosphériques froides et un nuage de gouttelettes d'eau en suspension dans l'air. L'eau va se déposer à la surface de l'avion et geler, formant ainsi une accrétion de glace. Différents types d'accrétion peuvent intervenir. De la glace dite sèche, nommée givre blanc (rime ice en anglais) se forme à très basse température, tandis que du givre transparent (glaze ice en anglais) faisant cohabiter de la glace avec un film d'eau liquide mobile se forme à une température plus élevée et proche du point de congélation. Des accrétions mixtes mélangeant givre blanc et givre transparent peuvent également être observées. Cette accrétion va modifier la forme extérieure des ailes, ce qui impacte l'aérodynamique en augmentant la trainée et en réduisant la portance (Bragg, Broeren, & Blumenthal, 2005; Tagawa, Morency, & Beaugendre, 2018). Le poids de l'appareil se retrouve également augmenté et les débris de glace peuvent être ingérés par les moteurs. Ainsi, le givrage est à l'origine de plusieurs incidents et accidents, parfois fatals, au cours des décennies passées. Il est possible de citer le crash du vol Air France Rio-Paris en 2009, causé par le givrage des sondes Pitot (Conversy, Chatty, Gaspard-Boulinc, & Vinot, 2014) ou le crash du vol Air Ontario 1363 en 1989 (Moshansky, 1992). Pour réduire les risques, des systèmes d'antigivrage et de dégivrage sont installés sur les avions. Pour pouvoir concevoir ces systèmes et les positionner adéquatement, des études sont réalisées en amont pour analyser les mécanismes du givrage (Cao, Tan, & Wu, 2018a). Une partie de ces études est basée sur la modélisation et la simulation numérique, notamment la mécanique des fluides numériques (Computational Fluid Dynamics CFD), du phénomène de givrage.

Les simulations numériques sont basées sur le couplage d'un écoulement d'air, couramment simulé avec une approche RANS (Reynolds Averaged Navier-Stokes), du calcul des trajectoires d'impact des gouttelettes et du changement de phase de l'eau à la surface de l'avion

(Dai, Zhu, Zhao, & Liu, 2021). La simulation d'écoulement d'air permet, avec une géométrie dépourvue de glace, de calculer le champ de vitesse autour de la géométrie, le coefficient de friction et le coefficient de transfert de chaleur à la surface. Le champ de vitesse obtenu permet de calculer l'impact des gouttelettes d'eau sur la géométrie. Enfin, les coefficients surfaciques de friction et de transfert de chaleur sont utilisés par le solveur d'accrétion de glace pour calculer le changement de phase et le ruissellement du film d'eau liquide dans le cas du givre transparent. L'un des paramètres les plus influents sur l'accrétion de glace est la rugosité de surface aux premiers instants du givrage. Les premières gouttelettes solidifiées vont créer une rugosité de surface qui va altérer à la fois le transfert de chaleur et la friction à la surface de l'aile. Le transfert de chaleur et la friction sont les paramètres-clefs pilotant l'accrétion de glace tout au long de sa croissance (Harry, Radenac, Blanchard, & Villedieu, 2021). De fil en aiguille, il est possible de conclure que la rugosité de surface initiale est un paramètre déterminant dans la forme finale de glace (McClain, Vargas, & Jen-Ching, 2016). Cette rugosité est prise en compte dans les modèles RANS impliqués dans une simulation de givrage via une extension rugueuse des modèles de turbulence, par exemple Spalart-Allmaras rugueux (Aupoix & Spalart, 2003), et une correction thermique rugueuse, par exemple la correction 2PP (Morency & Beaugendre, 2020). Souvent, cette rugosité est modélisée par l'approche de rugosité de grain de sable équivalent. Cependant, la rugosité de surface en conditions givrantes est difficile à mesurer expérimentalement, ce qui laisse une incertitude quant aux valeurs et paramètres de rugosité à entrer dans les simulations. Bien que des méthodes récentes permettent une mesure expérimentale de rugosité (Baghel, Sotomayor-Zakharov, Knop, & Ortwein, 2023), un défi additionnel est que les modèles RANS ne réagissent pas tous de la même façon à une rugosité donnée (Morency & Beaugendre, 2020). Autrement dit, la rugosité à imposer dans une simulation dépend à la fois du cas test et des modèles employés. Les modèles employés constituent bien souvent une chaîne de modèles utilisés en séquence et usuellement composée du modèle RANS (incluant son modèle de turbulence et son modèle de traitement de la rugosité), du modèle de captation des gouttelettes et du modèle d'accrétion de glace. Dans la littérature, la rugosité semi-empirique couramment employée en simulation de givrage résulte souvent de méthodes intégrales pour la résolution de la couche limite, rarement calibrées sur un modèle RANS en particulier (Shin, 1996). Bien que des méthodes d'estimation

plus poussées commencent à voir le jour (Gallia, Bellosta, & Guardone, 2023), une méthodologie systématique d'estimation de rugosité spécifique pour des modèles RANS donnés reste à développer pour le givrage aéronautique.

Les modèles employés dans la thèse pour l'écoulement d'air sont la simulation RANS incluant le modèle de turbulence Spalart-Allmaras rugueux et la correction thermique 2PP. Le modèle de givrage utilisé, baptisé SU2-ICE, est inspiré du Shallow Water Icing Model (Bourgault et al., 2000). La question de recherche est donc la suivante : comment estimer la rugosité de surface à imposer dans une simulation CFD de givrage pour un cas test défini et la combinaison de modèles RANS, Spalart-Allmaras rugueux, correction thermique 2PP et SU2-ICE ? Les sous-questions qui peuvent émaner de cette problématique relèvent de la quantification de la sensibilité d'une prédiction d'accrétion avec SU2-ICE à la rugosité imposée dans la simulation RANS et à la manière de calibrer cette rugosité, a priori inconnue, à partir d'observations expérimentales, comme celle de la Figure 0.1.

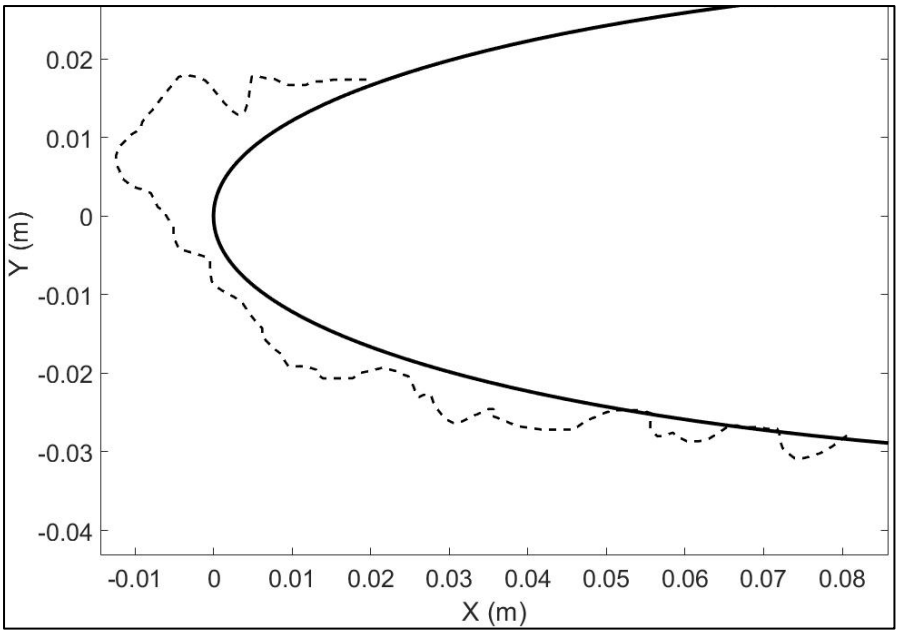

Figure 0.1 Exemple de forme de glace expérimentale (pointillés)
sur un profil NACA0012

Sur la Figure 0.1, la forme de glace est connue et mesurable, mais comment en déduire la rugosité de surface initiale à imposer dans le modèle RANS utilisé pour simuler une accrétion respectant au mieux la forme expérimentale ? En effet, la forme de glace macroscopique visible ne permet en rien de déduire la rugosité microscopique présente à l'instant initial de l'accrétion, et encore moins la rugosité requise à entrer dans les modèles. L'objectif de ce projet de Doctorat est d'apporter une méthodologie permettant de répondre à cette problématique et les sous-questions associées. Il est à noter que d'autres paramètres, tels que la captation des gouttelettes, le modèle de turbulence ou encore le modèle de givrage influencent également la forme de glace. La thèse se focalise seulement sur la rugosité de surface initiale.

0.2 Objectif du Projet

L'objectif du projet est de proposer, développer et valider une méthodologie permettant d'estimer la rugosité de surface à imposer dans un modèle RANS pour prédire une forme de glace s'approchant le plus possible de l'observation expérimentale dans un contexte de givrage aéronautique. Plus spécifiquement, les sous objectifs associés sont (1) de quantifier la sensibilité de l'épaisseur locale d'une accrétion de glace à la rugosité, via les indices de Sobol, dans le cadre de la chaîne de modèles employée dans le projet; (2) de mettre en place une méthode permettant de calibrer la rugosité dans une simulation RANS pour obtenir un transfert de chaleur surfacique coïncidant avec des données expérimentales; (3) de finaliser la méthodologie en utilisant séquentiellement la simulation RANS et l'accrétion de glace pour calibrer par inversion Bayésienne la rugosité pour simuler une accrétion souhaitée en 3D; et (4) de proposer une distribution spatiale non-uniforme de rugosité permettant d'obtenir des formes de glace plus conformes aux expériences par rapport à une distribution spatiale uniforme.

0.3 Méthodologie et Organisation du Document

Pour parvenir aux quatre objectifs cités à la section 0.2, la thèse par articles est découpée comme suit :

- Le premier article, formant le CHAPITRE 1 et publié en octobre 2023 (Ignatowicz, Morency, & Beaugendre, 2023b), est une revue de littérature recensant les différents modèles employés en CFD, et plus particulièrement en Reynolds Averaged Navier-Stockes (RANS), pour prendre en compte la rugosité de surface dans les simulations. La thématique du givrage y est également abordée avec les moyens spécifiques couramment mis en œuvre pour représenter la rugosité irrégulière et incertaine observée en conditions givrantes;

- Le CHAPITRE 2, article publié en mars 2021 (Ignatowicz, Morency, & Beaugendre, 2021c), traite de la mise en place d'un modèle de givrage, simplifié en 2D, basé sur le modèle de Messinger et couplé à une simulation air RANS. La rugosité de surface imposée dans la simulation RANS est variable, ce qui permet la génération d'une base de données de formes de glace. Cette base de données est ensuite modélisée par un métamodèle de type chaos polynomial. Une analyse de sensibilité de Sobol est ensuite effectuée sur le métamodèle pour quantifier la sensibilité de la forme de glace, comme son épaisseur et son étendue le long de la géométrie, aux paramètres de rugosité de surface;

- Le CHAPITRE 3, publié en mai 2022 (Ignatowicz, Solaï, Morency, & Beaugendre, 2022) a pour objectif de calibrer la rugosité en mettant en œuvre une méthode de calibration permettant de prédire avec une simulation RANS un transfert de chaleur proche des résultats expérimentaux dans un canal courbé rugueux. Dans ce chapitre, le transfert de chaleur y est étudié seul car il est la clé de voûte pour simuler un givrage adéquat dans les étapes suivantes du projet traitant de la calibration d'une accrétion de glace 3D. Comme pour le CHAPITRE 2, une base de données est générée, cette fois-ci constituée de transferts de chaleur obtenus pour différentes rugosités. La base de données est ensuite modélisée par un métamodèle qui permet d'effectuer la calibration de rugosité. Les méthodes de calibration employées sont une inversion Bayésienne et un algorithme génétique, permettant de comparer les deux approches. Il est ainsi possible de vérifier que de telles calibrations permettent d'estimer la rugosité inconnue

au départ et de retrouver une distribution de transfert de chaleur avec moins de 5% d'erreur par rapport à l'expérience;

- Le CHAPITRE 4, chapitre de livre publié en mai 2023 (Ignatowicz, Beaugendre, & Morency, 2023), représente le cœur de la thèse et expose la méthodologie développée dans son entièreté : simulation d'écoulement d'air RANS, accrétion de glace et procédure de calibration faisant intervenir la création de métamodèles et une inversion Bayésienne. La méthodologie permet d'appliquer la calibration de rugosité par inversion Bayésienne pour des cas de givrage sur une géométrie 2.5D. Dans ce chapitre, l'implémentation du modèle de givrage 3D dans SU2-CFD est détaillée, ainsi que sa mise à contribution dans des cas de givrage de type givre transparent. En employant cette méthode, les accrétions de glace prédites permettent un accord satisfaisant avec moins de 6% d'erreur sur l'épaisseur de glace par rapport aux formes expérimentales. Cependant, les résultats observés suggèrent qu'une amélioration est possible en remplaçant la rugosité uniforme par une distribution spatiale non-uniforme;

- Finalement, le CHAPITRE 5 est une application de la méthodologie du CHAPITRE 4 à une calibration de rugosité non-uniforme. Ce travail, présenté lors de la Conférence Internationale sur le Givrage de la SAE (Ignatowicz, Morency, & Beaugendre, 2023a) permet de prédire des accrétions de glace avec une forme plus en accord avec les accrétions expérimentales, grâce à un plus grand nombre de paramètres à calibrer provenant de la dépendance spatiale de la rugosité. Les erreurs quadratiques moyennes observées sur l'épaisseur de glace entre les prédictions et les formes expérimentales sont inférieures à 0.3% de la longueur de corde. Ce chapitre permet d'illustrer la flexibilité de la méthodologie proposée, qui peut s'adapter à différentes distributions spatiales de rugosité sans changer la structure d'analyse en place.

Un résumé des principales thématiques abordées dans les chapitres de la thèse est donné dans le Tableau 0.1.

Tableau 0.1 Thématiques des chapitres de la thèse

CHAPITRE 1 (Article)	Revue de littérature : la rugosité en RANS et en givrage
CHAPITRE 2 (Article)	Étude de sensibilité à la rugosité d'une accrétion avec modèle de givrage 2D
CHAPITRE 3 (Article)	Calibration de la rugosité pour prédire les transferts de chaleur en 2D
CHAPITRE 4 (Article)	Calibration de la rugosité pour les prédictions d'accrétions de glace avec un modèle de givrage 3D
CHAPITRE 5	Extension de la méthodologie 3D à une rugosité non uniforme

Pour donner un aperçu de la méthodologie employée, ainsi que des principaux modèles et quantités en jeu, la Figure 0.1 illustre la structure de travail mise en place dans cette thèse.

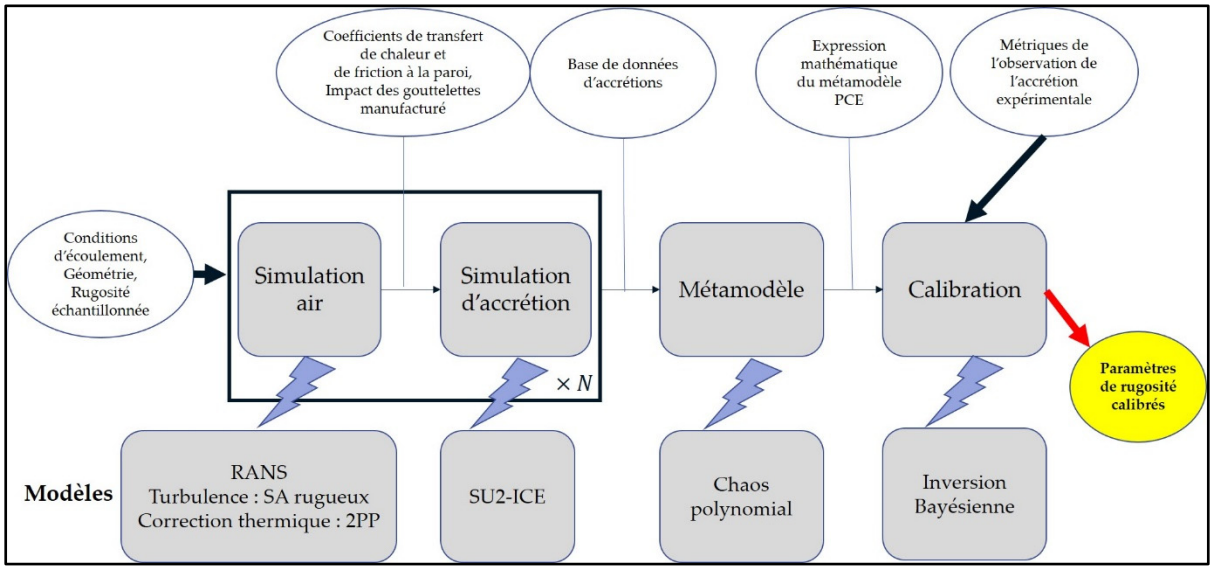

Figure 0.1 Synthèse de la méthodologie mise en œuvre

Les modèles en jeu seront décrits de façon détaillée dans les différents chapitres de cette thèse. De façon synthétique les différentes étapes sont : (1) La simulation d'écoulement d'air avec un modèle RANS incluant un modèle de turbulence rugueux avec correction thermique ; (2) Une simulation d'accrétion de glace avec SU2-ICE ; (3) Une création de métamodèles de type chaos polynomial ; (4) Une calibration de rugosité par inversion Bayésienne. Il est à noter que la séquence simulation air – simulation d'accrétion est répétée *N* fois, avec une rugosité différente par simulation. La simulation air permet de fournir au solveur d'accrétion les coefficients de transfert de chaleur et de friction en paroi. Les *N* accrétions obtenues constituent une base de données qui est modélisée par le métamodèle. Enfin, le métamodèle ainsi que les observations expérimentales permettent de calibrer la rugosité pour obtenir une prédiction d'accrétion se rapprochant au mieux de l'observation.

0.4 Contributions et Publications Additionnelles

Au-delà des quatre articles publiés durant la thèse, les résultats intermédiaires et finaux ont été présentés à l'occasion de sept conférences nationales et internationales :

- La conférence CASI AERO2019 (Ignatowicz, Morency, & Beaugendre, 2019a) : effet du modèle de rugosité sur les formes de glace en 2D;
- Le Colloque International Franco-Québecois en Énergie (CIFQE) 2019 (Ignatowicz, Morency, & Beaugendre, 2019b) : présentation sous forme d'affiche du contenu de la CASI AERO2019;
- La conférence 3AF AERO2020+1 (Ignatowicz, Morency, & Beaugendre, 2021b), conférence reportée à 2021 pour cause de pandémie avec une présentation axée sur la sensibilité des transferts de chaleur à la rugosité;
- La conférence de la CFD Society of Canada (CFDSC) 2021 (Ignatowicz, Morency, & Beaugendre, 2021a), présentant les premières implémentations du modèle de givrage 3D effectuées dans SU2-CFD;
- La conférence 3AF AERO2022 (Ignatowicz, Morency, Beaugendre, & Solaï, 2022) à Supaéro à Toulouse : présentation des résultats du CHAPITRE 3 sur la calibration des transferts de chaleur 2D;

- La conférence CFDSC 2023 à Sherbrooke : présentation des résultats de la méthodologie complète avec rugosité non uniforme;
- La conférence Internationale sur le givrage de la SAE (International Conference on Icing of Aircraft, Engines, and Structures) à Vienne en Autriche (Ignatowicz et al., 2023a) : présentation des résultats de calibration de rugosité non uniforme.

Pour résumer, les principales contributions scientifiques de ce Doctorat ont été de démontrer la pertinence de l'emploi de la méthode de calibration Bayésienne de la rugosité dans un contexte de givrage aéronautique où des relations semi-empiriques historiques de rugosité prévalent depuis plusieurs décennies. Cette méthode de calibration permet d'estimer des paramètres de rugosité spécifiques pour une chaîne donnée de modèles. Cela permet de raffiner le choix de rugosité en se détachant des corrélations semi-empiriques usuellement employées dans la littérature pour les modèles à rugosité de grain de sable équivalent. L'implémentation dans SU2-CFD du solveur de givrage 3D est également une contribution connexe nécessaire à l'atteinte des objectifs du projet. Bien qu'employant un modèle existant, cette implémentation a été le grand défi technique de ce Doctorat, nécessitant une intégration efficace du solveur de givrage dans le code SU2-CFD, puis une vérification et une validation approfondie.

CHAPITRE 1

SURFACE ROUGHNESS IN RANS APPLIED TO AIRCRAFT ICE ACCRETION SIMULATION: A REVIEW

Kevin Ignatowicz [a], François Morency [b], Héloïse Beaugendre [c]

[a, b] Département de Génie Mécanique, École de Technologie Supérieure,
1100 Notre-Dame Ouest, Montréal, Québec, Canada H3C1K3
[c] Université de Bordeaux, INRIA, CNRS, Bordeaux INP, IMB, UMR 5251
33405, Talence, France

Article publié dans « Fluids », octobre 2023

1.1 Abstract

Experimental and numerical fluid dynamics studies highlight a change of flow structure in the presence of surface roughness. The changes involve both wall heat transfer and skin friction, and are mainly restricted to the inner region of the boundary layer. Aircraft in-flight icing is a typical application where rough surfaces play an important role in the airflow structure and the subsequent ice growth. The objective of this work is to investigate how surface roughness is tackled in RANS with wall resolved boundary layers for aeronautics applications, with a focus on ice-induced roughness. The literature review shows that semi-empirical correlations were calibrated on experimental data to model flow changes in the presence of roughness. The correlations for RANS do not explicitly resolve the individual roughness. They principally involve turbulence model modifications to account for changes in the velocity and temperature profiles in the near-wall region. The equivalent sand grain roughness (ESGR) approach emerges as a popular metric to characterize roughness and is employed as a length scale for the RANS model. For in-flight icing, correlations were developed, accounting for both surface geometry and atmospheric conditions. Despite these research efforts, uncertainties are present in some specific conditions, where space and time roughness variations make the simulations difficult to calibrate. Research that addresses this gap could help improve ice accretion predictions.

Keywords: RANS, heat transfer, roughness, aircraft ice accretion, CFD, equivalent sand grain roughness.

1.2 Introduction

Fluid dynamics studies, both experimental and numerical, intend to understand the fluid flow inside or above complex geometries. Among the applications often encountered are flows in pipes (Gao, Li, Nezhad, & Behshad, 2022), flows around aerial or terrestrial vehicles (Howell, Forbes, Passmore, & Page, 2017; Marquet, Leontini, Zhao, & Thompson, 2022) or flows and wind in urban zones (Jafari & Alipour, 2021). On the computational fluid dynamics (CFD) side, the simplest approach to model the walls and solid parts of the geometry is to assume smooth surfaces (Kaya, Kok, & Kurt, 2021; Omoware, Maheri, & Azimov, 2014). The smooth approach has its limits. In practice, several geometries have irregular surfaces with roughness of various origins. Wear, deposit, for example in turbines (Bons, 2010), or ice accretion on an aircraft surface (Kontogiannis, Prakash, Laurendeau, & Moens, 2018) cause roughness. Experimental studies showed different flow structures and behaviour between rough and smooth surfaces (Hosni, Coleman, Garner, & Taylor, 1993). The influence of roughness is mainly concentrated in the near-wall region and affects the turbulent boundary layer (Kadivar, Tormey, & McGranaghan, 2021), particularly the inner layer. The boundary layer modification increases flow metrics such as the wall heat transfer and the skin friction (Suga, Craft, & Iacovides, 2006). Experimental studies have tackled this for decades (Botros, 2016; Schlichting, 1937), highlighting heat transfers, and skin friction increases in the presence of roughness. Therefore, the mathematical models used in CFD should account for roughness to produce accurate predictions.

CFD simulations can either resolve the flow around individual roughness elements or model the effects of roughness. Direct Numerical Simulation (DNS) is one possible way to resolve a flow around surface roughness elements. DNS became popular over the last decade, with the increase in computational power (Forooghi, Stroh, Schlatter, & Frohnapfel, 2018; Javanappa & Narasimhamurthy, 2019). Large Eddy Simulation (LES) also resolves individual roughness elements, but with a lower computational cost (De Marchis, 2016; Rao, Jefferson-Loveday, Tucker, & Lardeau, 2014). Nevertheless, the computational cost of DNS and LES limits their application to simple geometries and is impractical for industrial problems. The modeled approaches present better applicability and wider ranges of use compared to the resolved

approaches. The Reynolds Averaged Navier-Stokes (RANS) is popular in an industrial context since it does not require as much computational power as DNS or LES (Blazek, 2005).

In RANS models, the effects of turbulent fluctuations is taken care of with an additional stress term in the Navier-Stokes equations. This stress term is usually assumed proportional to the wall normal velocity gradient, and the proportionality factor is called the eddy viscosity. The eddy viscosity turbulence models, such as the Spalart-Allmaras (SA) model (Spalart & Allmaras, 1992) or the k-ω model (Menter, 1994), compute the eddy viscosity by solving one (SA) or two (k-ω) transport equations. In a context of rough geometries with RANS, these turbulence models are commonly adapted to account for roughness (Aupoix & Spalart, 2003; Chedevergne, 2021). Experimental skin friction obtained using manufactured roughness patterns help calibrate the rough turbulence models (Schlichting, 1937). Sometimes, the rough turbulence models over predict the wall heat fluxes (Morency & Beaugendre, 2020). This inaccuracy led to the development of so-called thermal correction models aiming to reduce the heat fluxes. Morency and Beaugendre (Morency & Beaugendre, 2020), Chedevergne (Chedevergne, 2018), Suga et al. (Suga et al., 2006), and Aupoix (Aupoix, 2015) derived thermal corrections to use with the rough turbulence models. Most of the thermal correction models increase the turbulent Prandtl number to reduce the wall heat fluxes. The correction depends on the roughness geometric characteristics. Apart from the rough turbulence models, the discrete element roughness method (DERM) is another modelled approach used in CFD (Hanson & Kinzel, 2016; Hanson, Kinzel, & McClain, 2019). The DERM directly adds the roughness effects in the mass, momentum, and energy equations of the flow. The DERM adds source terms to the flow equations to account for blockage, drag, and heat transfer induced by roughness (Aupoix, 2016). Chedevergne recently used the DERM helped by experimental surface topography measurements to finely quantify the source terms in the model (Chedevergne, 2023). The intensity of the additional source terms varies with the roughness geometric characteristics.

Experimental setups can characterize the roughness geometries. Modern measurement techniques allow a precise mapping of experimental surfaces, for example with laser

measurements (Jayabarathi & Ratnam, 2022). Particle velocimetry methods are able to measure the velocity around rough surfaces (Mejia-Alvarez & Christensen, 2013), helping in the identification of typical flow structures. Roughness measurements show highly irregular roughness patterns in most engineering applications (Kuwata, Yamamoto, Tabata, & Suga, 2023). These irregular patterns are usually non-trivial to input in the CFD models, since uncertainty persists. A roughness pattern requires quantifiable metrics to model it with CFD. Common metrics statistically characterize the height and/or spacing of the roughness elements on a surface (R. Leach, 2013), and are used to describe a given roughness pattern. For RANS turbulent flow description, one popular metric is the equivalent sand grain roughness (ESGR) height, k_s, introduced almost one century ago by Nikuradse (Nikuradse, 1933). The ESGR height allows the definition of a roughness pattern with a single metric. k_s is the diameter of the packed spheres that would give the same skin friction as the actual real roughness pattern (Schlichting, 1937), obtained experimentally or geometrically resolved with DNS. k_s is relevant for random and regular roughness patterns similar to sand grain paper. For regular roughness patterns, correlations related k_s to some geometrical parameters of the roughness elements (Dirling, 1973; Sigal & Danberg, 1990). However, this single metric can fail to predict the skin friction for highly irregular roughness patterns, for example, in a context of ice-induced roughness on an aircraft (McClain et al., 2016).

Aircraft icing is a specific application of flow over a rough surface. At the early stages, ice accretion creates surface roughness that increases the wall heat transfer and modifies the final ice shape (Liu & Hu, 2018). For CFD-based ice accretion simulations, the usual framework employs a RANS airflow solver, a droplet impingement solver, and an accretion solver (Bourgault-Cote, Docampo-Sánchez, & Laurendeau, 2018). The RANS airflow solver must model surface roughness to increase the wall heat transfer and the wall skin friction (Kontogiannis et al., 2018). k_s is used to characterize the roughness pattern in most ice accretion software, for example in FENSAP-ICE (Akbal, Ayan, Murat, & Ozgen, 2023), IGLOO3D (Radenac, Gaible, Bezard, & Reulet, 2019), or LEWICE (Shannon & McClain, 2019). Ice-specific semi-empirical correlations are developed to relate the roughness pattern to the atmospheric conditions and the airfoil geometry (Fortin, 2019; Ruff & Berkowitz, 1990; Shin,

Berkowitz, Chen, & Cebeci, 1991; Shin & H. Bond, 1992). In most ice accretion software, the surface roughness imposed in the model is constant and uniform all over the surface (Lavoie, Pena, Hoarau, & Laurendeau, 2018), even if experimental observations show non-uniform roughness patterns over the airfoil surface (Baghel et al., 2023; Fortin, 2019; Hansman, Yamaguchi, Berkowitz, & Potapczuk, 1989). A recent study followed these observations and derive non-uniform roughness distributions (Han & Palacios, 2017) to obtain a heat transfer distribution closer to the experiment. Research efforts are still needed to improve the roughness models as some ice accretion simulations fail at predicting a satisfactory ice shape compared to the experiment (Laurendeau et al., 2022).

This review paper investigates both RANS approaches with wall resolved boundary layers (denoted as wall resolved RANS for the rest of the paper) that account for roughness in aeronautics flows and the special case of ice-induced roughness in aircraft in-flight icing. The objective is to review (1) how roughness is modelled in RANS in the scope of the ESGR and (2) what the specific roughness treatments required for aircraft icing are. First, the roughness geometrical characterization is depicted, with a focus on the usual metrics and the ESGR approach. Second, the roughness impact on the turbulent flow structures is depicted, highlighting some rough turbulence model implementations for wall resolved RANS. Finally, the roughness impact on the in-flight aircraft ice accretion is detailed. This last section also highlights the semi-empirical correlations and models for ice-induced roughness description.

1.3 Roughness Geometrical Characterization in Aerodynamics

This section gives an insight on how the presence of roughness impacts the flow structure in the boundary layer. The first subsection develops the roughness pattern characterizations classically employed in CFD, such as the statistical metrics. The second subsection focuses on the particular case of the ESGR height, a metric typically used in RANS applications.

1.3.1 Geometrical Parameters

In engineering, the spectrum of roughness patterns encountered varies from regular well-ordered configurations to highly irregular and uncertain geometries such as in ice accretion (Caccia & Guardone, 2023) or heterogeneous surface state (Ravenna et al., 2022). Roughness patterns are mathematically described by quantifiable parameters. Through the years, standards have normalized the description of surface states. The SAE J448 (Committee, 2023), the ISO 1302 norm (Heldt, 2006; R. Leach, 2013; Richard Leach, 2013), or the ISO 4287 norm (Todhunter, Leach, Lawes, & Blateyron, 2017) are among the international standards used. The parameters are defined either on a slice of the surface to represent the peaks and valleys amplitudes, or on an area to finely represent the spatial organization of the surface. The main metrics encountered for a surface description are:

- *Ra*, the arithmetic mean height;
- *Rq*, the root mean square height;
- *Rv,* the maximum valley depth;
- *Rp,* the maximum peak height;
- *Rz*, the maximum peak to valley height;
- *Sk*, the skewness;
- *Ku*, the kurtosis.

Figure 1.1 represents a generic rough area and a slice of a rough surface and identifies the most common amplitude metrics. For a rough profile sampled with N points, each one with a height y_i from the smooth mean-zero line, the expressions for the previous parameters are given in equations (1.1) to (1.7).

$$Ra = \frac{1}{N}\sum_{i=1}^{N}|y_i| \tag{1.1}$$

$$Rq = \sqrt{\frac{1}{N}\sum_{i=1}^{N} y_i^2} \tag{1.2}$$

$$Rv = |\min(y_i)| \tag{1.3}$$

$$Rp = \max(y_i) \tag{1.4}$$

$$Rz = Rv + Rp \tag{1.5}$$

$$Sk = \frac{1}{NRq^3}\sum_{i=1}^{N} y_i^3 \tag{1.6}$$

$$Ku = \frac{1}{NRq^4}\sum_{i=1}^{N} y_i^4 \tag{1.7}$$

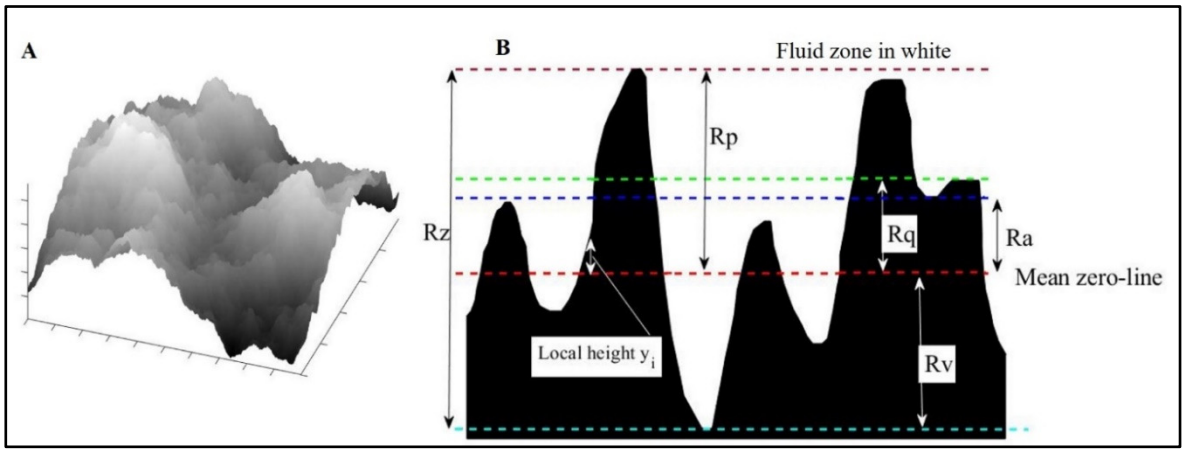

Figure 1.1 (A) Example of rough area, with fluid flowing above and (B) a rough profile with the usual metrics

In the cases of 3D roughness patterns covering an area, some authors introduced spatial parameters to account for the spacing and the wetted and/or frontal area of the roughness (Flack

& Schultz, 2010). The shape parameter Λ is a roughness parameter commonly used in the literature. The shape parameter suggested by Dirling (Dirling, 1973) is a function of the average roughness element spacing d_k, the roughness height k, the frontal area of a roughness element A_f, and the total windward wetted area of a roughness element A_s. Equation (1.8) presents the mathematical definition of the shape parameter defined by Dirling.

$$\Lambda_{Dirling} = \left(\frac{d_k}{k}\right)\left(\frac{A_f}{A_s}\right)^{-\frac{4}{3}} \tag{1.8}$$

Sigal and Danberg (Sigal & Danberg, 1990) introduced a modified definition of the shape parameter by using a surface ratio to account for the roughness element proximity. The total smooth surface S, before roughness addition, and the total frontal area S_f are accounted for in the expression (equation (1.9)). The value of the exponent suggested by Sigal and Danberg was calibrated to match Schlichting's data (Schlichting & Gersten, 2017).

$$\Lambda_{Sigal} = \left(\frac{S}{S_f}\right)\left(\frac{A_f}{A_s}\right)^{-\frac{8}{5}} \tag{1.9}$$

The correlations of Dirling and Sigal and Danberg require the geometric characteristics of a single roughness element, such as A_f or A_s. These correlations are based on regular roughness elements such as spheres, cones, or rods. Therefore, the correlations may not be sufficient for irregular roughness with various geometries. To include such irregular cases, van Rij et al. (van Rij , Belnap , & Ligrani, 2002) suggested another variant of the shape parameter definition. The total roughness windward wetted area S_s is used in that case (equation (1.10)). This definition requires detailed representations of the roughness pattern to extract S_s.

$$\Lambda_{Rij} = \left(\frac{S}{S_f}\right)\left(\frac{S_f}{S_s}\right)^{-\frac{8}{5}} \tag{1.10}$$

These geometrical features are useful to calculate an important parameter for the rough turbulent flow: the equivalent sand grain roughness.

1.3.2 The Equivalent Sand Grain Roughness (ESGR)

To quantify the roughness effects, the ESGR constitutes a length scale often used in engineering fields. Nikuradse (Nikuradse, 1933) carried out experiments with sand-grain-like roughness patterns. The roughness pattern was modeled as packed identical spheres whose diameter is called the sand grain roughness (SGR) height. This approach suits regular roughness patterns having a sand-grain texture well. For irregular roughness, Colebrook et al. (Colebrook, White, & Taylor, 1937) introduced the ESGR height, often denoted k_s. The ESGR height relates non-uniform roughness patterns effects to the SGR height effects on the boundary layer (Flack & Schultz, 2010). The mathematical definition of the ESGR is obtained knowing the flow velocity U at a normal distance y above the surface (Schlichting & Gersten, 2017). u_τ denotes the friction velocity and κ is the von Kármán constant.

$$k_s = \exp\left(\kappa \lim_{y\to 0}\left(8.0 + \frac{1}{\kappa}\ln(y) - \frac{U(y)}{u_\tau}\right)\right) \tag{1.11}$$

Without the knowledge of $U(y)$, the ESGR height is correlated to the geometrical configuration of the roughness elements. Dirling (Dirling, 1973) established a correlation for cones or spheres elements. Bons (Bons, 2002, 2010) worked on correlations for turbine blades roughness. Sigal and Danberg (Sigal & Danberg, 1990) derived ESGR correlations for transversal roughness such as bars and rods, while van Rij et al. (van Rij et al., 2002) developed correlations for 3D irregular roughness. Botros (Botros, 2016) recently extended the pioneer studies of Nikuradse and Colebrook for steel pipes. Table 1.1 presents some correlations used to compute the ESGR k_s.

Table 1.1 ESGR correlations classically used in engineering

Authors	ESGR correlation
Dirling (Dirling, 1973)	$\frac{k_s}{k} = 0.0164{\Lambda_{Dirling}}^{3.78}$ for $\Lambda_{Dirling} \leq 4.915$ $\frac{k_s}{k} = 138.9{\Lambda_{Dirling}}^{-1.9}$ for $\Lambda_{Dirling} > 4.915$
Bons (Bons, 2002)	$\log\left(\frac{k_s}{k}\right) = -0.43\log(\Lambda_{Sigal}) + 0.82$
Sigal & Danberg (Sigal & Danberg, 1990)	$\frac{k_s}{k} = 0.003215{\Lambda_{Sigal}}^{4.925}$ for $1.4 \leq \Lambda_{Sigal} \leq 4.89$ $\frac{k_s}{k} = 8$ for $4.89 < \Lambda_{Sigal} < 13.25$ $\frac{k_s}{k} = 151.71{\Lambda_{Sigal}}^{-1.1379}$ for $13.25 \leq \Lambda_{Sigal} \leq 100$
Van Rij et al. (van Rij et al., 2002)	$\frac{k_s}{k} = 1.583 \times 10^{-5}{\Lambda_{Rij}}^{5.683}$ for $\Lambda_{Rij} \leq 7.842$ $\frac{k_s}{k} = 1.802{\Lambda_{Rij}}^{0.03038}$ for $7.842 < \Lambda_{Rij} < 28.12$ $\frac{k_s}{k} = 255.5{\Lambda_{Rij}}^{-1.454}$ for $\Lambda_{Rij} \geq 28.12$
Botros (Botros, 2016)	$k_{s,Colebrook} = 1.306Rq + 0.078Rq^2$ $k_{s,Nikuradse} = 2.294Rq$

1.4 Roughness Regimes and Rough Turbulence Models

This section depicts roughness impacts on the flow structure and reviews how RANS models tackle roughness. The first subsection shows how the presence of roughness in a flow alters

the boundary layer, defining the roughness regimes encountered. The second subsection presents some RANS approaches used to include the roughness in the computation, including the velocity and thermal corrections required to model the flow over a rough surface.

1.4.1 The Rough Flow Regimes

The roughness modifies the near-wall flow behavior compared to a smooth surface. Smooth surfaces were extensively studied for almost a century with the definition of the so-called law-of-the-wall (Heng, Duo, & Hongyi, 2020; Reichardt, 1951; Von Kármán, 1931). The smooth theory was extended to rough surfaces to face industrial applications. For the rough turbulent boundary layer, a roughness Reynolds Re_s number is defined. The symbol ν appearing in equation (1.12) stands for the kinematic viscosity of air.

$$Re_s = \frac{k_s u_\tau}{\nu} \tag{1.12}$$

Three main roughness regimes can be observed:

- The hydraulically smooth regime if $Re_s \leq Re_{s,smooth}$;
- The transitionally rough regime if $Re_{s,smooth} \leq Re_s \leq Re_{s,rough}$;
- The fully rough regime if $Re_s > Re_{s,rough}$.

Qualitatively, these regimes, illustrated in Figure 1.2, correspond to:

- Roughness elements small compared to the viscous sublayer thickness (hydraulically smooth);
- Roughness elements in the same order of thickness as the viscous sublayer thickness (transitionally rough); and
- Roughness elements larger than the viscous sublayer thickness and ending inside the buffer or the logarithmic layer (fully rough) (Kadivar et al., 2021). The roughness effect of the flow field is no more limited to the viscous sublayer (Ghanadi & Djenidi, 2022).

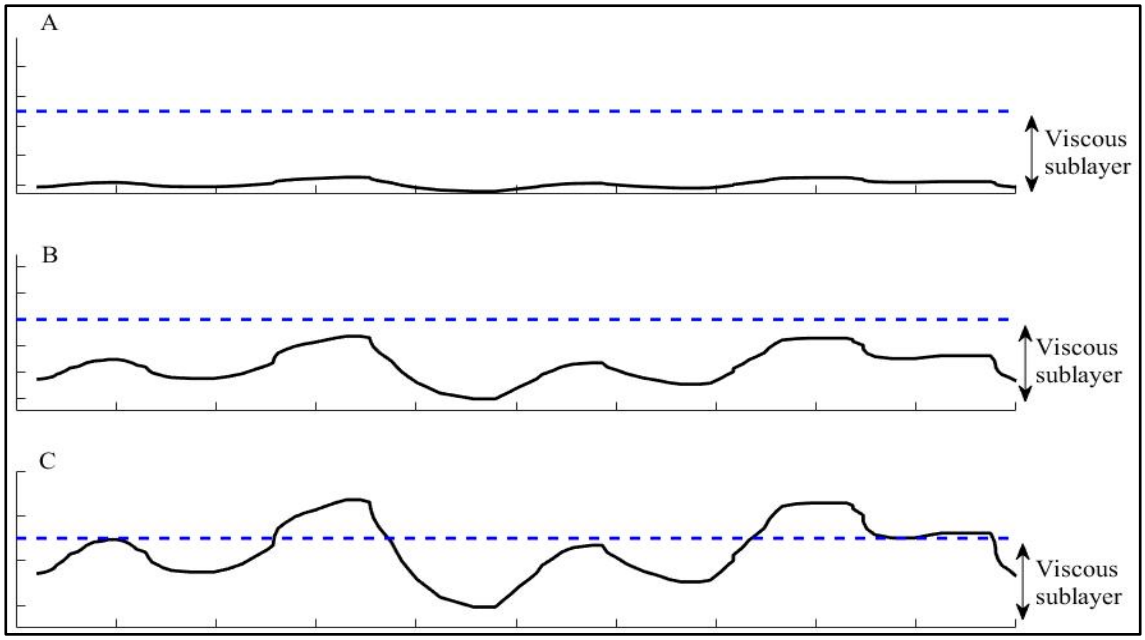

Figure 1.2 (A) Hydraulically smooth; (B) Transitionally rough; and (C) Fully rough. The dashed line corresponds to the viscous sublayer thickness and the solid line represents the rough surface

$Re_{s,smooth}$ and $Re_{s,rough}$ delimit the regimes and take different values depending on the type of roughness encountered. Nikuradse (Nikuradse, 1933) was a pioneer in the field and suggested values for uniform sand grain roughness. Ligrani & Moffat (Ligrani & Moffat, 1986) suggested values for spherical roughness elements. Langelandsvik et al. derived tailored values for commercial steel piping (Langelandsvik, Kunkel, & Smits, 2008). Schultz & Flack (Schultz & Flack, 2007) established values for surface scratches. These common values are:

- Nikuradse: $Re_{s,smooth} = 5$ and $Re_{s,rough} = 70$
- Ligrani & Moffat: $Re_{s,smooth} = 15$ and $Re_{s,rough} = 50$
- Langelandsvik et al.: $Re_{s,smooth} = 1.4$ and $Re_{s,rough} = 18$
- Schultz & Flack: $Re_{s,smooth} = 2.5$ and $Re_{s,rough} = 25$

These theoretical and experimental developments are the basis for the CFD models aiming at accounting for surface roughness. The most common implementations used for RANS modelled approaches are reviewed in the following subsection.

1.4.2 RANS Implementations to Account for Roughness

The roughness effects mainly create a velocity deficit in the boundary layer compared to a smooth surface. This leads to a downward shift of the log-Law by a value ΔU^+ (Flack & Schultz, 2010), as in equation (1.13) where C is a constant.

$$U^+ = \frac{1}{\kappa}\ln(y^+) + C - \Delta U^+ \tag{1.13}$$

This theoretical shift is confirmed by experimental studies for example from ONERA and Boeing (Aupoix & Spalart, 2003), compared to the smooth profile (Heng et al., 2020), as illustrated in Figure 1.3.

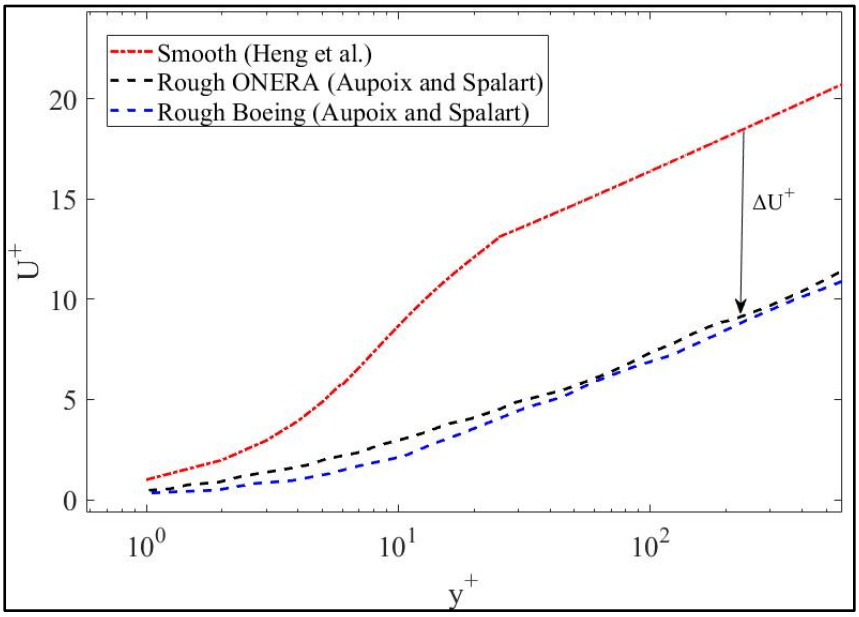

Figure 1.3 Velocity shift in the case of rough walls
and comparison with the smooth case
Adapté de Aupoix & Spalart (2003, p. 460)
et Heng et al., (2020, p. 3317)

The velocity shift indicates an increase in the friction velocity, and by extension, in the wall shear stress and skin friction coefficient. The amplitude of the velocity shift is a function of

the roughness parameters, mainly Re_s. Therefore, RANS requires to accurately model the velocity shift ΔU^+ to accurately predict the rough skin friction.

To account for roughness in a RANS model, the turbulence models are adapted. A decade after its original publication, the Spalart-Allmaras (SA) turbulence model (Spalart & Allmaras, 1992) received a rough extension (Aupoix & Spalart, 2003). The original SA turbulence model solves one transport equation for the turbulence variable $\tilde{\nu}$. The computation of the turbulent variable enables the knowledge of the turbulent eddy viscosity μ_t, function of the wall distance, required for the RANS equations closure. The rough version of the SA turbulence model redefines the wall distance from its smooth value d to d_{rough}, using the ESGR.

$$d_{rough} = d + 0.03k_s \tag{1.14}$$

The main modification of the SA turbulence model is the wall boundary condition, which is $\tilde{\nu}_{wall} = 0$ for a smooth case. For the rough version, a gradient normal to the wall, with n being the normal direction, is imposed.

$$\left(\frac{\partial \tilde{\nu}}{\partial n}\right)_{wall} = \frac{\tilde{\nu}_{wall}}{0.03k_s} \tag{1.15}$$

Similarly, the two-equation k-ω turbulence model (Menter, 1994), gained its roughness extensions through the years. Wilcox (Wilcox, 2006) was the first to derive a rough extension in 1998 before adding some corrections in 2006. The wall boundary condition for the parameter ω is altered. ρ is the fluid density and μ is the dynamic viscosity.

$$\omega_{wall} = \frac{\rho u_\tau}{\mu} S_r \tag{1.16}$$

With

$$\begin{cases} S_r = \left(\frac{50}{Re_s}\right)^2 \text{ for } Re_s < 25 \\ S_r = \frac{100}{Re_s} \text{ for } Re_s \geq 25 \end{cases} \quad (1.17)$$

This model has the disadvantage of requiring a very fine mesh in the near wall (Patel & Yoon, 1995) and is not fully compatible with the original SST formulation (Hellsten & Laine, 1997). Later, Knopp et al. (Knopp, Eisfeld, & Calvo, 2009) suggested a new formulation for the rough *k-ω* turbulence model to improve the weaknesses of the original rough extension. Apart from the SA and *k-ω* turbulence models, the *k-ε* model also received its rough extension (Durbin, Medic, Seo, Eaton, & Song, 2001). These rough versions predict accurate skin frictions compared to experimental data (Morency & Beaugendre, 2020). This allows an evaluation of the friction velocity and of the roughness Reynolds number Re_s (equation (1.12)).

Several studies showed that the rough velocity profile and the velocity shift ΔU^+ (see Figure 1.3) are functions of the roughness Reynolds number Re_s (Grigson, 1992; Kays & Crawford, 1993; Radenac, Kontogiannis, Bayeux, & Villedieu, 2018). Equation (1.18) shows Nikuradse (Nikuradse, 1933) estimation for the rough log-Law in a fully rough regime.

$$U^+ = \frac{1}{\kappa}\ln\left(\frac{y^+}{Re_s}\right) + 8.5 \quad (1.18)$$

More recently, Radenac et al. (Radenac et al., 2018) suggest using the relation developed by Grigson (Grigson, 1992) based on the work of Colebrook (Colebrook et al., 1937) to directly estimate the velocity shift.

$$\Delta U^+ = \frac{1}{\kappa}\ln\left(1 + \frac{Re_s}{e^{1.3325}}\right) \quad (1.19)$$

Another alternative, developed by Kays and Crawford (Kays & Crawford, 1993), gives a variant to compute the velocity shift.

$$\Delta U^+ = \frac{1}{\kappa}\ln(Re_s) - 2.98 \tag{1.20}$$

Although most correlations are valid in a fully rough regime, other are derived to fit all regimes. Following the works from Nikuradse, equations (1.21) to (1.23) cover all regimes from hydraulically smooth (equation (1.21)), to transitionally rough (equation (1.22)) and fully rough (equation (1.23)) (Kadivar et al., 2021).

$$\Delta U^+ \tag{1.21}$$

$$= \begin{cases} 0 & \\ \frac{1}{\kappa}\ln\left(5.23\left(\frac{Re_s - Re_{s,smooth}}{Re_{s,rough} - Re_{s,smooth}}\right) + 0.253Re_s\right)\sin\left(\frac{\pi}{2}\frac{\ln\left({}^{Re_s}/_{Re_{s,smooth}}\right)}{\ln\left({}^{Re_{s,rough}}/_{Re_{s,smooth}}\right)}\right) & (1.22) \\ \frac{1}{\kappa}\ln(5.23 + 0.253Re_s) & (1.23) \end{cases}$$

In all models, the velocity shift is zero in a hydraulically smooth regime. For very small roughness elements, the effects on the flow vanish due to the viscosity (Kadivar et al., 2021; Orych, Werner, & Larsson, 2022). Commercial CFD software with wall resolved RANS approaches, such as STAR-CCM+, implement the roughness effect such as equations (1.21) to (1.23) (Andersson, Oliveira, Yeginbayeva, Leer-Andersen, & Bensow, 2020). By default, the constants 5.23 and 0.253 in equations (1.21) to (1.23) are set but tunable by the user, such as the values for $Re_{s,smooth}$ and $Re_{s,rough}$.

Even if the skin friction is accurate, the wall heat transfer is not correctly predicted for some rough cases. Past studies (Aupoix, 2015; Morency & Beaugendre, 2020; Suga et al., 2006) reported an overestimation of the wall heat fluxes when the rough turbulence models are employed. Similar to the velocity profile, the temperature profile is shifted in the boundary layer (Aupoix, 2015) above roughness. Kays and Crawford (Kays & Crawford, 1993) gave a

formulation for the temperature shift ΔT^+, where Pr_t is the turbulent Prandtl number and C_{Pr} is a function of the laminar Prandtl number Pr.

$$\Delta T^+ = \frac{Pr_t}{\kappa}\ln\left(\frac{Re_s}{32.6}\right) + C_{Pr} - 1.25Pr^{0.44}Re_s{}^{0.2} \tag{1.24}$$

The prediction of the wall heat transfer in the RANS models requires to accurately predict the temperature shift ΔT^+.

According to the investigations of Suga et al. (Suga et al., 2006), the heat flux overestimation comes from the trapped recirculating flow between the roughness elements. These recirculation zones create a thermal barrier reducing the heat flux, as schemed in Figure 1.4.

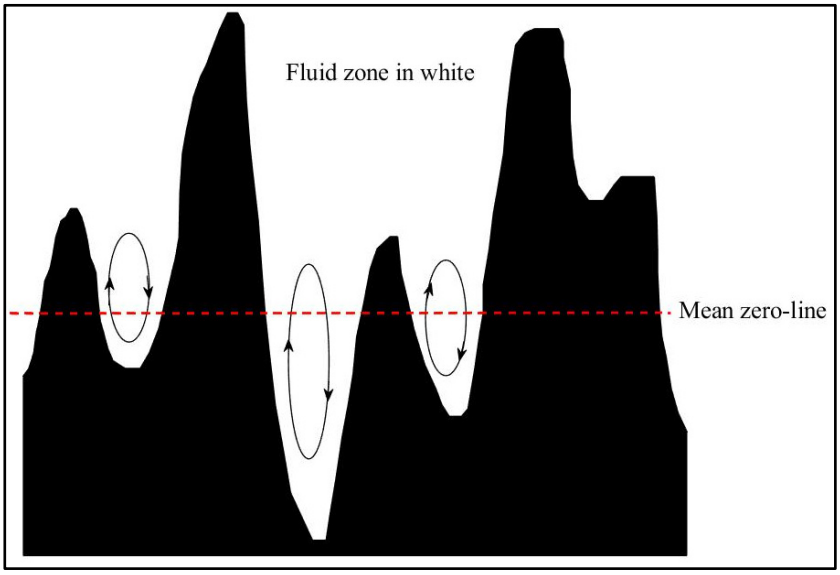

Figure 1.4 Illustration of the trapped fluid between roughness elements

The thermal correction models (Aupoix, 2015; Morency & Beaugendre, 2020; Suga et al., 2006) intend to account for these recirculation zones. The common approach in the literature is to locally increase the turbulent Prandtl number Pr_t. This impacts both the thermal

conductivity and the temperature shift (equation (1.24)). The thermal correction models add ΔPr_t to the turbulent Prandtl number, allowing the modification of the thermal conductivity.

$$Pr_{t,rough} = Pr_t + \Delta Pr_t \tag{1.25}$$

Suga et al. (Suga et al., 2006) derived the following expression for the turbulent Prandtl number correction, where ε_s and ε_y are the local turbulent kinetic energy at the ESGR height and at the height y from the wall, respectively.

$$\Delta Pr_t = C_0 \max\left(0, 1 - \frac{y\sqrt{\varepsilon_y}}{k_s\sqrt{\varepsilon_s}}\right) \tag{1.26}$$

$$C_0 = \frac{5.5}{1 + \left(\frac{k_s\sqrt{\varepsilon_s}}{70\nu}\right)^{6.5}} + 0.6 \tag{1.27}$$

The thermal correction model from Suga et al. only requires one roughness parameter, k_s, to compute the thermal correction.

Morency and Beaugendre (Morency & Beaugendre, 2020) derived a 2-parameter thermal correction model by blending the works from Ligrani et al. (Ligrani, Moffat, & Kays, 1979), Dipprey and Sabersky (Dipprey & Sabersky, 1963), and Owen and Thomson (Owen & Thomson, 1963), and the integral method from Kays and Crawford (Kays & Crawford, 1993). The general form of ΔPr_t is inspired from the thermal correction model from Aupoix (Aupoix, 2015).

$$\Delta Pr_t = Fexp\left(-\frac{d_{rough}}{k}\right) \tag{1.28}$$

The expression of F is given by equation (1.29).

$$F = g\frac{\kappa}{3.02}\frac{{Re_s}^{0.45}Pr^{0.8}}{1.92} \tag{1.29}$$

The factor g damps the correction in a transitionally rough regime. The limits used to separate the hydraulically smooth ($g = 0$), transitional, and fully rough ($g = 1$) regimes corresponds to the $Re_{s,smooth} = 5$ and $Re_{s,rough} = 70$ values suggested by Nikuradse (Nikuradse, 1933).

A third thermal correction model is the 3-parameter model of Aupoix (Aupoix, 2015). The turbulent Prandtl number correction ΔPr_t is the same as in equation (1.28), but with an alternate definition for the factor F, function of the velocity shift ΔU^+, and a geometrical correction parameter S_{corr}. S_{corr} corresponds to the ratio between the rough wetted area (i.e., accounting for the wetted area of the roughness elements) and the smooth wetted area, with the through below the recirculation zone (see Figure 1.4) neglected. The factor F is expanded in equation (1.30).

$$F = A\Delta U^{+2} + B\Delta U^{+} \tag{1.30}$$

The factors A and B are defined in the following equations (1.31) and (1.32).

$$A = (0.0155 - 0.0035S_{corr})\left(1 - \exp\left(-12(S_{corr} - 1)\right)\right) \tag{1.31}$$

$$B = -0.08 + 0.25\exp\left(-10(S_{corr} - 1)\right) \tag{1.32}$$

ΔU^+ being a function of Re_s, the correction suggested by Aupoix requires three roughness parameters: k_s; k; and S_{corr}.

The RANS models depicted in this subsection predict both wall shear stress and wall heat flux over roughness. The next section gives an insight into a specific application of rough surfaces: aircraft icing.

1.5 The Specific Case of Aircraft Icing

In-flight ice accretion simulation commonly relies on RANS and rough turbulence to model airflow. This section first depicts the models used in aircraft ice accretion simulations and how surface roughness plays a key role in the process. The second subsection reviews the roughness semi-empirical correlations developed to determine the roughness pattern above ice surfaces.

1.5.1 The Ice Accretion Process: A Roughness-Dependent Phenomenon

Ice accretion studies address in the safety concerns induced by ice build-up on aircraft surfaces (Cao et al., 2018a; I.A.T.A., 2016). The studies apply to both ice-induced aerodynamic degradation (Bragg et al., 2005; Esmaeilifar, Raj, & Myong, 2022) and shedding debris (Bennani, Villedieu, Salaun, & Trontin, 2014; Ignatowicz, Morency, & Lopez, 2019). Initially carried out experimentally (Dukhan, Masiulaniec, Dewitt, & Fossen, 1999b; Liu & Hu, 2018; Shin & H. Bond, 1992), ice accretion studies have been supplemented by numerical simulations with the increase of computational power (Caccia & Guardone, 2023; Fujiwara, Bragg, & Broeren, 2020; Gori, Bellosta, & Guardone, 2023).

For numerical simulations, Messinger (Messinger, 1953) pioneer works develop a well-known model to compute the ice growth on an aircraft surface. The Messinger model has been improved through the years to include features such as unsteadiness, shear-stress driven liquid film, or partial differential equation formulation (Ayan & Ozgen, 2017; Bourgault, Beaugendre, & Habashi, 2000; Myers, 2001; C. Zhu, Fu, Sun, & Zhu, 2012). The original Messinger model computes the mass and the energy balance in a control volume composed of a moving liquid film and an ice layer, as shown in Figure 1.5.

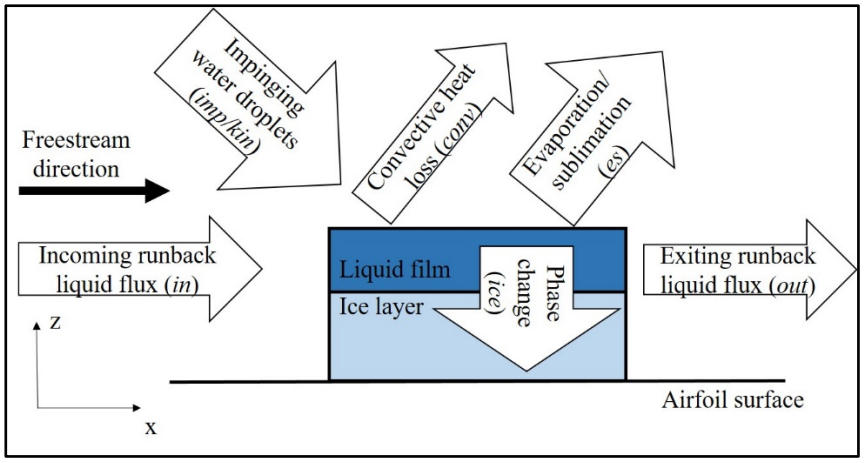

Figure 1.5 Typical control volume for ice accretion simulations

The white arrows in Figure 1.5 symbolize the main contributions to the mass balance (equation (1.33)) and the energy balance (equation (1.34)) where $\dot{m}$ (kg/s) and $\dot{Q}$ (J/s) are the mass flux rate and energy flux rate, respectively. The subscripts correspond to the ones illustrated in Figure 1.5.

$$\dot{m}_{in} + \dot{m}_{imp} - \dot{m}_{ice} - \dot{m}_{es} - \dot{m}_{out} = 0 \tag{1.33}$$

$$\dot{Q}_{conv} + \dot{Q}_{es} + \dot{Q}_{imp} - \dot{Q}_{kin} - \dot{Q}_{ice} - \dot{Q}_{in} = 0 \tag{1.34}$$

The accretion can be seen as a phase change problem where the liquid film freezes, releasing latent heat during the process. In a control volume, the water phase is determined by the internal energy. If the energy in the control volume is lower than the solidification energy, the water is solid. If the energy in the control volume is higher than the fusion energy (the solidification energy plus the latent heat of phase change), the water is liquid. When the total energy of the control volume is between the energy of solidification and the energy of fusion, ice and liquid water coexist, and a glaze ice state is observed. The contributions remain almost identical among the ice accretion models, with some additions such as the radiation or the conductivity through ice (Ignatowicz et al., 2021a; Lavoie et al., 2018). The variables in equations (1.33) and (1.34) were described by Özgen and Canibek (Özgen & Canıbek, 2008). Among the

variables, several depends on quantities obtained at the airflow computation step, such as the heat transfer coefficient h_c obtained from the wall heat flux ϕ, the wall temperature T, and the recovery temperature T_{rec}.

$$h_c = \frac{\phi}{T - T_{rec}} \tag{1.35}$$

More precisely:

- The evaporation/sublimation mass and energy variables depend on the heat transfer coefficient (MacArthur, Keller, & Luers, 1982);
- The convective heat loss is a function of the heat transfer coefficient;
- The runback velocity is a function of the skin friction coefficient in the shear-stress driven liquid film models (Ignatowicz et al., 2021a; C. Zhu et al., 2012).

Both heat transfer and wall shear stress are functions of the surface roughness pattern and impact the computed ice shape. The development of surface roughness in the early stages then drives the ice accretion process (Liu, Zhang, Tian, & Hu, 2020). This surface roughness is usually uncertain, both in space and time, raising a difficulty to correctly model it. Experimental measurements using photogrammetry and 3D scanning highlight a spatial variation of the roughness, with a smoother zone around the stagnation point (Baghel et al., 2023; Han & Palacios, 2014). Additional studies allow the monitoring of the temporal evolution of the roughness characteristics (Wang et al., 2022). To highlight the spatial roughness variation, the experimental measurements from Han & Palacios (Han & Palacios, 2014) were conducted on a NACA0012 airfoil and Baghel et al. (Baghel et al., 2023) used the High Altitude Pseudo Satellites (HAPS) airfoil. Variation of measured experimental *Ra* (equation (1.1)) and *Rq* (equation (1.2)) against the chord fraction on the upper part of the airfoil are shown in Figure 1.6. The x-axis origin corresponds to the stagnation point location. Figure 1.7 highlights the temporal roughness variation obtained on a 0.33 m chord, 0.3 m span NACA0012 wing at −5° angle of attack (Wang et al., 2022). Figure 1.7 plots *Ra* (equation

(1.1)) against the exposure time for various freestream velocities (V) and total temperatures (T_{total}). Figure 1.6 and Figure 1.7 also give indications on the magnitude of roughness height usually encountered in aircraft ice accretion. This surface roughness only characterizes the very first moments of the ice accretion. The roughness models the surface irregularities of size similar to the boundary layer thickness. The ice then grows on the rough airfoil, driven by the heat transfer and shear stress, and can reach large size and thickness. In the case of ice accretions larger than the boundary layer thickness, strategies such as geometry update (Fossati, Khurram, & Habashi, 2012) or the immersed boundary method (de Rosa, Capizzano, & Cinquegrana, 2023) are required to account for the wall macroscopic deformation. The multi-layer approach allows updating the airflow during the simulation, as the accretion is computed layer by layer. In most cases, the single layer approach is preferred. The single layer approach only relies on the initial flow field obtained on the rough airfoil without any large ice accretion. In some cases, the single and multi-layer approach can lead to similar results (Lavoie et al., 2018).

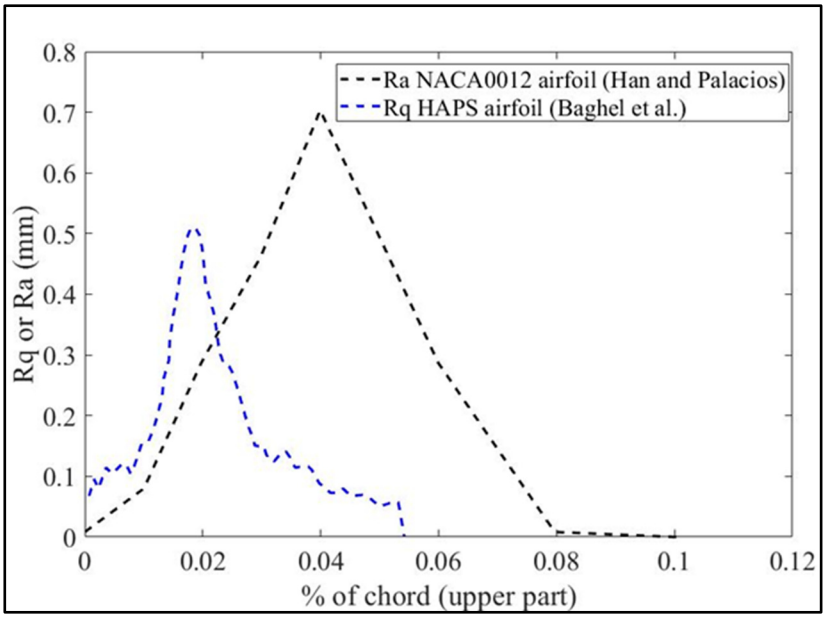

Figure 1.6 Experimental spatial roughness measurements
Adapté de Han & Palacios (2014, p. 15)
et Baghel et al., (2023, p. 9)

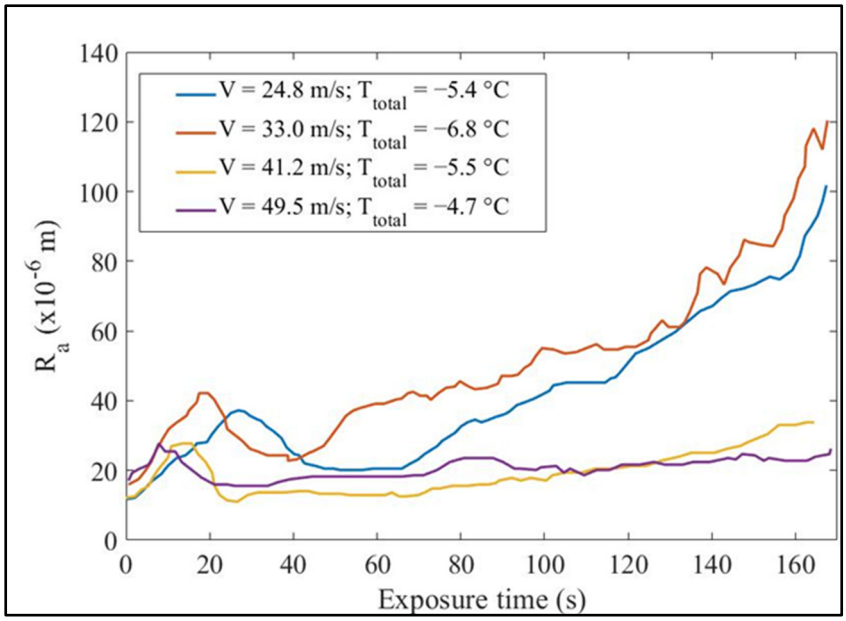

Figure 1.7 Experimental roughness temporal evolution measurements
Adapté de Wang et al., (2022, p. 18)

Figure 1.8 illustrates the influence of the thermal correction model on the ice shape in numerical simulations. Figure 1.8 highlights how the changes in the heat transfer coefficient (equation (1.35)), resulting from the chosen thermal correction, impact the final ice shape on a NACA0012 airfoil in glaze conditions (Ignatowicz et al., 2019a). The results are presented for the smooth SA turbulence model (Spalart & Allmaras, 1992), the rough SA without thermal correction (Aupoix & Spalart, 2003), the rough SA with the Aupoix thermal correction (Aupoix, 2015), and for the rough SA with Morency and Beaugendre thermal correction (Morency & Beaugendre, 2020).

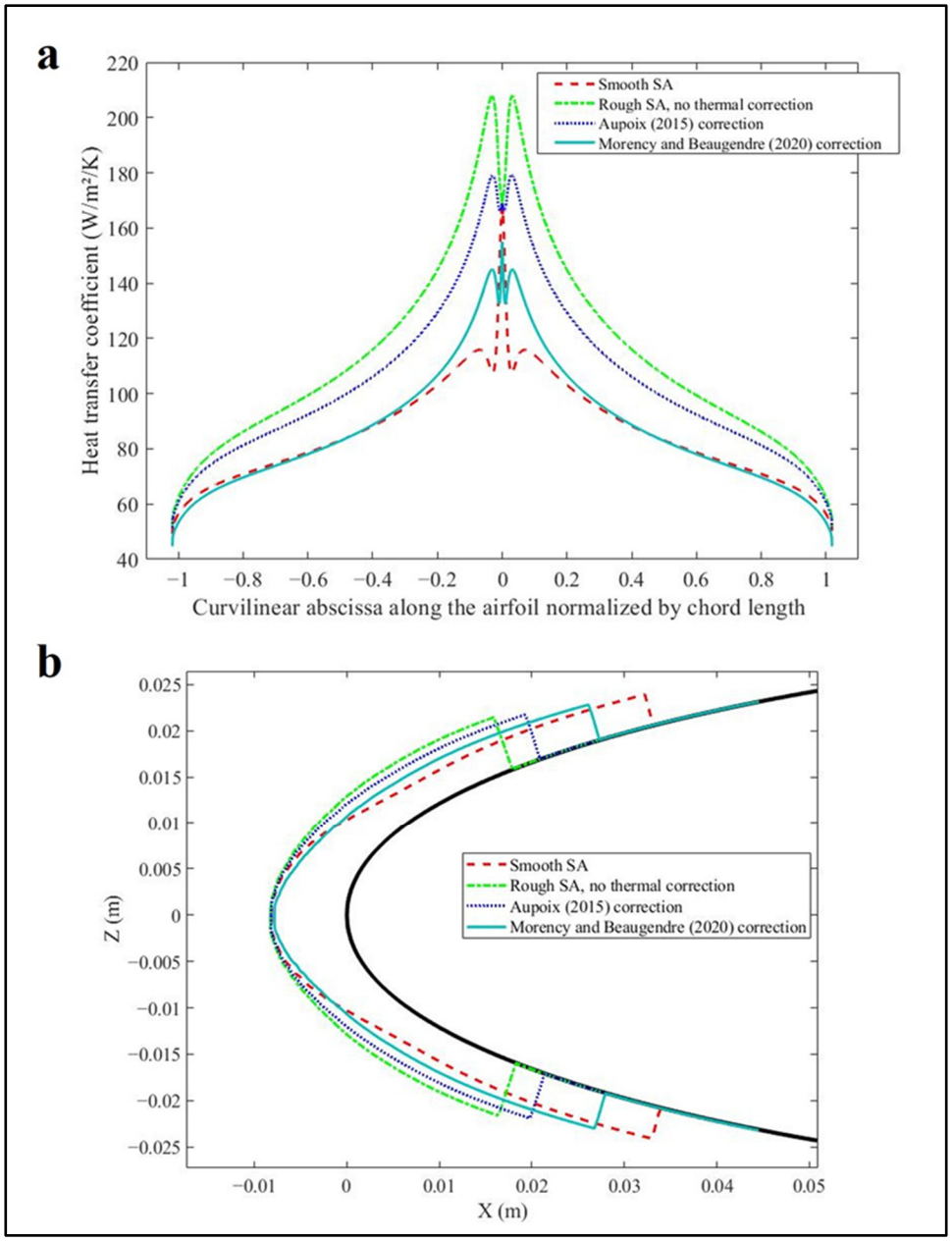

Figure 1.8 (a) Heat transfer coefficient for different models
and (b) Resulting ice shapes
Adapté de Ignatowicz et al., (2019a, p. 8 et p. 12)

Given the uncertainty and complex roughness patterns in the experimental setups, empirical correlations were developed to take surface roughness into account in the numerical simulations. These correlations are reviewed in the next subsection.

1.5.2 Empirical Roughness Correlations in Ice Accretion Simulations

Usual roughness correlations developed for sand grain paper, manufactured roughness elements, and more regular roughness patterns must be adjusted for irregular ice-induced roughness. Ice-specific roughness height and ESGR correlations were developed in an attempt to mimic the experimental observations. The early correlations assumed a uniform roughness pattern for the sake of simplification and kept the same roughness for all atmospheric conditions (Wright, Gent, & Guffond, 1997). Gent et al. (Gent, Markiewicz, & Cansdale, 1987) suggested a roughness height function of the liquid water content (LWC), measuring the mass of liquid water droplet in a given volume of dry air (usually expressed in g/m^3), the freestream velocity, the ambient air temperature, and the airfoil chord length c. Ruff (Ruff & Berkowitz, 1990) suggested a correlation for a uniform ESGR estimation. Shin and Bond (Shin & H. Bond, 1992) extended this correlation to include the dependency to the median volume diameter (MVD) of the water droplets, noticing that this dependency vanishes for MVD below 20 μm. The correlations from Ruff (Ruff & Berkowitz, 1990) and Shin and Bond (Shin & H. Bond, 1992) take the general form given by equation (1.36). The coefficients *A, B, C,* and *D* are functions of the LWC, the freestream temperature, the freestream velocity, and the MVD (for (Shin & H. Bond, 1992) only), respectively.

$$k_s = A_{LWC} \times B_T \times C_{V\infty} \times D_{MVD} \times 0.001177 \times c \tag{1.36}$$

Recent works by CIRA still use the Shin and Bond uniform relation to determine k_s (Cinquegrana et al., 2023). The commercial software FENSAP-ICE initially used Shin and Bond uniform correlation (Beaugendre, Morency, Habashi, & Benquet, 2003; Shin et al., 1991), or a constant user-defined k_s. These uniform roughness correlations are still available in the FENSAP-ICE package and are regularly used (Martini, Ibrahim, Contreras Montoya, Rizk, & Ilinca, 2022). FENSAP-ICE later received a non-uniform roughness beading model accounting for the roughness variability in space and time (ANSYS, 2020; Croce, Candido, Habashi, Aubé, & Baruzzi, 2009; Ozcer et al., 2011). Li et al. (Yan, Chao, Shi-nan, & Du, 2011) also developed a non-uniform roughness distribution in FENSAP-ICE, accounting for

the state of the liquid water. In case of a continuous liquid film, the roughness height depends on the film height h_w as in equation (1.37), where g_z is the gravitational constant, $|\boldsymbol{\tau}_{wall}|$ is the wall shear stress magnitude, and μ_w is the water viscosity. In the case of scattered beads, the gravitational forces and water surface tension drive the roughness height.

$$k = \frac{3}{4}\frac{|\boldsymbol{\tau}_{wall}|}{\mu_w}\sqrt{\frac{{h_w}^3}{g_z}} \tag{1.37}$$

Fortin et al. (Fortin, Laforte, & Ilinca, 2006), also derived a specific roughness height correlation function of the local wall shear stress and local water film thickness. Anderson and Shin (Anderson & Shin, 1997) also developed a non-uniform roughness height correlation, based on the local freezing fraction *f*. The freezing fraction is the proportion of incoming water (runback and impingement) that actually freezes in a control volume. This roughness height correlation, used in the ice accretion software LEWICE (Wright, 2008), is given in equation (1.38).

$$k = \frac{1}{2}\sqrt{0.15 + \frac{0.3}{f}} \tag{1.38}$$

Fortin (Fortin, 2019) recently developed a logarithmic correlation for the ESGR height that includes the local collection efficiency β, the water latent heat of fusion L_{fus}, the water fusion temperature T_0, and the recovery temperature T_{rec} alongside the liquid water content LWC (equation (1.39)).

$$\frac{{k_s}^{0.3}}{c^{0.3}} = 0.0167 \ln\left(\beta\frac{LWC}{\rho}\frac{L_{fus}}{c_{pg}(T_0 - T_{rec})}\right) + 0.1874 \tag{1.39}$$

To account for the spatial variability of the roughness height, and following the LEWICE correlation (equation (1.38)), Han & Palacios (Han & Palacios, 2017) derived a parabolic roughness distribution with respect to the wrapped distance s from the stagnation point. This correlation, with the smooth width a and the icing limit b as parameters, takes the form of equation (1.40).

$$k(s) = \left[\frac{-4k_0}{(b-a)^2}\left(s - \frac{b+a}{2}\right)^2\right] + k_0 \tag{1.40}$$

The parameters a, b, and k_0 in equation (1.40) are mainly dependent on the local freezing fraction, the accumulation parameter (Han & Palacios, 2017), and the airfoil leading edge radius. The correlation somehow fits the experimental roughness height, as plotted in Figure 1.9.

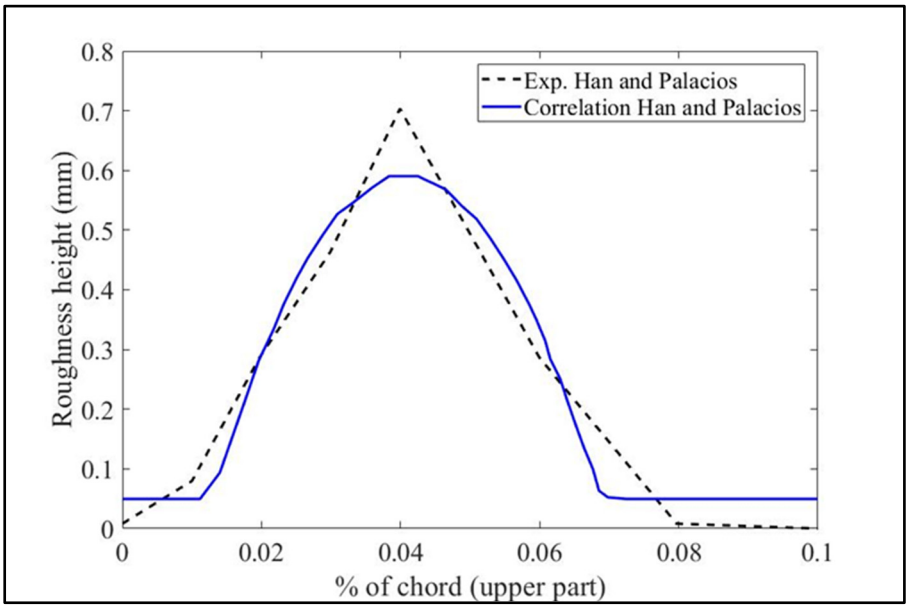

Figure 1.9 Parabolic correlation from Han and Palacios (equation (1.40))
Adapté de Han & Palacios (2017, p. 5)

The recent advances made in ONERA with the IGLOO3D suite combine both experimental measurements and empirical correlation for the roughness estimation (Radenac et al., 2019). IGLOO3D relies on the thermal correction model from Aupoix (Aupoix, 2015) (see subsection 1.4.2, equations (1.30) to (1.32)). S_{corr} and the roughness height k are measured from experimental short-time-exposure accretions and k_s is then computed using the semi-empirical correlation from Flack & Schultz (Flack & Schultz, 2010). The research work at NASA with the GlennICE code adopts a slightly different approach, where the roughness metric Rq is directly computed using the freezing fraction, the pressure coefficient, and the total temperature. The heat transfer coefficient is then augmented by a correction function of Rq (Wright, Rigby, & Ozoroski, 2023).

Despite all the research efforts to develop roughness correlations for numerical simulations, existing roughness models fail to predict some experimental ice shapes. The roughness models, as well as the accretion models, are probably not universal and their results depend on both test case and code used (Laurendeau et al., 2022; Lavoie et al., 2018). Data-driven calibration methods and uncertainty quantification techniques are emerging solutions that could establish roughness patterns specifically tailored for a given case/code configuration. Such methods are already used for roughness estimation in other engineering fields (Aghaei Jouybari, Junlin, Brereton, & Murillo, 2021). Up to recently, only a few published works utilize the methods to calibrate roughness patterns for ice accretion prediction. Although the calibrated roughness patterns lack universality, the methods open new perspectives for future investigations of roughness models and their impact on ice shapes.

1.6 Conclusion

This paper reviewed how roughness is tackled in wall resolved RANS and the representation of surface roughness in ice accretion simulations. Focusing on the RANS turbulence models with equivalent sand grain roughness (ESGR) approach, the survey established that specific adjustments are required for realistic predictions of both heat transfer and skin friction over surface roughness. These requirements are justified by the boundary layer flow modification induced by roughness, especially the viscous sub-layer. Semi-empirical correlations were

developed through decades to model the roughness geometry and ease its addition in the CFD models. The ice accretion phenomenon is a particular case of a rough surface, where the roughness pattern is highly uncertain, irregular, and difficult to measure. Ice accretion simulation codes need to account for ice roughness. Several icing-specific correlations relate roughness parameters to various atmospheric conditions and local ice properties on surfaces. The most complex correlations attempt to predict the roughness variability in space and time. A research gap was highlighted, showing that the roughness correlations may fail to predict correct ice shapes in some cases. This opens the perspective of using uncertainty quantification tools to improve the roughness pattern prediction for ice accretion simulations and detach the roughness estimation from the historical semi-empirical correlations. As a recommendation, other gaps still need attention such as a better understanding of the roughness time evolution.

1.7 Acknowledgments

The authors want to thank the TOMATO Association (Aéroclub de France), Paris, France, the Office of the Dean of Studies, ÉTS, Montréal, Canada, and SubstanceETS, Montréal, Canada. CFD computations were made on the supercomputer Cedar from Simon Fraser University. This research was enabled in part by support provided by Calcul Québec and the Digital Research Alliance of Canada (alliancecan.ca).

CHAPITRE 2

SENSITIVITY STUDY OF ICE ACCRETION SIMULATION TO ROUGHNESS THERMAL CORRECTION MODEL

Kevin Ignatowicz [a], François Morency [b], Héloïse Beaugendre [c]

[a, b] Département de Génie Mécanique, École de Technologie Supérieure,
1100 Notre-Dame Ouest, Montréal, Québec, Canada H3C1K3
[c] Université de Bordeaux, INRIA, CNRS, Bordeaux INP, IMB, UMR 5251
33405, Talence, France

Article publié dans « Aerospace », Mars 2021

2.1 Abstract

The effects of atmospheric icing can be anticipated by Computational Fluid Dynamics (CFD). Past studies show that the convective heat transfer influences the ice accretion and is itself a function of surface roughness. Uncertainty quantification (UQ) could help quantify the impact of surface roughness parameters on the reliability of ice accretion prediction. This paper aims to quantify ice accretion uncertainties and identify the key surface roughness correction parameters contributing the most to the uncertainties in a Reynolds-Averaged Navier-Stokes (RANS) formulation. Ice accretion simulations over a rough flat plate using two thermal correction models are used to construct a RANS database. Non-Intrusive Polynomial Chaos Expansion (NIPCE) metamodels are developed to predict the convective heat transfer and icing characteristics of the RANS database. The metamodels allow for the computation of the 95% confidence intervals of the output probability distribution (PDF) and of the sensitivity indexes of the roughness parameters according to their level of influence on the outputs. For one of the thermal correction models, the most influential parameter is the roughness height, whereas for the second model it is the surface correction coefficient. In addition, the uncertainty on the freestream temperature has a minor impact on the ice accretion sensitivity compared to the uncertainty on the roughness parameters.

Keywords: aircraft icing, roughness, convective heat transfer, sensitivity study, metamodel, Sobol indices, polynomial chaos expansion.

2.2 Introduction

Icing represents a major threat to in-flight safety. Ice accretion leads to increased aircraft weight, aerodynamic efficiency loss and a potential increase of up to more than 60% in drag (Tagawa et al., 2018). In the 1997–2006 period, 13% of weather-related accidents were caused by icing (Jones, Reveley, Evans, & Barrientos, 2008). The aerodynamic efficiency loss is determined by the geometry of the ice shape, mainly the thickness and extension (Bragg et al., 2005). Developments in numerical simulations, especially RANS-based simulations (Reynolds Averaged Navier-Stokes), have enabled the development of icing codes, useful for the effective anticipation of the icing process (Saeed, 2002). Even if icing codes share similar mathematical models and numerical methods, the predicted ice shapes can vary greatly for the same atmospheric conditions (RTO/NATO, 2001). The discrepancies between shapes can be explained by various reasons, both mathematical and numerical, among them the discrepancy between the convective heat transfer models. The fraction of the shape discrepancy that could be attributed to the thermal modeling remain to be quantified.

Most of the icing codes used to predict the ice accretion shape are based on the Messinger model (Messinger, 1953). The model uses a mass and energy balance involving the convective heat transfer to compute the ice growth on the airplane surface (Lavoie et al., 2018). Past studies have shown that the convective heat transfer, modeled by a convective heat transfer coefficient, has a major impact on the final shape of the ice accretion (Cao, Ma, Zhang, & Sheridan, 2012; Ignatowicz et al., 2019a). The convective heat transfer coefficient does play a key role in the geometry of the ice shape, which needs to be quantified.

The increase in surface roughness due to early ice formation has an impact on the convective heat transfer in the near-wall region. Experimental studies were conducted by NASA to measure the convective heat transfer coefficient, or, equivalently, the Stanton number, on a roughened NACA0012 airfoil (Newton, van Fossen, Poinsatte, & Dewitt, 1988; Poinsatte, Van Fossen, & Dewitt, 1991). More recently, Liu & Hu (Liu & Hu, 2018), Hosni et al. (Hosni et al., 1993), and Dukhan et al. (Dukhan, Masiulaniec, Dewitt, & Fossen, 1999a; Dukhan et al.,

1999b) also carried out related experiments, but on a roughened flat plate, highlighting the influence of the roughness characteristics on the Stanton number. An increase in the heat transfer coefficient was observed for a rough surface as compared to a smooth one, in both airfoil and flat plate cases. From the foregoing, it is therefore reasonable to expect that the initial surface roughness of the wing is influencing the complete icing process by acting on the convective heat transfer at the surface (Hansman et al., 1989; Ignatowicz et al., 2019a). Experimental studies show the variability of roughness characteristics, which depend mainly on the airfoil geometry (Fortin, 2019) and atmospheric conditions (Dukhan et al., 1999b). The incorporation of surface roughness in the RANS model is then subject to uncertainty due to the prevailing lack of knowledge on roughness characteristics in real in-flight situations. The RANS model's roughness parameters are thus epistemically uncertain variables.

To take into account the surface roughness, Aupoix (Aupoix, 2015) worked on improvements of the thermal boundary layer calculations by considering a local increment of the Prandtl number. The thermal correction model from Aupoix, denoted as the HAX model, uses three parameters to incorporate surface roughness in simulations: the roughness height, the equivalent sand grain roughness, and the surface correction coefficient. Another thermal correction model, called the 2PP model, was developed and is also used in the present study (Morency & Beaugendre, 2020). This model relies on two parameters: the roughness height and the equivalent sand grain roughness. The parameters involved in both the HAX and 2PP models are denoted as the roughness parameters for the rest of the paper. To further improve these two models, sensibility studies can play a key role in establishing the most sensitive parameters. Once identified, it will be possible to vary these parameters in experiments or high-fidelity simulations in order to further calibrate and improve the thermal models.

For uncertain input parameters, the uncertainty quantification (UQ) enables the evaluation of the probability distribution function (PDF) of the output of interest and a complete sensitivity analysis (Sudret, Marelli, & Wiart, 2017). A relatively small sample of RANS simulations is needed, and a metamodel is generated based on these sample results. This metamodel allows us to quickly compute a large number of new heat transfer coefficients and ice accretion results.

The Non-Intrusive Polynomial Chaos Expansion (NIPCE) is commonly used for metamodel generation (Marelli & Sudret, 2019). The NIPCE is an efficient approach to estimate measurement uncertainties when complex systems are involved, thus explaining its widespread use in UQ (Cinnella, Congedo, Parussini, & Pediroda, 2010; Weissenbrunner et al., 2016), especially in aeronautics applications (Schaefer, Romero, Schafer, Leyde, & Denham, 2020). The NIPCE approach is also used in turbulence modelling for UQ, as carried out in (Schaefer, Cary, Mani, & Spalart, 2017) to assess the Spalart-Allmaras uncertainty due to the epistemically uncertain model coefficients.

The sensitivity of an output parameter to the input parameter(s) can be evaluated by using a variance-based decomposition (Chen & Jin, 2005; Saltelli et al., 2008). In the variance-based family, the Sobol indexes allow for an estimation of the main (first-order indexes) and interaction (second- and higher-order indexes) effects of an input parameter on the model output (Chan, Saltelli, & Tarantola, 1997). The Sobol indexes classify the input parameters according to their level of influence on a specific output parameter. UQ coupled to NIPCE and Sobol indexes has been used for simulations in aeronautics (Kato, Ito, & Lepot, 2010; Tabatabaei, Raisee, & Cervantes, 2019) and heat transfer (P. Zhu, Yan, Song, Li, & Feng, 2016). Despite UQ's wide use in aeronautics and heat transfer applications, no published paper has yet thoroughly characterized, from a statistical point of view, the sensitivity of ice accretion to surface roughness parameters. The closest related work is from Raj et al. (Raj, Yee, & Myong, 2020), where the sensitivity of the ice accretions to the equivalent sand grain roughness is compared to the sensitivity to ice density, droplet distribution and number of ice layers. However, no comparison is made for the roughness parameters between them.

The present work is a first attempt to use UQ in aircraft icing to relate directly heat transfer model parameters to ice shape predictions. In addition, UQ allows the identification of the key parameters. The technical challenge in this case is double. First, an efficient way of generating a large sample set had to be used: making a sensitivity study requires a large database. The metamodel approach is well suited to this challenge, avoiding the computational effort that computational fluid dynamics (CFD) simulations would have required. Secondly, a reliable

gauge of the importance of each roughness parameter was needed. The Sobol indexes give us the opportunity of directly reading on a bar chart the classification of the parameters depending on their level of influence on ice accretion. The objective is to quantify ice accretion uncertainty and identify the key roughness parameters contributing the most to the uncertainty of the thermal correction models for RANS equations. The importance of roughness parameters uncertainty compared to the freestream temperature uncertainty on the ice accretion shape is also investigated. To reduce the number of parameters, avoid curvature effects on ice growth and pressure gradients, the airfoil is replaced by a flat plate.

Metamodels generated from a sample of RANS simulations, alternatively using the HAX (Aupoix, 2015) and the 2PP (Morency & Beaugendre, 2020) thermal correction models, are constructed to predict the convective heat transfer and ice accretions on a flat plate. For the ice accretion part, the flat plate has the droplet collection efficiency of a NACA0012, to be representative of an airfoil. The NIPCE metamodels are then used for UQ and to evaluate the Sobol sensitivity indexes associated with the roughness height, the equivalent sand grain roughness, the surface correction coefficient in the case of the HAX model and, finally, the freestream temperature. The novelty of the current work resides in the application of the NIPCE metamodeling method to rough icing simulations. The NIPCE has low sample requirements compared to the traditional Monte-Carlo methods used in the past (DeGennaro, Rowley, & Martinelli, 2015). In similar applications, Raj et al. (Raj et al., 2020) use the radial basis function (RBF) metamodeling. The performance of polynomial-type metamodels, like the NIPCE, compared to RBF methods, is better for small sample designs, giving higher regression coefficients (Hussain, Barton, & Joshi, 2002). This enhanced accuracy, which combined with the fast response due to the low sample sizes led to the choice of this tool to perform the metamodeling.

The paper starts with a presentation of the physical set-up where the flat plate geometry used is presented and contextualized, along with the HAX and 2PP RANS thermal correction models and the ice accretion model. Then, the methods retained for UQ and sensitivity analysis, including the NICPE metamodeling and the Sobol indexes, are described. Finally, the

last section focuses on the results obtained from the simulations and the metamodeling process by highlighting the PDFs of the outputs and the Sobol indexes associated with the roughness parameters. The results allow for the determination of the most influential roughness parameter for both thermal correction models, and show the relative importance of roughness uncertainty compared to the freestream temperature uncertainty on the ice accretion shape.

2.3 Physical Set-Up

The goal of this section is, first, to define the test case geometrical configuration in the context of the RANS equations coupled to a Messinger model for ice accretion prediction. In this study, RANS equations are solved using a thermal correction model — either the HAX model or the 2PP model, which is presented in the second part of the section.

2.3.1 Convective Heat Transfers over a Rough Flat Plate

For an iced wing, the quasi-random and unknown characteristics of surface roughness introduce uncertainties in the RANS model. The initial uncertainty on roughness characteristics propagates throughout the thermal correction and ice accretion models, leading to uncertain ice accretion characteristics. Similarly to the previous work of Dukhan et al. (Dukhan et al., 1999b), a rough flat plate geometry is used to model an airfoil, neglecting the pressure gradient effects on the flow. The flat plate represents the upper part of the airfoil, that was unrolled and retains the curvilinear impinging water droplet collection efficiency of the airfoil, as shown on Figure 2.1a. These assumptions allow for the computing of an ice accretion similar to what is seen on the airfoil, but neglect the curvature effects. Neglecting the curvature effects will produce a slightly underestimated ice thicknesses compared to a curved airfoil. In addition, the absence of positive pressure gradient will increase the boundary layer thickness. This flat plate simplification should not impact the study conclusions, since the sensitivity is ultimately monitored, and not the absolute ice thickness. The epistemic uncertainty is illustrated by two different roughness characteristics (see Figure 2.1b). Given their geometrical differences, these patterns lead to different convective heat transfer coefficients (see Figure 2.1c), which in turn cause differences in the characteristics of ice accretions (see Figure 2.1d).

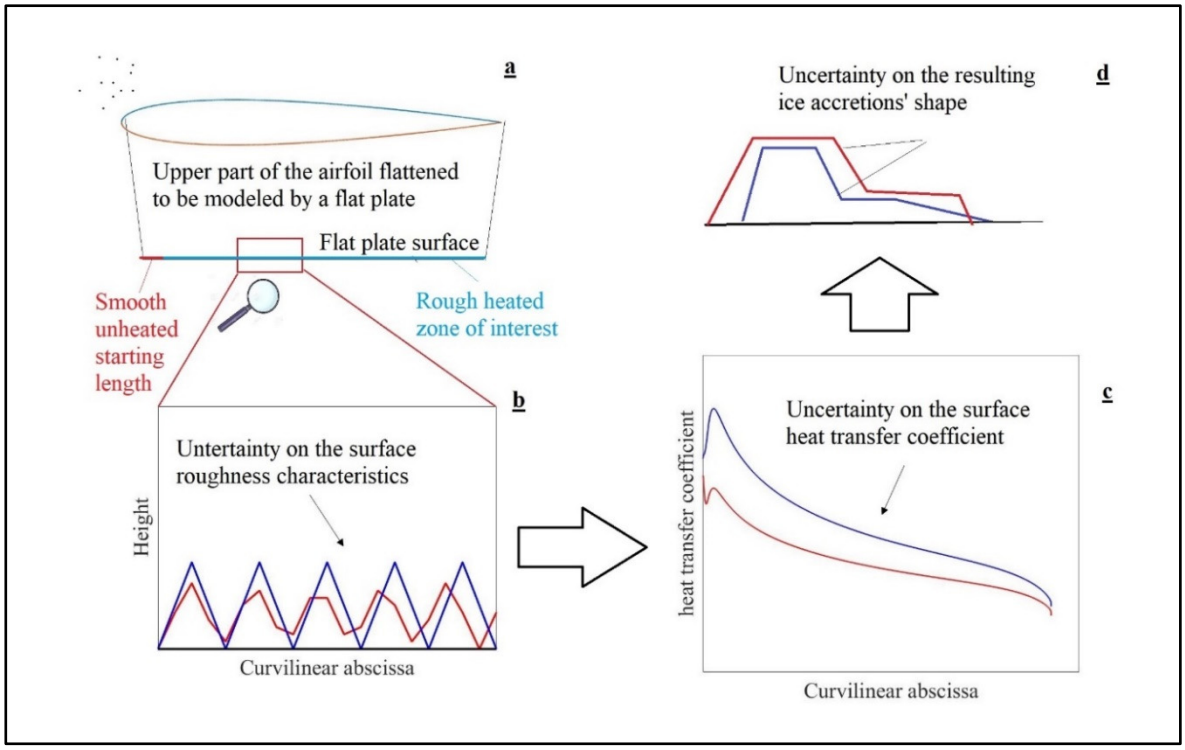

Figure 2.1 Uncertainty propagation from surface roughness to ice accretion shape

The database needed to obtain the metamodels relies on RANS simulations. The geometry used in the present work is a 2-m-long horizontal flat plate. This geometry is commonly used in CFD validation (Economon, Palacios, Copeland, Lukaczyk, & Alonso, 2015), and the mesh size is selected according to a grid study presented in (Morency & Beaugendre, 2020). The 2D mesh of the domain consists of a structured domain of 137 by 97 cells with 114 points on the flat plate surface. The growth rate in the direction perpendicular to the plate is 1.3, and the y^+ value is between 0.45 and 1.35. In a rough configuration, with this mesh, the difference with the experimental results of Hosni et al. (Hosni et al., 1993) for the Stanton number evaluation was less than 7% for both the HAX and 2PP thermal correction models. In addition, the flat plate configuration was extensively studied both numerically (Yanxia, Yewei, Chunhua, & Xian, 2010) and experimentally (Dukhan et al., 1999b) in the context of aircraft ice accretion studies. The complete 2.33 m by 1 m domain is sketched in Figure 2.2. The leading edge of the flat plate is located 0.33 m downstream of the domain inlet.

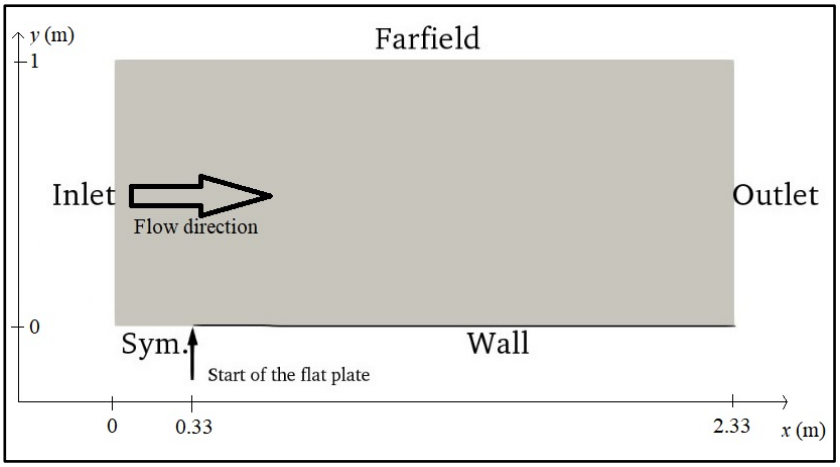

Figure 2.2 Visual representation of the computational domain

2.3.2 Air Mathematical Models

The compressible flow field coming through the inlet boundary of Figure 2.2 is at Mach 0.2. The Reynolds number based on the length of the plate is 9 million. The Boeing correction for roughness (Aupoix & Spalart, 2003) and the thermal correction models are implemented in the Spalart-Allmaras turbulent model of the SU2 6.2.0 solver (Economon et al., 2015; Morency & Beaugendre, 2020). To obtain the convective heat transfer, the surface temperature is set to 273.15 K, while the ambient air is at 262.04 K. In accordance with the experimental set-up of Dukhan et al.(Dukhan et al., 1999b), the first 5.2 cm of the plate are unheated, adiabatic, and smooth. This starting length allows the boundary layer at the beginning of the rough zone to have a thickness of 1.83 mm.

Two RANS thermal correction models are alternatively used: the HAX model (Aupoix, 2015), and the 2PP model (Morency & Beaugendre, 2020). Mainly, these models quantify the shift ΔT^+ of the nondimensional wall temperature in the thermal boundary layer induced by surface roughness. This shift was first observed for the velocity profile, further denoted as ΔU^+ (Nikuradse, 1933).

The temperature shift ΔT^+ is modelled by increasing the turbulent Prandtl number Pr_t by an additional ΔPr_t in the near-wall region. For the HAX model (Aupoix, 2015), the Prandtl number correction ΔPr_t is a function of the velocity shift ΔU^+, the distance to the wall d, the roughness height k, the equivalent sand grain roughness k_s, and a non-dimensional corrected surface ratio S_{corr} (Radenac et al., 2018). This computation only applies in the region located fewer than five times the roughness height away from the wall (i.e., $d/k < 5$).

$$\Delta Pr_t = (A(\Delta U^+)^2 + B\Delta U^+) exp\left(-\frac{d}{k}\right) \tag{2.1}$$

With:

$$A = (0.0155 - 0.0035 S_{corr})(1 - e^{-12(S_{corr}-1)}) \tag{2.2}$$

$$B = -0.08 + 0.25 e^{-10(S_{corr}-1)} \tag{2.3}$$

$$\Delta U^+ = \frac{1}{\kappa \cdot \log\left(1 + \frac{Re_s}{exp(1.3325)}\right)} \tag{2.4}$$

The 2PP model (Morency & Beaugendre, 2020), depends only on two parameters, k and k_s:

$$\Delta Pr_t = g \times 0.07083 \times {Re_s}^{0.45} \times Pr^{0.8} \times exp\left(-\frac{d}{k}\right) \tag{2.5}$$

In equation (2.4) and equation (2.5), the roughness Reynolds number Re_s is defined as $u_\tau k_s/\nu$. Finally, $g = 1$ if $Re_s \geq 70$; $g = \frac{\ln(Re_s)-\ln(5)}{\ln(70)-\ln(5)}$ if $5 < Re_s < 70$ and $g = 0$ if $Re_s \leq 5$.

2.3.3 Ice Accretion Model

Once the heat transfer along the flat plate is known, the ice accretion simulations can be performed. To compute the 2D ice accretions, the Messinger approach is used (Lavoie et al.,

2018; Messinger, 1953). The basis of this approach is to compute the ice growth rate in a control volume using a mass and an energy balance. The control volume and the contributions to the balances are illustrated in Figure 2.3.

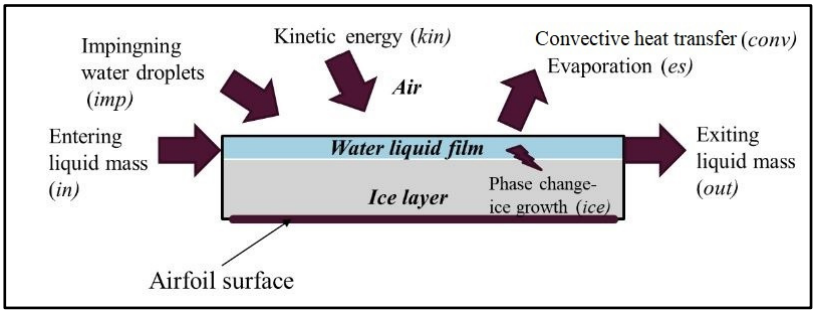

Figure 2.3 Control volume and energy and mass terms used in the Messinger icing model

The mass balance (see equation (2.6)) and the energy balance (see equation (2.7)) are given by the following set of two equations:

$$\dot{m}_{in} + \dot{m}_{imp} - \dot{m}_{ice} - \dot{m}_{es} - \dot{m}_{out} = 0 \tag{2.6}$$

$$\dot{Q}_{conv} + \dot{Q}_{es} + \dot{Q}_{imp} - \dot{Q}_{kin} - \dot{Q}_{ice} - \dot{Q}_{in} = 0 \tag{2.7}$$

The subscripts appearing in equation (2.6) and (2.7) are defined in Figure 2.3. More details on the terms involved and the resolution procedure are given in the literature (Ignatowicz et al., 2019a; Özgen & Canıbek, 2008). The convective heat transfer, whose coefficient is obtained by the models involved in the previous two subsections, has the general expression given by equation (2.8):

$$\dot{Q}_{conv} = h_c(T_w - T_{rec}) \tag{2.8}$$

with the recovery temperature given by:

$$T_{rec} = T(1 + Pr^{1/3} \cdot \frac{\gamma - 1}{2} M^2) \tag{2.9}$$

The collection efficiency over a NACA0012 airfoil was applied on the flat plate surface and is shown in Figure 2.4, where *s* represents the curvilinear abscissa along the airfoil surface, and *c* represents the chord. The air freestream velocity is 64.9 m/s, the liquid water content is 1.3 g/m^3, the droplets diameter is 20 µm, and the angle of attack is 0°. Only the upper part of the airfoil, studied through the flat plate representation, is plotted. Note that the plot of Figure 2.4 is translated for the simulations to have *s/c* = 0 at the very beginning of the rough zone (at *x* = 5.2 cm), to have a nonzero boundary layer thickness representative of an airfoil stagnation point.

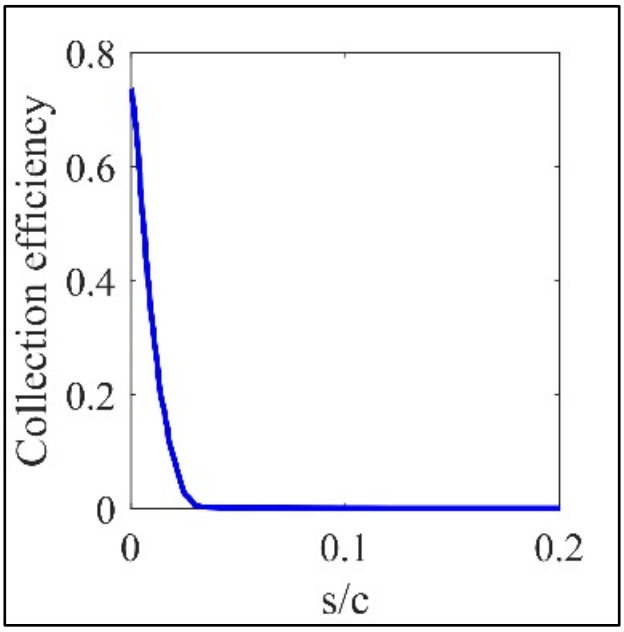

Figure 2.4 Collection efficiency of the upper part
of the NACA0012 airfoil as used on the
flat plate surface
Adapté de Özgen & Canıbek (2008, p. 310)

The icing model presented was successfully verified in previous studies (Ignatowicz et al., 2019b), and the ice accretion dependency on the roughness parameters was preliminarily

highlighted (Ignatowicz et al., 2019a). The ice thickness is linked to the ice accretion mass, through the ice density of 917 kg/m^3, and the exposure time was fixed to 480 s for this work.

2.4 Uncertainty Quantification and Sensitivity Analysis Method

UQ is used to evaluate the ice accretion uncertainties caused by the heat transfer model parameters in the presence of surface roughness and to identify the most influential parameters. In this section, the uncertain parameter sampling and the NIPCE metamodeling are first depicted, followed by the Sobol indexes definition. In this work, the expression "output of interest", denoted as Y_i, refers to either one of the following features: (1) the local value of the convective heat transfer coefficient at a specified point or (2) the ice accretion characteristics: maximum thickness or ice extension.

2.4.1 Uncertain Parameter Sampling and Metamodel

The UQ analysis is used to determine how the roughness' epistemic uncertainty can impact the PDFs of the ice accretion characteristics. The uncertain inputs of the thermal correction models' parameters are the roughness height k, its ratio with the equivalent sand grain roughness k_s/k and the corrected surface ratio S_{corr} for the HAX model (Aupoix, 2015) and k, k_s/k for the 2PP model (Morency & Beaugendre, 2020). The choice of the ratio k_s/k instead of k_s alone comes from the fact that k and k_s are linked, for example, with the Dirling relation (Dirling, 1973).

The roughness height k was experimentally studied in the literature. For example, Dukhan et al. (Dukhan et al., 1999b), give a range of variations between 0.41 mm and 4.32 mm on a flat plate measuring 0.458 m by 0.458 m, at a Reynolds number of 2,000,000. These values correspond to the roughness elements observed in different atmospheric conditions, and which led to different surface roughness types. The parameter k_s is taken from Fortin (Fortin, 2019), who reviewed the validation test cases used for the LEWICE software (Wright, Struk, Bartkus, & Addy, 2015), and concluded on a range of variations for k_s between 0.309 mm and 1.247 mm for airfoils with a chord varying between 53.3 cm and 91.4 cm. Both of these ranges for k and

k_s are maintained in the present study and lead to a k_s/k ratio ranging between 0.288 and 0.753. The last input parameter, S_{corr}, is taken from Aupoix and has a value between 1 and 2.5 (Aupoix, 2015). For all the parameters, a uniform PDF between the margins given above is assumed. Although other values are possible in practice, Table 2.1 gives the distributions used in this study.

Table 2.1 Summary of the distributions for the input parameters

Parameter X_i	Minimum	Maximum	Distribution
k (mm)	0.41	4.32	Uniform
Ratio k_s/k	0.288	0.753	Uniform
S_{corr}	1	2.5	Uniform

With the range of distribution of each parameter defined, the input parameters can be sampled by Latin Hypercube Sampling (LHS), which is one of the methods commonly used to obtain random, but homogeneously spread, sample points (Stein, 1987). The HAX model has 190 sample simulations and the 2PP model 120, for their respective analyses, as shown in Figure 2.5. These sample size ranges are in agreement with the literature, which gives a sample size between 160 and 200 for a three-input model (Schaefer et al., 2017). For instance, Solaï et al. used a sample of 115 simulations for their analysis with four input parameters (Solaï, Beaugendre, Congedo, Daccord, & Guadagnini, 2019).

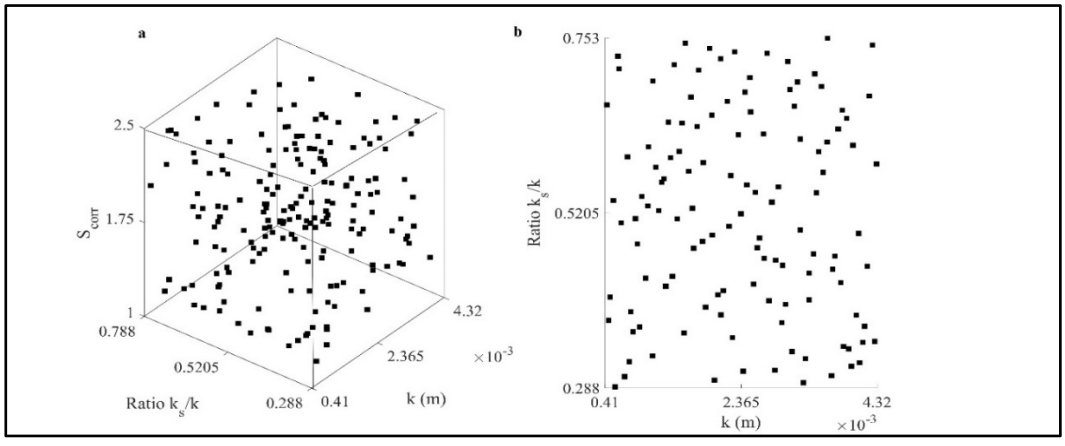

Figure 2.5 Sample points for (a) the HAX model and (b) the 2PP model obtained by Latin Hypercube Sampling

The sampling presented gives triplets (HAX model) or doublets (2PP model) of roughness parameters that are used as inputs for the RANS simulations. The database of convective heat transfer coefficients and ice accretion characteristics allows the construction of the metamodels.

The framework used for the UQ analysis, as well as for the subsequent sensitivity analysis, is the UQLab suite (Sudret et al., 2017). To be able to generate a large number of results (i.e., up to several thousand for the sensitivity analysis) without the need to run additional RANS simulations, three metamodels constructed from the database are used, as shown in Table 2.2. A metamodel can be represented as a function M estimating the output of interest Y_i from the input vector $\boldsymbol{X}$, whose components are X_j.

Table 2.2 Metamodels generated

Metamodel	Input parameters X_j		Output of interest Y_i
	HAX	2PP	
M_1	k, k_s/k, S_{corr}, x	k, k_s/k, x	Convective heat transfer coefficient value at position x
M_2	k, k_s/k, S_{corr}	k, k_s/k	Maximum ice accretion thickness
M_3	k, k_s/k, S_{corr}	k, k_s/k	Ice accretion extension

The method retained to create the metamodels is the NIPCE (Marelli & Sudret, 2019). This existing metamodeling tool is frequently used in UQ, and the present work specifically applies it to the UQ for roughness study in aircraft icing. This method is suitable for models with two and three input parameters. The general expression of a NIPCE metamodel is given by equation (2.10).

$$Y_i = M(\boldsymbol{X}) = \sum_{\alpha} y_\alpha \times \psi_\alpha(\boldsymbol{X}) \tag{2.10}$$

When generating a metamodel, the leave-one-out (*LOO*) error value allows an estimation of the metamodel quality. The *LOO* value, based on the mean square error between the observed and predicted values, quantifies the ability of the metamodel to predict an output value close to what the RANS computation would have calculated (Marelli & Sudret, 2019). The

computation of the *LOO* error relies on the cross-validation technique. For an N-sample design, the main aspect of the *LOO* calculation is to create N metamodels M^i, which are constructed on the CFD database where the i^{th} simulation was dropped, leaving *N*-1 sample points. The difference between the predicted value of the dropped sample by M^i and its real CFD value allows the computation of the *LOO* error (Blatman & Sudret, 2010) as in equation (2.11).

$$LOO = \frac{\sum_{i=1}^{N}\left(Y^{(i)} - M^{i}\left(X^{(i)}\right)\right)^2}{\sum_{i=1}^{N}(Y^{(i)} - \bar{Y})^2} \tag{2.11}$$

In equation (2.11), $X^{(i)}$ and $Y^{(i)}$ represent the input parameters of the i^{th} CFD sample simulation and the corresponding CFD output, respectively. Finally, $\bar{Y}$ is the mean value of the output of interest on the sample dataset. The *LOO* error is a common tool frequently used in metamodeling application. For instance, Jung et al. extensively used the *LOO* error for anti-icing performance metamodeling for engine intake (Jung, Raj, Rahimi, Jeong, & Myong, 2020).

2.4.2 Sobol Indexes Definition

The purpose of a sensitivity analysis is to identify the uncertain parameters that contribute the most to the variations observed on Y_i (Saltelli et al., 2008). Based on the results of the metamodels, the sensitivity of each Y_i to the X_i is quantified. The Sobol sensitivity indexes are based on the decomposition of the total variance of Y_i. The first-order Sobol index for X_i and the second-order Sobol index for X_i and X_j are defined by equation (2.12) and equation (2.13), respectively.

$$S_i = \frac{V(Y) - E\left(V(Y|X_i)\right)}{V(Y)} \tag{2.12}$$

$$S_{i,j} = \frac{V(Y) - E\left(V\left(Y\middle|X_i, X_j\right)\right)}{V(Y)} \tag{2.13}$$

Finally, for a generic study with three input parameters (*i, j, k*), the total Sobol index for the parameter *i* is:

$$S_i^{TOT} = 1 - (S_j + S_k + S_{j,k}) \tag{2.14}$$

According to Chan et al. (Chan et al., 1997), a parameter with a total Sobol index greater than 0.8 can be considered as "very important", with the total Sobol index between 0.5 and 0.8 as "important", between 0.3 and 0.5 as "unimportant" and "negligible" with an index below 0.3. Consequently, in the present icing application, a total Sobol index close to 1 characterizes an input parameter having a big effectiveness and influence on the ice accretion.

To study the impact of the temperature on the ice accretion sensitivity, the Sobol indexes are computed in two distinct sets of tests. First, the Sobol indexes are estimated on metamodels M_1, M_2 and M_3 as described in Table 2.2, with the roughness parameters as the only uncertain inputs. For the second set of tests, the temperature is added as an uncertain input parameter. Along with the roughness uncertain parameters of ice accretion metamodels M_2 and M_3, the freestream temperature T is added as an epistemically uncertain parameter varying uniformly between 261.5 K and 262.5 K. This last series of tests with an uncertain temperature is used to determine if ice accretion is more sensitive to the roughness uncertainty than to the temperature uncertainty.

2.5 Results and Discussion

With the RANS and the ice accretion models defined, the UQ and Sobol indexes can be applied to study the ice accretion uncertainties over a flat plate. For the outputs of interest, the goals are to evaluate the PDFs and the level of influence of the roughness parameters. For each metamodel and each thermal correction model, the following aspects retain attention: (i) the quality of the metamodel, quantified by the *LOO* error; (ii) the PDF of the outputs of interest, with the 95% confidence intervals; and (iii) the sensitivity of the outputs of interest to the input parameters, described by the Sobol indexes. For concision, one relevant figure is shown for

each aspect listed, and the remaining data for all possible metamodel/thermal correction model combinations are summarized in tables.

The outputs of interest listed in Table 2.2 are illustrated on Figure 2.6. Figure 2.6a shows the outputs of interest on a plot of the convective heat transfer coefficient versus the x position on the flat plate surface. Figure 2.6b shows the outputs of interest on a graphical representation of an ice accretion. Note that the zone of interest is only the rough part of the flat plate, beginning at x = 5.2 cm.

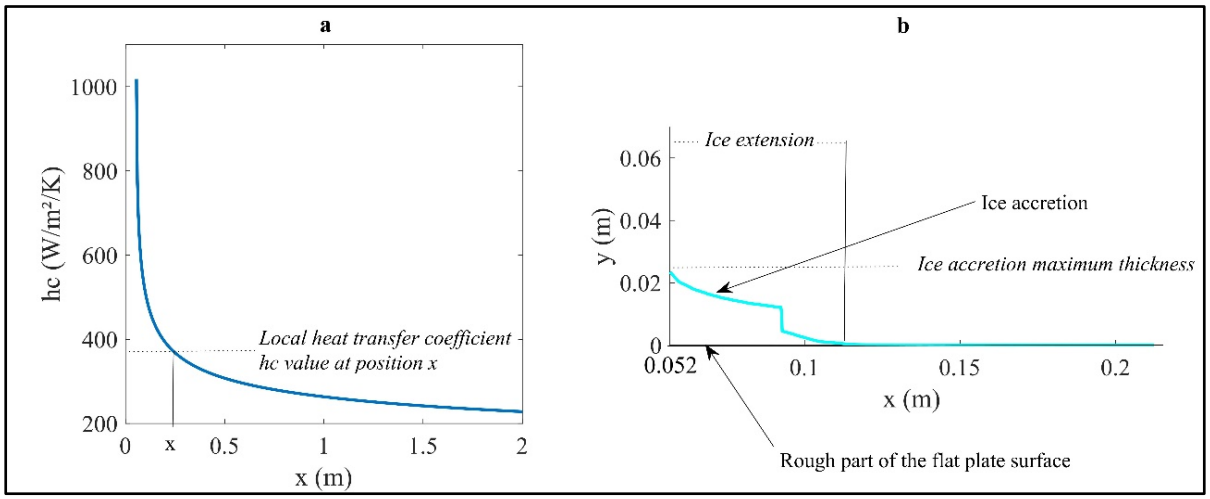

Figure 2.6 Outputs of interest for (a) the heat transfer coefficient and (b) the ice accretion

All the sample simulations will give the same global trends, as observed on Figure 2.6, with variations induced by the roughness from one sample to another. The convective heat transfer coefficient (Figure 2.6a) will present a maximum value at the stagnation point before decreasing when traveling downstream along the flat plate. For the ice accretion shape (Figure 2.6b), the maximum thickness will be at the stagnation point, corresponding to the location of maximum collection efficiency (see Figure 2.4). The thickness will decrease along the plate with the decrease of the collection efficiency. In addition, the runback water will end up freezing, giving the observed step, located, in the example of Figure 2.6b, at x = 0.08 m. The step is due to the fact that no more liquid water runs back further downstream.

2.5.1 Precision of the Metamodels Generated

Prior to looking at the *LOO* error value, the precision of the metamodel may be visualized by plotting the NIPCE prediction for the set of input parameters used for the RANS simulations versus the actual RANS calculated value. Figure 2.7 shows this scatter plot for the metamodel M_1 of the HAX model. Y_{RANS} represents the RANS-calculated values of the local convective heat transfer coefficient at x = 11.36 cm (with x = 0 taken at the very beginning of the flat plate), while Y_{NIPCE} represents the corresponding values predicted by the metamodel. The points for the 190 sample simulations are plotted and show that the metamodel M_1 for the HAX model has a good precision, with an absolute mean error between the RANS-calculated values and the NIPCE-predicted values of 0.90 W/m²/K and a linear regression coefficient of 0.9999. This regression coefficient value is higher than the ones commonly accepted in the literature for sensitivity analysis (Raj et al., 2020). The *LOO* error for this metamodel M_1 at x = 11.36 cm is 4.25×10^{-4}. The local position x = 11.36 cm was chosen among the 114 possible surface grid points to illustrate the behavior of the metamodel.

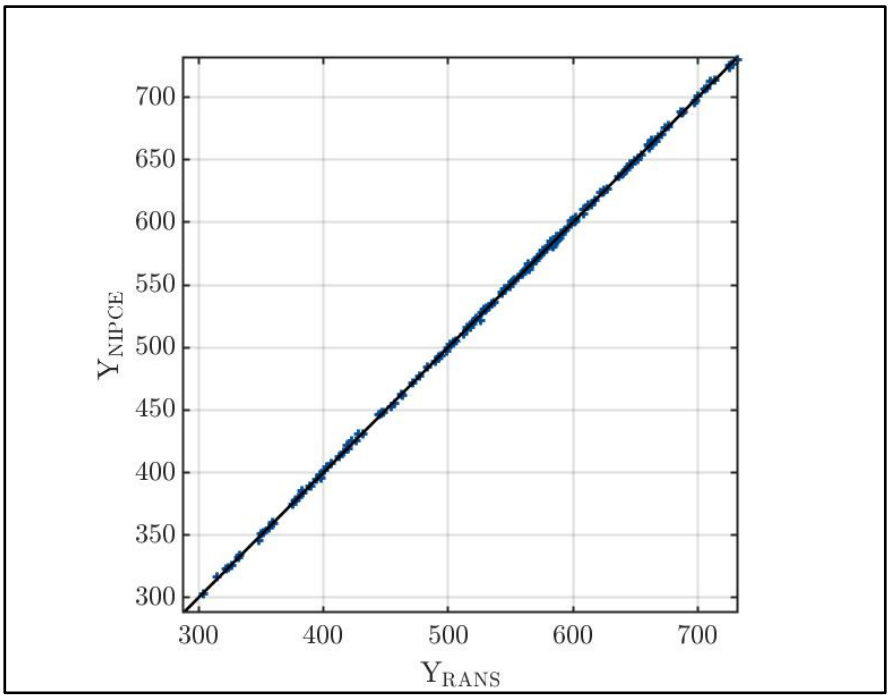

Figure 2.7 NIPCE predicted (M_1) vs. RANS calculated value
for the local heat transfer coefficient at x = 11.36 cm (HAX model)

The trend shown in Figure 2.7, with all the scatter points homogeneously packed close to the identity line, suggests a metamodel making accurate predictions. Checking the precision of all the metamodels leads to the *LOO* errors presented in Table 2.3.

Table 2.3 *LOO* errors for all the metamodels

Metamodel	Output of interest Y_i	*LOO* error	
		HAX	2PP
M_1	Heat transfer coefficient value at 11.36 cm	4.25×10^{-4}	2.15×10^{-4}
M_2	Maximum ice accretion thickness	4.12×10^{-3}	1.05×10^{-4}
M_3	Ice accretion extension	1.52×10^{-2}	4.49×10^{-4}

The values presented in Table 2.3 show that the convective heat transfer coefficient is well predicted by the metamodels: the *LOO* error for both HAX and 2PP is in the neighborhood of 10^{-4}, which is an acceptable value that leads to a precision similar to the one of Figure 2.7. Nevertheless, the 2PP model has a more predictable behavior than its HAX counterpart. The values show a *LOO* error two to four times smaller than the one of the HAX model for a given metamodel. For the ice accretion characteristics, the HAX model shows a loss of predictability since the *LOO* errors rise to the 10^{-3} to 10^{-2} range of values. On the other hand, the 2PP model still presents a well-predictable icing behavior with the *LOO* error once again in the 10^{-4} magnitude.

2.5.2 Outputs of Interest PDFs

The metamodel-generated databases allow the computation of the outputs of interest PDFs. Figure 2.8 shows all the ice accretion shapes obtained for (a) the HAX model and (b) the 2PP model. Additionally, for each of the models, one ice accretion chosen among the set is plotted alone for clear visualization. Each of the colored lines on the top charts of Figure 2.8 represents one specific accretion obtained with one particular sample run. For the single plotted accretion, the specific roughness parameters for the HAX model (a) are k = 1.14 mm, k_s/k = 0.599 and S_{corr} = 1.17, and for the 2PP model (b), k = 2.07 mm and k_s/k = 0.385. The general trend illustrated in Figure 2.6, with a step observed in the accretion, is visible for all the sample

accretions. Figure 2.8 shows that varying the roughness parameters changes the position of the step, which characterizes the ice extension along the surface.

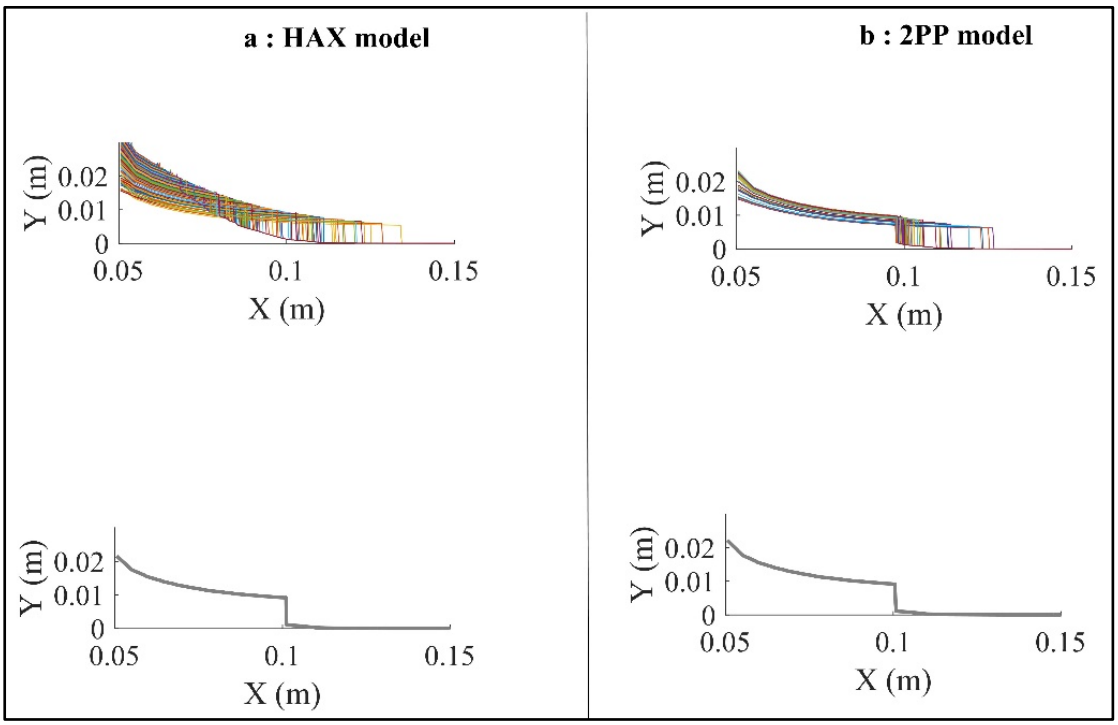

Figure 2.8 Examples of accretions obtained: (a) HAX model and (b) 2PP model

Using all 190 (HAX model) or 120 (2PP model) data sets allows for the computing of the NIPCE-predicted PDF of the outputs of interest. The NIPCE allows for an increase in sample size, but the PDF is similar to the PDF predicted with a sample size of 190 or 120. To verify this for the 2PP model, a sample of 10,000 doublets (k, k_s/k) was generated with the Latin Hypercube Sampling, and the NIPCE metamodel applied to the sample. The PDFs of the 120 and 10,000 NIPCE predictions are shown together in Figure 2.9, where the bars' heights are scaled by the total number of predictions for each case (i.e., 120 and 10,000, respectively).

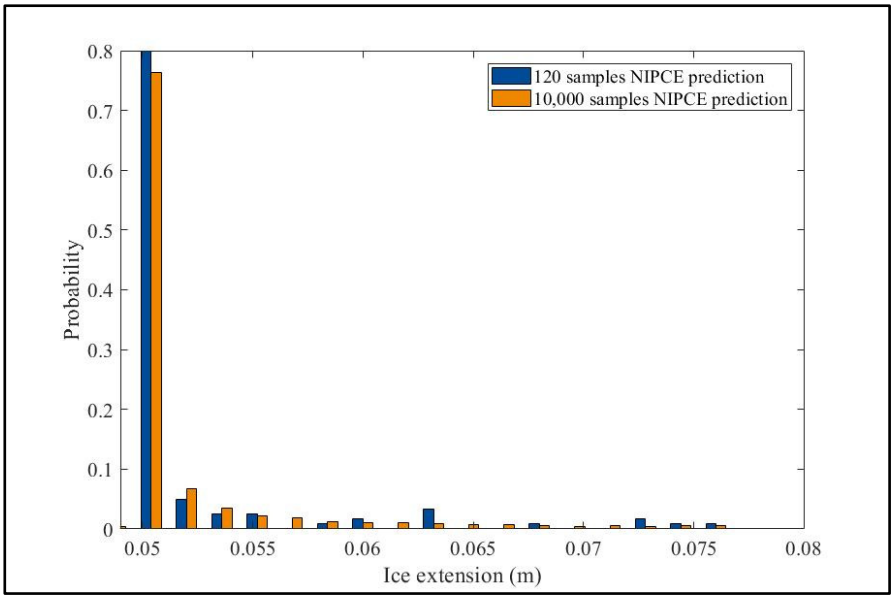

Figure 2.9 Comparison between NIPCE predictions for a varying sample size for the ice extension (metamodel M_3) and the 2PP model

Figure 2.9 shows a similar trend. A closer analysis allows for the determination of the PDF of the data in the figure. The fitted normal distributions, associated to the histograms of Figure 2.9, have their parameters μ and σ summarized in Table 2.4, with the 95% confidence intervals in square brackets. The first column in Table 2.4 gives the parameters for the NIPCE prediction histogram of Figure 2.9 obtained with 120 samples, and the second column gives the PDF parameters as extracted from the prediction with 10,000 samples. Note that the NIPCE metamodel obtained, defined by a polynomial as in equation (2.10), in both the sample sizes (120 and 10,000), is of degree 7.

Table 2.4 PDF of normal distribution parameters of Figure 2.9's histograms

120 samples NIPCE prediction	10,000 samples NIPCE prediction
μ = 0.0522 m [0.0512 ; 0.0531]	μ = 0.0521 m [0.0520 ; 0.0522]
σ = 0.0052 [0.0046 ; 0.0059]	σ = 0.0047 [0.0046 ; 0.0047]

The parameters in Table 2.4 show that the NIPCE prediction M_3 with 120 samples matches closely the prediction obtained with 10,000 samples. The PDF parameters of the NIPCE

response only change by a magnitude of 10^{-4} for μ and 0.0005 for σ. This aspect shows that the sample size of 120 was already enough to estimate the PDF of the output with a good precision. Nevertheless, the confidence intervals are reduced with the increase of the sample size: the confidence interval on μ for 120 samples is 1.9 mm wide, while it is 0.3 mm wide for the 10,000 samples. By applying the relation from Schaefer et al. (Schaefer et al., 2017), with an oversampling ratio of 3 for two uncertain parameters and a NIPCE of degree 7, the minimum sample size required for the problem is 108. This confirms, in addition to the graphical visualization, that the sample size of 120 is enough. This characteristic of having a high enough precision with the RANS sample size is also verified for all the other metamodels. To ensure a small confidence interval, the results obtained for a 10,000 sample size are kept. The normal distributions obtained for each metamodel with the NIPCE prediction with 10,000 samples are summarized in Table 2.5.

Table 2.5 Output PDF for each NIPCE prediction on the 10,000 sample size

Metamodel	Output of interest Y_i	Output PDFs' parameters	
		HAX	2PP
M_1	Heat transfer coefficient at x = 11.36 cm	μ = 544.2 W/m²K [542.1;546.3] σ = 106.0 W/m²K [104.8;107.7]	μ = 430.8 W/m²K [430.2;431.3] σ = 27.8 W/m²K [27.4 ; 28.2]
M_2	Maximum ice accretion thickness	μ = 0.0264 m [0.0263;0.0265] σ = 0.0046 m [0.0046 ; 0.0047]	μ = 0.0218 m [0.0218;0.0218] σ = 0.0017 m [0.0017 ; 0.0017]
M_3	Ice accretion extension	μ = 0.0512 m [0.0511; 0.0513] σ = 0.0061 m [0.0061 ; 0.0062]	μ = 0.0521 m [0.0520 ; 0.0522] σ = 0.0047 m [0.0046 ; 0.0047]

The data in Table 2.5 show that each thermal correction model predicts slightly different output PDFs for the same metamodel. The μ values in Table 2.5 show that, statistically, changing

from the HAX to the 2PP thermal correction model leads to a 21% variation in the heat transfer coefficient. This change in the heat transfer coefficient then leads to a 17% variation in the ice maximum thickness and only 1.8% of change in the ice extension. The standard deviation σ allows us to estimate the relative uncertainty and how the observed values spread around the mean μ. For a normal distribution, 99.7% of the data are in the range [μ − 3σ; μ + 3σ]. The σ values in Table 2.5 suggest a larger uncertainty on the outputs for the HAX model compared to the 2PP model. For the ice extension, the relative uncertainty in the 99.7% range [μ − 3σ; μ + 3σ] is about 36% for the HAX model and 27% for the 2PP model. The same calculation for the maximum ice thickness leads to a relative uncertainty of 52% for the HAX model and 23% for the 2PP model. As expected, these uncertainties on the accretion find their origin in the heat transfer uncertainties, which are 58% and 19% for the HAX and 2PP models, respectively. As an example, Figure 2.10 shows the difference in the distributions predicted by metamodel M_2 for the maximum ice thickness. The difference between the distributions predicted for the HAX model (orange) and the 2PP model (blue) is noticeable. The larger standard deviation for the HAX model is clearly visible, with a larger spread of the values around the mean compared to the 2PP model.

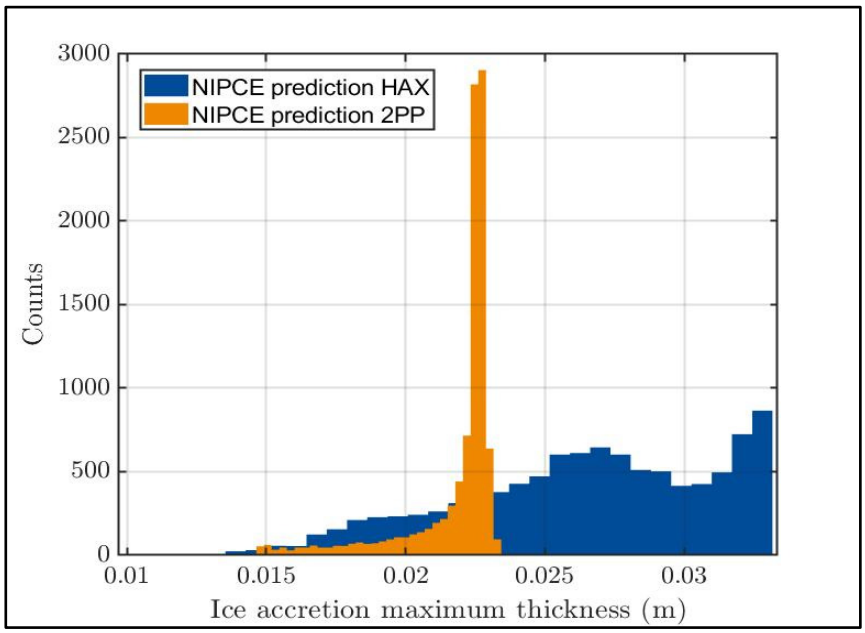

Figure 2.10 Differences in predicted distributions between the HAX and 2PP models for metamodel M_2 on the 10,000 samples

Figure 2.10 shows that the two thermal correction models predict different maximum ice thickness ranges: the 2PP model gives ice accretions with thicknesses of up to about 23 mm, while the HAX model predicts thicknesses of up to 33 mm.

2.5.3 Sensitivity Analysis: Calculation of the Sobol Sensitivity Indexes

2.5.3.1 Sensitivity to the Roughness Parameters

With the metamodels generated, the Sobol sensitivity indexes are evaluated for each input parameter. The 2PP model, with two input parameters, allows the computation of the Sobol indexes up to order 1, while the HAX model, with three input parameters, allows Sobol indexes of order 2. Figure 2.11 shows the Sobol indexes for the metamodel M_2, evaluating the maximum thickness of the ice accretion and the HAX thermal correction model. The values of the total Sobol indexes obtained for each metamodel are shown in Table 2.6. In Table 2.6, three positions have been chosen for the metamodel M_1, to highlight the differences of sensitivity when traveling on the flat plate.

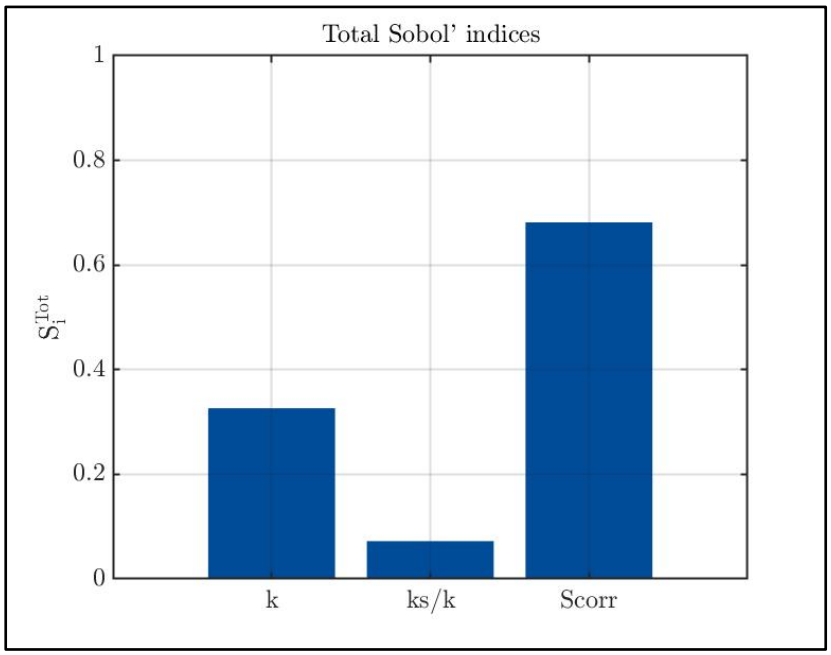

Figure 2.11 Total Sobol indexes for metamodel M_2 and the HAX thermal correction model

Table 2.6 Total Sobol sensitivity indexes for each metamodel

Metamodel	Output of interest Y	Total Sobol sensitivity indexes	
		HAX	2PP
M_1	Heat transfer coefficient at x = 11.36 cm	k: 0.239 k_s/k: 0.051 S_{corr}: 0.787	k: 0.820 k_s/k: 0.271
M_1	Heat transfer coefficient at x = 14.29 cm	k: 0.239 k_s/k: 0.050 S_{corr}: 0.787	k: 0.802 k_s/k: 0.291
M_1	Heat transfer coefficient at x = 27.48 cm	k: 0.248 k_s/k: 0.052 S_{corr}: 0.779	k: 0.756 k_s/k: 0.341
M_2	Maximum ice accretion thickness	k: 0.326 k_s/k: 0.072 S_{corr}: 0.682	k: 0.894 k_s/k: 0.202
M_3	Ice extension	k: 0.166 k_s/k: 0.088 S_{corr}: 0.822	k: 0.912 k_s/k: 0.288

The results in Figure 2.11 and Table 2.6 show, for the HAX model, that the parameter S_{corr} has the largest impact on every output of interest: S_{corr} contributes up to 68% to the variability of the maximum ice thickness and 82% for the ice extension. For the 2PP model (see Table 2.6), the roughness height k has the greatest influence on the outputs of interest as compared to the ratio k_s/k, going up to about 91%. The results observed for the 2PP model, where k has a greater influence than the ratio k_s/k, are also observed for the HAX model. According to the classification given by Chan et al. (Chan et al., 1997), S_{corr} is an important or very important parameter for every metamodel, while k and the ratio k_s/k are negligible or unimportant for the HAX thermal correction model. For the 2PP thermal correction model, k is very important compared to the ratio k_s/k, which is negligible. These results show that in the case of the HAX model, S_{corr} needs to be carefully quantified prior to launching a simulation, since the outputs of interest are the most sensitive to its value. The same conclusion can be drawn for the parameter k when using the 2PP model. Looking at the values in Table 2.6, it can be observed

that the roughness height k sees its level of influence decreasing as it gets away from the leading edge with the 2PP thermal correction. This observation is done by comparing the Sobol indexes from metamodel M_1 at x = 11.36 cm and further away at x = 14.29 cm and x = 27.48 cm, where the Sobol index for k decreases. Meanwhile, the Sobol indexes for k_s/k increase while traveling away from the leading edge. For the HAX model, the Sobol indexes for all three uncertain parameters remain quite steady when traveling downstream.

2.5.3.2 Sensitivity of the Ice Accretion to the Roughness Parameters and the Freestream Temperature

To highlight the importance of roughness parameters on the ice accretion shape compared to the freestream temperature, the freestream temperature T is now added as an epistemically uncertain variable, varying randomly between 261.5 K and 262.5 K, and the Sobol indexes are computed. For these tests, the parameters are summarized in Table 2.7.

Table 2.7 Metamodels used for the temperature impact study

Metamodel	Input parameters X_j		Output of interest Y_i
	HAX	2PP	
M_{2T}	k, k_s/k, S_{corr}, T	k, k_s/k, T	Maximum ice accretion thickness
M_{3T}	k, k_s/k, S_{corr}, T	k, k_s/k, T	Ice accretion extension

The new metamodels, with an increased number of uncertain input parameters, have a subscript "T" to avoid confusion. For the sake of concision, the *LOO* errors and outputs' PDFs of metamodels M_{2T} and M_{3T} are not displayed, but the precision is of the same order of magnitude as that of metamodels M_2 and M_3. The Sobol indexes of metamodel M_{2T} for the HAX thermal correction model are displayed in Figure 2.12.

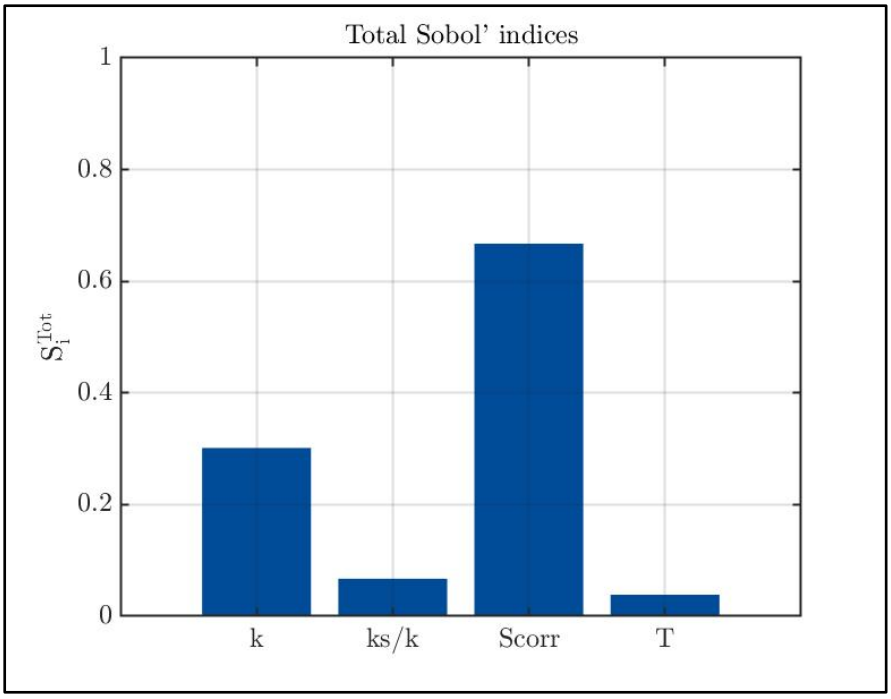

Figure 2.12 Total Sobol indexes for metamodel M_{2T}
and the HAX thermal correction model

Figure 2.12 shows that the temperature has a minor impact on the sensitivity of the ice accretion's maximum thickness. When comparing with Figure 2.11, it is also possible to note that the level of influence of the roughness parameters remains almost the same despite the addition of the temperature as uncertain. This negligible influence of the temperature is also observed for the other combinations of metamodel/thermal correction model, as summarized in Table 2.8.

Table 2.8 Total Sobol sensitivity indexes for the temperature impact study

Metamodel	Output of interest Y	Total Sobol sensitivity indexes	
		HAX	2PP
M_{2T}	Maximum ice accretion thickness	k: 0.302 k_s/k: 0.067 S_{corr}: 0.667 T: 0.039	k: 0.750 k_s/k: 0.170 T: 0.162
M_{3T}	Ice extension	k: 0.190 k_s/k: 0.050 S_{corr}: 0.784 T: 0.022	k: 0.681 k_s/k: 0.255 T: 0.176

The results in Table 2.8 show that for every metamodel and thermal correction model, the temperature is the least influent parameter. For the HAX thermal correction model, T is completely negligible, while for the 2PP model it has a greater impact, closer to k_s/k, but still far behind the level of influence of the roughness height k and still below 0.3. These results highlight the importance of the roughness model in the simulation, whose parameters have to be carefully selected, since their variation leads to bigger changes to the ice accretion shape than the temperature variation within 1 K. This relative importance of roughness on the accretion sensitivity compared to other factors related to ambient conditions has also been noticed in the literature. Raj et al. (Raj et al., 2020) showed that the roughness plays a bigger role in the accretion shape than the ice density, the droplet distribution and the evaporation.

The results show that the methodology retained is well suited to the ice accretion, since the NIPCE satisfactorily predicts the behavior of the output of interest. The NIPCE metamodeling gave fast responses and facilitated the analysis for the aircraft icing study. The results obtained using the NIPCE tool allow for a direct observation of the key features of the accretion's characteristics when roughness parameters are varying. Following that, the sensitivity analysis allowed us to determine that the outputs of interest are very sensitive to S_{corr} when using the HAX model, and to the roughness height k when using the 2PP model.

The ranges of the uncertain roughness parameters come from the literature, and uniform PDFs have been chosen. Changing the ranges and/or the PDFs might impact the results. Other types of metamodels can also be investigated. A similar study can also be conducted around an airfoil to highlight the effects of curvature and pressure gradient effects on the results. Furthermore, k, unlike S_{corr} and k_s/k, is linked to the skin friction coefficient, which is seldom available and known for an iced surface.

2.6 Conclusions

This paper has introduced an efficient methodology to quantify the sensitivity of the ice accretion characteristics to the thermal correction parameters on a rough flat plate. The objective of the paper to quantify the ice shape uncertainty and identify the key roughness parameters leading to this uncertainty was reached. The main parts of the methodology were the metamodeling process, using the Non-Intrusive Polynomial Chaos Expansion (NIPCE), and the sensitivity study computing the Sobol sensitivity indexes. The NIPCE metamodeling tool gave entire satisfaction regarding accuracy and quickly computed results with up to several thousand inputs. These features highlighted NIPCE's suitability for the study, despite its novel usage for aircraft icing with roughness analysis. The study allowed a comparison of two thermal correction models: the HAX model, with three input parameters, and the 2PP model, with two input parameters. The predicted ice accretion's maximum thickness is very sensitive to the choice of the thermal correction model and its respective parameters. Switching from the HAX to the 2PP thermal correction induces a 17% change in the maximum ice thickness. This aspect is mainly due to the impact of the thermal correction on the convective heat transfer, which is changed up to about 20%. In addition, the standard deviation study highlighted a larger relative uncertainty on the accretion for the HAX model, which can reach 52% on the ice maximum thickness compared to the uncertainty of 23% of the 2PP model. It was also concluded from the Sobol sensitivity indexes that the most influential parameter for the HAX model is S_{corr}, which is responsible of 68% and 82% of variations on the ice accretion's maximum thickness and extension, respectively. For the 2PP model, the roughness height k is the most sensitive parameter, responsible for about 90% of the changes in ice

thickness and extension. To improve the rough turbulence models, it seems necessary to reinforce the experimental databases by precisely measuring the heat transfer variations induced by typical ice roughness. The present work shows that the precise knowledge of the heat transfers associated to a specific roughness pattern is key to ensuring reliable numerical icing predictions. Future investigations will be conducted to apply the same methodology to an airfoil.

2.7 Acknowledgments

The authors would like to thank the TOMATO Association (Aéroclub de France), Paris, France; the Office of the Dean of Studies, ÉTS, Montréal, Canada, and SubstanceÉTS, Montreal, Canada. CFD computations were made on the Cedar supercomputer from Simon Fraser University, managed by Calcul Québec and Compute Canada.

CHAPITRE 3

DATA-DRIVEN CALIBRATION OF ROUGH HEAT TRANSFER PREDICTION USING BAYESIAN INVERSION AND GENETIC ALGORITHM

Kevin Ignatowicz [a], Elie, Solaï [b], François Morency [c], Héloïse Beaugendre [d]

[a, c] Département de Génie Mécanique, École de Technologie Supérieure,
1100 Notre-Dame Ouest, Montréal, Québec, Canada H3C1K3
[b] INRIA Bordeaux, Talence, France
[d] Université de Bordeaux, INRIA, CNRS, Bordeaux INP, IMB, UMR 5251
33405, Talence, France

Article publié dans « Energies », Mai 2022

3.1 Abstract

The prediction of heat transfers in Reynolds-Averaged Navier-Stokes (RANS) simulations requires corrections for rough surfaces. The turbulence models are adapted to cope with surface roughness impacting the near-wall behaviour compared to a smooth surface. These adjustments in the models correctly predict the skin friction but create a tendency to overpredict the heat transfers compared to experiments. These overpredictions require the use of an additional thermal correction model to lower the heat transfers. Finding the correct numerical parameters to best fit the experimental results is non-trivial, since roughness patterns are often irregular. The objective of this paper is to develop a methodology to calibrate the roughness parameters for a thermal correction model for a rough curved channel test case. First, the design of experiments allows the generation of metamodels for the prediction of the heat transfer coefficients. The polynomial chaos expansion approach is used to create the metamodels. The metamodels are then successively used with a Bayesian inversion and a genetic algorithm method to estimate the best set of roughness parameters to fit the available experimental results. Both calibrations are compared to assess their strengths and weaknesses. Starting with unknown roughness parameters, this methodology allows calibrating them and obtaining between 4.7% and 10% of average discrepancy between the calibrated RANS heat transfer prediction and the experimental results. The methodology is promising, showing the

ability to finely select the roughness parameters to input in the numerical model to fit the experimental heat transfer, without an a priori knowledge of the actual roughness pattern.

Keywords: Bayesian inversion, genetic algorithm, data-driven analysis, calibration, rough heat transfers, computational fluid dynamics.

3.2 Introduction

The numerical simulation of airflow above a rough wall differs from a classical smooth wall situation. The surface roughness creates a different near-wall behaviour, especially for the skin friction and the heat transfers. This led to the modification of the classical turbulence models to account for the roughness elements, like in (Aupoix & Spalart, 2003) for the Spalart-Allmaras model. The main characteristics of the rough extension of the Spalart-Allmaras model reside in setting a non-zero turbulence viscosity at the wall. Usually, these adapted models are specifically designed to predict the correct skin friction coefficients based on experimental benchmark cases. This attention given to the skin friction coefficients alone has a drawback: the predicted heat fluxes are higher than the experimentally measured ones. An additional thermal correction model is thus required to adjust heat fluxes. To correct the heat flux behaviour, (Suga et al., 2006) suggested increasing the turbulent Prandtl number close to the wall. Further thermal correction model developments carried out by (Aupoix, 2015) and recently by (Morency & Beaugendre, 2020) continued to aim at a turbulent Prandtl increase.

The thermal correction models take as input various parameters describing the roughness pattern of the surface. These parameters can be physically measurable, such as the roughness height, or numerical, such as the equivalent roughness. For instance, the thermal correction of (Aupoix, 2015), takes three input parameters and the two-Parameter Prandtl correction (2PP) of (Morency & Beaugendre, 2020), takes two. The latter 2PP thermal correction model is the one used in the present study. Previous works highlighted that the heat flux is sensitive to those roughness parameters and to the thermal correction model itself (Ignatowicz et al., 2021c; Morency & Beaugendre, 2020). Usually, the equivalent roughness is computed from the roughness shape using empirical relations such as (Dirling, 1973). Those relations were built

using manufactured regular roughness patterns, such as regularly spaced cones, hemispheres or pyramids. In many real-life situations, for example in aircraft icing (Shin, 1996), roughness patterns are irregular and present several uncertainties. Therefore, classical empirical relations can fail to correctly describe a roughness pattern in such situations.

To avoid the dependence on empirical relations in rough heat transfer CFD simulations, a data-driven approach can be used, provided that experimental data are available. This data-driven approach allows the recovery of the roughness parameters to input in the numerical model by processing the experimental data, without an a priori knowledge of the real roughness pattern. Machine learning and data-driven techniques have already been successfully applied in CFD, for example for the calibration of the turbulence model's constants in (Da Ronch, Panzeri, Drofelnik, & d'Ippolito, 2020), highlighting its potential.

Usually, the data-driven approach relies on metamodels. One of the most common metamodel families is the polynomial chaos expansion (PCE) (Marelli & Sudret, 2019). PCE metamodels are commonly used in problems where uncertainty propagation is studied, like in (Salehi, Raisee, Cervantes, & Nourbakhsh, 2017) and (Hosder, Walters, & Perez, 2006). Most of the time, the PCE approach allows building efficient metamodels from a CFD database, and these are used in lieu of the time-consuming CFD model (Rumpfkeil & Beran, 2020) for complex analyses. The PCE metamodeling was successfully applied in heat transfer applications, for instance in (Shahane, Aluru, & Vanka, 2019) or (Tabatabaei et al., 2019), highlighting its suitability for the present study. Globally, the coupling between PCE metamodeling and CFD has been extensively developed and applied during the last two decade (Najm, 2009; Zhang, Li, Zeng, Wang, & Yan, 2022). Once the metamodels are established, the sensitivity analysis can be performed, usually using the Sobol indices (Saltelli et al., 2008). This combination of PCE metamodels with Sobol sensitivity indices was previously used in a related work (Ignatowicz et al., 2021c). The Sobol indices allows the classification of the uncertain inputs according to their influence on the particular output of interest of a study using a variance-based approach. These commonly used indices are regularly employed in CFD sensitivity analysis (Resmini, Peter, & Lucor, 2016). Following the definition of the metamodels, the

calibration of uncertain roughness parameters can be performed. In the present work, two calibration methods will be assessed and compared: the Bayesian inversion and the genetic algorithm. The Bayesian inversion is a commonly used tool allowing model calibration and fine-tuning of numerical parameters (Wagner, Nagel, Marelli, & Sudret, 2021). The Bayesian inversion transforms the initial uncalibrated input's distribution into a refined posterior distribution, whose peak corresponds to the calibrated value (Muehleisen & Bergerson, 2016). This approach, using probability distributions instead of fixed values, allows flexibility in the interpretation of the calibration results. This calibration methodology was used in the context of the constant calibration of turbulence models (Guillas, Glover, & Malki-Epshtein, 2014). Fine tuning and optimization tasks suit the application of Bayesian inversion. The authors of (Morita et al., 2022) used Bayesian inversion for the shape optimization of a wall to obtain a prescribed pressure gradient distribution. This application presents similarities with the present work aiming at optimizing the surface roughness to obtain a given heat flux distribution. On the other side, classical calibration methods (i.e., non-Bayesian), such as the genetic algorithm, usually work in a non-probabilistic way, making their calibrated results strictly defined, without controlled flexibility. Classical calibration methods imply more intervention from the human modeller in post-processing, making the final results sensitive to the modeller's experience, expertise and biases (Reddy, Maor, & Panjapornpon, 2007). A genetic algorithm calibrates the problem using an approach similar to biological evolution (Yang, 2021). The final calibrated parameters are estimated by performing a method using selections, mutations and crossings between "generations" of parameters samples, like in the natural selection process. This type of calibration with genetic algorithm was already used in CFD applications (Khan, Islam, & Sazzad, 2021), and more specifically for optimization, like in (Oh & Chien, 2018) or (Owoyele et al., 2021). This use of genetic algorithms in the CFD field highlights the suitability of the method for the current application. The coupling between the PCE metamodeling and the optimization by Bayesian inversion or genetic algorithm was already used in numerical heat transfer applications (Wagner, Fahrni, Klippel, Frangi, & Sudret, 2019), showing the potential of the methodology. Additionally, in case of a low trustworthiness metamodel, coupling it with a Bayesian analysis allows one to consider the metamodel's uncertainty in the whole study (Ranftl & von der Linden, 2021).

The objective of this paper is to set up a methodology to calibrate the roughness parameters to input into the 2PP thermal correction model to match the experimental results of a given test case. More specifically, a rough curved channel geometry, inspired by (Suga et al., 2006), is used to set up the design of experiments (DOE) for heat transfers. Next, the DOE allows the generation of PCE metamodels predicting key features of the heat transfers on the wall. The next step is the sensitivity study, using the Sobol indices to identify the most sensitive parameters. Finally, the PCE metamodels are used in a calibration procedure to establish the roughness input parameters with the aim of retrieving the experimental heat transfer distribution in the curved channel. The calibration is done successively with a Bayesian approach and a genetic algorithm to compare both methods on the results discrepancies and practical application.

First, the test case geometry and setup will be described. Second, the 2PP thermal correction model is detailed, highlighting the role of the roughness parameters in the simulation. Next, the DOE construction is depicted prior to the description of the PCE metamodeling, the sensitivity study and the calibration procedures. Finally, the results are shown and compared, highlighting between 4.7% and 5.4% of average discrepancy after the Bayesian calibration compared to the experimental results. On the other side, the genetic algorithm approach gives between 5.7% and 10% of discrepancies.

3.3 Test Case Geometry and Setup

A specific curved channel test case is used for the application of the depicted methodology. This section will give details about the geometry used in the present study, along with the RANS setup to perform the flow simulation. The geometry and computational domain is detailed, prior to the domain mesh and numerical RANS configuration.

3.3.1 Physical Geometry and Boundary Conditions

The geometry used to apply the calibration work discussed in this paper is a curved channel experimentally studied by (Turner, Hubbe-Walker, & Bayley, 2000). This test case was

numerically studied by (Suga et al., 2006) few years later. The channel has a straight section followed by a curved one and another straight section. The channel height is 0.07 m while the overall curvilinear length is about 1.25 m. More specifically, the zone of interest is the rough bottom floor of the channel where the heat transfer coefficient will be monitored. Figure 3.1 illustrates the computational domain.

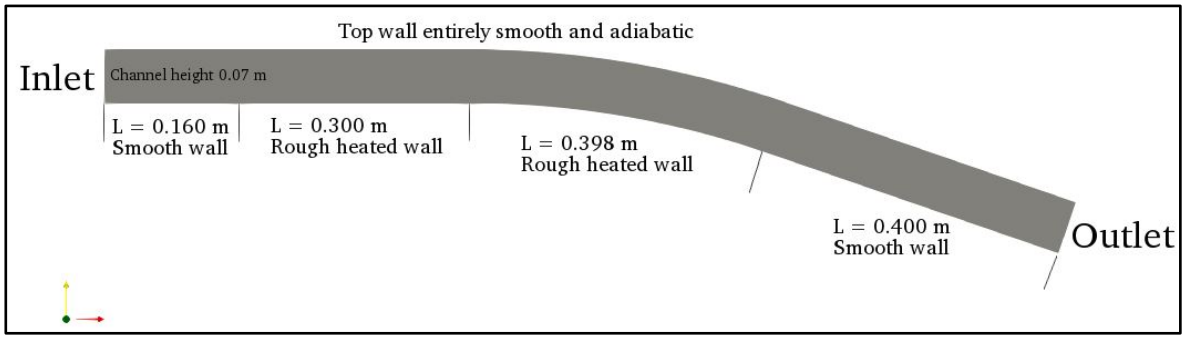

Figure 3.1 Geometry of the curved channel

The curved part of the channel's floor, whose curvilinear length is 0.398 m, is an arc of radius 1.200 m and an angle of 19°. The freestream values are a velocity magnitude of 40 m/s, an inlet total pressure of 102,304 Pa and a total temperature of 288.95 K. The boundary conditions are also displayed on Figure 3.1. The floor is divided into three main zones: an initial smooth and unheated wall, the rough and heated study zone (including the curved portion), and a downstream smooth unheated zone. The top wall is entirely smooth and adiabatic. The heated zones are isothermal at 303.15 K and their roughness parameters are the objective of the calibration. The roughness parameters' distribution will be detailed in Section 3.5.1.

3.3.2 Mesh and Numerical Setup

The geometry is discretized using quadrilateral elements in a structured mesh. The rough zone of interest is composed of 499 nodes in the stream-wise direction, while the channel height has 399 elements. Coarser meshes were tested, giving similar results on the benchmark test cases. The finest mesh was retained to cope with the various untested roughness patterns planned to

be run during the sampling of the DOE. The entire computational grid has 274,512 quadrilaterals. The first cell height is about 3 µm, which allows a y^+ below 1 for all the roughness ranges tested. The growth rate normal to the wall is 1.1. A close-up on the mesh near the floor is shown on Figure 3.2. The main outcomes of the mesh convergence study are detailed in the ANNEXE I.

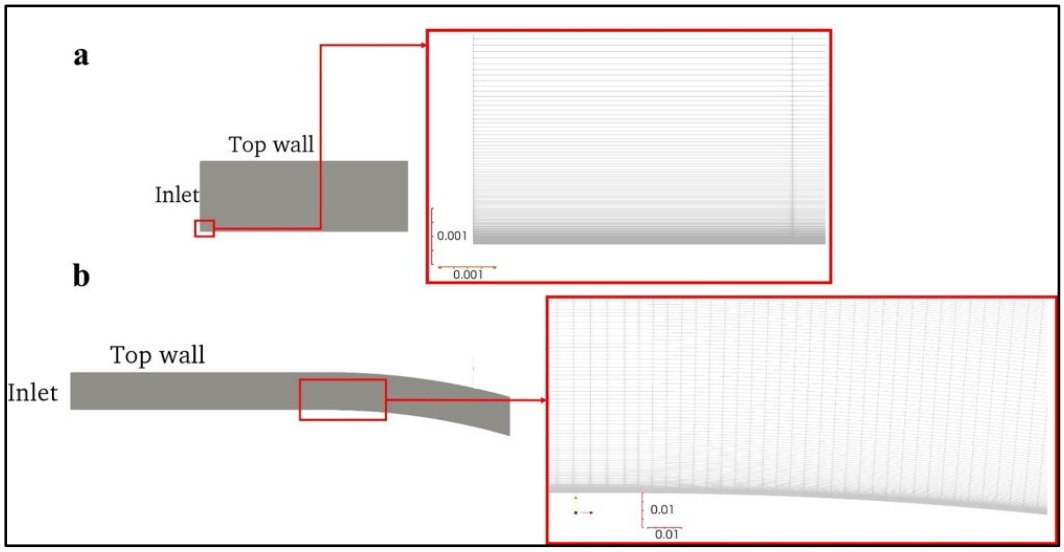

Figure 3.2 Close view on the mesh in the near-wall region: (a) Inlet area;
(b) transition straight/curved zone (scale in m)

The flow simulation is performed using the compressible RANS solver SU2 6.2 (Economon et al., 2015). The Reynolds number based on the total floor length is 3.2×10^6 and the Mach number is 0.118. To accelerate the convergence, the CFL number is set to 10. Finally, the convective fluxes are discretized using a Roe scheme with MUSCL reconstruction (Blazek, 2005). The solver used includes in-house implementations of the rough modification of the Spalart-Allmaras turbulence model (Aupoix & Spalart, 2003) and the addition of the 2PP (Morency & Beaugendre, 2020) thermal correction model. The next section will detail the mathematical model making up the thermal correction model.

3.4 2PP Thermal Correction Model

This section will give an overview of the equations of the 2PP thermal correction model. The 2PP thermal correction model was implemented into SU2, and aims at increasing the Prandtl number in the near-wall region to reduce the heat flux when the rough version of the Spalart-Allmaras turbulence model is used.

The 2PP thermal correction model achieves the goal of increasing the turbulent Prandtl number by computing an increment ΔPr_t. The model takes two roughness input parameters: the roughness height k (m) and the equivalent roughness k_s (m). Equation (3.1) allows the computation of ΔPr_t. In equation (3.1), Pr is the laminar Prandtl number and d is the distance to the wall.

$$\Delta Pr_t = g \times 0.07083 \times {Re_s}^{0.45} \times Pr^{0.8} \times exp\left(-\frac{d}{k}\right) \tag{3.1}$$

The roughness Reynolds number and the parameter g in equation (3.1) are detailed in equations (3.2) and (3.3).

$$Re_S = \frac{u_\tau k_s}{\nu} \tag{3.2}$$

$$g = \begin{cases} 1 \text{ if } Re_s \geq 70 \\ \dfrac{\ln(Re_s) - \ln(5)}{\ln(70) - \ln(5)} \text{ if } 5 < Re_s < 70 \\ 0 \text{ if } Re_s \leq 5 \end{cases} \tag{3.3}$$

In equation (3.2), u_τ is the friction velocity, and ν is the air kinematic viscosity. Finally, equations (3.1) to (3.3) highlighted that the roughness parameters have a direct impact on the Prandtl number correction, and thus on the predicted heat flux.

3.5 PCE Metamodeling

This section will depict the metamodeling process retained, using polynomial chaos expansion (PCE) metamodels. This step allows the creation of metamodels to predict the heat flux behaviour above any roughness pattern without the need for a complete CFD run. The first step of the metamodeling task is the creation of a numerical DOE. The PCE metamodels are then generated, and finally their accuracy is checked to ensure they are reliable enough for the study.

3.5.1 Design of Experiment (DOE)

To prepare the metamodeling and calibration steps, a numerical DOE of heat transfers for various roughness patterns is needed. First, the distribution of the input parameters k and k_s/k are defined to set the ranges for the sampling. Note that the ratio k_s/k is used instead of k_s alone, since it will allow one to directly evaluate the relation between the roughness height and the equivalent roughness. The present work is included in the broader scope of in-flight aircraft icing. Therefore, the typical ranges of variation of k and k_s/k are obtained from the icing literature (Dukhan et al., 1999b; Fortin, 2019). These ranges are wide enough to ensure that they are suitable for the current study, which is not specifically a simulation in icing conditions. The compilation of the distribution of all the input parameters is given in Table 3.1. The distributions are chosen as uniform since there is no a priori knowledge of the experimental roughness pattern.

Table 3.1 Distribution of the input parameters

Parameter	Minimum	Maximum	Distribution
k (mm)	0.41	4.32	Uniform
Ratio k_s/k	0.2	6.5	Uniform

Following the distributions of Table 3.1, a sampling is done using the Latin hypercube sampling (Stein, 1987). The sample size is defined according to the literature (Schaefer et al., 2017) for a response surface and gives, with an oversampling factor, 120 samples. Following the sampling, 120 CFD simulations of the curved channel are run. This allows the construction of a numerical heat transfer database, needed for the next metamodeling step.

3.5.2 Metamodels Generation

Once the heat transfer DOE is set up and ran, the metamodeling tool uses its output database to estimate a mathematical relation between the roughness parameters inputs and the heat flux output. For this study, polynomial chaos expansion (PCE) metamodels were chosen (Marelli & Sudret, 2019) and generated using the UQLab tool (Marelli & Sudret, 2019). The choice of this type of metamodel is motivated by its wide use in uncertainty quantification for CFD and aerodynamic applications (DeGennaro et al., 2015). The general form of a PCE metamodel is given by equation (3.4).

$$Y_i = M_i(\boldsymbol{X}) = \sum_{\alpha} y_\alpha \times \psi_\alpha(\boldsymbol{X}) \tag{3.4}$$

In equation (3.4), Y_i is the output of interest, $\boldsymbol{X} = (X_1, X_2)$ is the input parameters vector, M_i is the corresponding PCE metamodel defined by its coefficients y_α and the multivariate polynomials ψ_α of the decomposition. $\alpha = (\alpha_1, \alpha_2)$ is the multi-index with two components (since there are two input parameters, see Table 3.1). The multivariate polynomials ψ_α are obtained as the tensor product of the two (in the present application) univariate basis polynomials φ (equation (3.5)).

$$\psi_\alpha(\boldsymbol{X}) = \prod_{i=1}^{2} \varphi_{\alpha_i}(X_i) \tag{3.5}$$

The input parameters having a uniform distribution, the univariate basis polynomials are Legendre polynomials of indices α_i (Marelli & Sudret, 2019).

Three metamodels are generated, as listed in Table 3.2 where h_c is the heat transfer coefficient in W/m²K.

Table 3.2 The metamodels created

Metamodel	Output(s) of interest
M_1	h_c at the starting point of the rough zone, W/m²K
M_2	Mean relative error with experimental h_c (%)
M_3	h_c values at N_{out} equally spaced locations along the rough zone (multi-output), W/m²K

The second metamodel, M_2, predicts the mean relative error compared to the experimental results of (Suga et al., 2006). The mean relative error ε_r is the average of the relative errors taken on every mesh point (equation (3.6)).

$$\varepsilon_r = \frac{1}{N_{points}} \sum_{i=1}^{N_{points}} \left| \frac{h_{c,CFDi} - h_{c,EXPi}}{h_{c,EXPi}} \right| \tag{3.6}$$

In equation (3.6), N_{points} is the number of mesh points in the study zone, and $h_{c,CFDi}$ and $h_{c,EXPi}$ are the CFD predicted h_c at point i and the experimental h_c at point i, respectively.

M_3 is a multi-output metamodel evaluating in one estimation N_{out} values of h_c along the wall. Setting N_{out} to a high value allows one to predict the complete h_c distribution on the entire rough wall. The metamodel M_1 is separated from the metamodel M_3: this separation allows one

to compare the cases where the starting h_c is calibrated alone (M_1) and where several locations are simultaneously calibrated (M_3).

Once a metamodel is created, its evaluation on the inputs of the DOE allows the comparison of its prediction with the actual CFD prediction obtained when setting up the DOE. Doing a linear regression between the PCE prediction and the CFD output allows the computation of the R^2 coefficient (equation (3.7)).

$$R^2 = 1 - \frac{\sum(Y_{CFD} - Y_{PCE})^2}{\sum(Y_{CFD} - \bar{Y}_{CFD})^2} \tag{3.7}$$

In equation (3.7), Y_{CFD} and Y_{PCE} are the CFD and PCE predictions, respectively. $\bar{Y}_{CFD}$ is the mean value of the output of interest (CFD). An R^2 coefficient close to 1 ensures a PCE metamodel with a good accuracy, since it predicts outputs close to what the full CFD simulation gives. Once the metamodels are established, the next step is to use them for the sensitivity study and the calibration purpose.

3.6 Sensitivity Study

The sensitivity study allows the identification of the most sensitive parameter(s) in the model. Using the previously described PCE metamodels, the sensitivity analysis computes the Sobol indices, described in (Saltelli et al., 2008). These indices allow the classification of the input parameters from the most to the least sensitive. The Sobol index is a ratio of variances, taking values be-tween 0 and 1. For input parameters i and j, the first and second order Sobol indices are defined by equation (3.8) and equation (3.9), respectively.

$$S_i = \frac{V(Y) - E\big(V(Y|X_i)\big)}{V(Y)} \tag{3.8}$$

$$S_{i,j} = \frac{V(Y) - E\left(V\big(Y|X_i, X_j\big)\right)}{V(Y)} \tag{3.9}$$

In equations (3.8) and (3.9), Y is the output of interest, V is the variance operator, E the mean value, and the notation $Y|X_i$ denotes the output of interest when the i^{th} input parameter is fixed. The total Sobol index, which is monitored in the present study, for the i^{th} input parameter for a generic three parameters study is given by equation (3.10).

$$S_i^{TOT} = 1 - (S_j + S_k + S_{j,k}) \tag{3.10}$$

The total Sobol index gives the contribution of the variability of the i^{th} input and its interactions with the other inputs (here the j^{th} and k^{th}) on the response sensitivity. A total Sobol index close to zero means that the i^{th} parameter does not contribute much to the variability of the studied output. According to the classification criteria suggested by (Chan et al., 1997), an input parameter with a total Sobol index:

- above 80% is very important;
- between 50% and 80% is important;
- between 30% and 50% is unimportant;
- below 30% is negligible.

3.7 Model Calibration

Observing experimental results without an a priori knowledge of the roughness pattern is not helpful to precisely extract the roughness parameters. This task is even more non-trivial since the roughness parameters to input in the model vary depending on the thermal correction model chosen. The calibration is intended to estimate those roughness parameters by working on the PCE metamodels previously created. The Bayesian inversion calibration is first described prior to the genetic algorithm approach.

3.7.1 Bayesian Inversion Calibration

Based on the Bayes theorem (equation (3.11)), the principle of the Bayesian inversion is to get the posterior distributions $\pi(\theta|X_i)$ of input X_i, based on the assumed prior distributions (see Table 3.1) $\pi(\theta)$ and on the information provided by the experimental data. Here, θ denotes the distribution parameters and the | symbol denotes the conditional dependence. The posterior distributions are the distributions of the input parameters knowing the information brought by the experimental data.

$$\pi(\theta|X_i) = \frac{\pi(X_i|\theta) \cdot \pi(\theta)}{\pi(X_i)} \tag{3.11}$$

In equation (3.11), $\pi(X_i|\theta)$ is called the likelihood function and $\pi(X_i)$ is seen as a normalization constant called the marginal likelihood. The new posterior distributions are generally not uniform anymore and allow identifying the input parameter values that will produce an output that best fits the experimental data. Additionally, a discrepancy between the PCE output and the CFD prediction is given to the solver, along with the experimental observations themselves. For instance, a discrepancy between 0 W/m²K and 15 W/m²K means that up to 15 W/m²K of difference between the PCE and CFD predictions is expected. Numerically speaking, the Bayesian inversion is performed with the UQLab tool (Wagner et al., 2021). The computation of the posterior distribution is made using a Markov chain Monte Carlo (MCMC) algorithm. The samplers used in the study are the affine invariant ensemble algorithm (AIES) or the Metropolis-Hastings (MH) algorithm. For the purposes of the work, the MCMC solver is tuned to perform 70,000 iterations and generates 15 chains. The Bayesian solver setup for each metamodel is summarized in Table 3.3. For the metamodel M_2 (predicting the mean relative error with experimental data), the experimental observation is 0% of mean relative error. This means that the objective of the calibration is to obtain a mean relative error close to 0%.

Table 3.3 Bayesian solver settings

Metamodel calibrated	Objective of the calibration	Sampler	Discrepancy	Experimental observation supplied
M_1	Recovering the same starting value of h_c	AIES	Uniform [0; 15] W/m²K	255.1 W/m²K
M_2	Having a mean relative error with experimental h_c of 0%	AIES	Uniform [0; 5] %	0%
M_3	Recovering the same h_c values at the N equally spaced locations along the rough zone	MH	Uniform [0; 15] W/m²K	Experimental h_c at the N locations (W/m²K)

After having obtained the posterior distributions, the mean value or the maximum a posteriori (MAP) of these distributions can be estimated. These two statistics can be used to estimate which single values of input parameters lead to a model response close to the experimental data. After evaluating the PCE metamodels and the complete CFD simulation with the calibrated parameters, it is possible to assess the success −or not− of the calibration procedure. One can estimate if the model response is close to the experimental data. Additionally, the distributions of the model predictions using the posterior distributions should present less uncertainty (reduced variance) when using the prior distributions.

3.7.2 Calibration Using a Genetic Algorithm

The MatLab framework has a built-in genetic algorithm that is used in the study (Conn, Gould, & Toint, 1991; Goldberg, 1989). Its purpose is to find the set of input parameters that minimize an objective function. The default settings provided in the MatLab framework provide a straightforward application for the present case. The objective functions supplied to the genetic algorithm are summed up in Table 3.4.

Table 3.4 Objective functions for calibration with the genetic algorithm

Metamodel calibrated	Objective of the calibration	Objective function used
M_1	Recovering the same starting value of h_c	$\lvert M_1 - 255.1 \rvert$
M_2	Having a mean relative error with experimental h_c of 0%	$\lvert M_2 \rvert$
M_3	Recovering the same h_c values at the N_{out} equally spaced locations along the rough zone	$\lvert M_3[\mathrm{i}] - h_c[\mathrm{i}] \rvert$ $\mathrm{i} = 1..N_{out}$

Note that since the metamodel M_3 outputs multiple (N_{out}) values, the genetic algorithm is executed N_{out} times. Each one of the executions gives a set of calibrated parameters and the final retained parameters are obtained by doing an average or a weighted average over the N_{out} solutions. Most of the time, the simple averaging produces unsatisfactory results. The weighted average, with appropriate weight(s) on the most relevant output(s), allows one to improve the results, as shown in the next section.

3.8 Results

This section will display the results obtained all through the process described in the previous sections. First, the CFD results obtained initially before calibration are shown to illustrate the

baseline results. Following this, the characteristics and precision of the metamodels are shown prior to the sensitivity indices. Finally, the calibration results for both Bayesian inversion and genetic algorithm are displayed, prior to the comparison of both methods.

3.8.1 CFD Results before Calibration

Prior to the metamodeling and calibration process, the curved channel test case, as described in Section 3.3.1 and Section 3.3.2, is run alone to verify the CFD settings and mesh. This initial simulation, called here the baseline simulation, is the same as the one run for the mesh study with the fine mesh. The roughness height is k = 0.5 mm and the equivalent roughness is k_s = 1.55 mm. This baseline simulation also provides useful information about the convergence of the CFD configuration used. The iterative convergence residual curves are displayed on Figure 3.3.

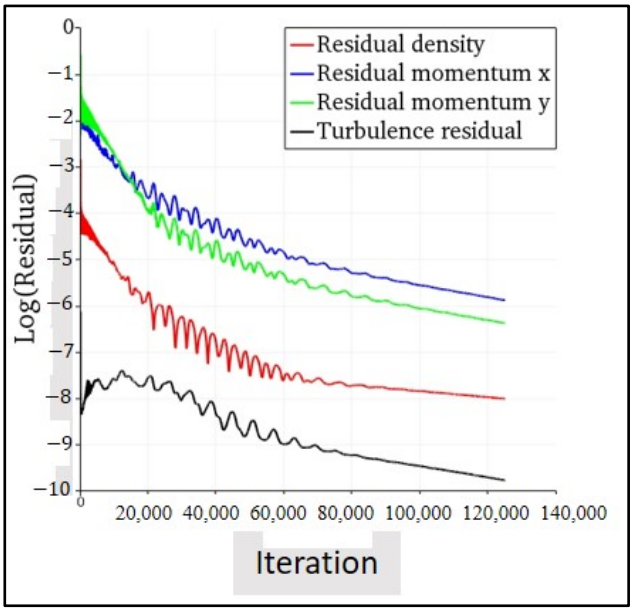

Figure 3.3 Iterative convergence of the baseline simulation

Figure 3.3 shows that after the prescribed number of iterations (125,000), the residuals are stable and decreased by at least three orders of magnitude. The configuration used has a

satisfactory convergence behaviour which confirms the choice of the numerical setup. The heat transfer results obtained with these settings are plotted on Figure 3.4.

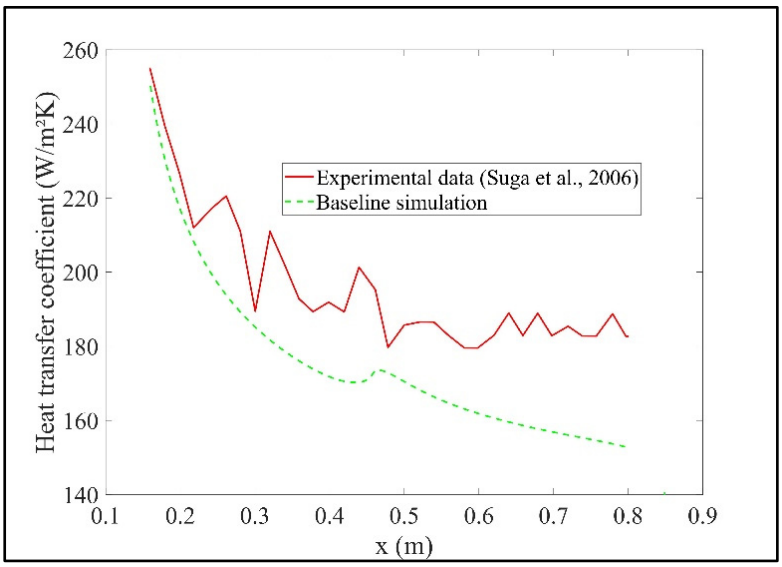

Figure 3.4 Baseline results before calibration

From Figure 3.4, it is possible to notice a relatively poor agreement with the experimental data. Finding the best roughness parameters is non-trivial, and it legitimates the use of the data-driven calibration approach used to match the literature.

3.8.2 Visualization of the DOE Outputs

After a sampling of the roughness parameters with the Latin hypercube method, 120 CFD simulations were run. The heat transfer databases obtained from the DOE are plotted in Figure 3.5, where each one of the black curves is the heat transfer coefficient of one simulation of the DOE. On Figure 3.5, the experimental data, in red, from the literature are shown.

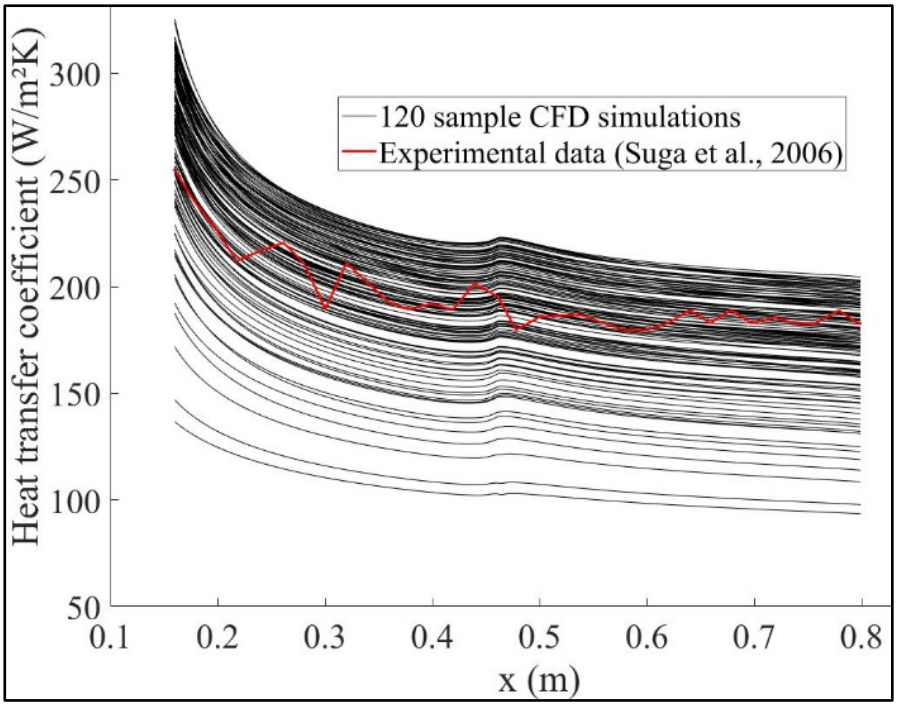

Figure 3.5 Database of heat transfer coefficients obtained with the DOE

By observing the experimental results, it is possible to notice oscillations resulting from the experimental uncertainty. Additionally, all the numerical simulations exhibit a sudden bump at x = 0.46 m, where the curved part of the channel starts. This local increase in the heat transfer coefficient is due to the flow acceleration in the curve portion. Studies in (Turner et al., 2000) quantified this increase in the heat transfer coefficient value at the start of the curve zone to be about 3%. Figure 3.5 shows that the target experimental results are included in the envelope defined by the sampling CFD simulations. This observation shows that the initial range of roughness parameters chosen contains the a priori unknown experimental values.

3.8.3 Characteristics of the Metamodels and Accuracy

The previous DOE is used as a basis for the PCE metamodel generation. Three metamodels are generated: one to predict the initial value of h_c along the rough zone, one to predict the mean relative error with experimental results and a third one to predict N_{out} values of h_c along the wall (see Table 3.2). For each metamodel, the resulting PCE is described with the

polynomial degree p and the number of terms in the expression (equation (3.4)). Additionally, the R^2 coefficient is calculated to assess the metamodel accuracy (equation (3.5)). The values obtained are gathered in Table 3.5. For the present study and for the rest of the paper, the metamodel M_3 is used with N_{out} = 6, meaning it computes six values of h_c regularly spaced along the wall. Note that the number of terms in equation (3.4), for a two input parameters study, is equal to $\frac{(p+2)!}{p!2!}$.

Table 3.5 R^2 coefficient for each metamodel

Metamodel	Output of interest	PCE degree p_{PCE}	Number of terms in equation (3.4)	R^2 coefficient
M_1	h_c at the starting point of the rough zone, W/m²K	10	66	0.99994
M_2	Mean relative error with experimental h_c (%)	10	66	0.99962
M_3	h_c values at 6 equally spaced locations along the rough zone (multi-output), W/m²K	Y_1 : 10	66	0.99994
		Y_2 : 9	55	0.99993
		Y_3 : 12	91	0.99999
		Y_4 : 10	66	0.99992
		Y_5 : 12	91	0.99999
		Y_6 : 12	91	0.99997

Table 3.5 shows that the PCEs obtained have a degree between 9 and 12, with the corresponding polynomial expressions having between 55 and 91 terms. All regression coefficients are above 99.9%, meaning an excellent agreement between the CFD results and the PCE-predicted results on the same sample. For comparison, (Prince Raj, Yee, & Myong, 2020) performed the same type of uncertainty quantification analysis with R^2 coefficients as low as 94.6%. For graphical visualization, the regression for M_2 (with R^2 of 99.96%) is plotted

on Figure 3.6 where Y_{PCE} and Y_{CFD} are the mean errors in percentage with the literature, as predicted by PCE and CFD respectively. For synthesis and concision, only the regression for M_2 is displayed, since it is the worst among the three (see Table 3.5).

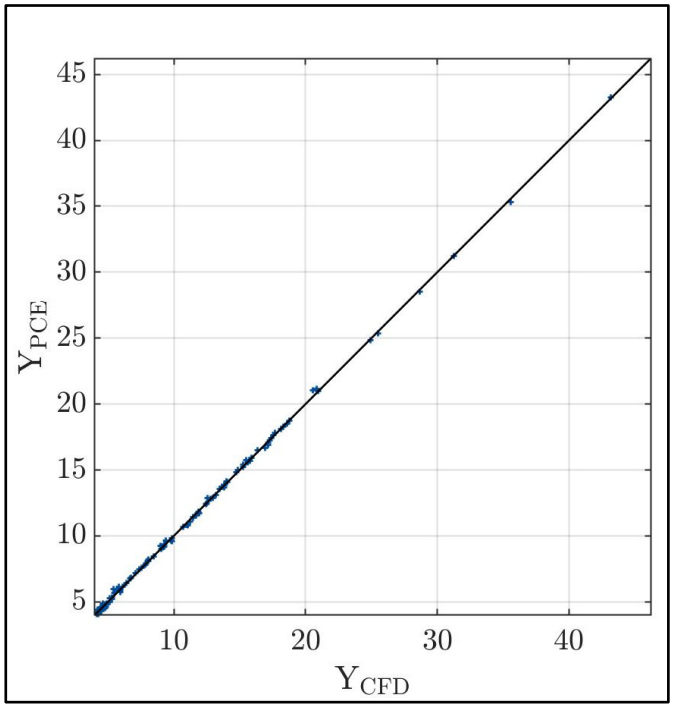

Figure 3.6 Regression between PCE and CFD predictions for metamodel M_2

Figure 3.6 shows that the results are close to the identity line, visually confirming the good value of the R^2 regression coefficient. This R^2 assessment shows that the metamodels generated are accurate and reliable enough to be used in the present application.

3.8.4 Sensitivity Study

Using the PCE metamodels, the sensitivity study allows the Sobol indices to be computed (see equation (3.8)). Table 3.6 gathers the total Sobol index values for each metamodel.

Table 3.6 Total Sobol indices

Metamodel	Total Sobol Indices
M_1	k: 0.1445 k_s/k: 0.8868
M_2	k: 0.3061 k_s/k: 0.9772
M_3	k: 0.1167 k_s/k: 0.9061

Table 3.6 shows that the roughness height k is the least sensitive parameter in each case, with a total index between 11% and 30%. The ratio k_s/k is the most dominant parameter of influence, with 88% to 97% sensitivity. According to the classification made by (Chan et al., 1997), k is a negligible parameter in the model sensitivity while k_s/k is a very important parameter. Therefore, the relation between k_s and k is more critical for the model output than their absolute values in millimetres.

3.8.5 Bayesian Inversion Calibration

The metamodels built are used as forward models for the MCMC algorithms, evaluated at each iteration of the chain. The target of the calibrations is to retrieve the features of the experimental results by estimating the best roughness parameters. These targets were listed earlier in Table 3.3. The target values (last column of Table 3.3) are inputted into the Bayesian module and the computation is carried out on the corresponding metamodel. For metamodels M_1 and M_2, the calibrated roughness parameters retained are the mean values of the posterior distribution. For metamodel M_3, the maximum a posteriori (MAP) is retained. The calibrated roughness parameters retained are listed in Table 3.7, along with the value (mean or MAP) chosen.

Table 3.7 Calibrated roughness parameters
(Bayesian inversion)

Calibrated metamodel	Values retained	Final calibrated roughness parameters
M_1	Mean	k = 2.2 mm k_s = 6.4 mm
M_2	Mean	k = 1.6 mm k_s = 4.2 mm
M_3	MAP	k = 1.8 mm k_s = 5.0 mm

The values in Table 3.7 are different from the ones tested in the baseline simulation, what explains the poor agreement with the literature prior to the calibration. Before assessing the quality of the calibrations, it is interesting to look at the main power of the Bayesian analysis: transforming the prior probability distributions of the inputs (uniform, see Table 3.1) into the calibrated posterior distributions, which are closer to Gaussian distributions. Figure 3.7 and Figure 3.8 illustrate as an example the prior and posterior distributions for the M_3 calibration for both k and k_s/k roughness parameters, respectively.

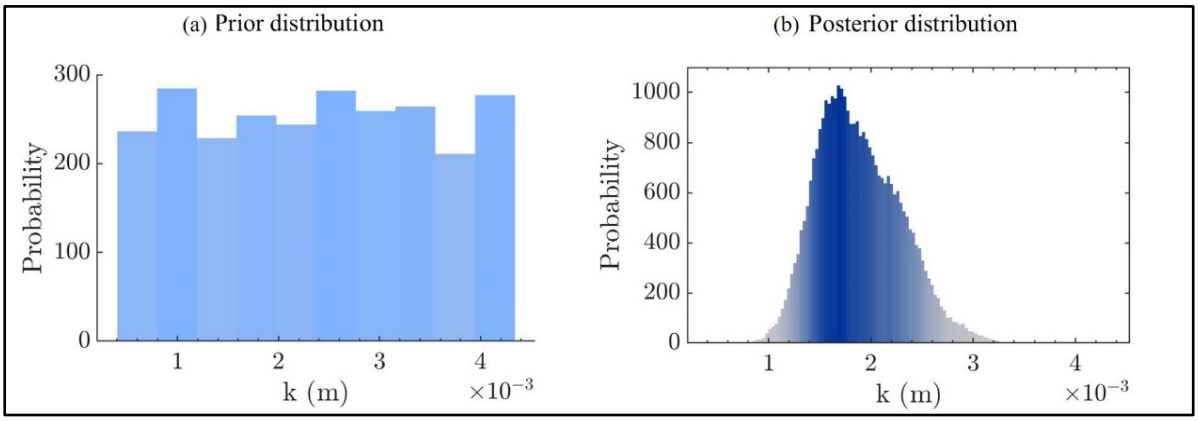

Figure 3.7 Prior (a) and posterior (b) distributions for the roughness height k (M_3 calibration)

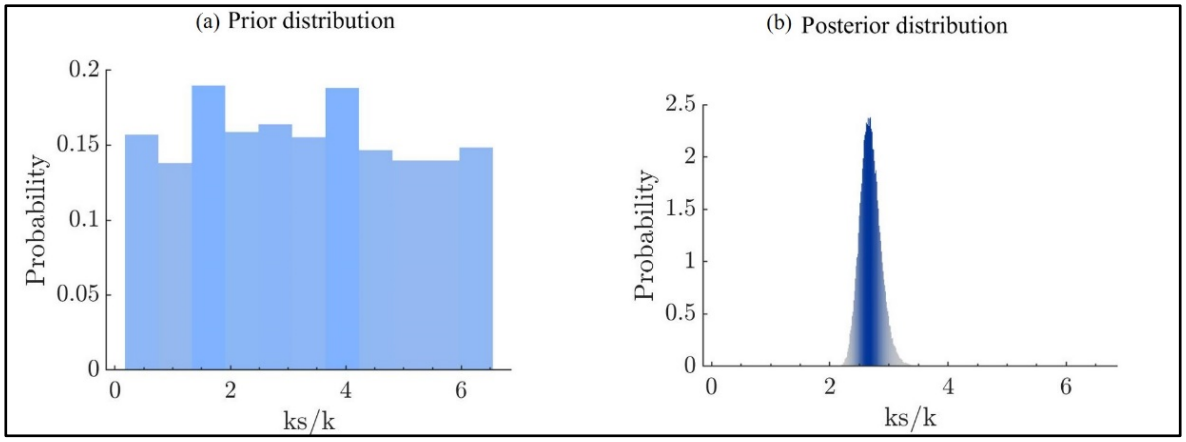

Figure 3.8 Prior (a) and posterior (b) distributions for the ratio ks/k (M_3 calibration)

In Figure 3.7 and Figure 3.8, it is possible to see the difference from the uncalibrated distributions (prior) to the posterior calibrated distributions. The calibrated values are clearly visible since the distributions are less spread and present peaks. Figure 3.7 and Figure 3.8 also allow visualizing graphically the meaning of the mean and MAP values: the mean is the mid value between the distribution's lower and upper limits, while the MAP value corresponds to the highest peak. From the posterior distributions, it is possible to recover the calibrated values of Table 3.7 for metamodel M_3: $k = 1.8$ mm and $k_s/k = 2.8$ (i.e., $k_s = 5.0$ mm). The observations highlight that the ratio k_s/k (Figure 3.8b) is finely calibrated with a smaller uncertainty compared to the roughness height k (Figure 3.7b). The posterior distribution for the ratio k_s/k exhibits a narrower peak, typical of a small variance.

For the metamodel M_1 and M_2, the calibrated roughness parameters from Table 3.7 are inputted into the CFD solver and the simulation is run to verify the new heat transfer obtained after calibration. Figure 3.9 shows the heat transfer using the calibrated roughness parameters for M_1 and M_2.

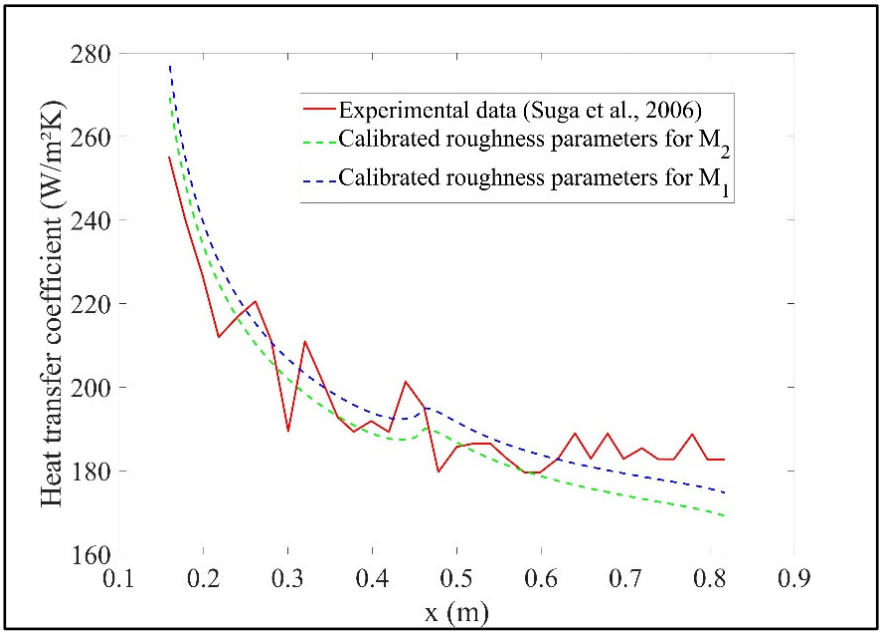

Figure 3.9 Heat transfer coefficient after Bayesian calibration

Figure 3.9 shows that the calibrated results have a better agreement with the experimental results compared to the baseline simulation of Figure 3.4. The calibration for M_1 allows one to obtain an average relative error with the experimental data of 4.7%. The relative error is computed as the average for the entire rough zone among all the grid points. The experimental data being available at about only 25 locations, the experimental values are interpolated at the grid points to allow the relative error calculation. The calibration for M_2 presents similar errors with the experimental data with 4.8% of relative mean error. Globally, both calibrations present satisfactory results, showing less than 5% of error on average compared to the experimental results. The results for the metamodel M_1 are higher than the one for the metamodel M_2, which is due to the higher roughness parameters in the case of M_1. This observation is in accordance with the usual experimental observation, where higher roughness elements lead to an enhanced heat transfer (Suga et al., 2006).

Figure 3.10 illustrates the calibrated results using the results for the metamodel M_3. Since M_3 outputs h_c values at different locations, it is possible to use the calibrated inputs to plot both PCE metamodel and CFD predictions.

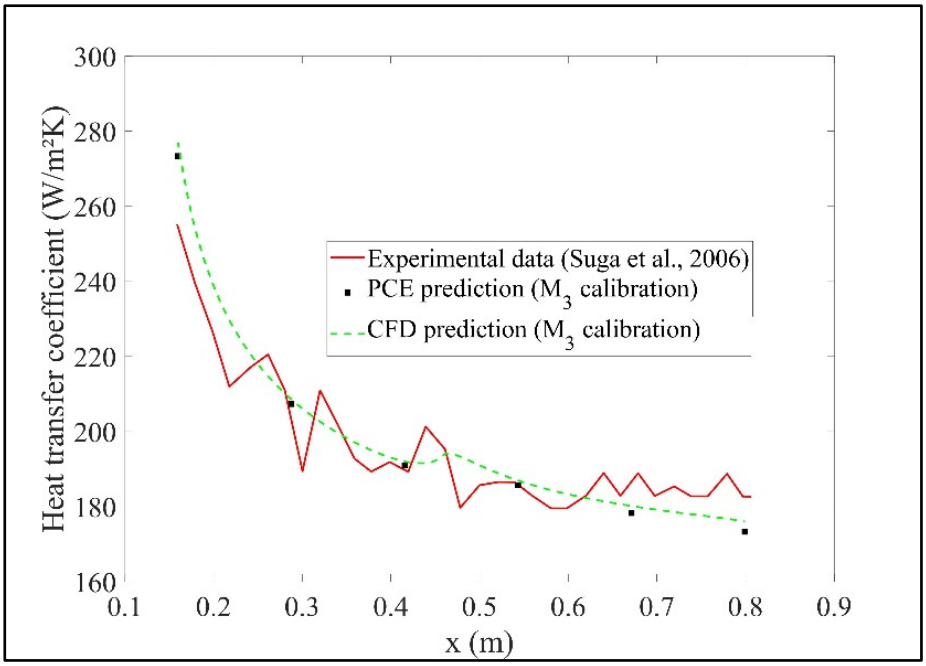

Figure 3.10 PCE and CFD predictions using
M3 calibrated values (Bayesian inversion)

Figure 3.10 is informative on several aspects: first, the PCE prediction using the calibrated roughness parameters presents a satisfactory agreement with the experimental data. Second, and most importantly, the CFD prediction is close to the PCE prediction. It allows assessing whether the PCE metamodel is reliable enough to predict a solution, and makes it a less costly and time-consuming tool which can replace the CFD on that particular application. Finally, the calibrated CFD results present a good agreement with the experimental data. The mean relative error with the experimental curve is 5.4%.

3.8.6 Genetic Algorithm Calibration

The same three metamodels are now calibrated with the genetic algorithm. The objectives of the calibrations remain the same, and the objective functions were listed earlier in Table 3.4. The calibrated results obtained are displayed below in Table 3.8. For the metamodel *M3*, the genetic algorithm outputs N_{out} calibrated parameters corresponding to each of the N_{out}

locations. The final retained parameters are computed by average or weighted average (where the initial point at the start of the rough zone has a weight of three).

Table 3.8 Calibrated roughness parameters (genetic algorithm)

Calibrated metamodel	Values retained	Final calibrated roughness parameters
M_1		k = 1.9 mm k_s = 3.1 mm
M_2		k = 4.3 mm k_s = 8.2 mm
M_3	Average among the N_{out} values	k = 3.0 mm k_s = 8.3 mm
M_3	Weighted average among the N_{out} values	k = 2.9 mm k_s = 7.1 mm

Figure 3.11 shows the CFD results using the calibrated parameters for the metamodels M_1 and M_2.

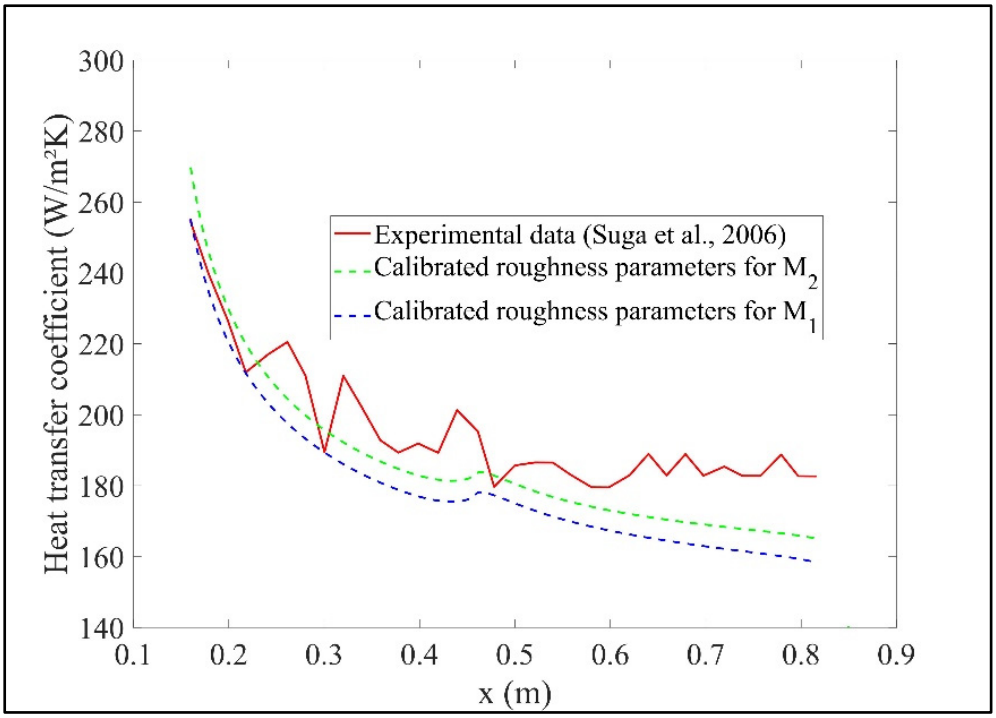

Figure 3.11 Heat transfer coefficient after genetic algorithm calibration

Figure 3.11 highlights that the agreement with the experimental data is better at the beginning of the rough zone and tends to present higher discrepancy at its end. The mean relative error for the metamodel M_1 is 8.2% and is 5.7% for metamodel M_2.

Figure 3.12 displays the PCE and CFD predictions using the calibrated values of metamodel M_3. The calibration shows better agreement in the middle and at the end of the wall. This feature has a drawback: the agreement at the beginning is not as good as for the metamodels M_1 and M_2. Taking the average roughness parameters gives a large overestimation of h_c at the start of the rough zone. Performing a weighted average, giving a weight of three to the first point, tends to lower the starting h_c value and globally lowers the values everywhere.

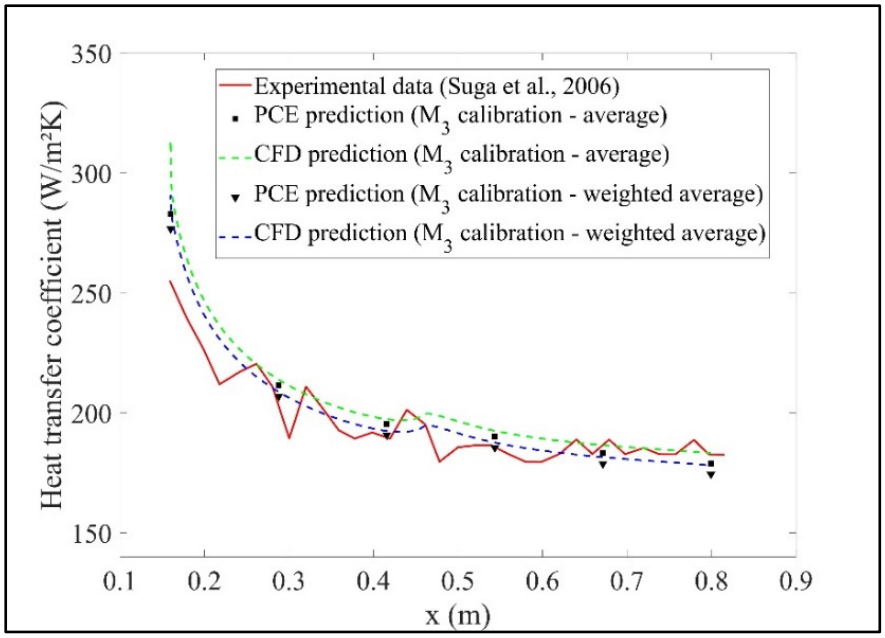

Figure 3.12 PCE and CFD predictions using M_3 calibrated values (genetic algorithm)

3.8.7 Comparison of Both Calibration Methods

After calibrating the metamodels using both Bayesian inversion and genetic algorithm approaches, the first comparison is the capacity for predicting the experimental data. This comparison is made by computing the mean relative error compared with experimental data. Table 3.9 gathered together the mean relative errors for both approaches.

Table 3.9 Errors with experimental data for each calibration

Calibrated metamodel	h_c mean relative error with experimental data	
	Bayesian inversion	Genetic algorithm[1]
M_1	4.7%	8.2%
M_2	4.8%	5.7%
M_3	5.4%	Avg: 10% W-Avg: 7.0%

The Bayesian calibration allows an agreement between the numerical results and the experimental data with an error about 5%. For the genetic algorithm, the errors are higher: they are between 5.7% and 10%. These values show an agreement not as good as the one obtained with the Bayesian inversion, despite displaying interesting behaviour at the beginning of the rough zone for the metamodels M_1 and M_2 (see Figure 3.11). By purely looking at the values in Table 3.9, the Bayesian inversion provides more satisfying and consistent results compared to the genetic algorithm. Note that the uncertainty in the experimental results was not considered. Given the oscillations observed on the experimental curve, one can estimate that the uncertainty in the experimental data is between 6% and 10%.

Nevertheless, by comparing Figure 3.9, Figure 3.10, Figure 3.11 and Figure 3.12, both methods have their own strengths and weaknesses. The calibrations for the metamodels M_1 and M_2 present a better agreement at the beginning of the rough zone for the genetic algorithm calibration (Figure 3.11) compared to the Bayesian inversion (Figure 3.9). When calibrating the starting value of h_c with the metamodel M_1, the genetic algorithm performs better since the starting value of h_c after calibration agrees better with the experimental data compared to the Bayesian inversion. On the other hand, the Bayesian inversion presents a better agreement

[1] For M_3, Avg: Average among the N_{out} outputs; W-Avg: Weighted average

between the calibrated results and the experimental data in the middle and at the end of the rough zone. For the metamodel M_3, the trend is the opposite: the Bayesian inversion (Figure 3.10) performs better at the beginning of the rough zone while the genetic algorithm (Figure 3.12) exhibits a better agreement at the end of the rough zone.

On usage, the Bayesian inversion is more automated and gives a more flexible output. The posterior distribution gives an idea of the uncertainty of the calibrated parameters. In the meantime, the output of the genetic algorithm is more rigid, since apart from the calibrated value, no distribution is given. In the case of a multi-output metamodel (M_3), the Bayesian inversion calibrates the model by working simultaneously on all outputs, thus estimating correlated calibrated parameters. The genetic algorithm works on each output independently, and requires a human intervention to establish the correlation between the outputs, like in the case of the weighted-average metamodel M_3. Modeller intervention can have a large impact on the results. Table 3.9 shows that changing the weight of the first output of the metamodel M_3 from one to three in the averaging decreases the error from 10% to 7%. An optimization of the weights in the future could improve the results even further.

The novelty of this work resides in the joint application of PCE metamodeling with a calibration method in the field of rough heat transfer prediction. Usually, unknown roughness patterns lead to large uncertainty in the aerothermal behaviour observed. With the methodology presented here, it is possible to reduce the lack of knowledge about a given experimental roughness pattern. As an extension, the present methodology can be applied to aircraft icing, where aerothermal and ice accretion behaviour depend strongly on the initial and uncertain (and unknown) roughness pattern (Ignatowicz et al., 2019a; Ignatowicz et al., 2021c). Finely calibrating the roughness parameters in an icing simulation will reduce one source of uncertainty that affects the final prediction of the ice shape.

3.9 Conclusions

The paper presents a methodology to perform a calibration of roughness parameters aiming at approaching experimental heat transfers. Two methods of calibration were compared: the Bayesian inversion and the genetic algorithm. Furthermore, this methodology was applied to a rough curved channel test case to illustrate its capacity. Starting with an unknown experimental roughness pattern, the procedure allowed the recovery of roughness parameters, providing between 4.7% and 5.4% of discrepancies with the experimental heat transfer when using Bayesian inversion calibration. In the case of the genetic algorithm, the agreement was above 5.7%, reaching 10%. The Bayesian inversion handled better than the genetic algorithm in the present application since its calibrated results fit the experimental data better. Furthermore, the Bayesian inversion behaves better in the case of multi-output metamodels, since it does not require manual tuning to account for each output contribution. This building of this methodology was achieved by combining polynomial chaos expansion (PCE) metamodeling and calibration techniques. The methodology showed high accuracy with respect to the PCE metamodels, confirming their suitability in the current application. The sensitivity analysis using the Sobol sensitivity indices highlighted that for this test case, the relation between the roughness height and the equivalent roughness plays a bigger role than the roughness height alone. The data-driven approach showed its suitability in CFD applications. In the case of unknown roughness patterns, it allows one to select the numerical parameters to input into a CFD simulation to retrieve the experimental data. Future extensions of the work will allow one to calibrate the roughness parameters not only to fit the heat transfer value but related quantities such as ice shape geometry in in-flight icing simulations.

3.10 Acknowledgments

The authors want to thank the TOMATO Association (Aéroclub de France), Paris, France, the Office of the Dean of Studies, ÉTS, Montréal, Canada, and SubstanceETS, Montréal, Canada. CFD computations were made on the supercomputer Cedar from Simon Fraser University, managed by Calcul Québec and Compute Canada.

CHAPITRE 4

NUMERICAL SIMULATION OF IN-FLIGHT ICED SURFACE ROUGHNESS

Kevin Ignatowicz [a], Héloïse Beaugendre [b], François Morency [c]

[a, c] Département de Génie Mécanique, École de Technologie Supérieure,
1100 Notre-Dame Ouest, Montréal, Québec, Canada H3C1K3
[b] Université de Bordeaux, INRIA, CNRS, Bordeaux INP, IMB, UMR 5251
33405, Talence, France

Chapitre de livre publié dans « Handbook of Numerical Simulation of In-Flight Icing »,
Mai 2023

4.1 Abstract

CFD is a primary tool used to assess the in-flight effects of atmospheric icing on aircraft. In-flight ice accretion codes use CFD computed quantities, such as shear stress and heat transfer, to predict ice shape formation over rough surfaces. The equivalent sandgrain roughness approach is the model commonly used in icing codes for the prediction of skin friction and heat fluxes over iced surfaces. Additional turbulent Prandtl number corrections can be added to the Reynolds Averaged Navier-Stokes (RANS) equations turbulence model to refine the heat transfer. Still, uncertainties persist in identifying the roughness parameters to input into the thermal correction, leaving the characterization of rough surfaces incomplete in terms of research. This chapter develops a methodology for the estimation of roughness input parameters based on the observation of experimental ice accretion. Metamodeling involving Polynomial Chaos Expansion (PCE) and calibration with a Bayesian inversion are employed. The methodology is applied to a NACA0012 airfoil, yielding a glaze ice cross-sectional area and maximum thickness with less than a 6% error from experiments. The approach opens perspectives for the estimation of appropriate case-dependent roughness parameters for RANS-based ice shape predictions.

Keywords: In-flight icing, ice accretion simulation, iced surface roughness, uncertainty quantification in icing, Polynomial Chaos Expansion, Bayesian inversion, icing model calibration.

4.2 Introduction

In-flight icing represents one of the main hazards threatening aircraft safety. Statistics show that icing is responsible for 17% of weather-related in-flight incidents (I.A.T.A., 2016). The main icing hazards are in the form of increased aircraft mass, risk of ice debris ingestion by the engine intakes, and the degradation of the aerodynamic performance when ice accretes on the lifting surfaces (Bragg et al., 2005). Several incidents and fatalities have occurred over the past decades as a result of in-flight icing. Among these, in 2009, the AF447 Air France Rio-Paris flight accident was caused by icing of the pitot tubes (Conversy et al., 2014). In-flight icing has also been suspected as a causal factor in the Comair-Delta connection flight 3272 tragedy in 1997, in which 29 people were killed (NTSB, 1997). In regard to this known safety threat, a lot of effort is invested in the prevention, analysis, and fight against ice formation on aircraft surfaces (Cao, Tan, & Wu, 2018b). This engineering problem is tackled both experimentally and numerically (Fujiwara et al., 2020). Concerning the experimental side, several aerodynamics studies have been carried out in real icing conditions or in cryogenic wind tunnels to understand the mechanisms behind ice accretion and their effects on flight (Zocca, Gori, & Guardone, 2017). These studies have led to more efficient anti-icing and de-icing devices on aircraft, reducing the potential issues associated with in-flight accretion (FAA, 2016). Experiments and flight tests are required to certify that an aircraft can indeed fly in icing conditions (FAA, 2006), and today, demonstrating this ability is a mandatory requirement in the certification process (FAA, 2007; Toulouse & Lewis, 2015).

Over the last two decades, numerical ice accretion simulations have become a major complementary tool to experimental tests. Since the early 2000s, these numerical tools have been used as part of the design and certification process (Habashi, Tran, Baruzzi, & Benquet, 2003). An in-flight ice accretion simulation combines the airflow around the aircraft obtained by computational fluid dynamics (CFD), a droplet impingement solver, and an ice accretion solver (Lavoie et al., 2018). Most ice accretion solvers are derived from the Messinger model, which, using a mass and energy balance, evaluates the phase change and ice accretion shape (Messinger, 1953). This model has been improved and extended through the years (Myers,

2001; C. Zhu et al., 2012) to include more physical phenomena, such as a shear stress-driven runback water film. The Shallow Water Icing Model (SWIM) is a partial differential equation (PDE) formulation of the Messinger model and is used in the FENSAP-ICE commercial code (Ansys, 2014; Bourgault et al., 2000). ONERA in France is involved in numerical icing development with the IGLOO2D suite (Trontin, Kontogiannis, Blanchard, & Villedieu, 2017) and the more recent IGLOO3D (Radenac et al., 2019). Several ice accretion models are embedded in commercial or research packages (Lavoie et al., 2018), as well as in open-source platforms such as OpenFOAM (Li & Paoli, 2019). Due to the complexity of icing physics and their inherent uncertainties, ice accretion models may end up predicting slightly, and sometimes substantially, different ice shapes for the same atmospheric conditions (Laurendeau et al., 2022). These uncertainties, in both models and measurements, are the reason why numerical predictions usually do not match experimental accretions. This challenge of unification and model accuracy has mobilized a lot of research efforts, ranging from early models (Wright, Gent, et al., 1997) to the latest developments (Szilder & Lozowski, 2018).

Within the ice accretion solvers, the energy balance involves a convective heat transfer term that has a large influence on the final predicted ice shape (Ignatowicz et al., 2019a). The convective term is obtained from the CFD airflow solution. For the CFD airflow computation over ice accretion, the rough surfaces create a challenge. The coupling between the airflow solver and the ice accretion solver relies mainly on the conjugate heat transfer solution (Bennani, Trontin, Chauvin, & Villedieu, 2020). From the start, the ice accretion process generates a surface roughness that must be accounted for by the flow simulation. Therefore, the Reynolds Averaged Navier-Stokes (RANS) CFD models adapt the classical turbulence models, such as the Spalart-Allmaras (SA) model, to account for the roughness elements (Aupoix & Spalart, 2003). The adapted turbulence models compute a non-zero turbulent viscosity at the wall. This non-zero turbulent viscosity aims to calibrate the skin friction coefficient against experimental benchmark test cases. The calibration against skin friction alone leads to a tendency among models to over-predict the heat fluxes, at least for the SA model (Morency & Beaugendre, 2020). An additional thermal correction model is thus needed to lower the heat fluxes. This challenge of thermal boundary layer modeling in ice accretion

simulations has been extensively studied, for example, by ONERA (Harry et al., 2021; Radenac, Bayeux, & Villedieu, 2020).

Increasing the turbulent Prandtl number in the near-wall region reduces the heat flux. This turbulent Prandtl number correction approach was used by Aupoix (2015) and Morency and Beaugendre (2020). The increase depends on the roughness pattern as it influences the measured heat flux (Ignatowicz et al., 2022). For in-flight icing, the Prandtl number correction leads to a modification of the predicted ice shapes (Ignatowicz et al., 2021c). Over iced surfaces, the roughness pattern presents a lot of irregularities and is seldom accurately measured. Ice accretion models, based either on boundary layer methods or CFD, use the equivalent sandgrain roughness to model the complex roughness pattern (Fortin, 2019). Through empirical relations, the equivalent sandgrain roughness links various known roughness patterns to the wall friction experimentally measured by Nikuradse (1933). These empirical relations have largely been calibrated based on regular manufactured roughness patterns with conical or hemispherical elements. This manufactured roughness can fail to model the strongly irregular and varying shapes of roughness patterns above iced surfaces (Shin, 1996). For iced surfaces, research is still going to determine the parameter values needed for an ice prediction to match an experimental ice shape (Han & Palacios, 2017).

The ice shape dependence on the roughness pattern can be studied through the metamodeling approach. This approach enables uncertainty quantification (UQ) analysis, where the metamodel replaces the original complex model (Raj et al., 2020). The Polynomial Chaos Expansion (PCE) metamodeling is often used with CFD for UQ (Najm, 2009). The PCE was first suggested by Wiener (1938), who employed Hermite polynomials. A PCE metamodel establishes a polynomial relationship between the uncertain input and the output of interest by training on a limited design of experiments (Marelli & Sudret, 2019).

For the validation of ice accretion simulations, the predicted ice shapes should present similarities or coincide with experimentally obtained accretions. Model development efforts seek to close the gap between predicted ice shapes and experimental shapes (Baumert,

Bansmer, Trontin, & Villedieu, 2018; Wright, Al-Khalil, & Miller, 1997). Through the convective heat transfer, the predicted ice shape is linked to the surface roughness pattern, which is a priori unknown, irregular, or highly uncertain in the experimental set-ups. The Bayesian inversion method enables the calibration of the roughness parameters to obtain an ice accretion agreeing with the experimental shape (Wagner et al., 2021). The Bayesian inversion method uses the PCE metamodel and the experimental observation as inputs. The inversion method calibrates the metamodel inputs to match the experimental observation (Lee, Mavris, Volovoi, & Yuan, 2011). The Bayesian inversion works in a probabilistic framework. For the metamodel inputs, the inversion computes the probability distribution that will best fit the output with experimental observations (Muehleisen & Bergerson, 2016). The metrics commonly measured on an experimental ice accretion are the maximum ice thickness, the ice thickness distribution, or the cross-sectional accretion area (Son, Oh, & Yee, 2012). In the CFD context, the Bayesian inversion is used for model calibration procedures, often for fine-tuning the constants of turbulence models (Da Ronch et al., 2020; Guillas et al., 2014; Khan et al., 2021). The Bayesian calibration is an inverse problem where the output (i.e., the reference observation) is known, and the computational work calibrates the model inputs (i.e., the roughness parameters in the present work) to produce the said output. Hence, the calibrated inputs produce the expected output for the specific test case on which the calibration is carried out. These calibrated model inputs may not suit different test cases. Kennedy and O'Hagan (2001) introduced the concept of context-specific model inputs, meaning that the inputs might be valid for a broad range of test cases included in the "context" of the initial calibration. In the present ice accretion application, past studies confirmed the case dependence of the roughness pattern, especially with respect to atmospheric conditions (Shin, 1996).

The objective of the present work is to suggest a calibration methodology for the surface roughness parameters in a glaze ice in-flight situation. More specifically, the 2-Parameter Prandtl (2PP) thermal correction for rough walls (Morency & Beaugendre, 2020) is used to correct the SA rough turbulence model heat transfer prediction in the open-source flow solver SU2 CFD (Economon et al., 2015). SU2 is also extended with the SU2-ICE accretion solver (Ignatowicz et al., 2021a), a Messinger-based ice accretion model. SU2-ICE is used to build a

database of ice shapes to study the accretion variability with the roughness pattern. The database is then substituted with a PCE metamodel. The PCE metamodel establishes the link between the 2PP correction's roughness input parameters and the ice shape metrics. The calibration is achieved using a Bayesian inversion to calibrate the 2PP correction's roughness input parameters. The process from PCE metamodeling to Bayesian inversion is carried out in the UQLab framework (Marelli & Sudret, 2019; Wagner et al., 2021). The first part of the paper presents the methodology and the tools employed in the study. The model section then details the rough adaptations of the CFD model, including the 2PP thermal correction model, and the SU2-ICE ice accretion model. The model's description continues with the PCE metamodeling and the Bayesian inversion calibration. After the methodology and model are presented, the results are provided, starting with a presentation of the glaze ice test cases. The three cases studied involve a 2.5D NACA0012 wing at a 4-degree angle of attack (Wright, Gent, et al., 1997). A grid convergence study and the verification of the SU2-ICE implementation follow. The metamodels' characteristics and accuracy are checked next. Finally, the results of the Bayesian inversion calibration for the glaze ice test cases are shown, highlighting the calibrated roughness parameters obtained. The calibrated roughness values depend on the atmospheric conditions.

4.3 Methodology

This section presents the steps needed to calibrate the roughness parameters. The process is carried out on a 2.5D NACA0012 airfoil in glaze ice conditions. The methodology workflow uses the open-source SU2 solver for airflow computation and ice accretion calculation. The CFD database created is then modeled by PCE metamodels using the UQLab suite. Finally, the calibration, using the Bayesian module of UQLab, estimates the roughness parameters that produce a relevant ice shape.

The main steps of the methodology, along with the models, the software used, and the quantities transferred between the steps, are shown in Figure 4.1. Steps 1 to 4 are decoupled and executed sequentially. First, the compressible SU2 RANS solver computes the airflow

with the SA Rough turbulence model augmented with the 2PP thermal correction model. The airflow velocity field enables the calculation of the droplet collection efficiency on the surfaces. The wall heat transfer coefficient and the wall shear stress are extracted from the airflow solution in a second step, namely, ice accretion simulation. The ice accretion solver, SU2-ICE, uses a Messinger-based, SWIM-inspired model, to output the 2.5D ice shape. The SU2-ICE solver performs single-layer ice accretions. The limitation of this approach lies in its use of an airflow solution not updated by the geometry deformation. The multi-layer approach usually predicts ice shape fittings closer to experimental accretion values. Nevertheless, it is common practice to use single-layer ice accretion simulations as a starting point. These simulations avoid intermediate remeshing, which can fail with classical mesh deformation algorithms in some cases (Pena, Hoarau, & Laurendeau, 2016). Steps 1 and 2 are run 120 times, each time with different roughness parameters, to build the CFD database. For step 3, the UQLab tool performs the construction of the PCE metamodels. These metamodels replace the raw database with polynomial relations between the roughness inputs and the ice shape characteristics. Step 4 is the evaluation of the calibrated roughness parameters with the UQLab Bayesian inversion module. The Bayesian inversion uses the PCE metamodels and observations from the literature for the computation of the calibrated roughness parameters.

The motivation behind the PCE metamodels usage is two-fold. First, it provides the Bayesian inversion module with a forward mathematical model suitable for its execution. Second, the PCE metamodels give a response 10^5 times faster than the CFD airflow and icing simulation combined. The CFD simulation is run on 192 cores for the airflow simulation, while the icing simulation runs on one core. In such a configuration, the airflow simulation represents more than 99.99% of the total CFD execution time (about 6 hours for the airflow, and less than one minute for the ice accretion). The PCE metamodel can compute the outputs of interest in less than 4 seconds on one core.

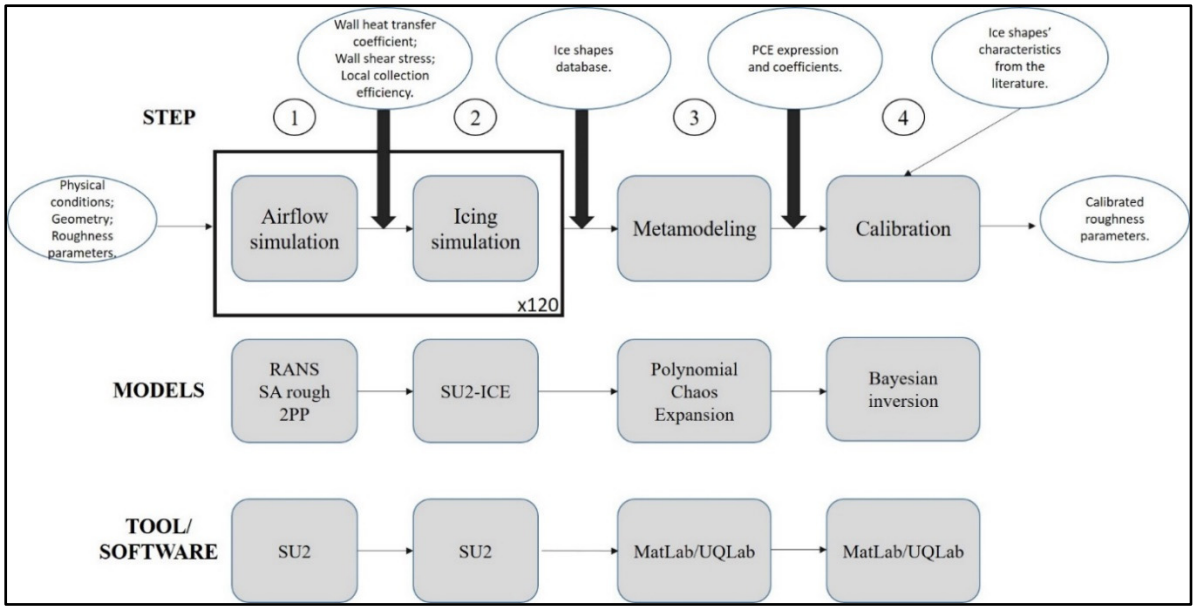

Figure 4.1 Steps involved in the calibration methodology

4.4 CFD Models

With the methodology overview shown, steps 1 and 2 (Figure 4.1) of the CFD models can be detailed. The SA rough turbulence model is first described by indicating the modifications implemented into the classical SA model. The 2PP rough thermal correction model is presented next, to identify the roughness parameters and their role in the heat flux computation. Lastly, the mathematical model and the algorithm employed within the SU2-ICE ice accretion solver are detailed.

4.4.1 Rough Extension of the SA Turbulence Model (SA Rough)

The energy equation in the RANS model (Blazek, 2005) involves the air thermal conductivity λ. For turbulent flows, the thermal conductivity is the sum of the laminar λ_{lam} and turbulent λ_t contributions (equation (4.1)):

$$\lambda = \lambda_{lam} + \lambda_t \tag{4.1}$$

The laminar and turbulent thermal conductivities are functions of the dynamic viscosity and the Prandtl number. Again, those quantities have a laminar and a turbulent value, as shown in equation (4.2):

$$\lambda = \left(\frac{C_{pa}\mu}{Pr} + \frac{C_{pa}\mu_t}{Pr_t}\right) \tag{4.2}$$

C_{pa} is the air specific heat at constant pressure, and μ is the air dynamic viscosity. Pr is the laminar Prandtl number (typically 0.72), Pr_t is the turbulent Prandtl number (typically 0.9), and μ_t is the turbulent viscosity. The turbulent viscosity is computed with the turbulence model. The classical SA turbulence model has one transport equation, for the turbulence variable $\tilde{\nu}$. Without the transition source, this transport equation is given by equation (4.3):

$$\frac{\partial\tilde{\nu}}{\partial t} + \frac{\partial\left(\tilde{\nu}u_j\right)}{\partial x_j} = c_{b1}(1-f_{t2})\tilde{S}\tilde{\nu} + \frac{1}{\sigma}\left[\frac{\partial}{\partial x_j}\left(\left(\frac{\mu}{\rho}+\tilde{\nu}\right)\frac{\partial\tilde{\nu}}{\partial x_j}\right) + c_{b2}\frac{\partial\tilde{\nu}}{\partial x_j}\frac{\partial\nu_t}{\partial x_j}\right] - \left(c_{w1}f_w - \frac{c_{b1}}{\kappa^2}f_{t2}\right)\left(\frac{\tilde{\nu}}{d}\right)^2 \tag{4.3}$$

where u_j and x_j are the velocity components and spatial coordinates, and ρ is the air density. The turbulent viscosity in equation (4.2) is computed as:

$$\mu_t = f_{v1}\rho\tilde{\nu} \tag{4.4}$$

The first adaptation for the SA rough model is to correct the wall distance from d to d_{rough} such that:

$$d_{rough} = d + 0.03k_s \tag{4.5}$$

with k_s being the equivalent sandgrain roughness or, for concision, “equivalent roughness”. Furthermore:

$$f_{v1} = \frac{\chi^3}{\chi^3 + c_{v1}^3} \tag{4.6}$$

where

$$\chi = \frac{\tilde{\nu}\rho}{\mu} + 0.5\frac{k_s}{d_{rough}} \tag{4.7}$$

The remaining terms and constants are detailed in Table 4.1.

Table 4.1 Terms and constants in the SA rough model

$\tilde{S} = \Omega + \frac{\tilde{\nu}}{\kappa^2 d_{rough}^2} f_{v2}$	$f_{t2} = c_{t3}\exp(-c_{t4}\chi^2)$	$c_{w2} = 0.3$
$\Omega = \sqrt{2w_{ij}{}^2}$	$w_{ij} = \frac{1}{2}\left(\frac{\partial u_i}{\partial x_j} - \frac{\partial u_j}{\partial x_i}\right)$	$c_{w3} = 2$
$f_{v2} = 1 - \frac{\tilde{\nu}}{\mu/\rho + \tilde{\nu} f_{v1}}$	$c_{b1} = 0.1355$	$c_{v1} = 7.1$
$f_w = g\left(\frac{1 + c_{w3}^6}{g^6 + c_{w3}^6}\right)^{1/6}$	$\sigma = \frac{2}{3}$	$c_{t3} = 1.2$
$g = r + c_{w2}(r^6 - r)$	$c_{b2} = 0.622$	$c_{t4} = 0.5$
$r = \min\left(\frac{\tilde{\nu}}{\tilde{S}\kappa^2 d_{rough}^2}, 10\right)$	$\kappa = 0.41$	$c_{w1} = \frac{c_{b1}}{\kappa^2} + \frac{1 + c_{b2}}{\sigma}$

Finally, the main feature of the SA rough turbulence model is the wall boundary condition (equation (4.8)):

$$\left(\frac{\partial \tilde{\nu}}{\partial n}\right)_{wall} = \frac{\tilde{\nu}_{wall}}{0.03 k_s} \tag{4.8}$$

In other words, the wall boundary condition, instead of having a zero $\tilde{\nu}$ at the wall, imposes a gradient normal to it.

4.4.2 2PP Thermal Correction Model

In the continuity of the SA rough development, the 2PP thermal correction model aims at reducing the wall heat fluxes. The wall heat flux q_{wall}, described by the Fourier law, is written in equation (4.9):

$$q_{wall} = -\lambda \left(\frac{\partial T}{\partial n}\right)_{wall} \tag{4.9}$$

where T is the temperature. The decrease of the thermal conductivity λ reduces the heat flux magnitude. This is done by increasing the turbulent Prandtl number Pr_t (see equation (4.2)). The 2PP thermal correction model replaces Pr_t with its corrected value $Pr_{t,rough}$:

$$Pr_{t,rough} = Pr_t + \Delta Pr_t \tag{4.10}$$

Close to the rough wall, the 2PP thermal correction adds ΔPr_t to the turbulent Prandtl number Pr_t value of 0.9. The roughness pattern, described by the roughness height k and the equivalent roughness k_s, influences the correction value. The expression of ΔPr_t is given by equation (4.11):

$$\Delta Pr_t = g \times 0.07083 \times {Re_s}^{0.45} \times Pr^{0.8} \times exp\left(-\frac{d}{k}\right) \tag{4.11}$$

The roughness Reynolds number Re_s and the parameter g in equation (4.11) are detailed in equations (4.12) and (4.13), where u_τ is the friction velocity (m/s) and ν (m²/s) is the kinematic air viscosity.

$$Re_S = \frac{u_\tau k_s}{\nu} \tag{4.12}$$

$$g = \begin{cases} 1 \text{ if } Re_s \geq 70 \\ \dfrac{\ln(Re_s) - \ln(5)}{\ln(70) - \ln(5)} \text{ if } 5 < Re_s < 70 \\ 0 \text{ if } Re_s \leq 5 \end{cases} \tag{4.13}$$

4.4.3 SU2-ICE Accretion Model

The airflow solution provides the heat fluxes, including the wall temperature information, and shear stresses at the wall needed for ice shape prediction. The impinging water droplets, or the droplet collection efficiency, are also required to perform an ice accretion simulation. A freezing film model, derived from (Bourgault et al., 2000), is implemented in the SU2 software. The model simulates different ice accretion regimes, including rime ice (i.e., only solid ice forming) and glaze ice (i.e., the coexistence of solid ice and runback liquid film). Unlike the flow computation performed in the complete 2.5D domain, the SU2-ICE solver is executed on the airfoil surface only, i.e., on a 2D surface zone. To define the icing zone, the wall boundary elements (quadrilateral or triangular cells) are converted into a proper zone. In the SU2 framework, the simulation is multizone: RANS in the flow domain and SU2-ICE on the selected surface. This creation of a 2D zone inside a 2.5D or 3D domain requires some adjustments to the SU2 framework. Surface elements with an associated area, instead of volume elements, are defined. The area S_{elem} of a 3D triangle with vertices A(x_A, y_A, z_A), B(x_B, y_B, z_B), and C(x_C, y_C, z_C), is given by equation (4.14). The area of a quadrilateral element is the sum of the two triangles that compose it:

$$S_{elem} = \frac{1}{2}\sqrt{\begin{vmatrix} x_A & x_B & x_C \\ y_A & y_B & y_C \\ 1 & 1 & 1 \end{vmatrix}^2 + \begin{vmatrix} y_A & y_B & y_c \\ z_A & z_B & z_c \\ 1 & 1 & 1 \end{vmatrix}^2 + \begin{vmatrix} z_A & z_B & z_C \\ x_A & x_B & x_c \\ 1 & 1 & 1 \end{vmatrix}^2} \tag{4.14}$$

In equation (4.14), the vertical brackets denote the determinant of the 3×3 matrix. Verification tests on a 3D NACA0012 wing, using equation (4.14) for each surface element, allowed for recovering the analytical total area of the wing.

The ice accretion problem is illustrated in Figure 4.2 for one surface element. The mass and energy contributions to the water film are illustrated with white arrows: gains point towards the film, while losses point outward. The mathematical expression of each term will be developed throughout the subsection.

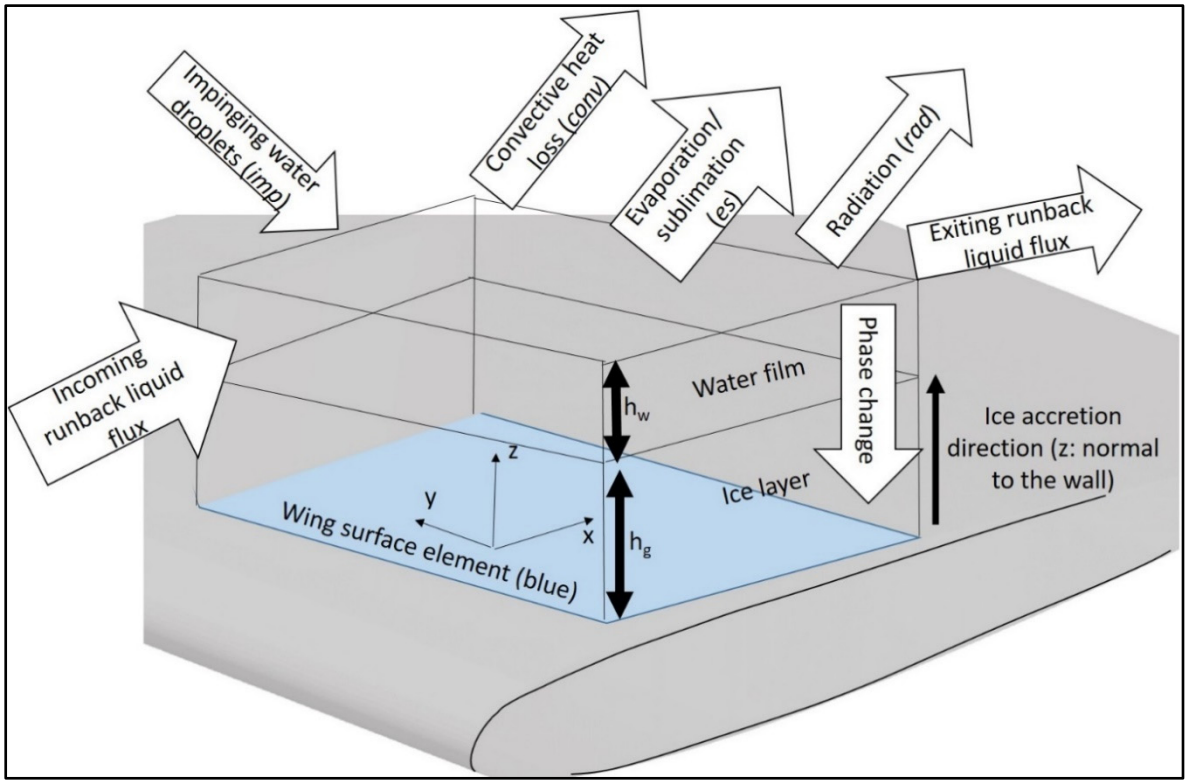

Figure 4.2 Visualization of heat and mass contributions to the icing problem

The SU2-ICE model is a Partial Derivative Equation (PDE) formulation of the original Messinger ice accretion model. The SU2 software can solve any generic PDE models in the form given in equation (4.15):

$$\frac{\partial \boldsymbol{W}}{\partial t} + \frac{\partial \boldsymbol{F}}{\partial \boldsymbol{x}} = \boldsymbol{S} \tag{4.15}$$

where $\boldsymbol{W}$ is the vector of conservative variables, $\boldsymbol{F}$ stands for the convective fluxes, $\boldsymbol{S}$ is the source term, t is the time and $\boldsymbol{x}$ is the vector of the spatial coordinates.

The SU2-ICE model is based on two equations: a mass balance and an energy balance, meaning that the vector in equation (4.15) has two components. Figure 4.2 highlights the contributions to the mass and energy balances from the point of view of the water film: the impinging water droplets, the convective heat, the evaporation/sublimation, the radiation, and the phase change are source terms (source and sinks). The aerodynamic heating is included in the convective heat loss, since the recovery temperature, and not the freestream temperature, is used as a reference (see equation (4.25)). The runback water (incoming and exiting) constitutes the liquid convective flux. The direction of travel of the runback water film is driven by the air shear stress $\boldsymbol{\tau_{wall}}$ computed at the airflow simulation step. The film velocity is detailed in the next paragraph and equation (4.19). More specifically, the terms $\boldsymbol{W}$, $\boldsymbol{F}$, and $\boldsymbol{S}$ of the SU2-ICE PDE system are given by equations (4.16) to (4.18). The source term is split into $\boldsymbol{S_0}$ and the ice accretion part $\boldsymbol{S_g}$:

$$\boldsymbol{W} = \begin{pmatrix} \rho_w h_w \\ \rho_w h_w C_{pw} (T_w - 273.15) \end{pmatrix} \tag{4.16}$$

$$\boldsymbol{F} = \begin{pmatrix} \rho_w h_w \overline{\boldsymbol{u}} \\ \rho_w h_w C_{pw} (T_w - 273.15) \overline{\boldsymbol{u}} \end{pmatrix} \tag{4.17}$$

$$\boldsymbol{S} = \begin{pmatrix} \dot{m}_{imp} - \dot{m}_{es} - \rho_g \dfrac{\partial h_g}{\partial t} \\ \dot{Q}_{imp} - \dot{Q}_{es} - \dot{Q}_{rad} - \dot{Q}_{conv} + \rho_g \dfrac{\partial h_g \left(L_{fus} - C_{pg}(T_w - 273.15)\right)}{\partial t} \end{pmatrix}$$

$$\boldsymbol{S} = \begin{pmatrix} \dot{m}_{imp} - \dot{m}_{es} \\ \dot{Q}_{imp} - \dot{Q}_{es} - \dot{Q}_{rad} - \dot{Q}_{conv} \end{pmatrix} + \begin{pmatrix} -\rho_g \dfrac{\partial h_g}{\partial t} \\ \rho_g \dfrac{\partial h_g \left(L_{fus} - C_{pg}(T_w - 273.15)\right)}{\partial t} \end{pmatrix} \tag{4.18}$$

$$\boldsymbol{S} = \boldsymbol{S_0} + \boldsymbol{S_g} = \begin{pmatrix} S_{01} \\ S_{02} \end{pmatrix} + \begin{pmatrix} S_{g1} \\ S_{g2} \end{pmatrix}$$

The subscripts *w* and *g* denote the water liquid film and the solid ice, respectively. The other subscripts are presented in Figure 4.2. Furthermore, ρ (kg/m^3) is the density, h (m) the thickness, C_p (J/kg/K) is the specific heat at constant pressure, and L_{fus} (J/kg) is the water latent heat of fusion. $\dot{m}$ (kg/m²/s) and $\dot{Q}$ (J/m²/s) designate the mass rate and energy rate, respectively. T_w (K) is the film temperature, assumed to be constant along the film thickness and equal to the wall temperature. Finally, the average film velocity $\overline{\boldsymbol{u}}$ (m/s) is given by equation (4.19), where μ_w (Pa·s) is the water viscosity. This average velocity is computed assuming a linear velocity profile in the wall's normal direction, with a no-slip (i.e., film velocity of zero) condition at the wall:

$$\overline{\boldsymbol{u}} = \frac{h_w}{2\mu_w} \boldsymbol{\tau_{wall}} \tag{4.19}$$

The source terms appearing in $\boldsymbol{S}$ (equation (4.18)), described in Özgen and Canibek (2008) and Beaugendre (2003), are given in the following equations (4.20) to (4.25).

$$\dot{m}_{imp} = LWC \times \beta \times V_\infty \tag{4.20}$$

$$\dot{m}_{es} = \frac{0.7}{C_{pa}} \times h_c \times \frac{P_{vw} - P_{v\infty}}{P_\infty} \tag{4.21}$$

$$\dot{Q}_{imp} = \dot{m}_{imp}\left(C_{pw}(T_\infty - 273.15) + \frac{u_{drop}^2}{2}\right) \tag{4.22}$$

$$\dot{Q}_{es} = \begin{cases} L_s \times \dot{m}_{es} \; if \; (T_w - 273.15) < 0 \\ L_e \times \dot{m}_{es} \; if \; (T_w - 273.15) \geq 0 \end{cases} \tag{4.23}$$

$$\dot{Q}_{rad} = \sigma\varepsilon(T_w^4 - T_\infty^4) \tag{4.24}$$

$$\dot{Q}_{conv} = h_c(T_w - T_{rec}) \tag{4.25}$$

In equations (4.20) to (4.25), the new quantities and the new symbols appearing are:

- LWC, the liquid water content of the ambient air, kg/m^3;
- β, the local collection efficiency;
- V_∞, the freestream air velocity, m/s;
- h_c, the local convective heat transfer coefficient, W/m^2/K;
- P_{vw} and $P_{v\infty}$, the surface and ambient saturation vapor pressure, respectively, Pa (see equation (4.27));
- P_∞, the freestream pressure, Pa;
- T_∞, the freestream temperature, K;
- u_{drop}, the local magnitude of the droplet impact velocity, m/s;
- L_s and L_e, the latent heat of sublimation and evaporation of water, respectively, J/Kg;
- σ, the Boltzmann constant, W/m^2/K^4;
- ε, the emissivity of ice;
- T_w, the surface temperature, assumed to be the film temperature, K;
- T_{rec}, the recovery temperature of ambient air, K (see equation (4.26)).

The convective heat loss, sensitive to the roughness (see the CFD subsections 4.4.1 and 4.4.2), is involved in the icing process through h_c in the evaporation/sublimation (equations (4.21) and (4.23)) and convective (equation (4.25)) terms. The recovery temperature, a function of the freestream Mach number M, and the saturation vapor pressure require additional equations. These are shown in equations (4.26) and (4.27), respectively:

$$T_{rec} = T_{\infty}(1 + 0.17926 \times M^2) \tag{4.26}$$

$$P_v = 3386 \times (0.0039 + 6.8096 \times 10^{-6}\tilde{T}^2 + 3.5579 \times 10^{-7}\tilde{T}^3) \tag{4.27}$$

where the temperature $\tilde{T} = 72 + 1.8(T - 273.15)$.

Note that the PDE system of equation (4.15) has two equations, for three unknowns: the ice thickness h_g, the film thickness h_w, and the surface temperature T_w. To allow the resolution of the system, additional inequalities are added. The so-called compatibility relations are developed in equation (4.28):

$$\begin{cases} h_w \geq 0 \\ h_w(T_w - 273.15) \geq 0 \\ \rho_g \dfrac{\partial h_g}{\partial t} \geq 0 \\ \rho_g \dfrac{\partial h_g}{\partial t}(T_w - 273.15) \leq 0 \end{cases} \tag{4.28}$$

Physically speaking, these compatibility relations state that:

1) The water film thickness must be positive or zero;
2) A water film exists only if the surface temperature is above or equal to 273.15 K;
3) Ice accretion rate must be positive or zero, i.e., no ice melting;
4) Ice accretion occurs only if the surface temperature is below or equal to 273.15 K.

The flux $\boldsymbol{F}$ of the PDE system is discretized using a Roe scheme, with a second-order MUSCL reconstruction (Blazek, 2005). The moving water film can be seen as a discontinuity at the waterfront and the Roe scheme is suitable for the present application. SU2 uses the dual mesh approach, meaning that each node of the initial primal mesh – where the variables are stored – is the cell centre of a dual cell. The convective flux is then computed through the edges of the dual mesh. The constructed dual control volumes are centered on a primal grid node (Figure 4.3). The MUSCL approach (van Leer, 1979) consists in computing the reconstructed states at the dual control volume edges, called the left (L) and right (R) states (Figure 4.3). These reconstructed states are used in lieu of the nodal values at the points *i* and *j* for the flux calculation. In SU2, the left reconstructed state for a generic quantity *U* is computed with equation (4.29):

$$U_L = U_i + \psi_L \times \overrightarrow{\boldsymbol{x_i}} \cdot \overrightarrow{\boldsymbol{grad}}(U)_i \tag{4.29}$$

where U_i is the quantity value at point *i* and $\overrightarrow{\boldsymbol{x_i}}$ is the vector joining point *i* to the edge *e*. ψ_L is the limiter function, damping the solution in case of large gradients. The limiter used in the present application is the one suggested by (Venkatakrishnan, 1993). Similarly, the right state is reconstructed by substituting *L* for *R,* and *j* for *i*, in equation (4.29).

Let us consider an edge in the dual mesh, as in Figure 4.3, to illustrate and define the nomenclature for the flux discretization. The vector $\vec{\boldsymbol{n}}$ is the outward-pointing dimensional normal vector, whose norm is equal to the length of the edge.

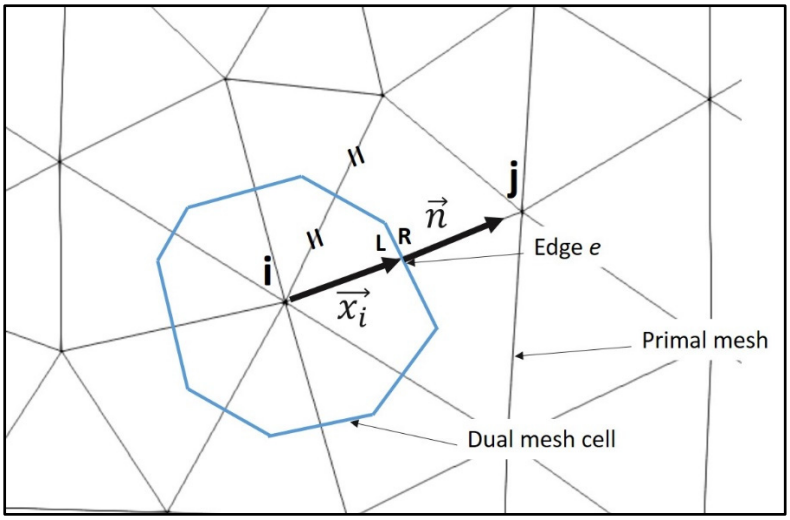

Figure 4.3 Scheme of a dual control volume (blue)
and useful nomenclature

Keeping the notation of Figure 4.3, the flux $\boldsymbol{F_e}$ through the edge *e* from point *i* to point *j* is defined as in equation (4.30):

$$\boldsymbol{F}_e = \frac{1}{2}(\boldsymbol{F}_L + \boldsymbol{F}_R)\cdot\vec{\boldsymbol{n}} - \frac{1}{2}|\boldsymbol{A_e}|\cdot\vec{\boldsymbol{n}}\cdot(\boldsymbol{W_R} - \boldsymbol{W_L}) \tag{4.30}$$

where $\boldsymbol{A_e}$ is the Roe matrix associated with the edge *e*. In the case of the SU2-ICE PDE system, the matrix $\boldsymbol{A_e}$ is given by equation (4.31). For concision, the expression $(T_w - 273.15)$ is replaced by $\bar{T}$, with the appropriate subscripts.

$$\boldsymbol{A_e} = \begin{bmatrix} 2\bar{\boldsymbol{u}}_{\boldsymbol{LR}} & 0 \\ C_{pw}\bar{T}_{LR}\bar{\boldsymbol{u}}_{\boldsymbol{LR}} & \bar{\boldsymbol{u}}_{\boldsymbol{LR}} \end{bmatrix} \tag{4.31}$$

The quantities with the subscript *LR* designate the Roe averaging between the left and the right states. The water density is assumed constant, and the Roe averaging degenerates into a simple averaging between the left and the right states. Following the general development of the Roe scheme in equation (4.30), it is possible to expand the equations and give the full formulation of $\boldsymbol{F_e}$ (equation (4.32)). The mass and energy terms in $\boldsymbol{F_e}$ are denoted F_1 and F_2, respectively.

$$\boldsymbol{F}_e = \begin{bmatrix} 0.5\rho_w[(h_{wL}\overline{\boldsymbol{u}}_{\boldsymbol{L}} \cdot \vec{\boldsymbol{n}} + h_{wR}\overline{\boldsymbol{u}}_{\boldsymbol{R}} \cdot \vec{\boldsymbol{n}}) - 2|\overline{\boldsymbol{u}}_{\boldsymbol{LR}} \cdot \vec{\boldsymbol{n}}|(h_{wR} - h_{wL})] \\ 0.5\rho_w C_{pw}[(h_{wL}\overline{T}_L\overline{\boldsymbol{u}}_{\boldsymbol{L}} \cdot \vec{\boldsymbol{n}} + h_{wR}\overline{T}_R\overline{\boldsymbol{u}}_{\boldsymbol{R}} \cdot \vec{\boldsymbol{n}}) - |\overline{\boldsymbol{u}}_{\boldsymbol{LR}} \cdot \vec{\boldsymbol{n}}|(\overline{T}_{LR}(h_{wR} - h_{wL}) + (h_{wR}\overline{T}_R - h_{wL}\overline{T}_L))] \end{bmatrix}$$
$$\boldsymbol{F}_e = \begin{bmatrix} F_1 \\ F_2 \end{bmatrix} \tag{4.32}$$

To avoid excessively long expressions in equation (4.32), the scalar products, often referred to as contravariant velocity, are not expanded. The normal-projected velocity in 3D is given by equation (4.33) for velocity $\boldsymbol{u}$:

$$\boldsymbol{u} \cdot \vec{\boldsymbol{n}} = \begin{pmatrix} u_1 \\ u_2 \\ u_3 \end{pmatrix} \cdot \begin{pmatrix} n_1 \\ n_2 \\ n_3 \end{pmatrix} = u_1 n_1 + u_2 n_2 + u_3 n_3 \tag{4.33}$$

For the temporal resolution, the equations are solved using a forward explicit Euler method. In the early stage of icing, the time step Δt_i on the cell i of area Ω_i is driven by the film velocity $\overline{\boldsymbol{u}}_i$ and the CFL number set at 0.9 (equation (4.34)). In SU2, the summation of the projected velocity on each edge normal surrounding the point i is used. Since the time stepping is global, the smallest time step among all the cells is kept for the current iteration (equation (4.35)).

$$\Delta t_i = \frac{CFL \times \Omega_i}{|\overline{u_i} \cdot \sum \vec{n}|} \tag{4.34}$$

$$\Delta t = min(\Delta t_i) \tag{4.35}$$

To avoid the special case of a dry surface (for example, at the initial time) without a film velocity (leading to an undefined time step), the precursor film approach is used (Myers, Charpin, & Chapman, 2002). This approach considers a virtual film thickness of about 10^{-10} m, only used for the time step evaluation. The physical exposure time of an ice accretion simulation is usually several hundreds of seconds, while the initial time steps can fall below 10^{-5} s, depending on the film velocity. To avoid too many iterations (and a large computation

time) the quasi-steady approach is used. During the ice accretion simulation, the airflow-related quantities remain constant: the impingement, momentum, shear stress, and heat transfer coefficient are steady. The SU2-ICE solver is implemented to detect the moment when the quasi-steady state is reached and then extrapolates the accretion until the final exposure time (Lavoie, 2017). Specifically, the mass and energy root mean square residuals are computed according to equation (4.36) and (4.37), respectively[2].

$$Res_{mass} = \sqrt{\frac{1}{N}\sum_{i=1}^{N}\left[\rho_g\left(\frac{h_{gi}^{n} - h_{gi}^{n-1}}{\Delta t_n} - \frac{h_{gi}^{n-1} - h_{gi}^{n-2}}{\Delta t_{n-1}}\right)\Omega_i\right]^2} \tag{4.36}$$

$$Res_{energy} = \sqrt{\frac{1}{N}\sum_{i=1}^{N}[\bar{T}_i^{n} - \bar{T}_i^{n-1}]^2} \tag{4.37}$$

The superscripts *n−2*, *n−1*, and *n* denote the time iterations, and Δt_n is the global time step at iteration *n*. The surface domain has a total of *N* cells. The logarithm of the residuals is monitored and when it reaches a user-defined low value (typically −8), the steady state is considered reached. The steady state corresponds to a constant film thickness, a constant surface (film) temperature, and a constant ice growth rate, as in equations (4.38) to (4.40), with *C* a constant value.

$$\frac{\partial h_w}{\partial t} = 0 \tag{4.38}$$

$$\frac{\partial T_w}{\partial t} = 0 \tag{4.39}$$

[2] Prendre note qu'un troisième résidu, basé sur l'évolution en masse du film liquide entre deux instants successifs et non finalisé au moment de la publication, est également utilisé.

$$\frac{\partial h_g}{\partial t} = C \tag{4.40}$$

The SU2-ICE explicit time scheme is based on a trial-and-error procedure, looping on every cell at each time iteration. Each state (dry, rime ice, glaze ice, or wet) is tested by solving the discretized system of PDE (see equation (4.44)), and the compatibility relations (equation (4.28)) are checked. Because the system has three unknowns for two equations, testing each state allows setting one of the unknowns to a fixed value, which means that only two unknowns remain. More specifically, when testing the:

- Rime ice regime, the film thickness h_w is set to zero (no liquid);
- Glaze ice regime, the temperature T_w is set to 273.15 K;
- Wet regime, the ice thickness h_g is set to zero (no ice).

The order of the tests is set considering the ambient temperature. Glaze ice usually appears when the air temperature is between 263.15 K and 273.15 K (Dai et al., 2021). Therefore, if the ambient air is above 263.15 K and below or equal to 273.15 K, the glaze ice is tested first. If not compatible, the rime ice is tested, and if needed, the wet regime is evaluated. In the case of an ambient air temperature below 263.15 K, rime ice is tested first, then glaze ice, and then the wet regime. When the air temperature is above 273.15 K, the wet regime is evaluated first, followed by the glaze and the rime regimes.

By looping on every cell at each time step, the ice accretion is computed. The discretized formulation of the PDE system of equation (4.15) for a cell of area Ω is given by equation (4.41). The sum of the convective fluxes is performed on the N_{neigh} edges of the cell. Δt is the current time step. The source term is split, according to equation (4.18).

$$\boldsymbol{W^n - S_g^n = W^{n-1} - S_g^{n-1} + \frac{\Delta t}{\Omega}\left(\left(\sum_{i=1}^{N_{neigh}} \boldsymbol{F_i^{n-1}}\right) + \Omega \boldsymbol{S_0^n}\right)} \tag{4.41}$$

By developing the terms, the fully expanded discretized formulation can be derived from equation (4.41), as in equation (4.44). For concision, the second term of equation (4.41), making the summation of the flux and source terms, is denoted $\boldsymbol{A}$. $\boldsymbol{A}$ has two components A_1 and A_2, corresponding to the mass equation and the energy equation. These terms are developed in equations (4.42) and (4.43). The terms F_1 and F_2 were developed in equation (4.32). S_{01} and S_{02} were expanded in equation (4.18).

$$A_1 = \frac{\Delta t}{\Omega}\left(\left(\sum_{i=1}^{N_{neigh}} F_{1i}^{n-1}\right) + \Omega S_{01}^{n}\right) \tag{4.42}$$

$$A_2 = \frac{\Delta t}{\Omega}\left(\left(\sum_{i=1}^{N_{neigh}} F_{2i}^{n-1}\right) + \Omega S_{02}^{n}\right) \tag{4.43}$$

The unknowns in equation (4.44) are the quantities at time *n*. Equation (4.44) is composed of the mass equation and the energy equation.

$$\begin{cases} \rho_w h_w^n + \rho_g h_g^n = \rho_w h_w^{n-1} + \rho_g h_g^{n-1} + A_1 \\ \rho_w h_w^n C_{pw} \bar{T}^n - \rho_g h_g^n \left(L_{fus} - C_{pg}\bar{T}^n\right) = \rho_w h_w^{n-1} C_{pw} \bar{T}^{n-1} - \rho_g h_g^{n-1}\left(L_{fus} - C_{pg}\bar{T}^n\right) + A_2 \end{cases} \tag{4.44}$$

Note that the source term $\boldsymbol{S_0}$ is evaluated at time *n*, which eases the convergence of the system, as suggested in Blazek (2005). In the glaze ice case, ($\bar{T}^n = 0$), equation (4.44) gives the ice and film thickness directly. The evaluation of other regimes requires additional strategies for the computation of the desired quantities. In the rime ice case ($h_w{}^n = 0$), equation (4.44) becomes:

$$\begin{cases} \rho_g h_g^n = \rho_w h_w^{n-1} + \rho_g h_g^{n-1} + A_1 \\ -\rho_g h_g^n \left(L_{fus} - C_{pg}\bar{T}^n\right) = \rho_w h_w^{n-1} C_{pw} \bar{T}^{n-1} - \rho_g h_g^{n-1}\left(L_{fus} - C_{pg}\bar{T}^n\right) + A_2 \end{cases} \tag{4.45}$$

The mass equation (fist component of equation (4.45)) needs the new surface temperature T_w^n, appearing in A_1 through the evaporative term (see equations (4.18), (4.21), and (4.26)). This new temperature is obtained by solving the energy equation (second component of equation (4.45)). This is achieved using an iterative Brent method (Brent, 2002) to solve for $\bar{T}^n$ in equation (4.46), which is the second component of equation (4.45) rearranged.

$$\rho_w h_w^{n-1} C_{pw} \bar{T}^{n-1} - \rho_g h_g^{n-1} \left(L_{fus} - C_{pg} \bar{T}^n\right) + A_2 + \rho_g h_g^n \left(L_{fus} - C_{pg} \bar{T}^n\right) = 0 \quad (4.46)$$

$\bar{T}^n$ is then used in the mass equation, and the new ice thickness is computed. The same situation is encountered in the wet case ($h_g^n = 0$), as in equation (4.47). The Brent algorithm is used to solve the energy equation (second component of equation (4.47)), before the resolution of the mass balance (first component of equation (4.47)).

$$\begin{cases} \rho_w h_w^n = \rho_w h_w^{n-1} + \rho_g h_g^{n-1} + A_1 \\ \rho_w h_w^{n-1} C_{pw} \bar{T}^{n-1} - \rho_g h_g^{n-1} \left(L_{fus} - C_{pg} \bar{T}^n\right) + A_2 - \rho_w h_w^n C_{pw} \bar{T}^n = 0 \end{cases} \quad (4.47)$$

For a dry surface, the energy equation is solved similarly to obtain the new surface temperature. In the dry case, there is no water or ice in the cell ($h_w = h_g = 0$), no impingement ($\dot{m}_{imp} = 0$), and no runback water from the neighbor cells ($\boldsymbol{F_1} = \boldsymbol{F_2} = 0$). There is no ice from the previous time step since ice cannot melt. The simplified energy equation in the dry case is given in equation (4.48), which is solved using a Newton-Raphson iterative method.

$$A_2 = \Delta t \boldsymbol{S_{02}^n} = 0 \equiv -\dot{Q}_{rad} - \dot{Q}_{conv} = 0 \quad (4.48)$$

The algorithm coded in SU2-ICE for one given cell is summarized with the following pseudo-code:

- If the cell is dry without surrounding wet or glaze cells, evaluate the dry regime (equation (4.48)). Update the values: $h_w = 0$, $h_g = 0$, and T_w using equation (4.48).
- Else,

- If $T_\infty \leq 263.15\ K$,
  - Evaluate the rime ice regime (equation (4.45)). Update the values: T_w using equation (4.46), $h_w = 0$, and h_g using first component of equation (4.45). Check the compatibility (equation (4.28)).
  - If rime ice is not compatible, evaluate the glaze ice regime (equation (4.44)). Update the values: h_w and h_g using equation (4.44) , and T_w = 273.15 K. Check the compatibility (equation (4.28)).
  - If glaze ice is not compatible, evaluate the wet regime (equation (4.47)). Update the values: T_w using second component of (4.47), h_w using first component of (4.47), and $h_g = 0$,

- If $263.15\ K\ < T_\infty \leq 273.15\ K$,
  - Evaluate the glaze ice regime (equation (4.44)). Update the values: h_w and h_g using equation (4.44), and T_w = 273.15 K. Check the compatibility (equation (4.28)).
  - If glaze ice is not compatible, evaluate the rime ice regime (equation (4.45)). Update the values: T_w using equation (4.46), $h_w = 0$, and h_g using first component of equation (4.45). Check the compatibility (equation (4.28)).
  - If rime ice is not compatible, evaluate the wet regime (equation (4.47)). Update the values: T_w using second component of equation (4.47), h_w using first component of equation (4.47), and $h_g = 0$.

- If $T_\infty > 273.15\ K$,
  - Evaluate the wet regime (equation (4.47)). Update the values: T_w using second component of equation (4.47), h_w using first component of equation (4.47), and $h_g = 0$. Check the compatibility (equation (4.28)).
  - If the wet regime is not compatible, evaluate the glaze ice regime (equation (4.44)). Update the values: h_w and h_g using equation (4.44), and T_w = 273.15 K. Check the compatibility (equation (4.28)).

- If glaze ice is not compatible, evaluate the rime ice regime (equation (4.45)). Update the values: T_w using equation (4.46), $h_w = 0$, and h_g using the first component of equation (4.45).

4.5 UQ and Calibration Models

This section details steps 3 and 4 (Figure 4.1). First, the metamodeling step, including the Design of Experiments (DOE) method used to build the CFD database, and the PCE metamodels construction, are depicted. Lastly, the Bayesian inversion calibration subsection sets out the procedure for the calibration of the roughness parameters using ice shapes from the literature.

4.5.1 Polynomial Chaos Expansion (PCE) Metamodeling

The PCE metamodels establish direct mathematical relationships between the roughness parameters and the ice shape outputs of interest, such as the thickness or the ice accretion cross-sectional area. The metamodels replace the CFD and ice accretion simulation to lower the cost of the UQ study and the calibration. The construction of the metamodel uses a design of experiments (DOE) for the input sampling strategy, and PCE, to simulate the output.

4.5.1.1 Input Sampling and Design of Experiment (DOE)

DOE samples the roughness model input parameters to create an ice shape database. The input parameters are the roughness height k and the ratio between the equivalent roughness k_s and k. The ratio k_s/k is preferred to k_s alone since it considers the relation between k and k_s. The two parameters influence the convective heat flux, and by extension, the final ice shape. For the roughness model input values, the relevant ranges are based on the literature (Dukhan et al., 1999b; Fortin, 2019). Table 4.2 summarizes the minimum and maximum values, and a uniform distribution is chosen for each parameter.

Table 4.2 Distribution of the input parameters

Parameter	Minimum	Maximum	Distribution
k	0.41 mm	4.32 mm	Uniform
Ratio k_s/k	0.2	6.5	Uniform

The number of samples N_s required for a metamodel creation depends on the number m of input variables (2 in the present case), the highest expected order p of the PCE (taken as 14), and the oversampling factor f_s. Equation (4.49) gives the expression for the evaluation of the number of samples (Schaefer et al., 2017).

$$N_s = f_s \times \frac{(m+p)!}{m!\,p!} \tag{4.49}$$

For an oversampling factor of 1.0, the number of samples is 120. The 120 input doublets (k; k_s/k) are generated using the Latin hypercube sampling. It spreads values homogeneously inside the input parameter range (Stein, 1987). The principle of the Latin hypercube sampling with two variables is to divide a 2D plane into 120 rows and 120 columns (in the present application). The 120 sample points are then chosen to ensure each line and each column contains one and only one sample point. The input values obtained are shown in Figure 4.4. The 120 input doublets are used for CFD and ice accretion simulations to output ice shapes. The database links the two parameters k and k_s to a unique ice shape, represented by a selected output of interest.

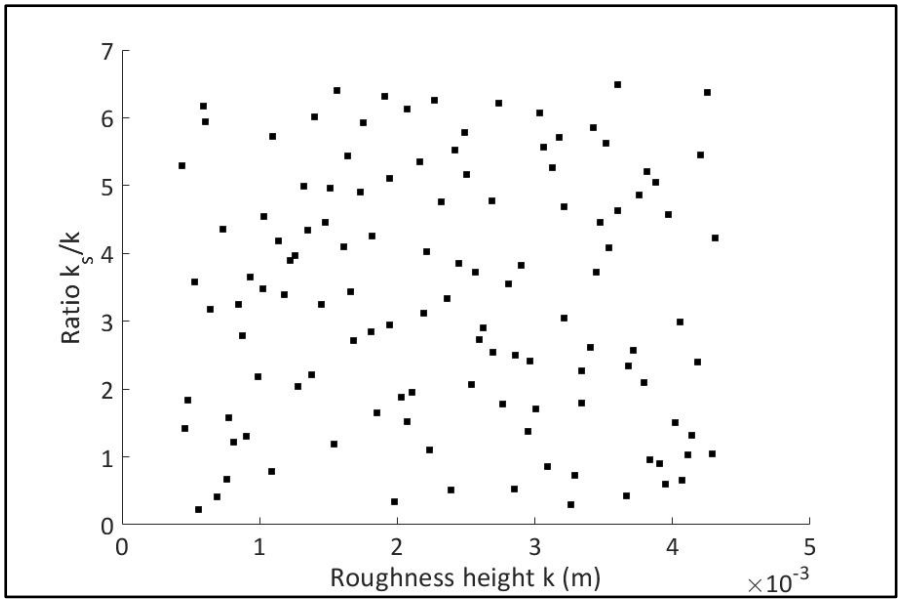

Figure 4.4 The input sample obtained by Latin hypercube sampling

4.5.1.2 PCE Creation

PCE is a common type of metamodel used for uncertainty quantification (Marelli & Sudret, 2019). A PCE metamodel M_i is composed of a sum of weighted multivariate polynomials, as developed in equation (4.50).

$$Y_i = M_i(\boldsymbol{X}) = \sum_{\alpha} y_\alpha \times \psi_\alpha(\boldsymbol{X}) \tag{4.50}$$

where Y_i is the output of interest, $\boldsymbol{X} = (k;\ k_s/k)$ is the input parameter vector, $\alpha = (\alpha_1, \alpha_2)$ is the multi-index with two components and y_α is the coefficient of the multivariate polynomial ψ_α. For a maximum degree p and 2 input parameters, the number of terms N_M in equation (4.50), detailed in equation (4.51), is equal to the sample size (equation (4.49)), with an oversampling factor of 1.0.

$$N_M = \frac{(p+2)!}{p! \times 2!} \tag{4.51}$$

The multivariate polynomials ψ_α are the tensor product of the two univariate basis polynomials ϕ (equation (4.52)).

$$\psi_\alpha(\boldsymbol{X}) = \prod_{i=1}^{2} \varphi_{\alpha_i}(X_i) \tag{4.52}$$

For uniform input distributions, the univariate polynomials are Legendre polynomials of indices α_1 and α_2.

The metamodels are created for two types of outputs of interest: the ice thickness (maximum or local) of the accretion and the accretion cross-sectional area. The maximum thickness and the cross-sectional area are simultaneously computed by the metamodel M_1. The second metamodel M_2 simultaneously computes the local thickness at N_{out} probe locations. N_{out} will be selected in the results section. These metamodels are defined in Table 4.3.

Table 4.3 The metamodels generated

Metamodel	Outputs of interest
M_1	Maximum ice thickness (m)- Ice cross-sectional area (m²)
M_2	Ice thickness at N_{out} probe locations (m)

The first metamodel is a low-fidelity predictor, quantifying two macroscopic descriptors of the accretion. The maximum thickness and the cross-sectional area can give a first insight into the "size" of the accretion, without the precise shape. On the other hand, the metamodel M_2 allows to simultaneously predict the ice shape at several locations, giving a better geometrical representation. One way to ensure the metamodel reliability is to evaluate its output on the same sample used for the CFD DOE. The R^2 regression coefficient (equation (4.53)) between

the PCE-predicted (Y_{PCE}) and the CFD-predicted (Y_{CFD}) output quantifies the precision of the metamodel. $\bar{Y}_{CFD}$ denotes the output mean value for the true CFD response. An R^2 coefficient close to 1 ensures that the PCE metamodel gives responses close to the CFD responses.

$$R^2 = 1 - \frac{\sum(Y_{CFD} - Y_{PCE})^2}{\sum(Y_{CFD} - \bar{Y}_{CFD})^2} \tag{4.53}$$

The leave-one-out error (*LOO*) is another tool available to quantify the accuracy of a metamodel (Marelli & Sudret, 2019). The principle of the *LOO* calculation is to create 120 metamodels M_{Loo}^i, each built on the original database by excluding the i^{th} data sample x^i. It is equivalent to training the model on a training set of 119 while keeping a testing set of 1. The cross-validation is assessed when comparing the M_{Loo}^i PCE prediction against the true value CFD^i of the i^{th} output of the database. The *LOO* error is calculated with equation (4.54).

$$LOO = \frac{\sum\left(CFD^i - M_{LOO}^i(x^i)\right)^2}{\sum CFD^i - \bar{Y}_{CFD})^2} \tag{4.54}$$

The sums are applied to all the database entries (1 to 120). The closer the *LOO* is to zero, the more accurate the metamodel will be against the CFD response.

4.5.2 Bayesian Inversion Calibration

Model calibration identifies the combination of roughness parameters (k; k_s/k) that produces an ice accretion that most closely approximates the shapes obtained in the literature. Here, the literature shapes are represented by the output of interest. This calibration is performed using the Bayesian inversion module of UQLab (Wagner et al., 2021). The Bayesian inversion works on the previously created PCE metamodels. Using the literature observations of the output of interest, the Bayesian solver computes the input parameters allowing to recover the observation. This calibration method relies on the Bayes theorem (equation (4.55)).

$$\pi(\theta|X_i) = \frac{\pi(X_i|\theta) \cdot \pi(\theta)}{\pi(X_i)} \tag{4.55}$$

The Bayesian inversion seeks to obtain the posterior distribution $\pi(\theta|X_i)$ of the input X_i, using the input prior distribution (see Table 4.2) $\pi(\theta)$ and the data provided by the literature observations. In equation (4.55), θ is the distribution parameter and the | symbol stands for the conditional dependence. The posterior distributions are the distributions of the input parameters, knowing the information provided by the observation data.

In equation (4.55), $\pi(X_i|\theta)$ is the likelihood function and $\pi(X_i)$ is analogous to a normalization constant called the marginal likelihood. The posterior distributions are usually no longer uniform. They identify the input parameter values that produce the output that most closely approximates the desired observation. Furthermore, a Gaussian discrepancy between the PCE output and the CFD prediction is provided to the solver. In the present application, a discrepancy of 2 mm (0.4% of the chord length) is assumed for the PCE thickness prediction and a discrepancy of 2×10^{-5} m² (between 2.5% and 4% of the total area) is assumed for the ice cross-sectional area. These discrepancies are analogous to measurement errors and represent the error between the metamodel prediction and the CFD output, estimating the measurement errors when reporting, plotting, and post-processing the experimental ice shapes. With the set-up tuned in UQLab, the posterior distribution computation is realized using a Markov chain Monte Carlo (MCMC) algorithm. The sampler used in the study is the Metropolis-Hastings (MH) algorithm. In this work, the MCMC solver is configured to perform 70,000 iterations and generates 15 chains. Once the posterior distributions are computed, the maximum a posteriori (MAP) of these distributions can be estimated. From a practical point of view, the MAP is the input value where a peak is observed on the distribution, and it is used to estimate the values of the input parameters leading to a model response close to the observation data.

4.6 Results for Various Glaze Ice Test Cases

This section applies the methodology to estimate the roughness parameters from experimental ice shape observations. The first subsection introduces the set-up used. The glaze ice test cases, including the computational domain, flow conditions, and mesh are presented. Next, a grid convergence study evaluates the uncertainties due to the mesh. The first subsection continues with the verification of the implementation of the SU2-ICE accretion model against the literature. The second subsection depicts the database obtained during the sampling and the PCE metamodels characteristics. It also presents the Bayesian inversion and the ice shapes obtained after calibration. Finally, the third subsection applies the methodology to test cases with other atmospheric conditions.

4.6.1 Physical Set-Up and Verification

4.6.1.1 Glaze Ice Test Cases

The rough thermal correction model and the ice accretion model enable the prediction of the ice shape on an initially rough airfoil. In the present paper, the NASA31, NASA32, and NASA36 glaze ice test cases are used (Wright, Gent, et al., 1997). The 2.5D geometry is a NACA0012 airfoil with a 0.53 m chord length at a 4-degree angle of attack. All the test case parameters are summarized in Table 4.4.

Table 4.4 Physical conditions for the glaze ice test cases

	NASA31	NASA32	NASA36
Freestream temperature	269.1 K	270.2 K	266.4 K
Freestream pressure	95,610 Pa	95,610 Pa	92,060 Pa
Chord length	0.53 m	0.53 m	0.53 m
Angle of attack	4°	4°	4°
Freestream velocity (Mach)	58.1 m/s (0.177)	58.1 m/s (0.177)	93.9 m/s (0.286)
Liquid water content (LWC)	1.30 g/m^3	1.30 g/m^3	1.05 g/m^3
Droplets median volume diameter (MVD)	20 µm	20 µm	20 µm
Total exposure time	480 s	480 s	372 s

The only difference between the NASA31 and the NASA32 cases is the freestream temperature. The NASA36 case has more discrepancies than the NASA31 case: the freestream temperature, the freestream pressure, the air velocity, the liquid water content, and the exposure time are different. The airflow is solved around the rough airfoil without any initial accretion. To this end, the compressible RANS solver of SU2 is used, with the SA rough turbulence model and the 2PP correction model. With Table 4.4 conditions, the Reynolds number based on the chord length is 2.2×10^6. For the computation of the wall heat transfer coefficient required for SU2-ICE, the wall is set as isothermal at 310 K for the flow computation. The discretization of the convective fluxes uses the JST scheme (Jameson, 2017), and the gradients are computed with the least-squares approach.

The computational domain for the flow simulation consists of an airfoil enclosed in a C-shaped volume. The far-field boundaries are positioned 500 chords away from the airfoil. The width of the domain, in the span direction, is 0.53 m. For the ice accretion simulations, the computational domain is the airfoil surface alone, still defined as a no-slip wall. The representation of the computational domain and the boundary conditions are presented in Figure 4.5.

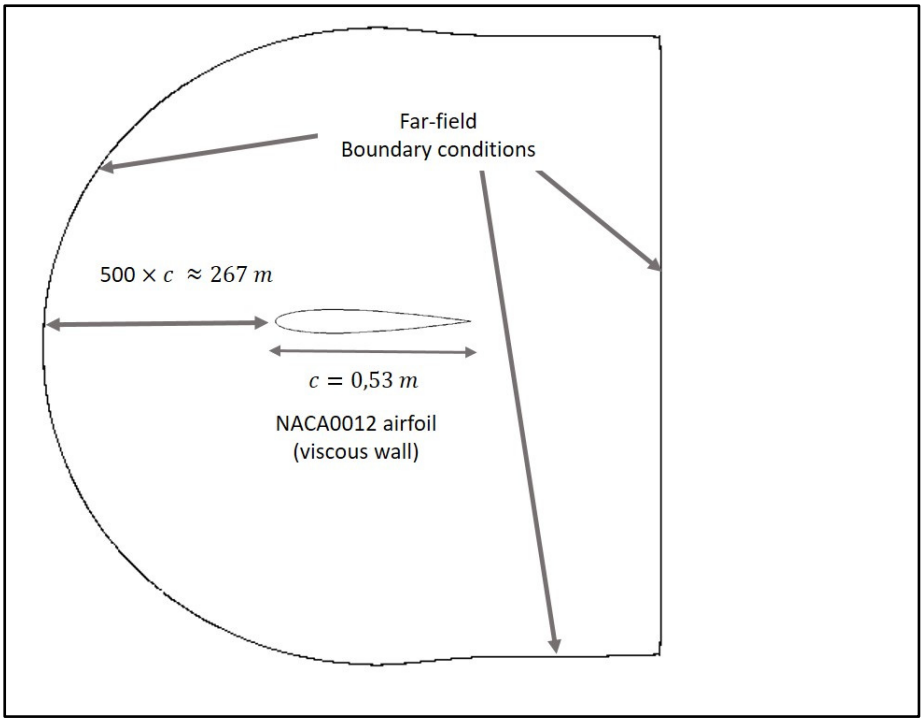

Figure 4.5 Computational domain for the simulation
(out of scale for airfoil visualization)

The NACA0012 mesh is provided by the NASA Turbulence Modeling Resource (NASA, 2013), and the 897-257 grid is chosen. The C-grid retained has 229,376 cells in the domain, with 512 quadrilaterals on the airfoil surface. The first cell height normal to the wall is 4×10^{-7}m, giving a y^+ of about 0.05. Views of the mesh are displayed in Figure 4.6.

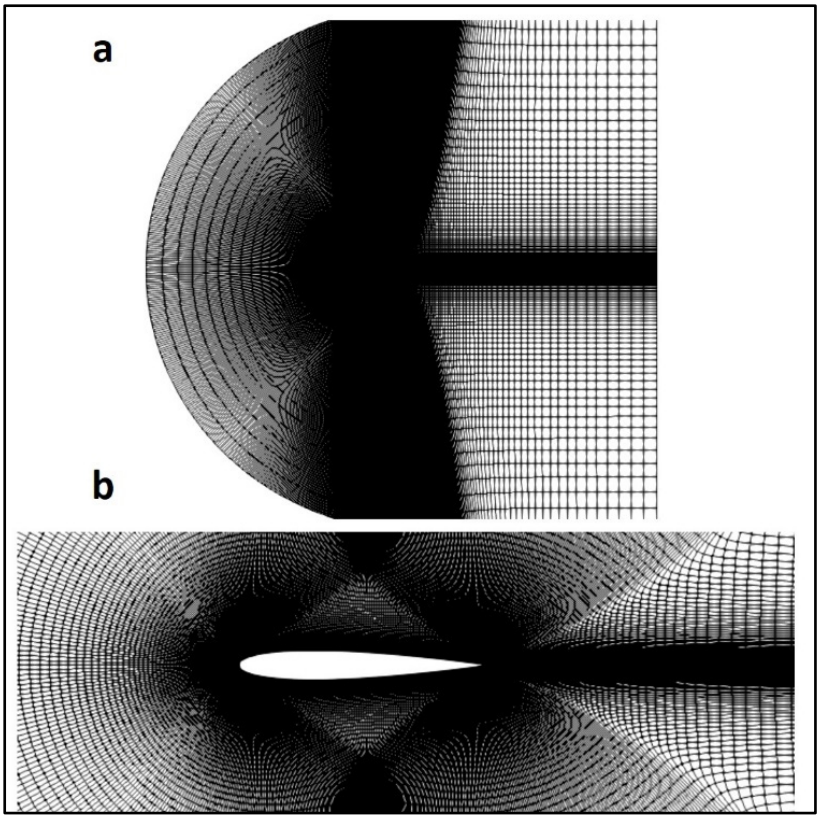

Figure 4.6 View of the grid: (a) Entire domain; (b) Airfoil zone

The surface roughness changes for the database generation and the calibration application, to monitor the ice shape dependence on the roughness pattern. The latter is applied uniformly on the entire airfoil surface.

The collection efficiencies used throughout this work are the ones from Özgen and Canibek (2008), for a freestream velocity of 50 m/s or 100 m/s and an MVD of 20 μm. The collection efficiency β is plotted against the curvilinear abscissa s normalized by the chord length c in Figure 4.7.

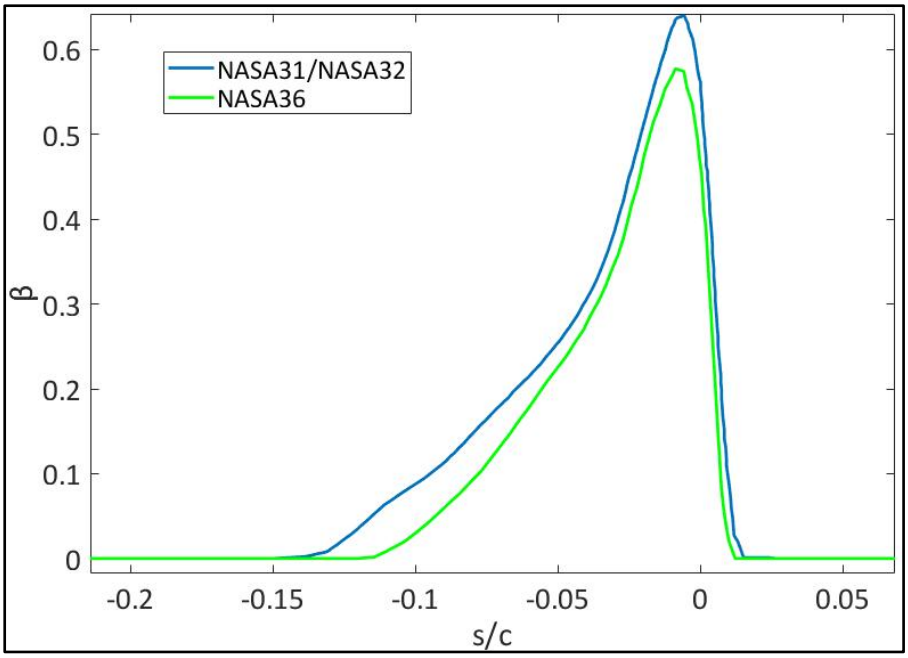

Figure 4.7 Collection efficiencies used in the study

4.6.1.2 Grid Convergence Study

The grid convergence study follows the methodology suggested by Celik et al. (2008). This method requires coarse, medium, and fine meshes. They respectively correspond to the 225-65, 449-129, and 897-257 NACA0012 mesh configurations in the NASA Turbulence Modeling Resource (NASA, 2013). The roughness parameters used are set to $k = 4.32$ mm and $ks = 0.864$ mm ($ks/k = 0.2$) for the CFD simulations. These values are taken in the range of roughness patterns previously described in Table 4.2. Two quantities are monitored: the accretion maximum thickness and the accretion cross-sectional area. These quantities, monitored by Son et al. (2012), are highlighted in Figure 4.8 for a generic accretion.

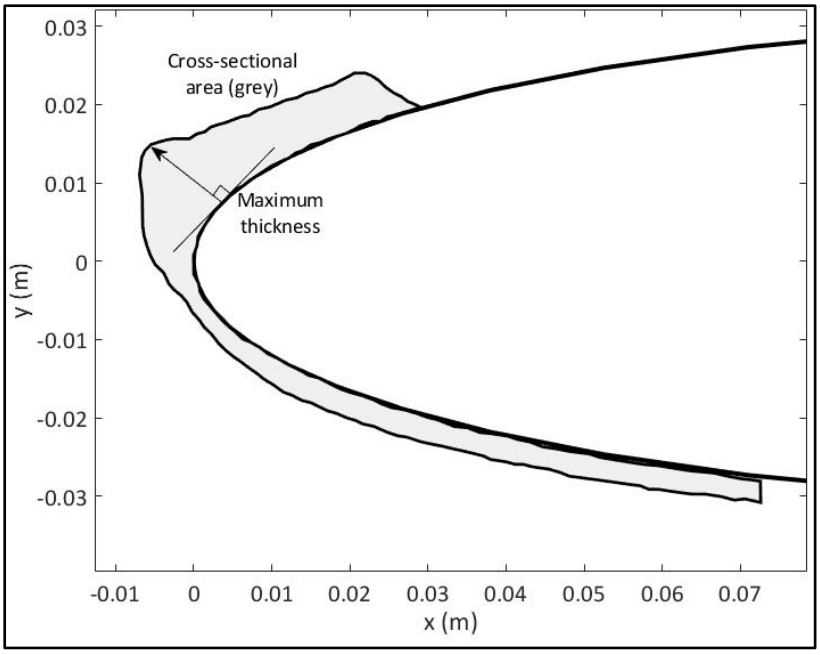

Figure 4.8 Ice accretion quantities of interest

For the three meshes, Figure 4.9 displays the ice accretions obtained. The thickness or the cross-sectional area variations with the mesh refinement enable the computation of the grid convergence index (GCI) as well as an order of convergence. The values for the quantities of interest are shown in Table 4.5.

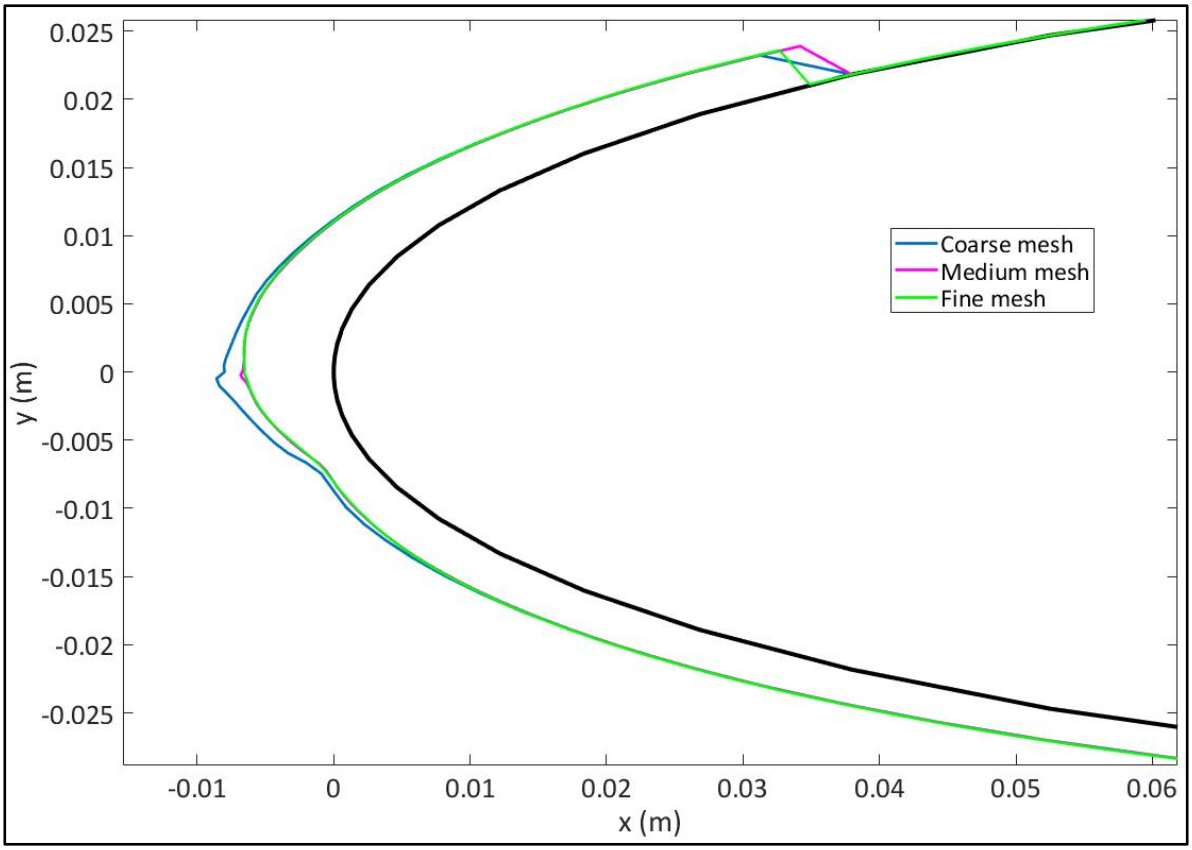

Figure 4.9 Accretions obtained on each mesh

The characteristic length l of the mesh is the square root of the surface of the wing (0.58 m² in this case) divided by the number of cells. The coarse mesh has 128 cells on the airfoil, while the medium and the fine meshes have 256 and 512 cells, respectively. The characteristic lengths for each mesh are summarized in Table 4.5, along with the outputs of interest values.

Table 4.5 Characteristic length and quantities of interest for each mesh

	l	Max. thickness	Cross-sectional area
Coarse mesh (3)	0.067 m	8.60 mm	7.48×10^{-4} m²
Medium mesh (2)	0.048 m	6.83 mm	7.31×10^{-4} m²
Fine mesh (1)	0.034 m	6.72 mm	7.17×10^{-4} m²

The order of convergence p and the GCI for the medium and fine meshes can be computed using equation (4.56) and equation (4.58). In these equations, QOI_i represents the quantity of interest value (Table 4.5) on the mesh i (1, 2, or 3; 1 being the finest). The ratios $r_{21}=l_2/l_1$ and $r_{32}=l_3/l_2$ are the refinement ratios between two consecutive meshes. Equation (4.57) computes the relative error between the two meshes i and j. The notations $\Delta_{21}= QOI_2 - QOI_1$ and $\Delta_{32}= QOI_3 - QOI_2$ are used to lighten the equations.

$$p = \frac{\left| ln\left(\left|\frac{\Delta_{32}}{\Delta_{21}}\right|\right) + ln\left(\frac{r_{21}^{p} - 1 \times sign\left(\frac{\Delta_{32}}{\Delta_{21}}\right)}{r_{32}^{p} - 1 \times sign\left(\frac{\Delta_{32}}{\Delta_{21}}\right)}\right)\right|}{ln\,(r_{21})} \tag{4.56}$$

$$e_a^{ij} = \left|\frac{QOI_j - QOI_i}{QOI_j}\right| \tag{4.57}$$

$$GCI^{ij} = \frac{1.25 e_a^{ij}}{(r^p - 1)} \tag{4.58}$$

Equation (4.56) is solved iteratively, using a Brent-Dekker method (Brent, 2002). GCI^{21} is the GCI value of the fine mesh, and GCI^{32} is that of the medium mesh. Table 4.6 gathers the convergence order and GCIs obtained for each quantity of interest.

Table 4.6 Convergence order and GCIs values

	Max. thickness	Cross-sectional area
p	8.2	1.80
GCI^{21}	0.0071%	0.9%
GCI^{32}	2.0%	3.4%

The GCIs are low, especially on the fine mesh (GCI^{21}), where they are below 1%. The GCIs measure the result uncertainties due to the mesh. For comparison, GCI values between 2% and 4% are commonly accepted in the literature (Baker, Kelly, & O'Sullivan, 2020). The fine mesh is retained for the rest of the study.

4.6.1.3 Verification of the SU2-ICE Solver (NASA31 case)

The verification is carried out on the NASA31 test case. From Figure 4.1, SU2-ICE requires the wall heat transfer coefficient and the wall shear stress from SU2-CFD. To reduce the uncertainty due to the heat transfer coefficient in the verification process, a manufactured heat transfer coefficient (Lavoie et al., 2018) is directly provided to SU2-ICE. This coefficient is plotted in Figure 4.10. On the other hand, the wall shear stress, used for the runback film, is computed with SU2-CFD, and is plotted in Figure 4.10 as well. In the present case, the assumption is that the skin friction coefficient value has a limited impact on the accretion metrics. The film thickness is small enough to neglect the temperature variations in the wall-normal direction. In addition, the model assumes that the film temperature equals the wall temperature. In the present 2.5D application, the direction of the wall shear stress (chord-wise) is correctly predicted by SU2-CFD, meaning a trustworthy runback direction. The literature skin friction coefficient is not provided, leaving uncertainty on its magnitude and the film thickness. The x-axis in Figure 4.10 is the curvilinear abscissa normalized by the airfoil chord. The collection efficiency used was plotted in Figure 4.7. The 2.5D ice shape obtained at the end of the 480 s exposure time is shown in Figure 4.11. The apparent discontinuous color changes on the accretion are due to the uneven ice shape near the leading edge. These irregularities lead to abrupt thickness changes, visible on the slice in Figure 4.12.

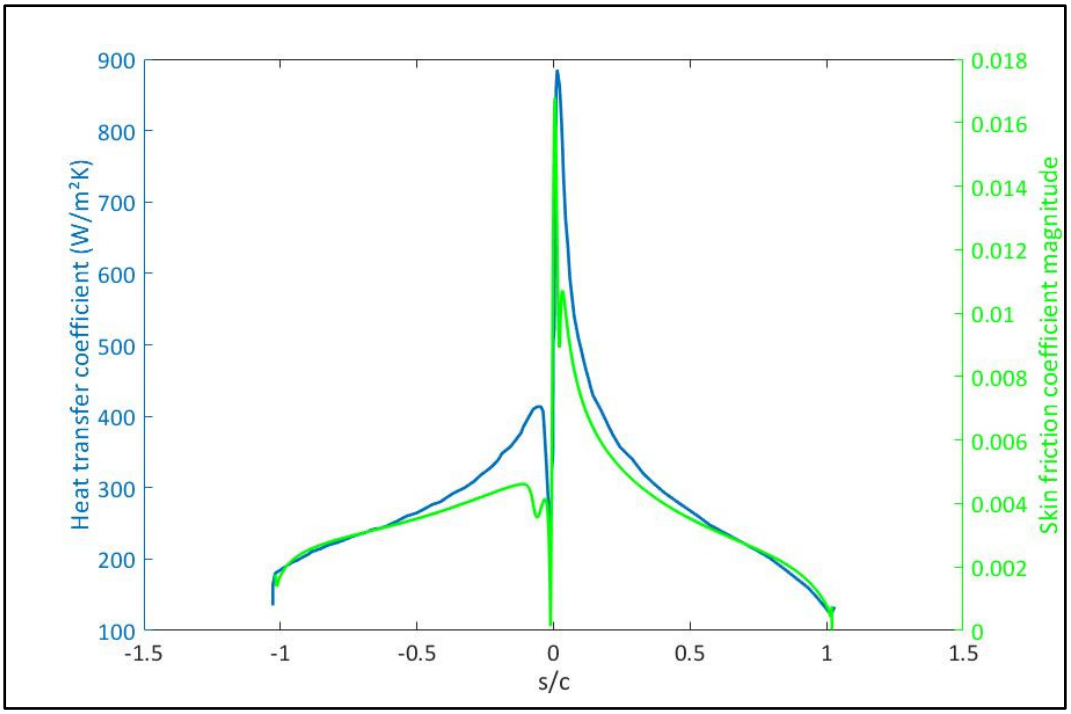

Figure 4.10 Manufactured heat transfer coefficient and SU2-computed skin friction coefficient used

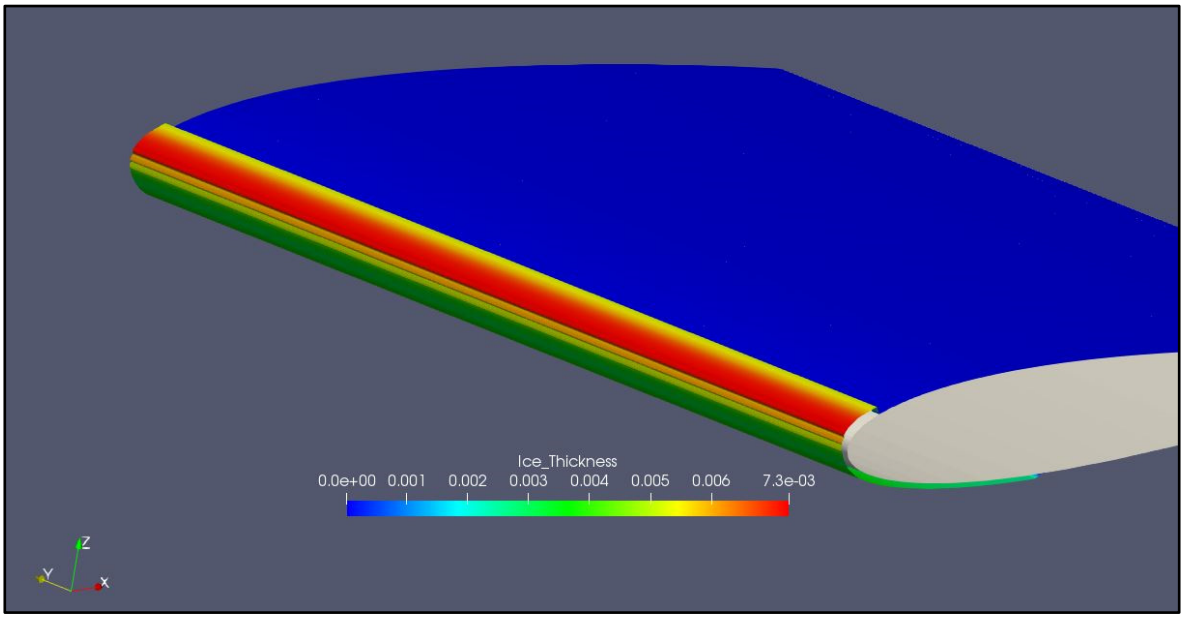

Figure 4.11 3D view of the accretion, colored by ice thickness (m)

Figure 4.12 compares the SU2-ICE cross-section with the experimental and numerical results obtained by NASA (Wright, Gent, et al., 1997) and Lavoie et al. (2018) for this test case. The NASA numerical prediction is obtained using a multilayer approach, while the current SU2-ICE and the references from Lavoie et al. (2018) perform single-layer simulations.

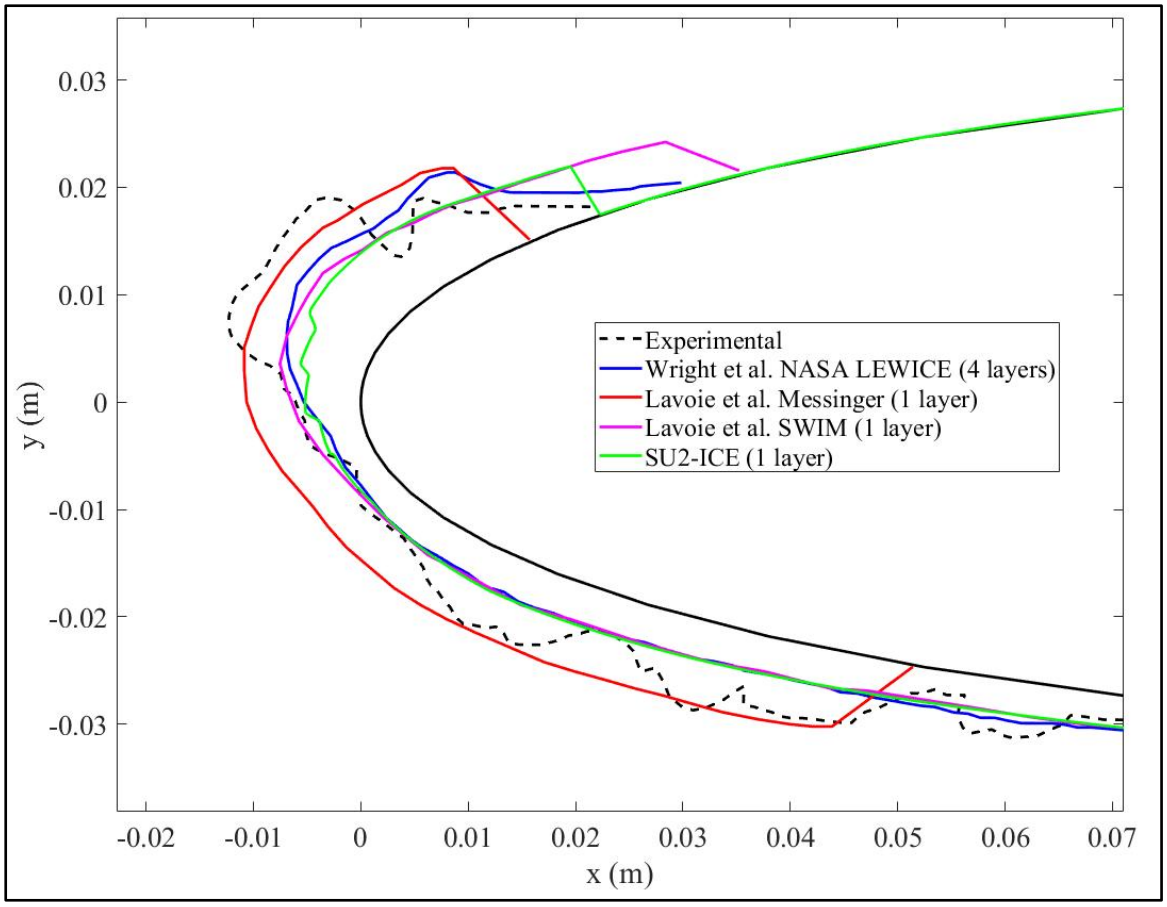

Figure 4.12 2D comparison of ice shapes for the NASA31 test case

Figure 4.12 shows an acceptable prediction from SU2-ICE versus the NASA and SWIM predictions. The ice thickness is the same on the pressure side of the wing. Additionally, the stagnation point ice thickness presents less than 1 mm of discrepancy with the literature, which represents less than 0.2% of the chord length. The discrepancies with the literature are mainly due to model differences. A discrepancy appears at the edge of the accretion on the suction

side. The verification showed that the model predicts the same ice thickness order of magnitude as the literature single- and multi-layer documented shapes.

4.6.2 PCE Metamodeling and Bayesian Inversion Calibration for the NASA31 Test Case

4.6.2.1 Database Sampling

Each simulation has a different roughness pattern and the heat flux computed at the wall change. Consequently, the ice shapes vary, feeding the database. Figure 4.13 displays the 120 accretions obtained in the database, highlighting the variations in shape due to the roughness input uncertainties. Each black line corresponds to one accretion.

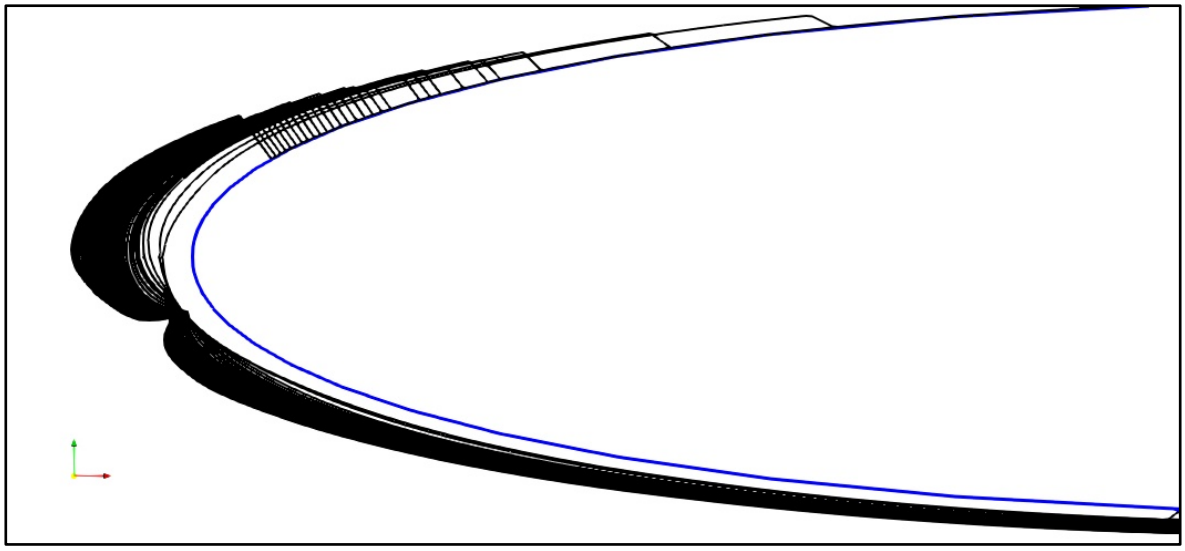

Figure 4.13 View of the different ice shapes making up the database

The distributions of the output of interest for the metamodel M_1 (maximum thickness and cross-sectional area) are plotted in histograms in Figure 4.14. The outputs of interest have a non-uniform distribution, even if the roughness input parameters are uniformly distributed. The maximum thickness is concentrated at 11 mm and the cross-sectional area at 7.2×10^{-4} m². Non-uniform distributions for the output of interest of the metamodel M_2 are also observed.

Figure 4.15 shows the distribution of the local ice thickness at two locations, A and B, in the first 0.25% of the chord length. These locations near the leading edge are chosen since they usually exhibit large ice thickness variations. Points A and B are chosen as illustrative samples among the multiple outputs of the metamodel M_2.

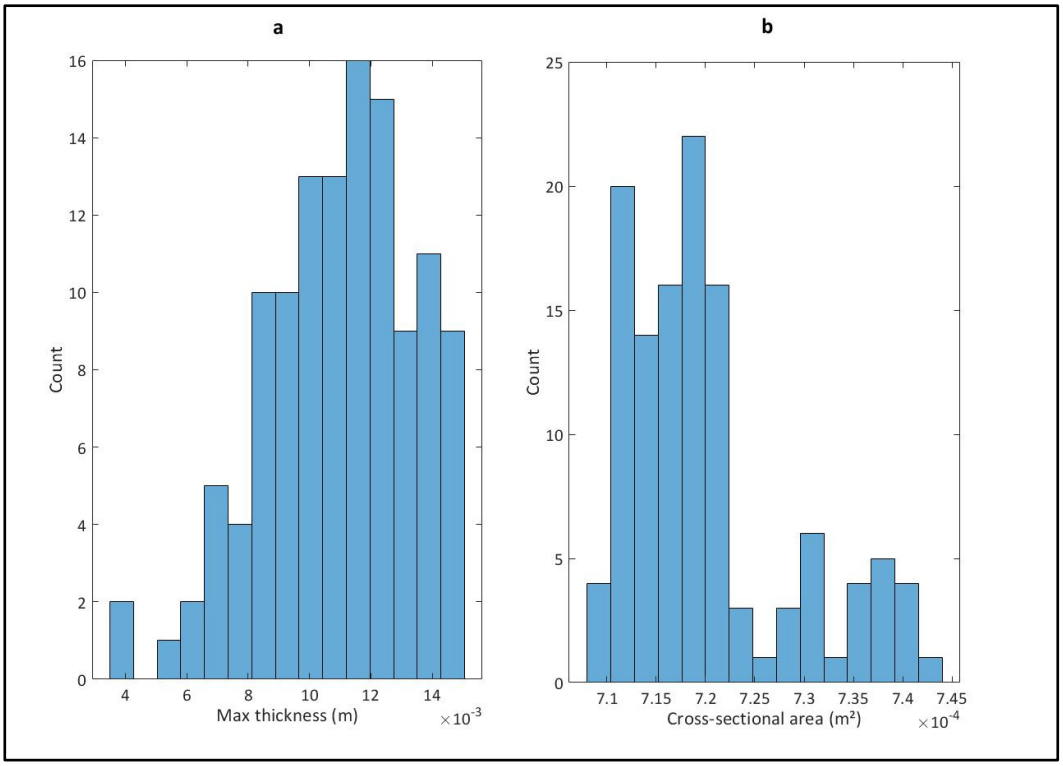

Figure 4.14 (a) Maximum thickness and
(b) cross-sectional area database distributions

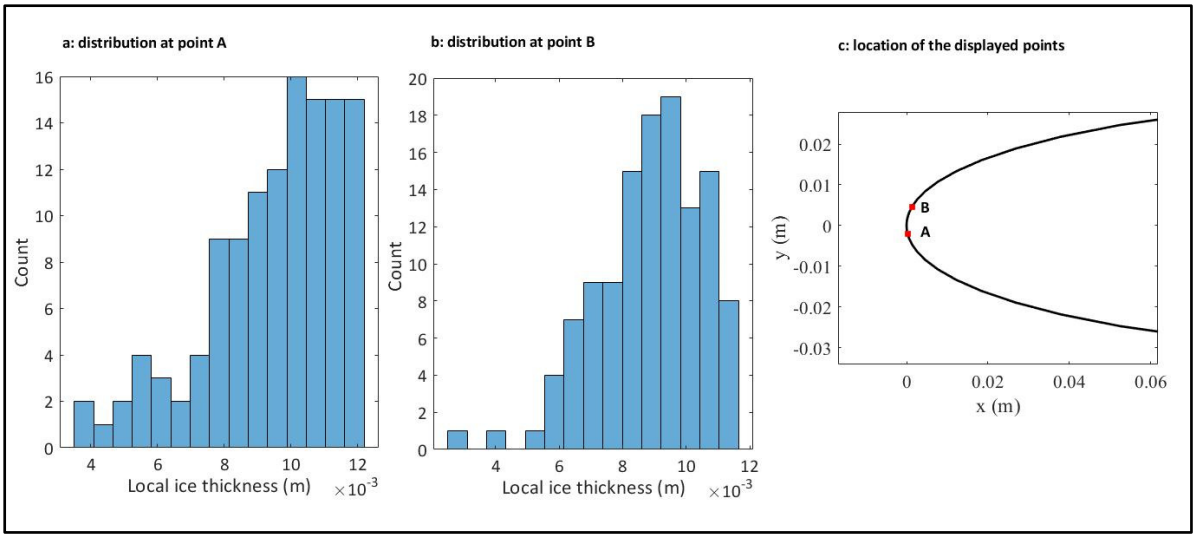

Figure 4.15 Ice thickness distribution at two locations in the leading edge region

4.6.2.2 PCE Metamodels

Two metamodels are generated, as listed in Table 4.3. A PCE metamodel is a polynomial (equation (4.50)) characterized by its degree and the number of terms in the sum. The verification of the PCE degree enables the verification of the DOE sample size (equation (4.49)). These characteristics are collated in Table 4.7 for the metamodel M1.

Table 4.7 Degree and composition of the metamodel M_1

Output of interest	PCE degree	Number of terms
Maximum ice thickness (m)	12	91
Cross-sectional area (m²)	10	66

The PCEs composing M_1 have a maximum degree of 5 and 12. The DOE sample size, estimated with a PCE degree of 14 (equation (4.49)), was enough. The corresponding number of terms in the PCE expression (equation (4.51)) is 21 and 91, respectively. The precision of the

metamodels is assessed through the calculation of the R^2 regression coefficient (equation (4.53)) and the *LOO* error (equation (4.54)). The R^2 and *LOO* values for each output of M_1 are displayed in Table 4.8.

Table 4.8 R^2 regression coefficients and *LOO* errors for each output of M_1

Output of interest	R^2	*LOO*
Maximum ice thickness (m)	0.99998	0.00019
Cross-sectional area (m²)	0.99951	0.0013

For both outputs, the R^2 regression coefficient is close to 1. This means that there is a good correlation between the CFD response and the PCE response on the same sample set (of size 120). These values of R^2 are higher than the usual tolerance accepted: similar studies in the literature have R^2 coefficients as low as 0.946 (Raj et al., 2020). For the *LOO* error, it varies between 0.019% and 0.13%, which is acceptable. For instance, in CFD applications, *LOO* error values between 0.5% and 3% are commonly accepted (Biswal, Sarkar, & Mahanta, 2020). Figure 4.16 plots the PCE response Y_{PCE} versus the CFD response Y_{CFD}. The closer the points are aligned on the identity line, the better the accuracy of the metamodel. In Figure 4.16, the good alignment on the identity line confirms the metamodels' accuracy on the sample set measured with the high R^2 coefficient values and the low *LOO* errors in Table 4.8.

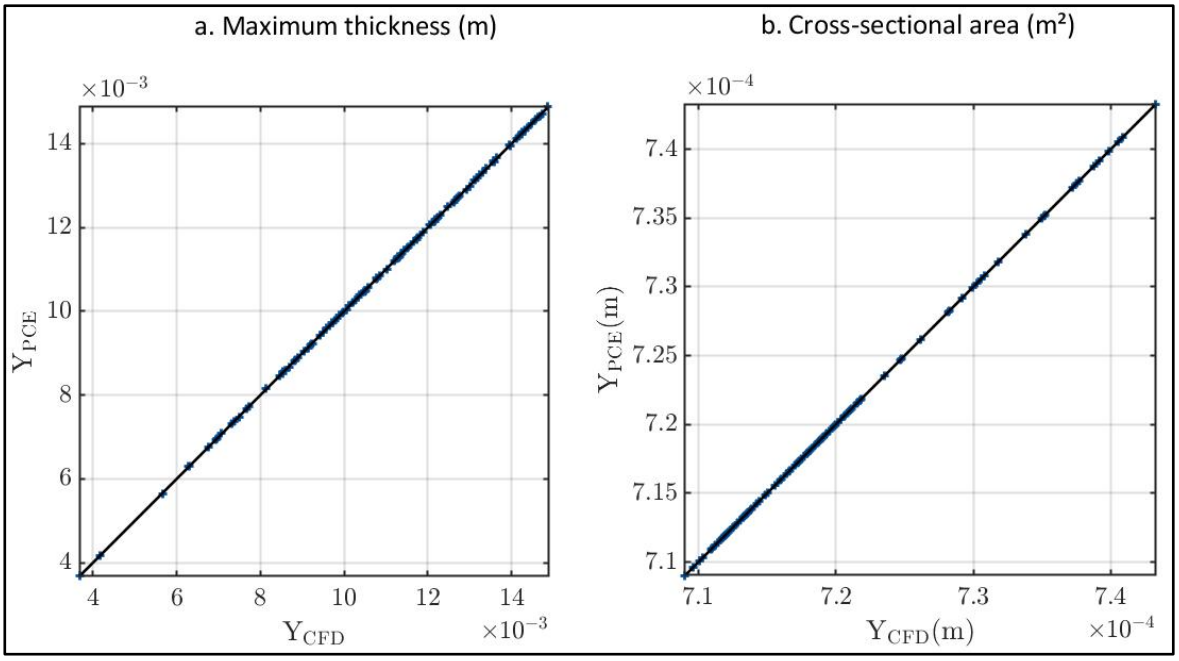

Figure 4.16 CFD/PCE regression for: (a) maximum thickness and (b) cross-sectional area

The metamodels created evaluate outputs for any combination of roughness parameters in the ranges specified earlier in Table 4.2. To visualize the PCE behaviour on a large sample, 10,000 doublets (*k; ks/k*) are generated by the Latin hypercube sampling. The outputs of interest are then evaluated on this large sample. Figure 4.17 displays the distributions of the outputs of interest.

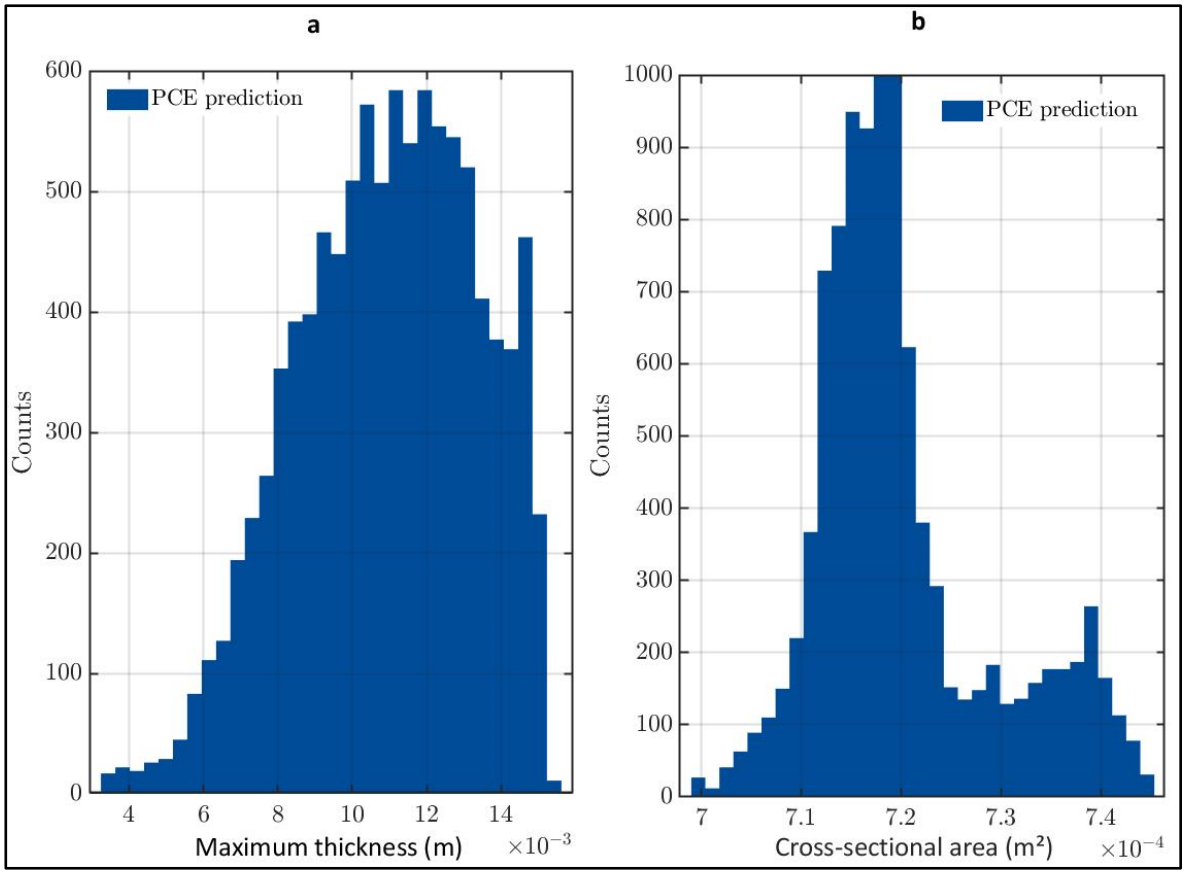

Figure 4.17 (a) Maximum thickness and (b) cross-sectional area distributions on a large sample

As in the CFD sample (Figure 4.14), the maximum thickness once again concentrates around 11 mm. The difference with Figure 4.14 is the absence of the peak around 7.1×10^{-4} m² in the case of a large sample. This increased value of the cross-sectional area indicates that a larger CFD sample would have statistically predicted bigger accretions.

The metamodel M_2 predicts the local ice thickness at N_p selected probe locations. The probe's locations are selected to cover the extent of the accretion, with a higher probe density in the first 1% of the airfoil chord length. The heat transfer coefficient and the skin friction coefficient (Figure 4.10) exhibit large gradients in that region. Large variations in ice accretion shape are expected in that particular region, requiring more probe points. The probe points are positioned on grid nodes, where the ice thickness is directly available in the CFD database. This approach

eliminates the risk of introducing uncertainties when interpolating the ice thickness outside the grid nodes. The mesh is denser in the leading edge region, enabling more probes in that zone. Different numbers of probes were tested: 5, 10, and 20. The choice of the number of probes (10) will be demonstrated in the next subsection by displaying the ice shapes after calibration. The 10 retained monitoring locations are shown in Figure 4.18.

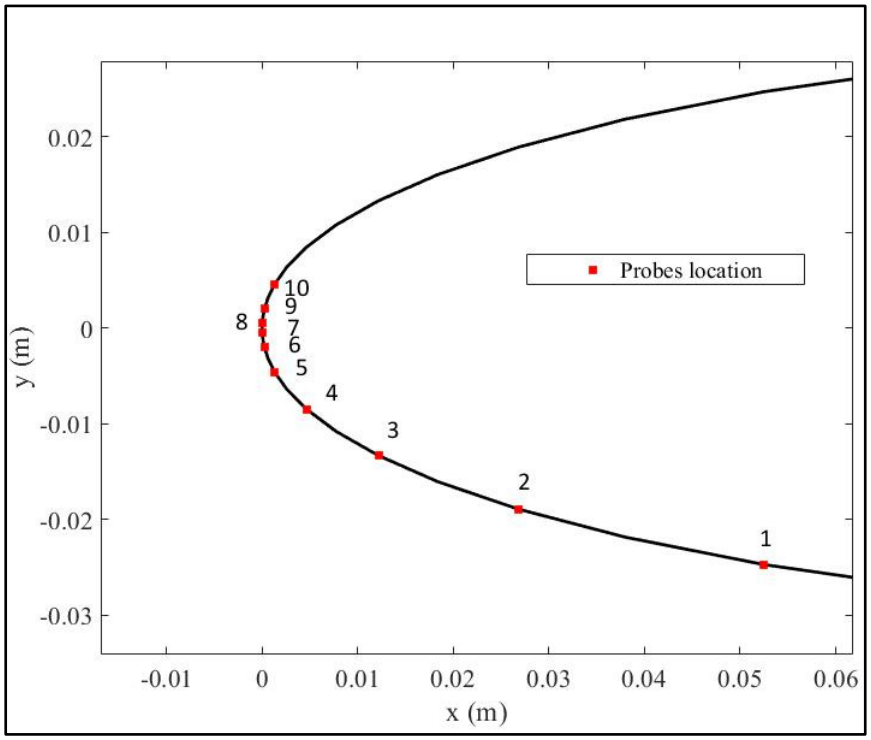

Figure 4.18 Location of the 10 probe points to monitor the local ice thickness

Since there are 10 outputs, the metamodel M_2 is composed of 10 independent PCE expressions. Their composition and maximal degree are summarized in Table 4.9. Similar to the metamodel M_1, each of the metamodel M_2 components has a regression coefficient and a LOO error to assess its accuracy versus the CFD response. These R^2 coefficients and *LOO* errors are also displayed in Table 4.9. The output number refers to the probe number in Figure 4.18.

Table 4.9 Characteristics of each component of the metamodel M_2

Output number	PCE degree	Number of terms	R^2	LOO
1	5	21	0.99864	2.8×10^{-3}
2	13	105	0.99994	3.3×10^{-4}
3	9	55	0.99993	4.8×10^{-4}
4	7	36	0.99971	8.4×10^{-4}
5	14	120	0.99999	5.6×10^{-5}
6	10	66	0.99983	7.2×10^{-4}
7	10	66	0.99996	4×10^{-4}
8	12	91	0.99993	3.2×10^{-4}
9	14	120	0.99999	9.5×10^{-5}
10	6	28	0.99982	4×10^{-4}

The maximal PCE degree varies between 5 and 14, illustrating the relevance of the DOE sample size (equation (4.49)). The R^2 coefficient values are in the same order of magnitude as the ones computed for the metamodels M_1. All the R^2 coefficient values are above 99.8%, pointing to a good accuracy for each of the 10 components. The LOO cross-validation error is low and between 0.005% and 0.28%, confirming the acceptable fit between the PCE and CFD predictions.

4.6.2.3 Bayesian Inversion Calibration

The last step of the methodology is calibration. Calibration is aimed at estimating the roughness parameters to input in the CFD model by observing an experimental accretion. These experimental shapes are derived from work carried out by NASA (Wright, Gent, et al., 1997). The numerical accretions from Lavoie et al. (2018), which use extended Messinger and SWIM

models, are used and displayed as a visual reference of what is accepted in the literature. The two numerical references from the literature use a single-layer approach, similar to the SU2-ICE implementation. The literature results are displayed together in Figure 4.19.

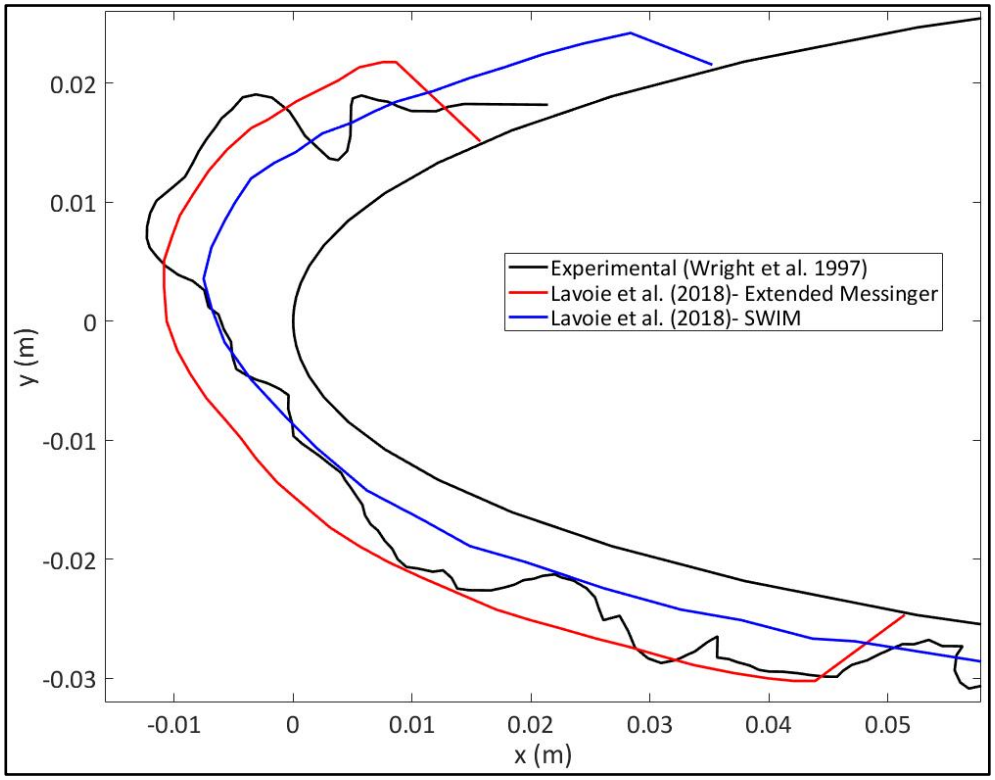

Figure 4.19 Reference accretions for the NASA31 test case

The metamodel M_1 is calibrated first. This calibration is denoted calibration #1. The graphical measurements taken in Figure 4.19 for the experimental accretion give the target value for the calibration of the metamodel M_1: the maximum thickness is 0.0137 m and the cross-sectional area is 7.36×10^{-4} m².

The calibration will be carried out by providing the experimental measurements to the Bayesian inversion solver. For M_1, the observation provided to the Bayesian solver is the combination of maximum thickness/cross-sectional area. After the Bayesian inversion calculation, the posterior distributions of the roughness parameters are displayed. These distributions are no longer uniform, unlike the prior distributions before calibration (seen in

Table 4.2). Figure 4.20 below shows the posterior distribution for both k and k_s/k roughness parameters.

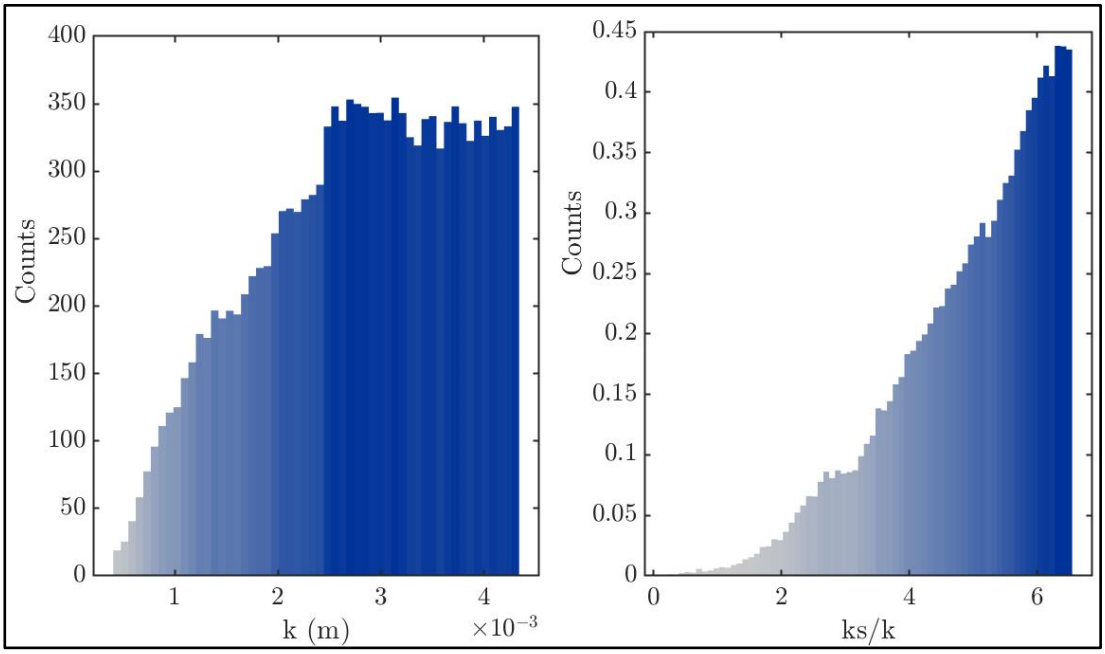

Figure 4.20 Roughness parameter posterior distributions

The calibrated roughness parameters are the maximum a posteriori (MAP) corresponding to the highest peak in the posterior distributions. The calibrated values for calibration #1 are:

- Roughness height k = 0.0040 m;
- Ratio k_s/k = 6.4;
- Corresponding equivalent roughness k_s = 0.0255 m.

Note that the ratio value of 6.4 is close to the upper limit of 6.5 determined in Table 4.2. Before assessing the quality of the calibration in a full CFD/accretion simulation, the PCE prediction with those calibrated values is estimated. The PCE values predicted using the metamodel M_1 are:

- A maximum thickness of 0.0148 m (+8.0% compared to the experimental measurement);
- A cross-sectional area of 7.37×10^{-4} m² (equal to the experimental measurement).

The last step is to run the CFD/accretion simulation using the calibrated roughness parameters. The values of the output of interest after the CFD simulation are:

- A maximum thickness of 0.0145 m (+5.8% compared to the experimental measurement);
- A cross-sectional area of 7.37×10^{-4} m² (equal to the experimental measurement).

The PCE metamodel M_1 could predict the CFD ice maximum thickness with a 2% discrepancy (0.0148 m instead of 0.0145 m) and the same cross-sectional area. The calibrated CFD prediction exhibits the same cross-sectional area as the experimental accretion. The maximum thickness is predicted with less than 6% of error with the experimental shape. The visual aspect of the ice shape obtained is illustrated in Figure 4.21.

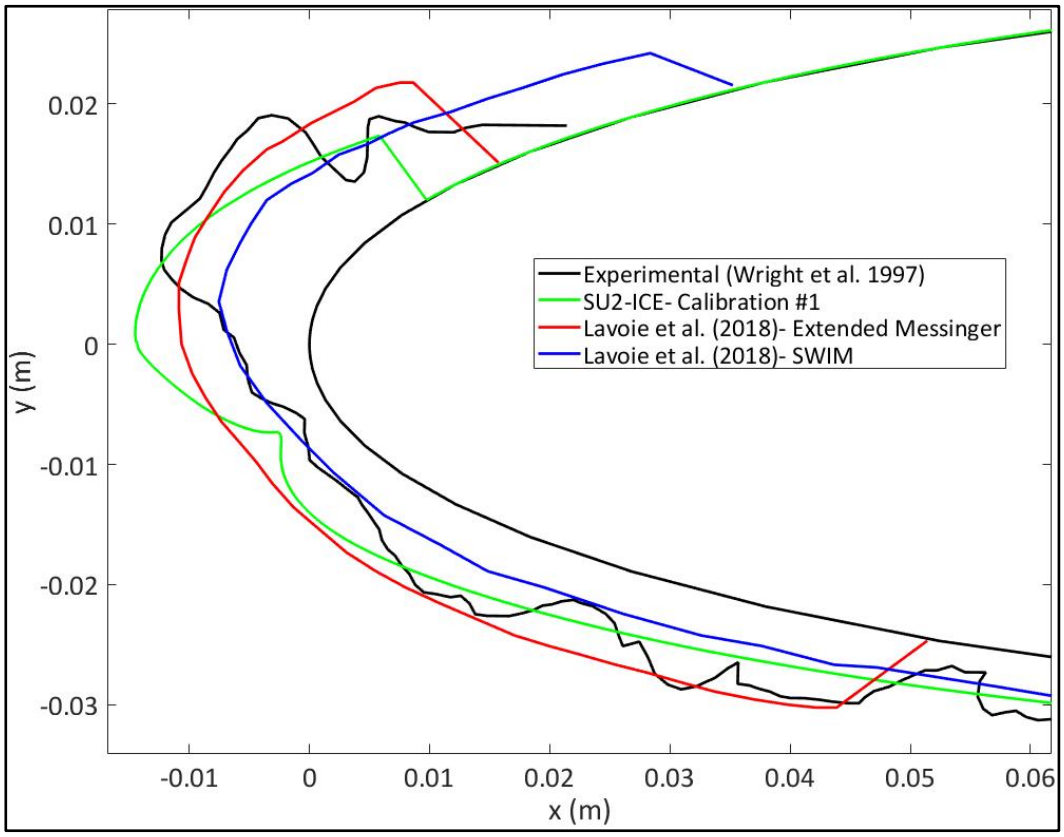

Figure 4.21 Ice shapes obtained by CFD after calibration #1

The SU2-ICE accretion exhibits a thickness discrepancy of less than 1% of the chord length with the experimental accretion on the pressure side. On the suction side, the location of the horn (i.e., where the maximum thickness occurs) is shifted and geometrically lower as compared to the literature. The 5.8% discrepancies figure with the experimental maximum thickness represents 0.8 mm of difference. This is about 0.15% of the chord length. These discrepancies are acceptable since other models used in the literature can predict shapes with more than 60% of thickness discrepancies with the experiment (Laurendeau et al., 2022). Despite these satisfactory maximum thickness predictions (less than 6% of relative error) and cross-sectional area predictions (the same as the literature), the geometry presents some local geometrical discrepancies. Nevertheless, the SU2-ICE thickness prediction lies mainly between the two shapes of Lavoie et al. (2018), except at the leading edge.

The second calibration, denoted calibration #2, is performed on the metamodel M_2. This metamodel is intended to offer a better local prediction. The numerous probe locations allow a better geometrical resolution compared to the macroscopic quantities monitored by M_1. The first task is to select the number of probe points. These are selected among the mesh nodes, where the ice thickness is available. 5, 10, and 20 monitoring points are tested to study the influence of the number of probes on the calibrated roughness parameters. Table 4.10 collates the calibrated roughness parameters for each test.

Table 4.10 Calibrated roughness parameters for the metamodel M_2, with different numbers of probes

Reference shape	Calibrated roughness height k			Calibrated ratio k_s/k		
	5 probes	**10 probes**	**20 probes**	**5 probes**	**10 probes**	**20 probes**
Experimental	0.0029 m	0.0025 m	0.0020 m	0.29	1.3	0.38

The values in Table 4.10 are different from the calibrated parameters obtained for the metamodel M_1. The ratio k_s/k increases by 348% between 5 and 10 probes and then decreases by 70% between 10 and 20 probes. The Bayesian inversion in UQLab gives equal weights for

all the outputs. The Bayesian inversion estimates the roughness parameters that best suit all the thicknesses monitored. The 20-probe configuration adds monitoring points in the thin ice zone of the pressure side, reducing the calibrated roughness parameters. The same observation is made with 5 probes: this time, there are not enough points in the thick region, and once again, the roughness parameter dragged lower. This analysis is confirmed by the display of the accretions obtained (Figure 4.22).

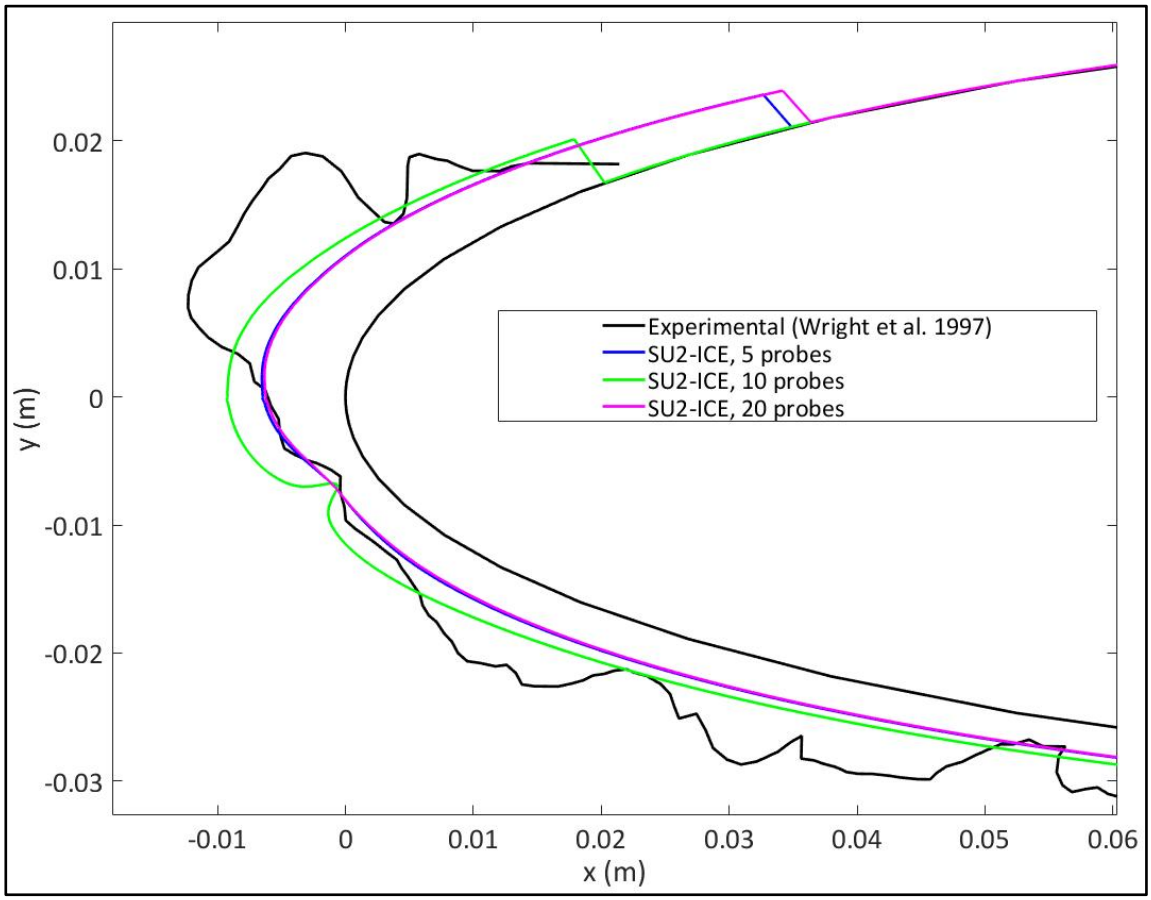

Figure 4.22 Accretions obtained with different probe numbers

The largest accretion is obtained with 10 probes, while 5 and 20 probes produce smaller accretions, far from the experimental dimensions. Therefore, to avoid excessively small and thin accretions, 10 probes are retained. The retained roughness parameters for calibration #2 are:

- Roughness height $k = 0.0025$ m;
- Ratio $k_s/k = 1.3$;
- Corresponding equivalent roughness $k_s = 0.0033$ m.

The retained SU2-ICE accretion is closer to the experimental accretion in the leading edge region ($y = 0$) than is the case in calibration #1. The ice shape is less bulky and thinner in this area. Nevertheless, the accretion still lacks thickness on the suction side, and the maximum thickness location has discrepancies with the reference results. The experimental, PCE-predicted, and CFD-predicted (using the previously calibrated roughness) ice thickness at the probe locations are collated in Table 4.11.

Table 4.11 Ice thicknesses at the probe locations in millimetres

Probe number	1	2	3	4	5	6	7	8	9	10
Experimental	2.5	4.5	7.5	4.0	2.5	5.5	6.0	6.0	7.5	14
PCE	2.9	3.6	4.5	5.4	4.6	8.4	9.1	9.2	9.0	7.7
CFD	2.9	3.6	4.5	5.4	4.6	8.3	9.1	9.2	9.0	7.7

The CFD simulations and PCE predictions were expected to produce similar values since the PCE and CFD have a good fit (high R^2 and low *LOO* error). A comparison between the PCE and CFD outputs shows once again that the PCE metamodel accurately predicts the CFD outputs. There are discrepancies between the PCE and the CFD only at probe 6, for an amount of 0.1 mm. This discrepancy represents a relative error of roughly 1.2%. In addition, 0.1 mm of error corresponds to 0.02% of the airfoil chord length.

Both calibrations #1 and #2 exhibit behaviours requiring improvement. The thickness and the cross-sectional area predictions are satisfactory, both in the same order of magnitude as the experimental shape.

4.6.3 Extension to Other Test Cases

The methodology extensively depicted for the NASA31 test case is now applied to the NASA32 and NASA36 glaze ice cases. For these two test cases, the reference ice shapes from the literature are generated by NASA (Wright, Gent, et al., 1997). For the test cases, NASA32 and NASA36, only some freestream quantities have changed compared to the NASA31 case, as stated previously in Table 4.4. These test cases are run using the same CFD set-up and mesh depicted in Section 4.6.1.1.

4.6.3.1 Calibration for the NASA32 Test Case

The NASA32 case is similar to the NASA31 case, with the same freestream velocity and collection efficiency. Therefore, the metamodels M_1 and M_2 are recalibrated, using the experimental observations from the literature: the maximum thickness is 0.0094 m and the cross-sectional area is 6.13×10^{-4} m². For the metamodel M_2, the ice thicknesses at the locations of the probes are given in Table 4.13, together with the PCE and CFD results. The calibrated roughness parameters for M_1 are (calibration #3):

- Roughness height k = 0.0038 m;
- Ratio k_s/k = 6.2;
- Corresponding equivalent roughness k_s = 0.0236 m.

The calibration of the metamodel M_2 gives (calibration #4):

- Roughness height k = 0.0024 m;
- Ratio k_s/k = 1.3;
- Corresponding equivalent roughness k_s = 0.0031 m.

The ice shapes obtained with SU2-ICE using calibration #3 and calibration #4 roughness parameters are shown in Figure 4.23. They compare satisfactorily with the experimental accretion, with an error of less than 1% of the chord length for the thickness prediction. Again, a comparison with the experimental reference is better on the pressure side of the airfoil. The

characteristics obtained for the SU2-ICE NASA32 accretions are listed in Table 4.12. The percentages of discrepancy with the literature are in brackets.

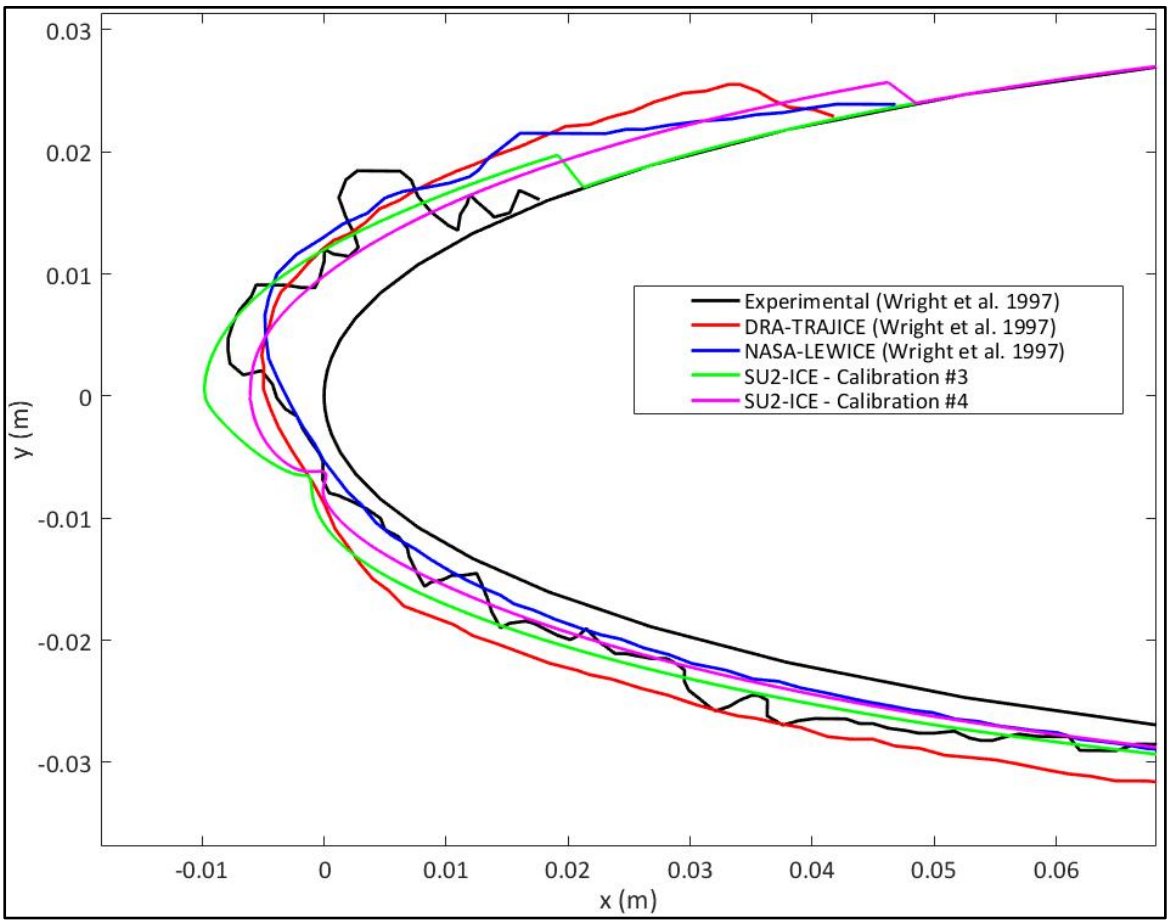

Figure 4.23 Ice shapes for the NASA32 test case

Table 4.12 CFD predictions for the NASA32 case

Roughness used	Maximum thickness	Cross-sectional area
calibration #3	0.0096 m (+2.1%)	7.1×10^{-4} m² (+15.8%)
calibration #4	0.0062 m (−34.0%)	7.1×10^{-4} m² (+15.8%)

Table 4.13 Ice thicknesses at the probe locations in millimeters (NASA32), calibration #4

Probe number	1	2	3	4	5	6	7	8	9	10
Experimental	3.0	2.7	1.7	1.7	1.7	2.0	3.6	4.0	8.0	8.0
PCE	2.9	3.6	4.4	5.3	4.6	8.3	9.0	9.1	9.0	7.6
CFD	1.9	2.4	3.0	3.6	3.1	5.5	6.0	6.1	6.0	5.1

SU2-ICE predicts a maximum ice thickness with 2.1% of discrepancies with the experimental one. Both calibrations overestimate the cross-sectional area (+15.8%). The observations are inverted for the calibration #4 roughness: the maximum thickness is underestimated by 34%. For calibration #3 and calibration #4, the maximum thickness discrepancies with the experimental shape represent 0.04% and 0.6% of the chord length, respectively.

4.6.3.2 Calibration for the NASA36 Test Case

The NASA36 test case presents large atmospheric variations as compared to the NASA31/32 cases (see Table 4.4). Therefore, all the steps previously taken for the NASA31 case are applied to the NASA36 case. The creation of a 120-accretion database using the Latin hypercube sampling, the PCE metamodels M_1 and M_2 creation, and the Bayesian inversion calibration are carried out. To avoid redundancy, only the main results of the methodology will be depicted

for the PCE characteristics. Once again, the PCE metamodels present a good accuracy, with all the R^2 regression coefficients being above 99.7% and *LOO* errors under 1×10^{-3}. For the Bayesian inversion, the experimental observations for the NASA36 accretion are provided. For the metamodel M_1, these observations show a maximum thickness of 0.0214 m and a cross-sectional area of 9×10^{-4} m². For the metamodel M_2, the ice thicknesses on the 10 probe points from the literature are shown in Table 4.15, along with the PCE and CFD results. The calibrated roughness parameters for M_1 are (calibration #5):

- Roughness height k = 0.0025 m;
- Ratio k_s/k = 3.6;
- Corresponding equivalent roughness k_s = 0.0090 m.

The calibration of the metamodel M_2 gives (calibration #6):

- Roughness height k = 0.0017 m;
- Ratio k_s/k = 4.9;
- Corresponding equivalent roughness k_s = 0.0083 m.

The calibrated roughness parameters are different from the NASA31 and NASA32 cases. As expected, the methodology produces different values for different cases. The ice shapes obtained with SU2-ICE using calibration #5 and calibration #6 roughness parameters are shown in Figure 4.24.

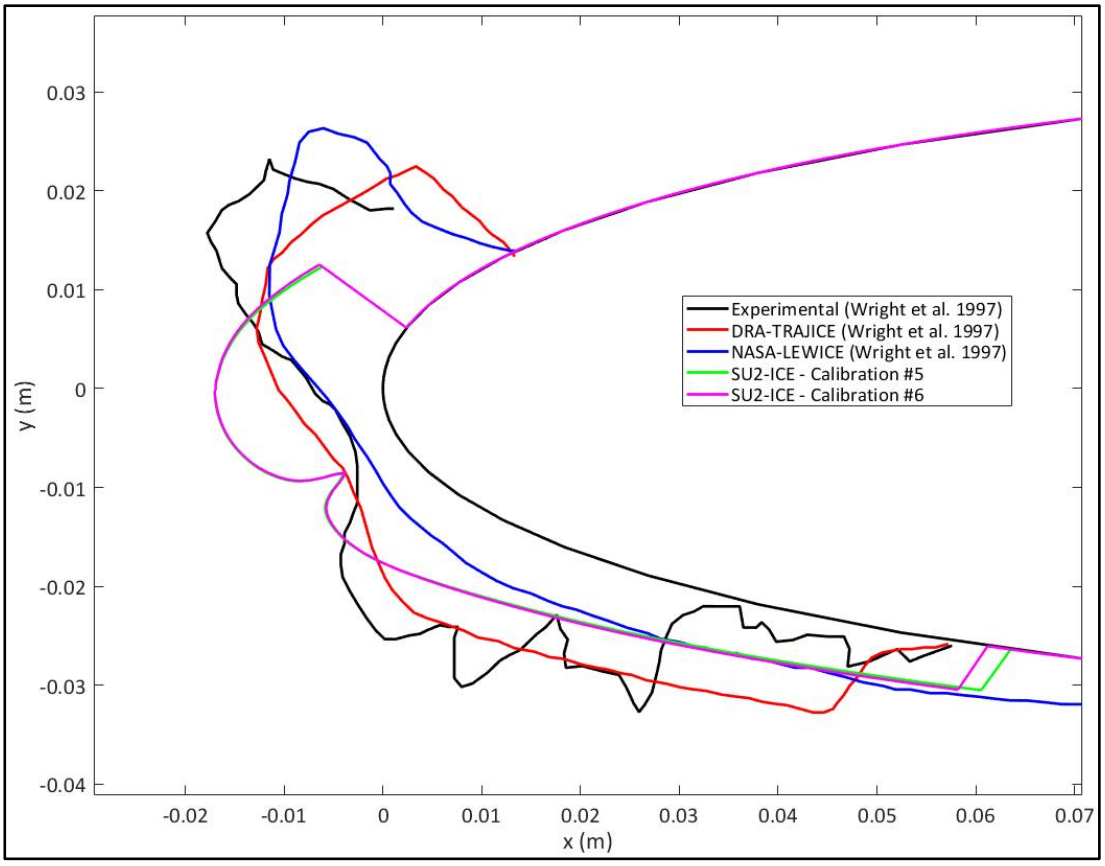

Figure 4.24 Ice shape obtained by CFD after calibrations #5 and #6

In Figure 4.24, calibration #5 and #6 accretions are almost identical. The shape obtained differs from the previous test cases, as expected. Table 4.14 brings together the main characteristics of the CFD accretions.

Table 4.14 CFD predictions for the NASA36 case

Roughness used	Maximum thickness	Cross-sectional area
calibration #5	0.017 m (−20.5%)	5.90×10^{-4} m² (−34.4%)
calibration #6	0.017 m (−20.5%)	5.89×10^{-4} m² (−34.5%)

Table 4.15 Ice thicknesses at the probe locations in millimeters, case NASA36, calibration #6

Probe number	1	2	3	4	5	6	7	8	9	10
Experimental	2.0	11.0	12.5	14.0	5.0	5.0	7.0	7.5	14.0	22.5
PCE	4.9	6.3	8.2	10.5	8.7	15.7	16.9	16.7	15.4	12.2
CFD	4.9	6.3	8.2	10.5	8.7	15.7	16.9	16.7	15.4	12.2

Table 4.14 quantifies the similarities graphically observed in Figure 4.24 between calibration #5 and calibration #6: the maximum thickness is the same and their cross-sectional areas have a difference of 1.5%. SU2-ICE predicts a maximum thickness having 20.5% of discrepancies with the literature. This represents an absolute discrepancy of 4.4 mm, corresponding to 0.8% of the chord length. The data in Table 4.15 shows that the PCE metamodel M_2 correctly predicted the ice thickness at the 10 probe locations: the CFD and PCE predictions are identical.

The methodology showed its ability to predict roughness parameters in various atmospheric conditions. These predicted roughness parameters are the most suitable for the models employed in the cases tested, according to the Bayesian module. Starting from an unknown roughness pattern, the method predicted relevant roughness parameters using only the experimental ice shape characteristics as indicators.

4.7 Conclusions

A calibration methodology was developed for the roughness parameters used in numerical ice shape prediction. The methodology was applied to demonstrate its ability to predict relevant roughness parameters for various glaze ice cases. More specifically, the roughness parameters involved in heat flux computation were estimated from experimental observations using a Bayesian inversion approach. Ice accretion itself was computed using an implementation of a

Messinger-based ice accretion model in the SU2 open-source CFD software. The dependence of the ice shape characteristics, such as the thickness or the cross-sectional area, on the roughness pattern, was studied using the polynomial chaos expansion (PCE) metamodeling approach. The metamodels generated allowed predicting the behaviour of the CFD model with high accuracy. The Bayesian inversion was applied to the PCE metamodels to calibrate the roughness parameters. These roughness parameters constitute an estimation of the model's parameters needed to obtain a relevant ice shape for a given test case. Applied to the NASA31 glaze ice test case, the methodology allowed to predict a maximum ice thickness with 5.8% of error, and the same cross-sectional area, as compared to the experimental reference. The methodology was used for other glaze ice test cases to test its generality. Applied to the NASA32 test case, the relative error fells to 2.1% for the maximum thickness prediction. This application showed that the estimated roughness parameters change from one test case to another, as expected, indicating that the method can handle different atmospheric conditions and experimental ice shapes. It estimates the surface roughness tailored for a given CFD model. Despite the acceptable prediction capacity of the methodology, some limitations of the current model formulation were highlighted. The current approach, with a single-layer accretion and unique roughness pattern throughout the wing, can use some improvements. The calibration results showed that the position of the horn was offset as compared to the experimental reference. Having a varying roughness pattern on the wing surface will help improve this aspect. A multi-layer approach is known to help predict ice accretions with large horns, such as in the NASA36 case, which was more delicate to calibrate.

This study highlighted how much the final ice shape prediction depends on the roughness parameters input into the CFD model. Therefore, correctly selecting the roughness parameters removes one of the main sources of ice shape uncertainty. This observation is even more important since the literature review showed that the optimal roughness parameters are model-dependent, even for a given test case. The approach combining PCE metamodeling and Bayesian inversion allows the computation of the optimum roughness parameters that best suit the numerical model used.

Future extensions of the work will involve non-uniform roughness patterns and multi-layer simulations, to improve the fit with experimental accretions, but at the cost of more unknown parameters. The shape of the non-uniform roughness distribution along the airfoil will be calibrated using two new parameters. The Reynolds' exponent seen in equation (4.11), kept at its 0.45 default value in the present paper, will also be played with to adjust the wall heat flux. This increase in degrees of freedom will allow a finer calibration of the ice accretion shape.

CHAPITRE 5

EXTENSION DE LA MÉTHODOLOGIE À UNE DISTRIBUTION DE RUGOSITÉ NON UNIFORME

5.1 Mise en Contexte

Le CHAPITRE 4 a permis de démontrer la pertinence de calibrer la rugosité de surface par une inversion Bayésienne lors d'une simulation d'accrétion de glace sur une aile. La méthode permet d'estimer la hauteur de rugosité k et la rugosité équivalente k_s, à imposer dans le modèle de turbulence et de correction thermique 2PP pour que la forme de glace finale soit proche de l'accrétion expérimentale. Les Figure 4.21, Figure 4.22, Figure 4.23 et Figure 4.24 montrent qu'en partant d'une rugosité de surface inconnue, il a été possible de la calibrer pour obtenir des accrétions de glace satisfaisantes par rapport aux formes expérimentales de la littérature. Néanmoins, des améliorations sont possibles et nécessaires, car la corne de l'accrétion (i.e. la zone présentant la plus forte épaisseur) n'est pas correctement positionnée malgré une épaisseur adéquate (pour les cas NASA31 et NASA32), voire assez mal prédite (cas NASA36). En observant la base de données générée pour le cas NASA31 (Figure 4.13), il est possible de remarquer que la corne est toujours placée au même endroit, et ce malgré les variations de k et k_s. La rugosité imposée étant uniforme partout sur le profil d'aile, seul un passage à une rugosité non uniforme permettrait de déplacer la corne de l'accrétion et de jouer sur sa position.

L'objectif de ce chapitre est d'appliquer la méthodologie développée au CHAPITRE 4 avec davantage de paramètres à calibrer pour raffiner la prédiction de l'accrétion de glace. Pour avoir des paramètres supplémentaires à calibrer, une distribution de rugosité non uniforme inspirée des travaux de Han et Palacios (2017) est implémentée, et des paramètres jusque-là utilisés à leurs valeurs par défaut dans le modèle 2PP vont être calibrés. Ce processus de calibration étendu permet d'obtenir des accrétions de glace dont l'épaisseur locale et la position de la corne présentent des accords plus conformes avec les formes expérimentales que dans le CHAPITRE 4. Ces résultats ont été présentés lors de la conférence internationale SAE sur le givrage en juin 2023 (Ignatowicz et al., 2023a).

5.2 Calibration Étendue de la Correction Thermique 2PP

5.2.1 Paramètres à Calibrer

Le modèle de correction thermique 2PP (Morency & Beaugendre, 2020), présenté dans les précédents chapitres, a été jusqu'à présent utilisé en calibrant les valeurs de k et k_s tout en conservant les autres paramètres à leurs valeurs par défaut, comme le montre l'équation (5.1), qui est identique à l'équation (4.11). La définition du nombre de Reynolds de rugosité Re_s, fonction de k_s, a été donnée par l'équation (4.12).

$$\Delta Pr_t = g \times 0.07083 \times {Re_s}^{0.45} \times Pr^{0.8} \times exp\left(-\frac{d}{k}\right) \tag{5.1}$$

Il est possible de réécrire cette formule en conservant son expression littérale, comme le montre l'équation (5.2).

$$\Delta Pr_t = g \times \frac{0.136}{Ckc} \times {Re_s}^{\alpha_p} \times Pr^{\beta_p} \times exp\left(-\frac{d}{k}\right) \tag{5.2}$$

Par identification entre les équations (5.1) et (5.2), les valeurs par défaut employées couramment dans la littérature (Dipprey & Sabersky, 1963; Morency & Beaugendre, 2020; Owen & Thomson, 1963), et utilisées dans les CHAPITRE 2, CHAPITRE 3 et CHAPITRE 4, sont ainsi :

- $Ckc = 1.92$;
- $\alpha_p = 0.45$;
- $\beta_p = 0.8$.

Faire varier ces trois paramètres conjointement avec k et k_s/k permettrait de calibrer le transfert de chaleur avec davantage de degrés de liberté. Pour s'assurer de la pertinence de calibrer tous les paramètres, une étude de sensibilité est menée pour quantifier l'influence de Ckc, α_p, β_p, k et k_s/k sur le coefficient de transfert de chaleur h_c sur un cas simple de plaque plane en 2D.

Seul le transfert de chaleur est étudié ici, de sorte qu'il n'y a pas de givrage lors de cette étude de sensibilité.

5.2.2 Étude de Sensibilité sur une Plaque Plane 2D

5.2.2.1 Présentation du Cas Test

Cette étude de sensibilité est réalisée sur un cas de plaque plane 2D dont le domaine de calcul et les conditions aux limites sont présentés sur la Figure 5.1.

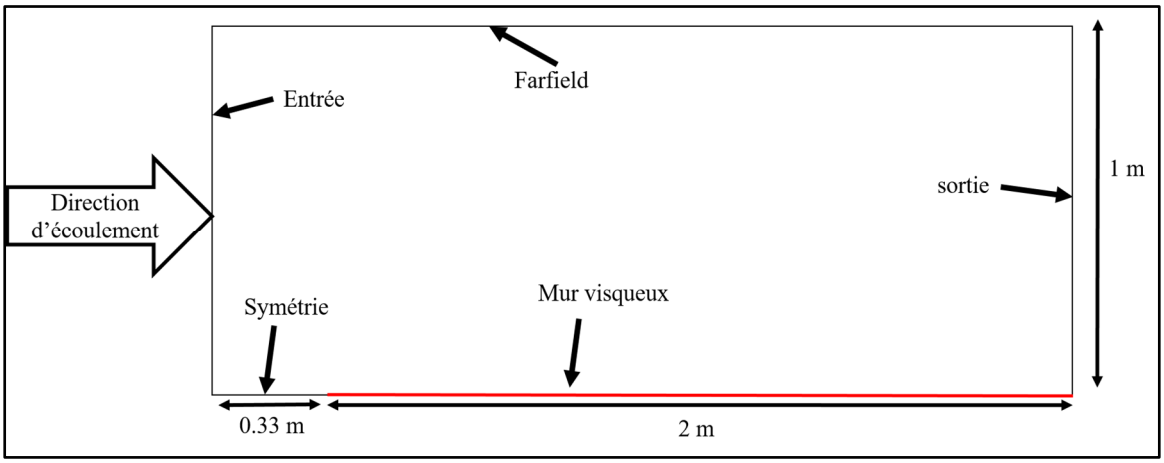

Figure 5.1 Domaine de calcul et dimensions pour le cas test de la plaque plane

Le domaine est discrétisé avec un maillage structuré de 13 056 quadrilatères (Figure 5.2). La hauteur de la première cellule au mur est de 2×10^{-6} m, donnant un y^+ de l'ordre de 0.9. Le taux de croissance normal à la paroi est de 1.1.

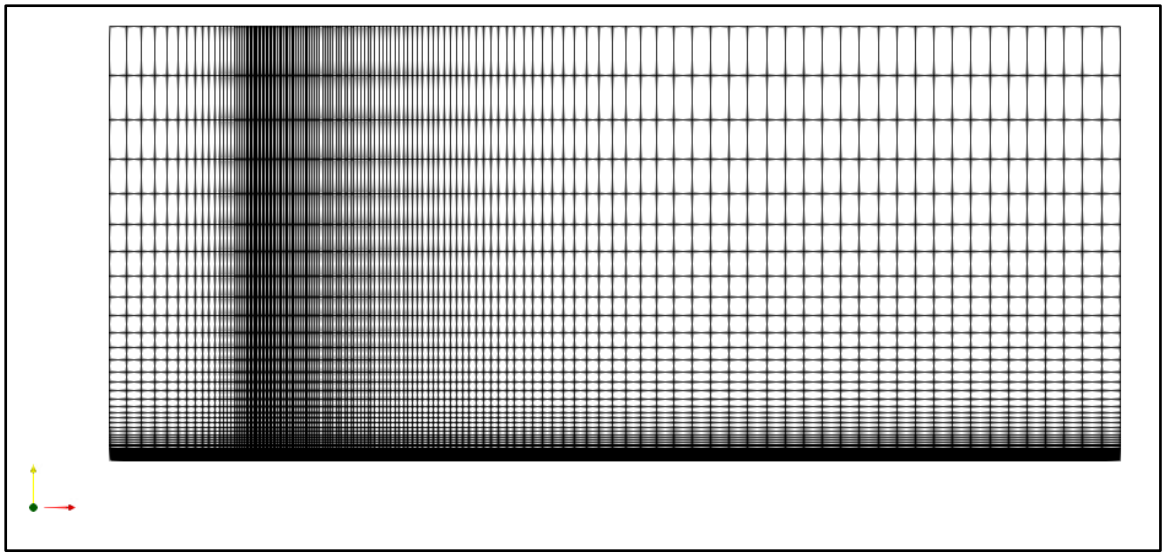

Figure 5.2 Maillage du domaine

Le solveur RANS de SU2 avec un schéma de discrétisation de Roe, le modèle de turbulence Spalart-Almaras rugueux (Aupoix & Spalart, 2003) et la correction thermique 2PP (Morency & Beaugendre, 2020) est utilisé avec les conditions suivantes :

- Nombre de Mach de 0.2;
- Température ambiante de 300 K;
- Mur visqueux isotherme à 320 K;
- Pression totale en entrée de 118 309 Pa.

La rugosité de surface employée est variable d'une simulation à l'autre, ce qui va permettre de bâtir la base de données nécessaire à l'étude de sensibilité.

5.2.2.2 Échantillonnage et Construction de la Base de Données

L'étude de sensibilité est basée sur le calcul des indices de Sobol, de façon identique à la méthode présentée dans les Sections 2.4.2 et 3.6 en utilisant un métamodèle de type chaos polynomial (PCE). Les cinq paramètres à étudier sont échantillonnés sur une plage de variation issue des données de la littérature (Dipprey & Sabersky, 1963; Owen & Thomson, 1963) et avec une distribution uniforme, telles que présentées dans le Tableau 5.1.

Tableau 5.1 Plages de variations pour l'étude de sensibilité

	Minimum	Maximum
k	0.41 mm	4.32 mm
k_s/k	0.2	6.5
α_p	0.1	0.6
β_p	0.34	0.9
Ckc	1.32	2.32

La taille de la base de données à générer est définie en envisageant un métamodèle PCE de degré 7. En reprenant l'équation (4.49) appliquée à cinq paramètres et un degré 7 (Schaefer et al., 2017), il vient, avec un facteur de sur-échantillonnage de 1.0 :

$$N_s = 1.0 \times \frac{(5+7)!}{5!\,7!} = 792 \tag{5.3}$$

Les 792 échantillons sont générés par Latin hypercube sampling sur les plages définies dans le Tableau 5.1.

5.2.2.3 Indices de Sensibilité de Sobol

Une fois la base de données de 792 simulations CFD générée, deux métamodèles PCE sont établis. Le premier prédit la valeur maximale du coefficient de transfert de chaleur (h_c) sur la plaque et le second sa valeur moyenne. La précision de ces deux métamodèles est satisfaisante, présentant un coefficient de régression R^2 de 0.999 dans les deux cas. La Figure 5.3 présente

la régression lorsque les prédictions des métamodèles sont comparées aux prédictions CFD sur les 792 entrées de l'échantillon. La prédiction des métamodèles est de bonne qualité, ce qui permet de les utiliser avec confiance pour la génération des indices de Sobol.

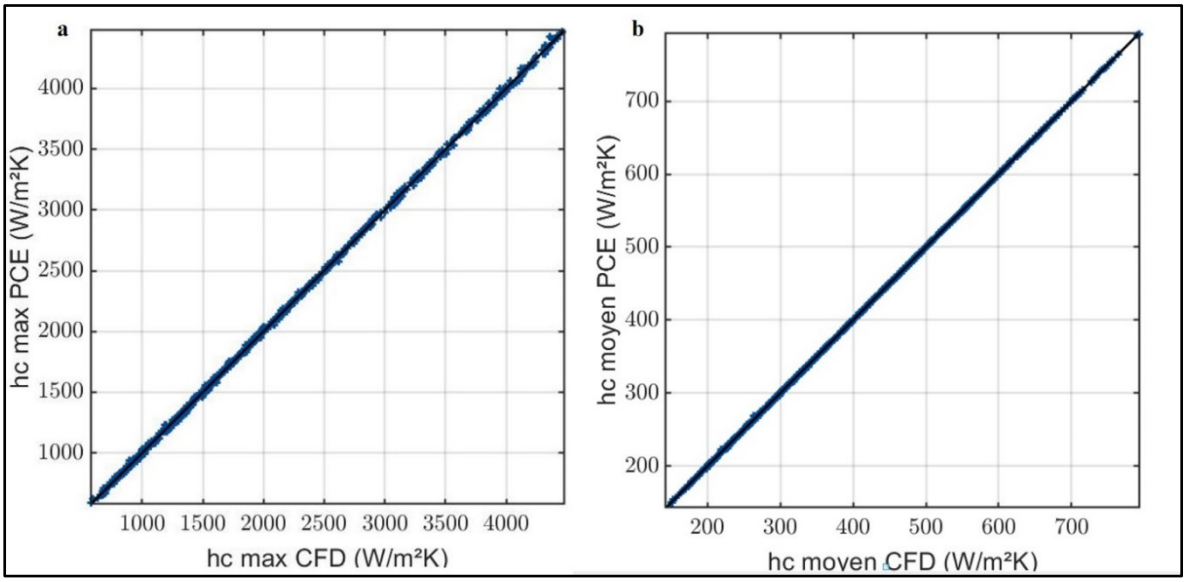

Figure 5.3 Régression entre la prédiction PCE et la CFD (a) pour h_c maximum et (b) pour h_c moyen

L'étude de sensibilité permet d'obtenir les indices totaux de Sobol présentés sur la Figure 5.4 pour la sensibilité de la valeur maximale de h_c et sur la Figure 5.5 pour la sensibilité de la valeur moyenne de h_c.

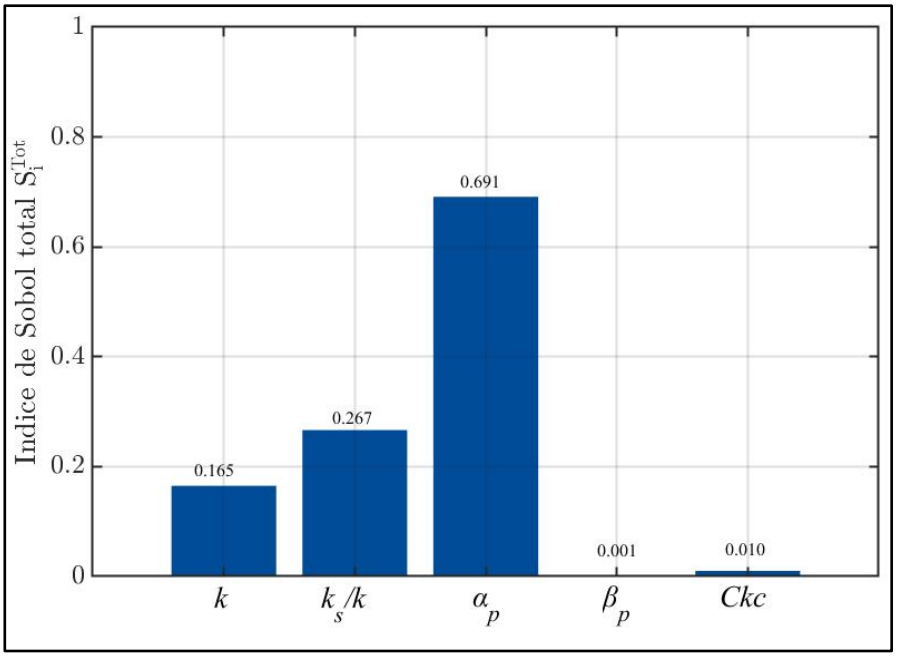

Figure 5.4 Indices de Sobol totaux (h_c maximum)

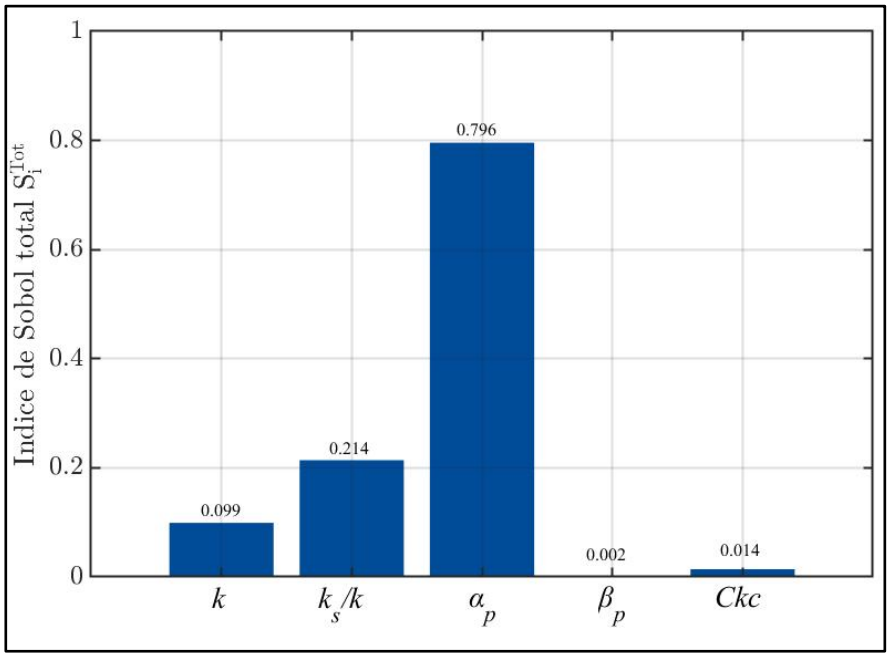

Figure 5.5 Indices de Sobol totaux (h_c moyen)

Les Figure 5.4 et Figure 5.5 permettent de dévoiler que h_c est majoritairement dépendant des trois paramètres k, k_s/k et α_p. D'après la classification effectuée par Chan et al. (1997), voir Section 2.4.2, il est possible de considérer les paramètres β_p et Ckc comme étant négligeables dans la variabilité du coefficient h_c. Par conséquent, il est possible de retirer β et Ckc de la liste des paramètres incertains et de les conserver à leurs valeurs par défaut pour la suite de l'étude. La calibration du modèle 2PP se focalisera ainsi uniquement sur k, k_s/k et α_p.

5.3 Proposition d'une Distribution de Rugosité Non Uniforme

Pour améliorer les prédictions d'accrétions de glace, notamment la position de la corne, une distribution non uniforme de la hauteur de rugosité k est mise en place, similairement à la distribution parabolique proposée par Han & Palacios (2017), voir équation (1.40). La distribution permet de déterminer la hauteur de rugosité en fonction de l'abscisse curviligne le long de la géométrie, que ce soit une plaque plane ou un profil d'aile par exemple. La distribution « cubique » proposée prend la forme donnée par l'équation (5.4).

$$k = -\frac{1}{a}\left|\left|s - s_0\right| - b\right|^3 + k_0 \tag{5.4}$$

Dans l'équation (5.4), s représente l'abscisse curviligne, s_0 l'abscisse curviligne du point de stagnation et k_0 est la hauteur de rugosité maximale. Les paramètres a et b permettent respectivement de jouer sur la largeur de la zone rugueuse et la position du pic de rugosité maximale. Des exemples de telles distributions en fonction de l'abscisse curviligne sont illustrés sur la Figure 5.6.

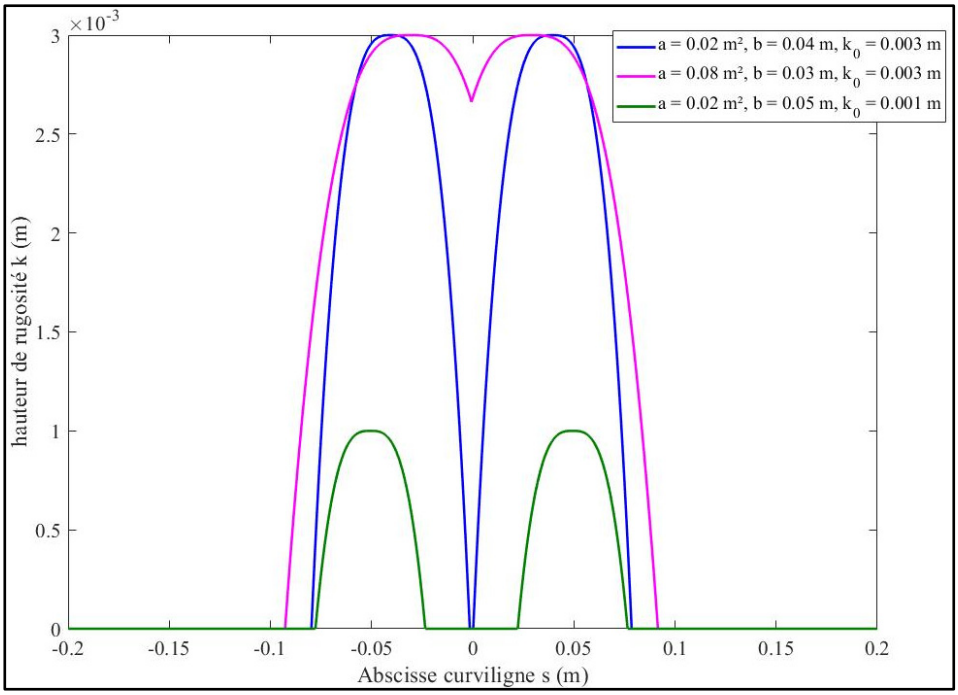

Figure 5.6 Exemples de distributions de rugosité

Cette nouvelle distribution de rugosité, symétrique autour du point de stagnation, va être utilisée dans ce chapitre en lieu et place de la distribution uniforme employée jusqu'à présent. Ainsi, la méthodologie du CHAPITRE 4 va être mise en œuvre à nouveau avec cette fois-ci cinq paramètres à calibrer :

- k_0;
- k_s/k;
- α_p;
- a;
- b.

Cette extension de la méthodologie permet premièrement d'améliorer grandement les prédictions d'accrétions et deuxièmement de démontrer la flexibilité de la méthode développée vis-à-vis du nombre de paramètres à calibrer. Il est en effet possible de changer la configuration des paramètres à calibrer, passant ici de deux paramètres (CHAPITRE 4) à cinq sans modification de la structure d'analyse implémentée.

5.4 Méthodologie Révisée

Toutes les étapes de la méthodologie présentée au CHAPITRE 4 sont réitérées ici en commençant par la génération d'une base de données pour chaque cas test à étudier. Le nombre de paramètres à calibrer étant supérieur, la taille de la base de données est plus conséquente. En reprenant l'équation (5.3) avec un facteur de sur-échantillonnage de 1.06, 840 simulations sont nécessaires pour bâtir la base de données. Le sur-échantillonnage choisi résulte des premiers essais préliminaires qui ont démontré qu'environ 6% des simulations étaient inexploitables en raison de configurations de rugosité provoquant des problèmes de convergence de la solution. Une autre différence avec le CHAPITRE 4 est l'emploi du maillage médium 449-129 avec 256 cellules à la surface de l'aile en prévision du plus grand nombre de simulations à lancer, plus gourmand en ressources de calcul, en lieu et place du maillage fin. Le maillage médium a montré lors de l'étude de convergence en maillage avoir un GCI de l'ordre de 2% sur l'épaisseur maximale de glace, ce qui est tout à fait acceptable pour être utilisé (voir Section 4.6.1.2).

Dans ce chapitre, le métamodèle créé est semblable au métamodèle M_2 du CHAPITRE 4, voir Table 4.3. Il s'agit d'un métamodèle PCE multi-sorties estimant simultanément l'épaisseur de glace en différents points de contrôle sur le profil NACA0012. La Figure 5.7 résume les entrées et sorties du métamodèle employé ici. La position et le nombre de points de contrôle est un paramètre modifiable par l'utilisateur, qui peut les choisir parmi les nœuds du maillage surfacique du profil NACA0012. La calibration Bayésienne ultérieure se fait sur les points de contrôle choisis, ce qui permet de mettre l'accent sur une zone particulière à calibrer, comme la corne par exemple. Ces points de contrôle disponibles (jaune) sont illustrés sur la Figure 5.8 où sont également représentés les points projetés normalement sur l'accrétion expérimentale (rouge). Pour cette illustration, l'accrétion du cas NASA31 est employée. La distance entre un point de contrôle jaune et son projeté rouge sur l'accrétion correspond à l'épaisseur de glace locale fournie au solveur Bayésien en guise d'observation expérimentale de référence.

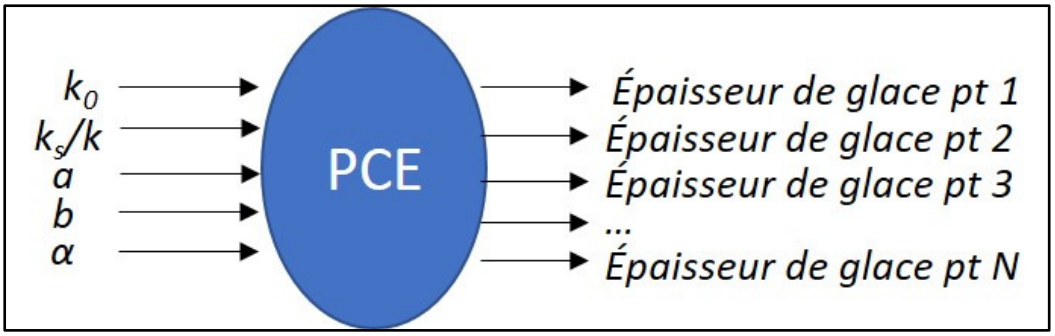

Figure 5.7 Entrées/sorties du métamodèle PCE

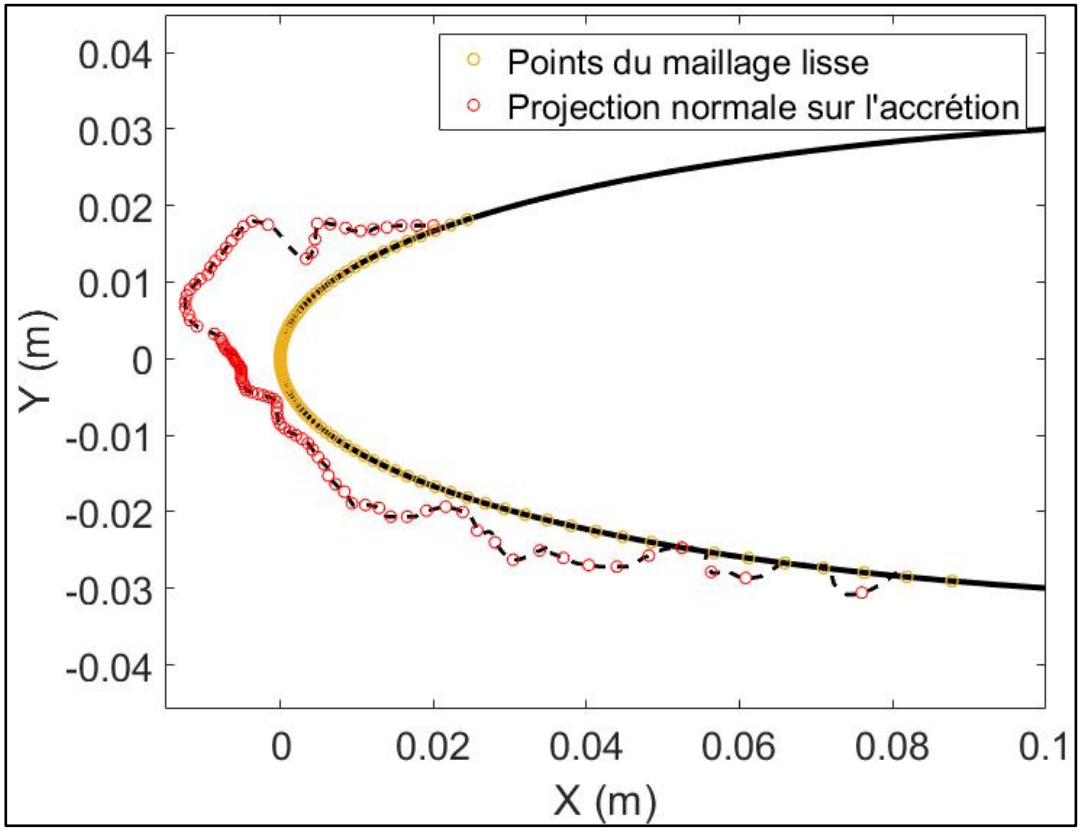

Figure 5.8 Aperçu des points de contrôle disponibles (jaune) et de leur projection sur l'accrétion expérimentale (rouge)

La zone d'accrétion expérimentale pour le cas NASA31 illustré sur la Figure 5.8 couvre 103 points de contrôle. En supposant que le nombre de points de contrôle retenus pour la calibration peut varier de 1 à 103 en prenant toutes les combinaisons possibles, cela représente environ 10^{31} possibilités de métamodèles. Il va de soi que seule une petite partie de ces configurations

peut être testée. Lorsqu'une configuration de métamodèle est choisie, le solveur Bayésien calcule dans la foulée les paramètres de rugosité qui permettent de prédire au mieux avec SU2-ICE l'épaisseur de glace expérimentale aux points de contrôle retenus. Les paramètres de rugosité calibrés sont ensuite utilisés dans une simulation CFD complète pour générer la forme de glace dite calibrée.

Pour juger si une accrétion calibrée obtenue avec SU2-ICE est satisfaisante par rapport à la forme expérimentale, deux critères sont évalués : (1) L'aspect visuel, ce qui reste malgré tout assez subjectif; (2) La valeur d'une erreur quadratique moyenne (RMS pour root mean square en anglais) calculée sur l'ensemble de tous les points de contrôle disponibles (et non seulement les points de contrôle retenus) qui constitue un jugement plus quantitatif que l'inspection visuelle. Cette erreur ε_{RMS} est calculée à l'aide de l'équation (5.5), où $h_{CFD,i}$ est l'épaisseur de glace prédite par SU2-ICE au point i, $h_{EXP,i}$ est l'épaisseur expérimentale mesurée au point i et N_{points} le nombre total de points de maillage sur l'intégralité du profil d'aile, soit 254 pour le maillage utilisé.

$$\varepsilon_{RMS} = \sqrt{\frac{\sum_{i=1}^{N_{points}} (h_{CFD,i} - h_{EXP,i})^2}{N_{points}}} \tag{5.5}$$

5.5 Calibration Revue des Cas de Givre Transparent (Glaze Ice)

Dans ce chapitre, quatre cas test vont être calibrés pour éprouver la méthode révisée employant une rugosité non uniforme. Hormis les cas NASA31, NASA32 et NASA36 du CHAPITRE 4 qui vont être calibrés de nouveau, le cas NASA30 va également être scruté. Les paramètres propres à chaque cas test sont résumés dans le Tableau 5.2. Dans cette thèse, le régime étudié est en majorité le givre transparent (glaze ice) dont le comportement a été vérifié dans la section 4.6.1.3. Néanmoins, SU2-ICE a également la capacité de simuler des régimes de givre blanc, sans film liquide (rime ice), et des régimes entièrement liquides avec uniquement un film d'eau ruisselant. La vérification du comportement de SU2-ICE pour ces deux derniers cas est placée en ANNEXE II.

Tableau 5.2 Synthèse des conditions propres à chaque cas test

	NASA31	**NASA32**	**NASA36**	**NASA30**
Température ambiante	269.1 K	270.2 K	266.4 K	266.3 K
Pression ambiante	95 610 Pa	95 610 Pa	92 060 Pa	95 610 Pa
Corde du NACA0012	0.5334 m	0.5334 m	0.5334 m	0.5334 m
Angle d'attaque	4°	4°	4°	4°
Vitesse d'écoulement (Mach)	58.1 m/s (0.177)	58.1 m/s (0.177)	93.9 m/s (0.286)	58.1 m/s (0.177)
Contenu en eau liquide (LWC)	1.30 g/m^3	1.30 g/m^3	1.05 g/m^3	1.30 g/m^3
Diamètre median des gouttelettes (MVD)	20 µm	20 µm	20 µm	20 µm
Temps total d'exposition	480 s	480 s	372 s	480 s

5.5.1 Cas NASA31

Le cas test NASA31, décrit en détail dans la Section 4.6.1 est repris pour calibrer la prédiction d'accrétion par rapport à la forme expérimentale de la NASA (Wright, Gent, et al., 1997). La Figure 5.9 montre l'allure de la base de données obtenue. Cette base de données a été analysée pour s'assurer que toutes les solutions air avaient correctement convergé concernant le coefficient de transfert de chaleur convectif. En comparant cette base de données avec celle obtenue pour une rugosité uniforme (Figure 4.13), il est possible de remarquer que dorénavant, la corne n'est pas toujours au même endroit d'une accrétion à l'autre. Cette base de données sert de support à la création du métamodèle PCE.

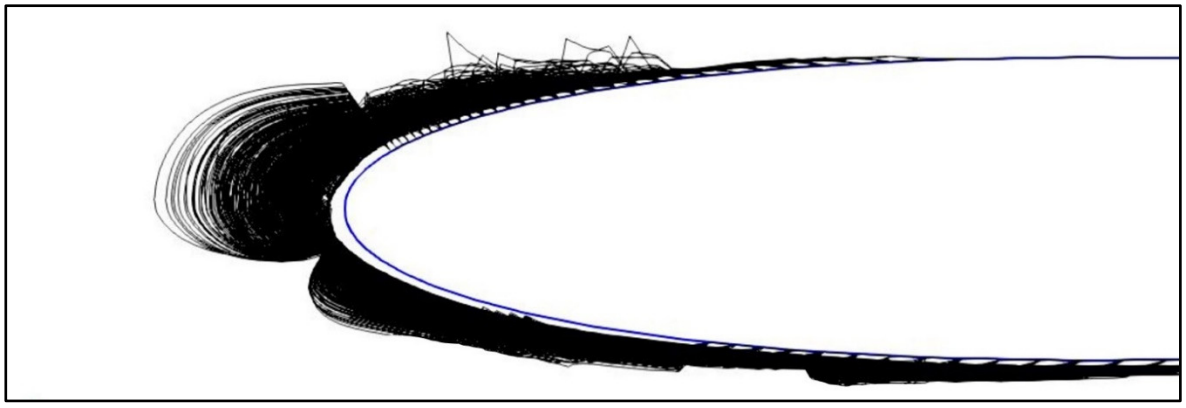

Figure 5.9 Base de données de 840 accrétions (cas NASA31)

Plusieurs configurations de métamodèles ont été testées, avec un nombre de points de contrôle variant de 11 à 103 pour évaluer la qualité de la calibration. Le Tableau 5.3 regroupe les six configurations testées. Les configurations #5-5 et #5-6 ont été pensées de façon à privilégier la calibration au niveau de la corne qui est souvent considérée comme la partie critique d'une accrétion.

Tableau 5.3 Configuration de métamodèles testées

Calibration	Configuration de points de contrôle (Figure 5.8)	Nombre de points de contrôle
#5-1	1 sur 10	11
#5-2	1 sur 5	21
#5-3	1 sur 2	52
#5-4	Tous les points	103
#5-5	1 sur 5 hors de la corne et tous les points dans la corne.	72
#5-6	Seuls les points dans la corne	64

Seule la meilleure calibration parmi les six (tant visuellement que par le calcul d'erreur RMS) est présentée ici, à savoir la calibration #5-6. Les cinq autres calibrations sont regroupées dans l'ANNEXE III. Pour cette calibration #5-6, la configuration des 64 points de contrôle retenus est montrée sur la Figure 5.10.

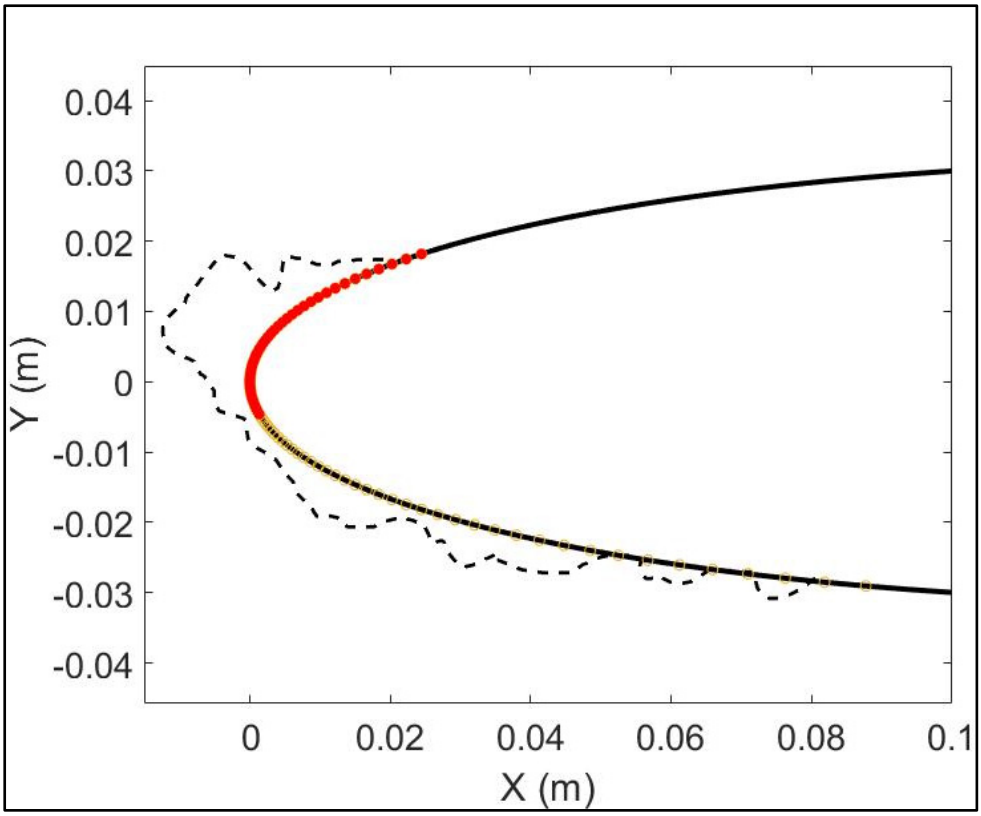

Figure 5.10 Points de contrôle retenus (rouge plein) et non retenus (jaune) pour la calibration #5-6

Les paramètres de rugosité calibrés renvoyés par l'inversion Bayésienne, correspondant au maximum a posteriori (MAP), pour la calibration #5-6 sont :

- k_0 = 1.7 mm;
- k_s/k = 2.8;
- α_p = 0.22;
- a = 0.058 m²;
- b = 0.045 m.

L’emploi de ces paramètres de rugosité permet de tracer sur la Figure 5.11 la distribution de rugosité calibrée pour le cas test NASA31 et les modèles utilisés dans ce projet.

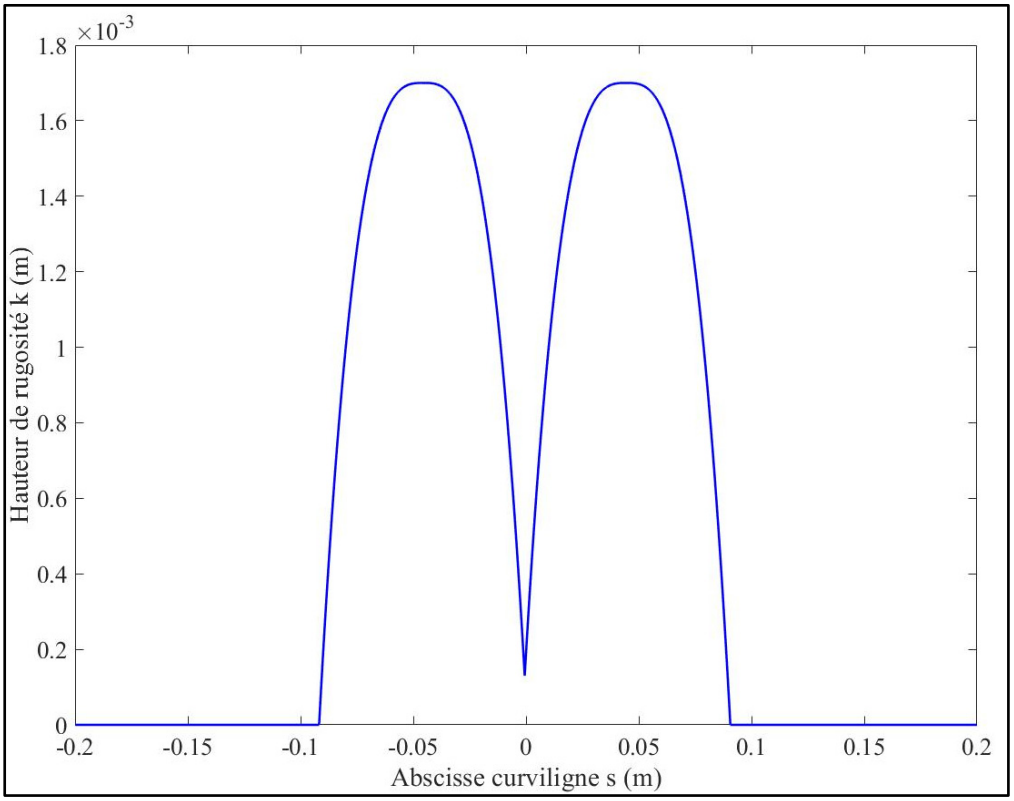

Figure 5.11 Distribution de rugosité calibrée pour le cas NASA31

L’accrétion de glace obtenue avec les paramètres de rugosité calibrés est illustrée sur la Figure 5.12, où est également renseignée l’erreur RMS calculée avec l’équation (5.5).

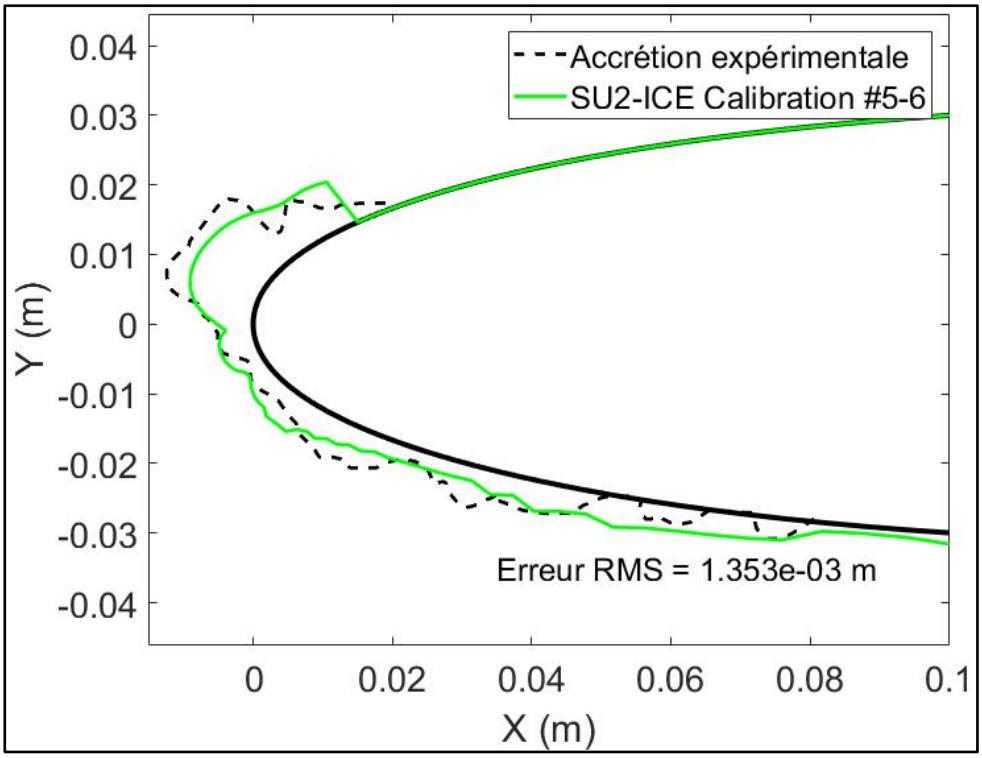

Figure 5.12 Accrétion calibrée obtenue avec SU2-ICE (cas NASA31)

L'accrétion présente un très bon accord visuel avec l'accrétion expérimentale et une erreur RMS de 1.35 mm, ce qui représente 0.2% de la longueur de corde. La comparaison avec la Figure 4.21 montre que la nouvelle calibration employant une rugosité non uniforme permet une meilleure prédiction de la position de la corne et globalement une accrétion qui a une allure se rapprochant de la forme expérimentale. L'erreur RMS obtenue, voir équation (5.5), est inférieure à celles calculées sur les prédictions d'accrétions communément publiées dans la littérature pour le cas NASA31 (Lavoie et al., 2018; Wright, Gent, et al., 1997). L'accrétion obtenue par Lavoie et al. et l'accrétion de la DRA sont monocouches au même titre que SU2-ICE. L'accrétion de la NASA avec LEWICE a été obtenue avec quatre couches. La Figure 5.13 compare l'accrétion SU2-ICE avec quelques accrétions prédites dans la littérature. Les erreurs RMS correspondant à ces accrétions, calculées également avec l'équation (5.5) à partir des formes publiées dans la littérature, sont regroupées dans le Tableau 5.4.

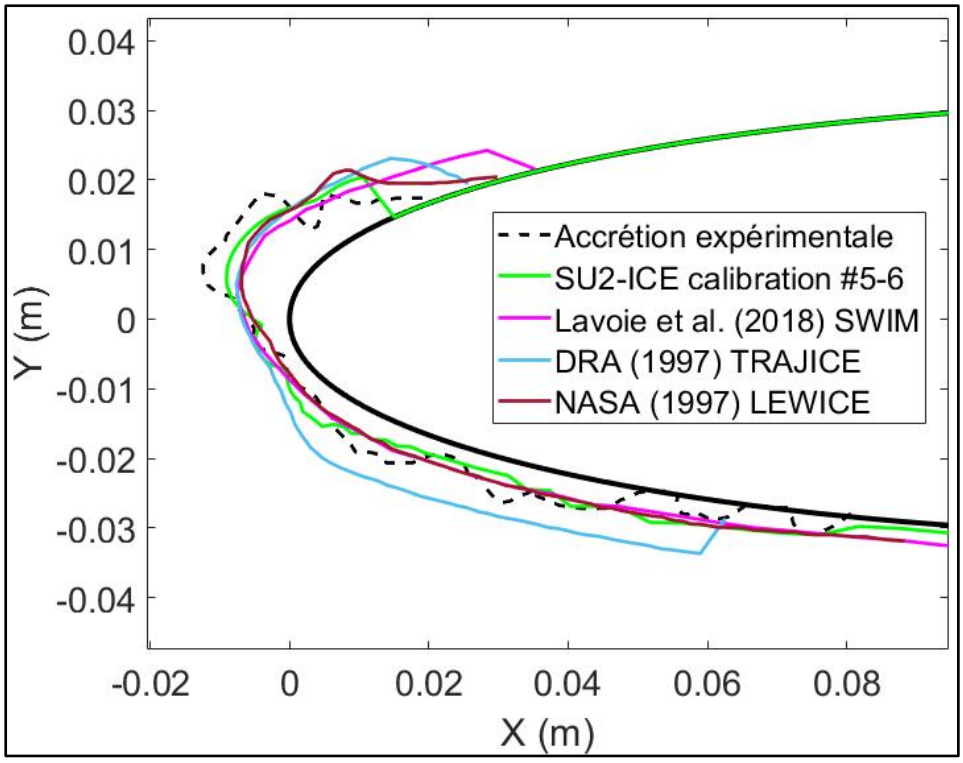

Figure 5.13 Comparaison entre SU2-ICE et les prédictions numériques de la littérature (cas NASA31)

Tableau 5.4 Comparaison des erreurs RMS entre les prédictions d'accrétions (NASA31)

Accrétion	**Erreur RMS (m)**
SU2-ICE calibration #5-6	1.35×10^{-3}
Lavoie et al. (2018) SWIM	1.74×10^{-3}
DRA (1997) TRAJICE	2.23×10^{-3}
NASA (1997) LEWICE	1.59×10^{-3}

Les résultats de la Figure 5.13 et du Tableau 5.4 indiquent une bonne prédiction de l'accrétion en comparaison avec ce qui est usuellement accepté dans la littérature, cette erreur pouvant atteindre 2.2 mm dans certains cas contre seulement 1.35 mm dans la présente étude.

5.5.2 Cas NASA32

Le cas NASA32 a lui aussi été traité à nouveau pour améliorer la prédiction par rapport au chapitre précédent. La même méthodologie que celle décrite ci-dessus pour le cas NASA31 est reprise. Tout d'abord, une base de données est générée, illustrée sur la Figure 5.14. La meilleure calibration est à nouveau celle menée en prenant uniquement les points de contrôle situés dans la corne de l'accrétion expérimentale NASA32 (46 points), comme illustré sur la Figure 5.15. Il est à noter que pour le cas NASA32, 100 points de contrôle sont disponibles dans la zone d'accrétion expérimentale.

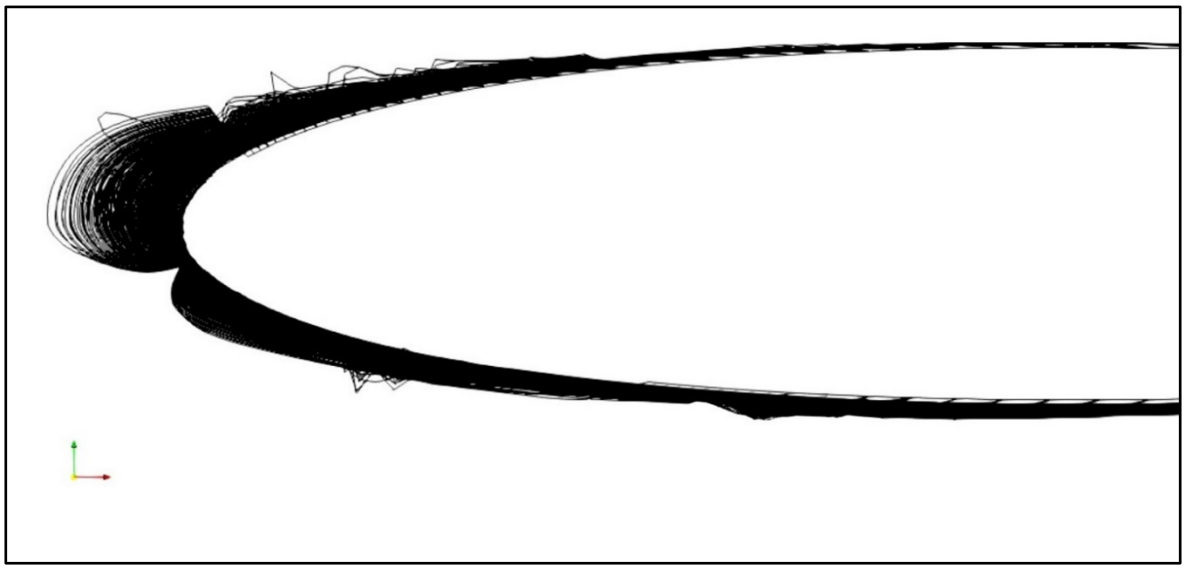

Figure 5.14 Base de données de 840 accrétions (cas NASA32)

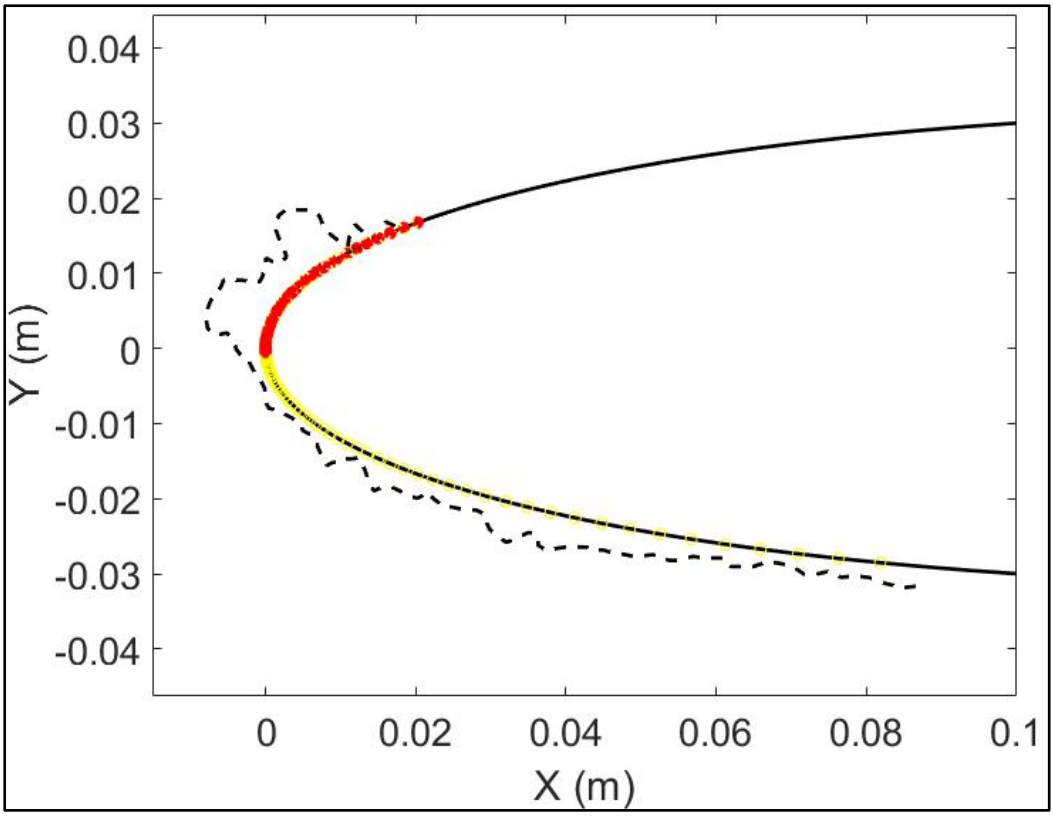

Figure 5.15 Points de contrôle (rouge plein) retenus pour la calibration NASA32

Les paramètres de rugosité calibrés calculés par le solveur Bayésien sont :

- k_0 = 0.95 mm;
- k_s/k = 4.3;
- α_p = 0.45;
- a = 0.084 m²;
- b = 0.045 m.

La distribution de rugosité correspondant à ces paramètres est tracée sur la Figure 5.16.

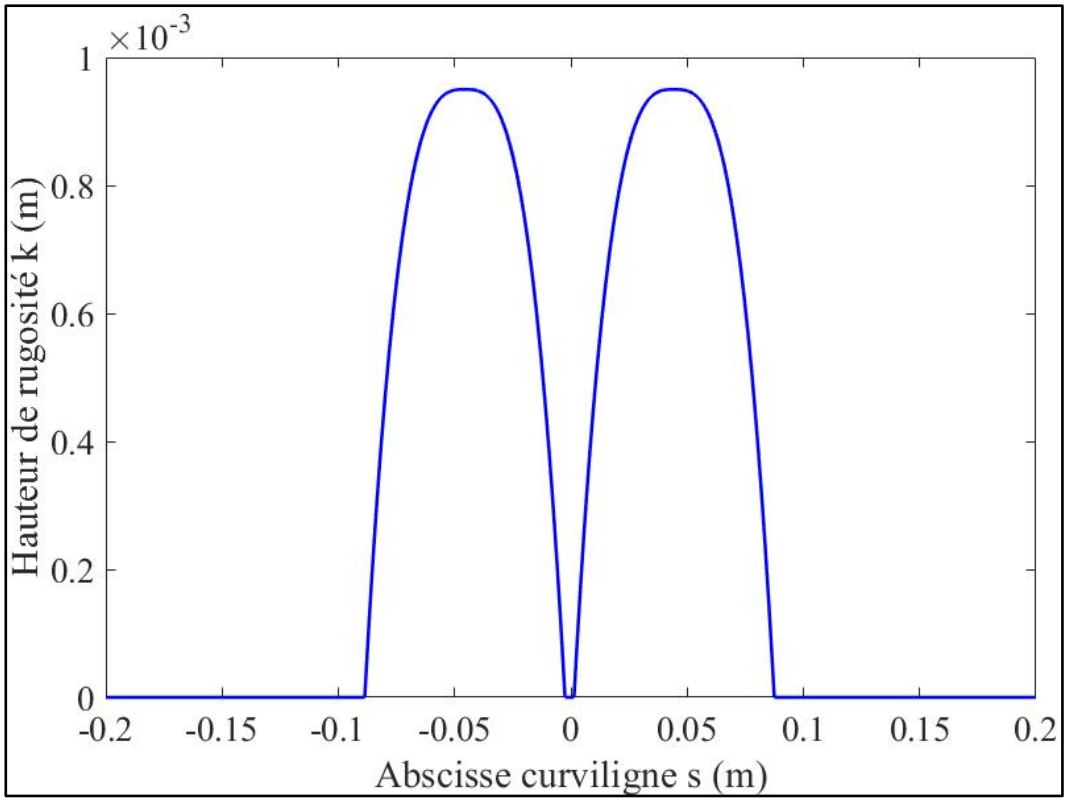

Figure 5.16 Distribution de rugosité calibrée pour le cas NASA32

La forme de glace obtenue est présentée sur la Figure 5.17. La forme de glace prédite est plus proche de l'expérimental comparé à la Figure 4.23, notamment dans la zone de la corne. Néanmoins, la limite d'accrétion sur l'extrados est plus éloignée que la forme expérimentale, ce qui trahit une surestimation du ruissellement dans le cas de SU2-ICE pour ce cas test. L'erreur RMS observée ici est à nouveau inférieure à 1.5 mm et représente 0.3% de la corde.

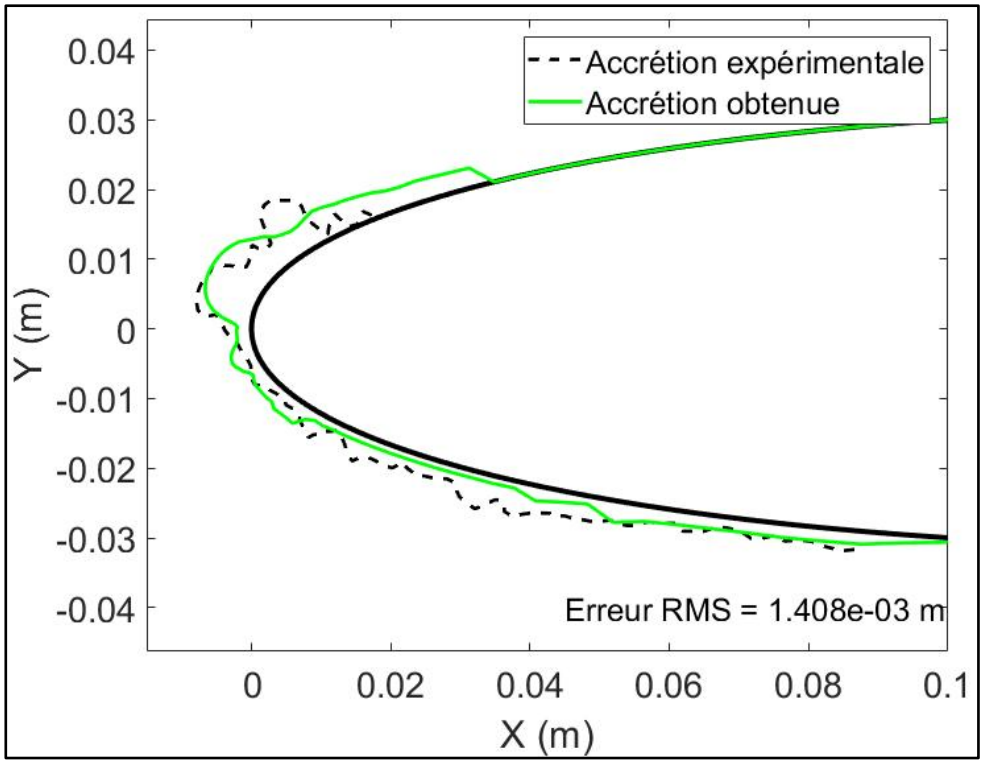

Figure 5.17 Accrétion calibrée obtenue avec SU2-ICE (cas NASA32)

Il est à nouveau possible de comparer ces résultats avec les prédictions de la littérature (Wright, Gent, et al., 1997) pour confirmer que l'erreur obtenue avec la prédiction SU2-ICE est conforme à ce qui est usuellement accepté parmi les résultats publiés. La comparaison entre l'accrétion SU2-ICE et les accrétions de la DRA, la NASA et l'ONERA est illustrée sur la Figure 5.18. À nouveau, l'accrétion de la DRA avec TRAJICE est monocouche tandis que la NASA (LEWICE) a généré une accrétion avec 4 couches. L'ONERA emploie une méthode avec une couche de prédiction améliorée ensuite par une étape de correction. Les erreurs RMS (équation (5.5)) pour chaque accrétion sont consignées dans le Tableau 5.5. L'erreur RMS observée pour SU2-ICE est à nouveau du même ordre de grandeur que la littérature et est notamment plus basse que pour les prédictions ONERA et DRA. En observant la Figure 5.18, il est possible de remarquer que le ruissellement sur l'extrados est également surestimé par les prédictions de la littérature.

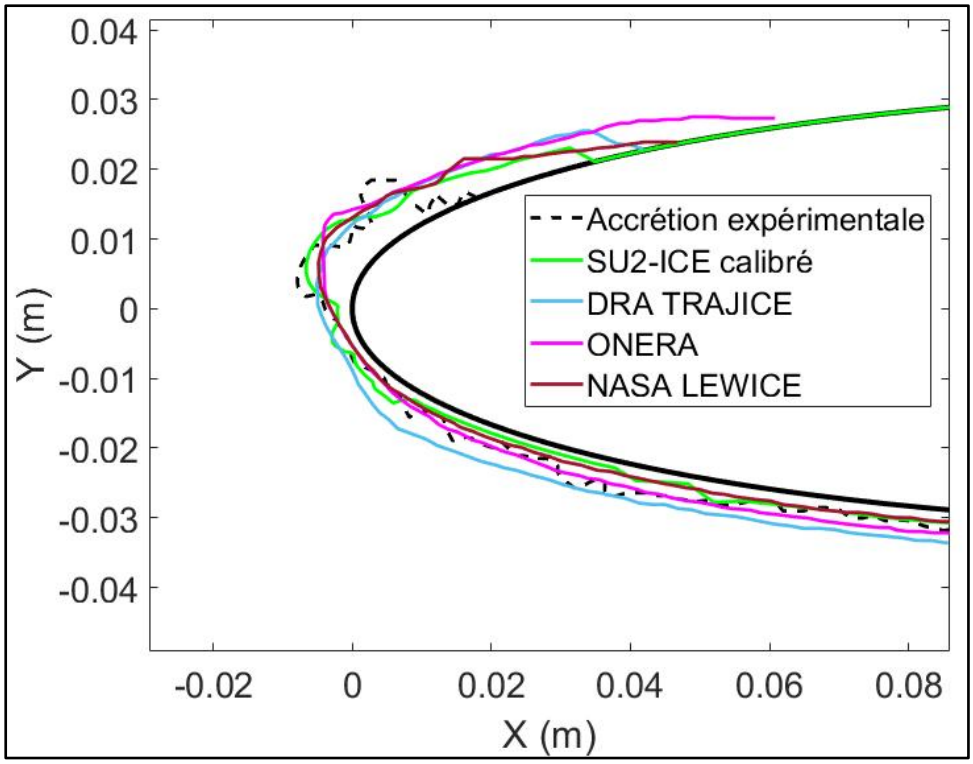

Figure 5.18 Comparaison entre SU2-ICE et les prédictions numériques de la littérature (cas NASA32)

Tableau 5.5 Comparaison des erreurs RMS entre les prédictions d'accrétions (NASA32)

Accrétion	**Erreur RMS (m)**
SU2-ICE calibré	1.41×10^{-3}
ONERA (1997)	1.57×10^{-3}
DRA (1997) TRAJICE	1.66×10^{-3}
NASA (1997) LEWICE	1.28×10^{-3}

5.5.3 Cas NASA36

Le cas NASA36 était le plus délicat à calibrer dans le CHAPITRE 4. Ceci est dû à la forme de l'accrétion expérimentale présentant une corne assez prononcée et aux formes moins régulières que les cas NASA31 et NASA32. Les calibrations menées avec une rugosité uniforme ont montré que des améliorations étaient requises pour ce type d'accrétions (voir Figure 4.24 où la forme obtenue est perfectible). Une base de données est à nouveau créée pour ce cas test puis la calibration est faite. La meilleure calibration obtenue est celle en retenant tous les points de contrôle disponibles dans la zone d'accrétion expérimentale, soit 88 points, comme illustré à la Figure 5.19.

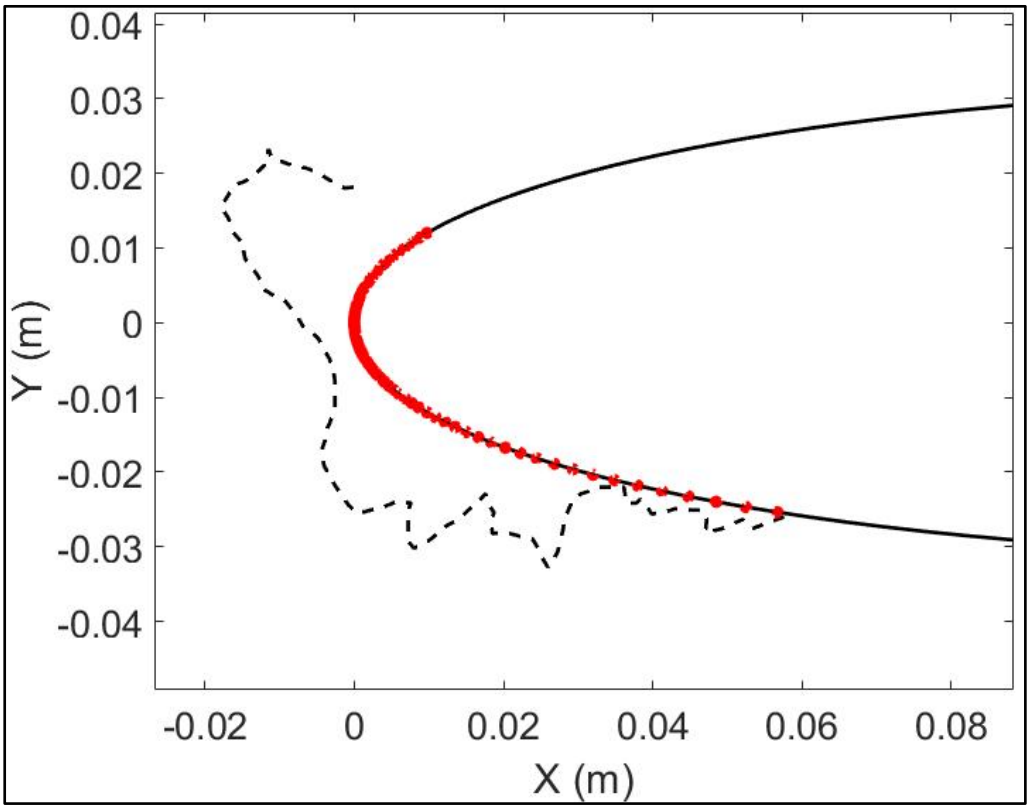

Figure 5.19 Points de contrôle (rouge) retenus pour la calibration NASA36

Les paramètres de rugosité calibrés calculés par le solveur Bayésien sont :

- k_0 = 4.3 mm;

- $k_s/k = 6.1$;
- $\alpha_p = 0.15$;
- $a = 0.087$ m²;
- $b = 0.071$ m.

La distribution de hauteur de rugosité correspondante est illustrée sur la Figure 5.20.

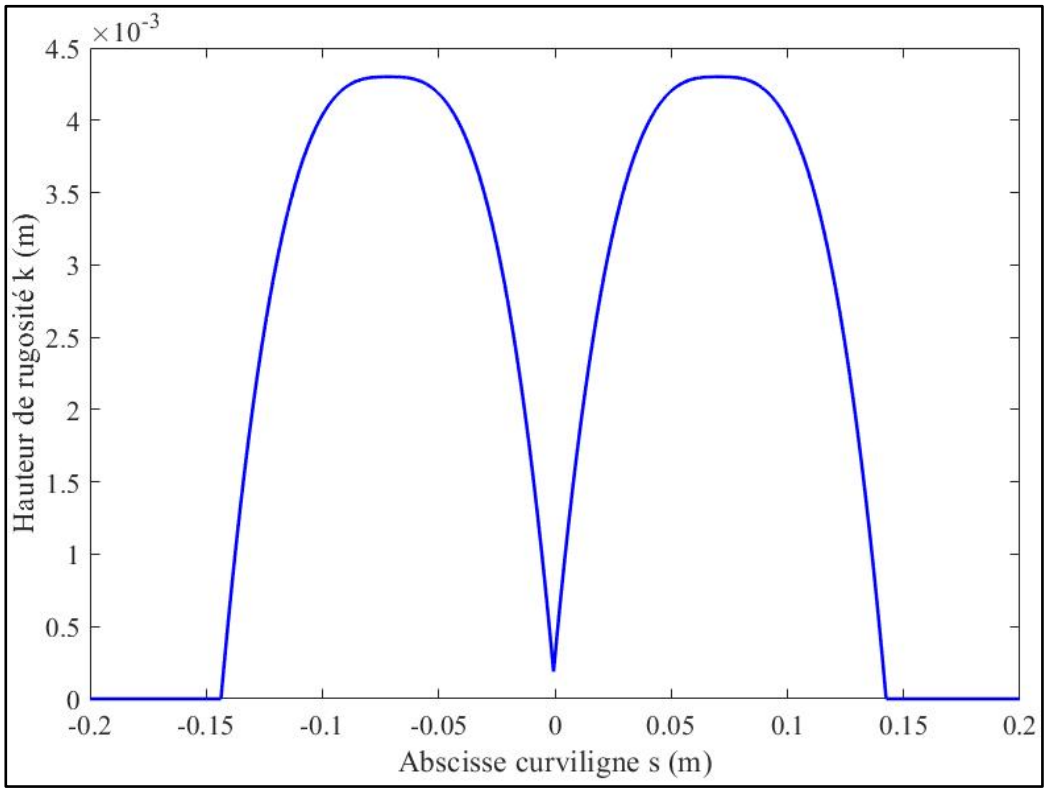

Figure 5.20 Distribution de rugosité calibrée pour le cas NASA36

La forme de glace prédite par SU2-ICE avec de tels paramètres de rugosité est illustrée sur la Figure 5.21. L'erreur RMS, calculée avec l'équation (5.5), est bien plus grande que les cas NASA31 et NASA32, atteignant 5.3 mm. Néanmoins, la prédiction est plus en accord visuellement par rapport à la calibration effectuée pour le cas NASA36 dans le chapitre précédent, voir Figure 4.24. Notamment, les limites d'accrétions sont assez proches des limites expérimentales et la corne tend à être positionnée au bon endroit. L'observation de la taille est

la position de la corne montre de meilleures similitudes avec la forme expérimentale que dans le CHAPITRE 4.

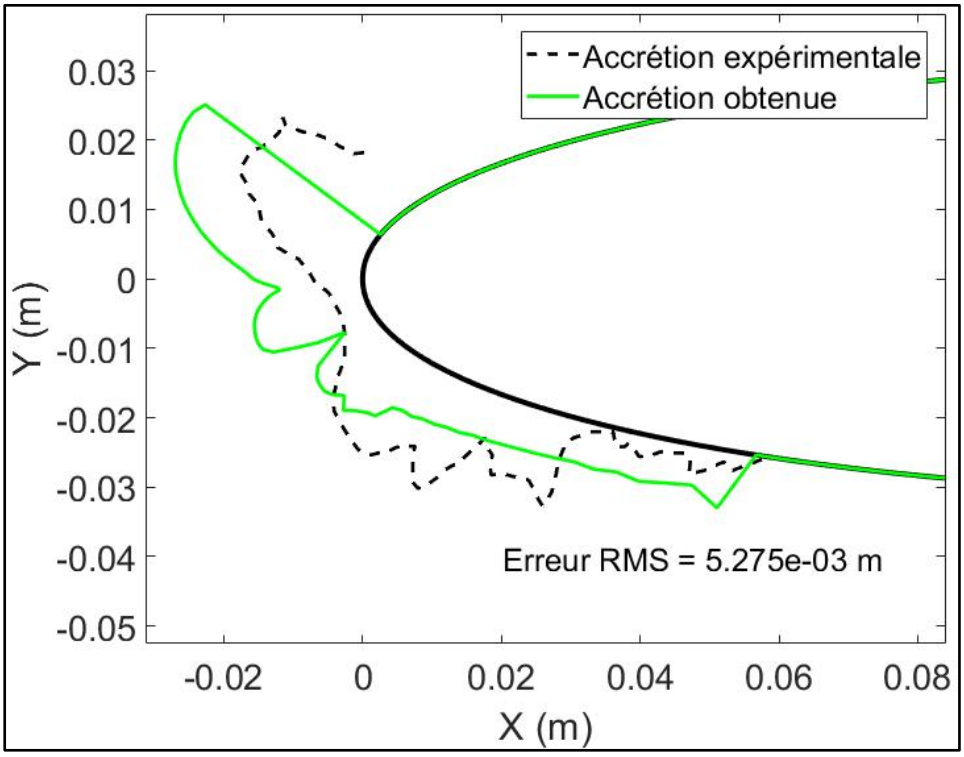

Figure 5.21 Accrétion calibrée obtenue avec SU2-ICE (cas NASA36)

Cette accrétion calibrée est à nouveau comparée aux prédictions de la DRA, de l'ONERA et de la NASA. La Figure 5.22 montre que contrairement au CHAPITRE 4, l'accrétion obtenue par SU2-ICE présente une meilleure similitude avec les accrétions de la littérature. Bien qu'un peu basse, la corne présente une épaisseur comparable à celle obtenue par la NASA et l'ONERA avec des simulations multicouches. La prédiction de l'épaisseur maximale de la corne est cependant bien plus proche de l'épaisseur expérimentale par rapport à la prédiction monocouche de la DRA. Ce type d'accrétion à forte corne montre la limitation des simulations monocouches, où la corne peine à être correctement prédite. Une accrétion multicouche permettrait notamment de mettre à jour l'efficacité de captation et la position du point de stagnation. Néanmoins, la forme obtenue présente des caractéristiques visuelles semblables à ce qui est usuellement publié pour ce cas test, ce qui est une amélioration par rapport au

CHAPITRE 4. Les erreurs RMS sont comparées dans le Tableau 5.6. Il est possible de remarquer que l'erreur RMS de SU2-ICE est assez élevée, pénalisée par la mauvaise position de la corne qui accentue l'erreur.

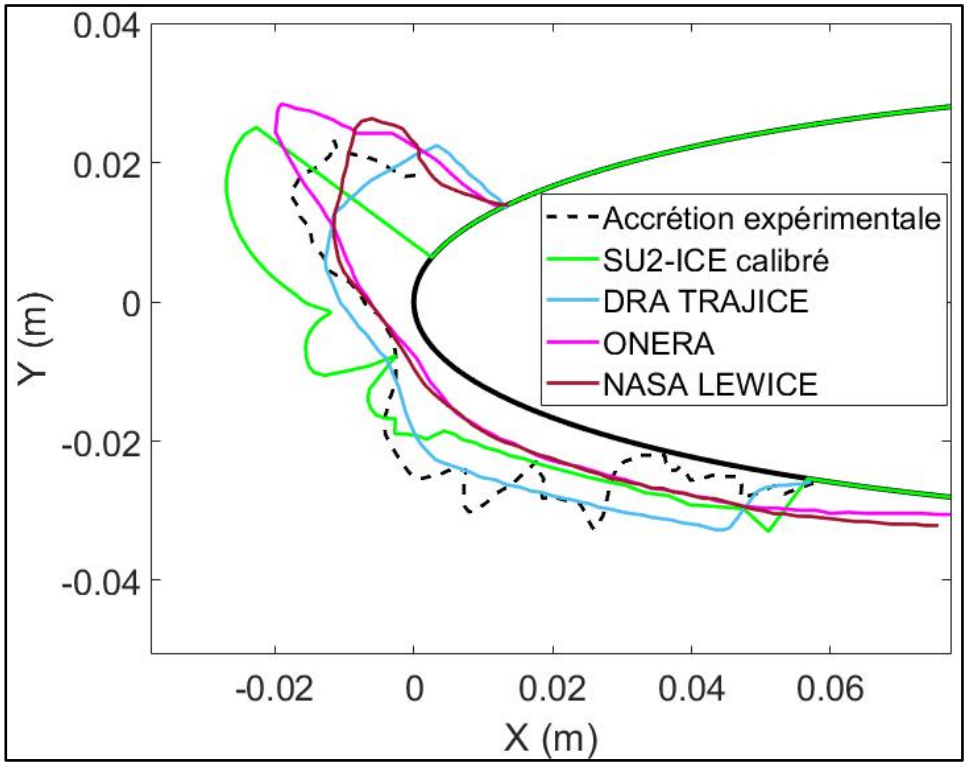

Figure 5.22 Comparaison entre SU2-ICE et les prédictions numériques de la littérature (cas NASA36)

Tableau 5.6 Comparaison des erreurs RMS entre les prédictions d'accrétions (NASA36)

Accrétion	**Erreur RMS (m)**
SU2-ICE calibré	5.28×10^{-3}
ONERA (1997)	3.45×10^{-3}
DRA (1997) TRAJICE	2.75×10^{-3}
NASA (1997) LEWICE	3.30×10^{-3}

5.5.4 Cas NASA30

Pour finir, un dernier cas test est étudié, le cas NASA30. Ce cas présente des conditions atmosphériques similaires aux cas NASA31 et NASA32 (Tableau 5.2), mais avec une température plus faible. Une base de données est à nouveau générée. La meilleure calibration est celle obtenue en retenant 52 points de contrôle dans la corne de l'accrétion expérimentale, comme illustré sur la Figure 5.23.

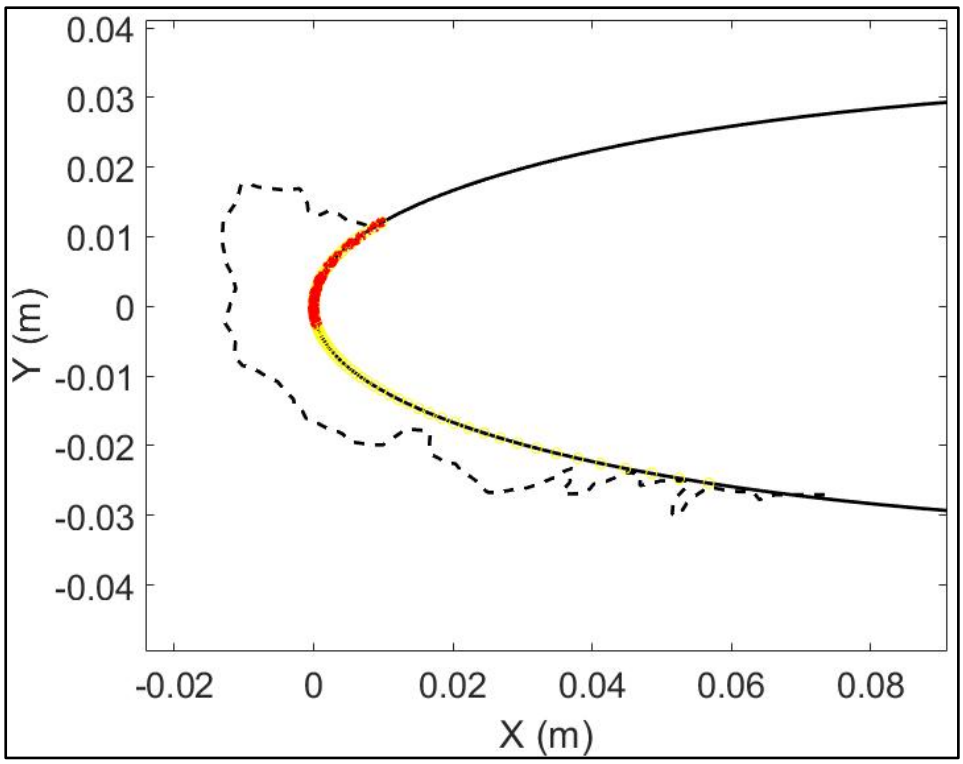

Figure 5.23 Points de contrôle (rouge) retenus pour la calibration NASA30

Les paramètres de rugosité calibrés calculés par le solveur Bayésien sont :

- k_0 = 3.2 mm;
- k_s/k = 5.9;
- α_p = 0.5;
- a = 0.023 m²;
- b = 0.039 m.

La distribution de hauteur de rugosité correspondante est illustrée sur la Figure 5.24.

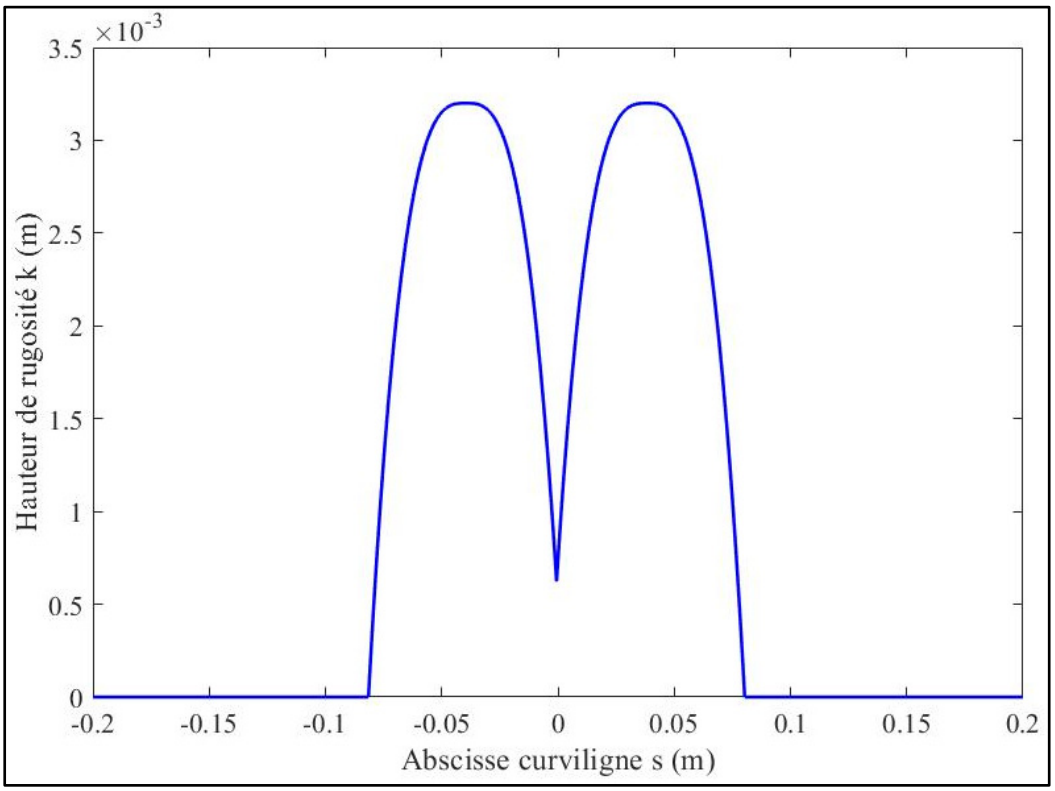

Figure 5.24 Distribution de rugosité calibrée pour le cas NASA30

L'accrétion obtenue avec ces paramètres de rugosité calibrés est tracée sur la Figure 5.25. L'erreur RMS (équation (5.5)) est de l'ordre de 1.9 mm, ce qui représente moins de 0.3% de la longueur de corde. Un retour à une accrétion moins épaisse, par rapport au cas NASA36, permet de retrouver une erreur RMS en dessous de 2 mm.

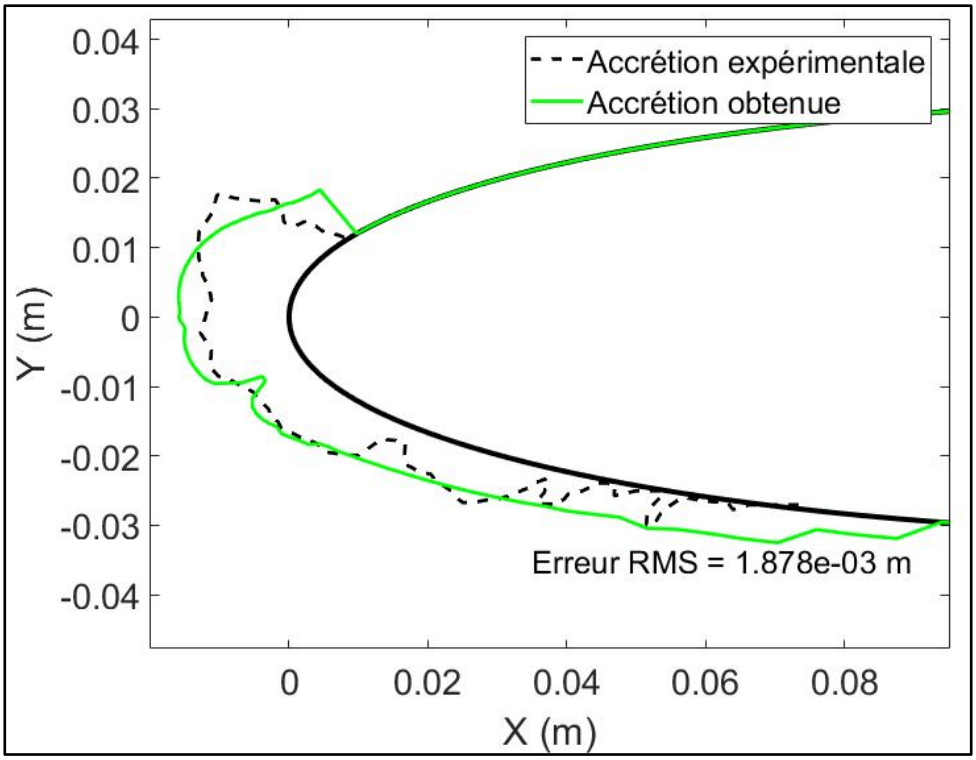

Figure 5.25 Accrétion calibrée obtenue avec SU2-ICE (cas NASA30)

Cette accrétion est maintenant comparée avec des prédictions de la littérature sur la Figure 5.26 : l'accrétion monocouche de Özgen et Canibek (2008), l'accrétion monocouche de la DRA et l'accrétion à quatre couches de la NASA. Ce quatrième cas test confirme à nouveau la capacité de SU2-ICE à prédire des accrétions similaires à celles de la littérature. La prédiction est également visuellement plus proche de la forme expérimentale comparée à l'accrétion monocouche de Özgen et Canibek. Il est intéressant de noter que toutes les accrétions présentent la même limite d'accrétion sur l'extrados, qui d'ailleurs coïncide avec la limite expérimentale. Les erreurs RMS sont une nouvelle fois comparées dans le Tableau 5.7, où il est possible de remarquer que SU2-ICE présente l'erreur RMS la plus basse parmi les accrétions comparées.

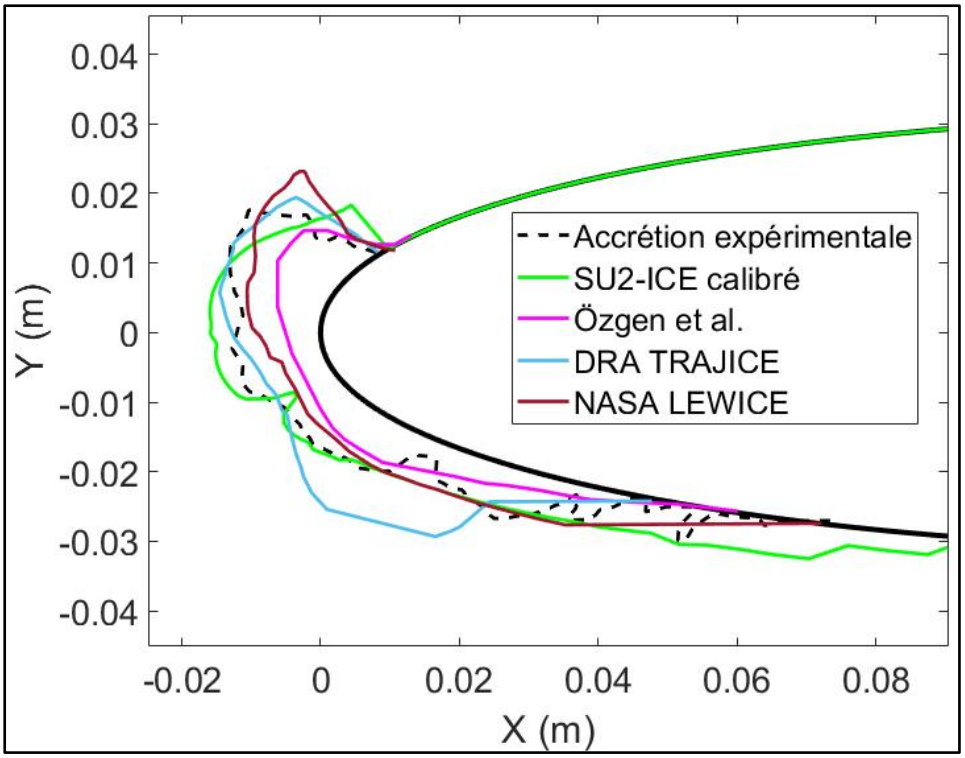

Figure 5.26 Comparaison entre SU2-ICE et les prédictions numériques de la littérature (cas NASA30)

Tableau 5.7 Comparaison des erreurs RMS entre les prédictions d'accrétions (NASA30)

Accrétion	**Erreur RMS (m)**
SU2-ICE calibré	1.88×10^{-3}
Özgen et Canibek (2008)	3.24×10^{-3}
DRA (1997) TRAJICE	2.12×10^{-3}
NASA (1997) LEWICE	2.17×10^{-3}

5.6 Bilan

Cette application de la méthodologie à une rugosité non uniforme a permis d'améliorer les prédictions d'accrétions avec SU2-ICE pour quatre cas de givre transparent (glaze ice). L'étude a permis de calibrer les paramètres de rugosité de façon plus fine que la rugosité uniforme du CHAPITRE 4, puisque des paramètres spatiaux et du modèle de correction thermique sont venus s'ajouter aux paramètres à calibrer.

La Figure 5.27 permet de rassembler les hauteurs de rugosité calibrées pour les quatre cas étudiés ici : NASA30, NASA31, NASA32 et NASA36. Le cas NASA36 présente une rugosité qui tranche avec les trois autres en raison des conditions d'écoulement, de contenu en eau liquide et de durée d'exposition qui sont différents (Tableau 5.2). La comparaison entre les trois cas NAS30, NASA31 et NASA32 est plus intéressante puisque les conditions sont strictement les mêmes à l'exception de la température ambiante : 266.3 K (NASA30), 269.1 K (NASA31) et 270.2 K (NASA32). La tendance qui se dessine est que la rugosité augmente lorsque la température diminue. Le cas le plus « chaud », le NASA32, présente la hauteur de rugosité la plus faible avec une zone restreinte complètement lisse autour du point de stagnation. Cette tendance est contraire, par exemple, aux relations empiriques comme celle de Shin et al. (1991) qui supposent une augmentation de la rugosité avec la température. La tendance qui se dessine, à savoir une diminution de la hauteur de rugosité avec la température reste à confirmer avec plus que trois cas test.

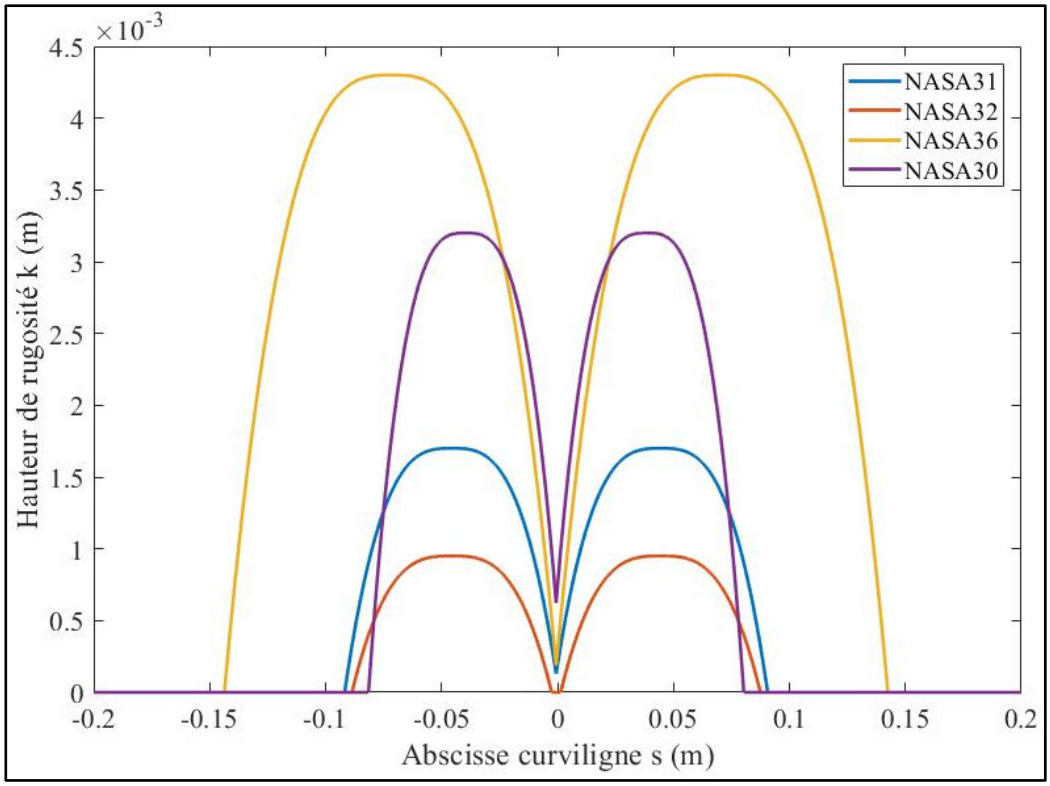

Figure 5.27 Comparaison des hauteurs de rugosité calibrées pour chaque cas test

Ce chapitre a permis de démontrer que la méthodologie développée durant ce Doctorat s'adapte à un changement de paramètres à calibrer. Il a mis en avant le potentiel de la méthode pour estimer des distributions de rugosité sur-mesure pour les cas tests simulés avec la chaîne de calcul SU2-CFD (RANS et 2PP) et SU2-ICE. Pour le moment, chaque cas test doit être calibré mais une extension possible du travail serait de calibrer plus de cas tests dans diverses conditions atmosphériques en vue d'explorer la création d'une corrélation permettant de prédire la distribution de rugosité à partir des paramètres atmosphériques.

CONCLUSION

Ce projet de Doctorat a permis de proposer, mettre au point et valider une méthodologie permettant d'estimer les paramètres de rugosité à imposer dans une simulation RANS de givrage aéronautique à la simple connaissance de la forme de glace expérimentale. Cet objectif a été atteint en subdivisant le projet en sous-objectifs. Tout d'abord, une étude de sensibilité en 2D a permis de se familiariser avec la dépendance d'une accrétion de glace à la rugosité de surface. Ce sous-objectif, thématique du CHAPITRE 2, a été atteint en implémentant une version 2D du modèle de givrage de Messinger puis en effectuant une étude de sensibilité par indices de Sobol. L'étude de sensibilité a été rendue possible grâce à la construction d'une base de données d'accrétions modélisée ensuite par un métamodèle de type chaos polynomial. Cette étude a permis de constater que la hauteur de rugosité était un paramètre clé dans la variabilité de la forme de glace. La comparaison de deux modèles de correction thermique a également montré la sensibilité des prédictions d'accrétions aux modèles employés. Face à cette sensibilité à la rugosité, il a été nécessaire d'implémenter une méthode de calibration de la rugosité pour pouvoir prédire efficacement les résultats expérimentaux, ce qui constitue le second-sous objectif du projet.

Ce second sous-objectif est abordé dans le CHAPITRE 3 où l'étude de sensibilité est complétée par une calibration de la rugosité via une inversion Bayésienne et un algorithme génétique. Dans le CHAPITRE 3, seul le transfert de chaleur est étudié en prévision de son impact sur le givrage. L'inversion Bayésienne est plus performante et facile d'utilisation que l'algorithme génétique puisqu'elle a nécessité moins de paramétrage manuel. L'inversion Bayésienne permet de calibrer une rugosité initialement inconnue pour retrouver un transfert de chaleur avec moins de 5% d'erreur relative par rapport aux résultats expérimentaux. La structure d'analyse et de calibration implémentée a montré son potentiel d'application dans ce chapitre. La calibration de la rugosité pour des accrétions de glace en 3D constituait naturellement la suite du projet.

Avant la calibration sur des géométries 3D, ou 2.5D, un solveur de givrage en 3D doit être développé. Celui-ci, baptisé SU2-ICE, et inspiré du Shallow Water Icing Model, est codé dans la structure de SU2-CFD. Ce travail d'implémentation prédit des formes de glace aéronautique, tout d'abord de givre blanc puis de givre transparent en passant par un ruissellement liquide sans glace. SU2-ICE a été mis à contribution dans le CHAPITRE 4 où la calibration par inversion Bayésienne est employée pour trouver la rugosité de surface permettant une bonne prédiction d'accrétion. La comparaison entre les prédictions et les accrétions expérimentales a permis de mettre en avant le potentiel de la méthode, même si l'hypothèse de rugosité constante employée montre certaines limites.

Le dernier sous-objectif propose une distribution de rugosité non-uniforme sur le profil d'aile pour s'affranchir de l'approximation de rugosité constante. Abordé dans le CHAPITRE 5, la rugosité non-uniforme permet d'améliorer les calibrations d'accrétions par rapport au chapitre précédent en proposant une distribution spatiale de rugosité dite cubique. Cette amélioration de la démarche se consacre à la calibration de cinq paramètres de rugosité au lieu de deux. Ce nombre de paramètres accru a permis d'obtenir des formes de glace présentant un accord visuel plus conforme et ayant une erreur quadratique moyenne de moins de 0.3% de la corde par rapport aux formes expérimentales. Le CHAPITRE 5 a permis de calibrer quatre cas tests, permettant de déterminer des paramètres de rugosité pour différentes conditions atmosphériques. Les bons résultats obtenus ont également montré la nécessité d'employer une distribution de rugosité non-uniforme pour prédire au mieux les accrétions réelles avec une approche monocouche.

Le projet bénéficie à la recherche en givrage dans la mesure où il est désormais possible de déterminer une rugosité sur-mesure pour un couple cas test/modèle. La méthodologie mise au point, en plus d'avoir permis l'implémentation d'un solveur de givrage dans le code libre de droits SU2-CFD, peut être employée telle quelle pour calibrer la rugosité dans un modèle RANS. Cela permettrait de s'affranchir des corrélations semi-empiriques en vigueur depuis plusieurs décennies et offrant des résultats parfois peu convaincants. À terme, cela peut permettre de mieux comprendre le phénomène de givrage qui est encore très complexe à

appréhender de par son caractère irrégulier, incertain et sensible aux conditions atmosphériques. Notamment, la compréhension des premiers instants du givrage avec l'apparition de la rugosité de surface sera accrue. Le givrage étant à l'origine d'accidents aériens, son étude poussée, aussi bien expérimentalement que numériquement comme ici, permet d'apporter une pierre à l'édifice en vue d'augmenter la sécurité aérienne, et continuer de faire du transport aérien le moyen de locomotion le plus sûr au monde.

RECOMMANDATIONS

Pour le moment, la méthode proposée nécessite une calibration systématique de chaque cas test de givrage étudié. Une investigation future serait de continuer dans cette voie en calibrant encore plus de cas tests de façon à générer une base de données de paramètres de rugosité, et ainsi pouvoir extraire une corrélation, via un métamodèle, liant la rugosité aux conditions atmosphériques et d'écoulement. Cette corrélation serait la signature du comportement des codes SU2-CFD (2PP notamment) et SU2-ICE, ce qui permettrait de pouvoir prédire la rugosité à imposer dans le modèle à la simple connaissance des conditions atmosphériques sans déployer la méthode de calibration actuelle à chaque fois. Il s'agirait ainsi de proposer une nouvelle corrélation semi-empirique de rugosité, mais développée spécifiquement pour SU2-CFD et SU2-ICE. Pour cet axe de recherche, la méthodologie consisterait à utiliser la méthodologie du CHAPITRE 5 sur une vingtaine de cas de givre transparent. Ce travail permettra d'estimer une vingtaine de paramètres de rugosité calibrés k, k_s/k, α_p, a et b. Par la suite, l'utilisation d'un métamodèle de type chaos polynomial permettra de mettre en relation ces paramètres calibrés avec les conditions atmosphériques et ainsi tenter de trouver une corrélation entre les données atmosphériques et les paramètres de rugosité. Il est à noter que le métamodèle généré pourra lui-même faire office de corrélation et être utilisé comme moyen de calculer la rugosité pour n'importe quelles conditions atmosphériques. Le métamodèle sera ainsi l'outil qui prendra en entrée les paramètres atmosphériques (température, contenu en eau liquide, vitesse, …) et renverra instantanément les valeurs de k, k_s/k, α_p, a et b à imposer dans la simulation RANS avec la correction 2PP et SU2-ICE. Une autre piste à explorer serait l'utilisation d'autres géométries que le NACA0012.

Concernant SU2-ICE, l'implémentation effectuée est entièrement 3D. Néanmoins, le travail mené durant cette thèse s'est principalement concentré sur des applications en 2.5D, avec une seule cellule dans la direction de l'envergure. Il serait intéressant de tester le code sur une géométrie pleinement 3D. Autre piste de réflexion, l'impact des gouttelettes est pour le moment fourni au code sous forme de fichier d'entrée. Coupler SU2-ICE avec un solveur de calcul d'impact des gouttelettes permettrait d'améliorer la prédiction de l'efficacité de

captation, mais aussi de pouvoir aborder d'autres géométries dont les données d'impact ne sont pas a priori connues. Enfin, la simulation de givrage multicouches, dont les options ont déjà été implémentes dans SU2-ICE, serait une étape importante vers l'amélioration du code. Cette évolution du code nécessiterait au préalable de finaliser le solveur de calcul d'impact des gouttelettes ainsi que le traitement de déformation du maillage entre chaque couche. Pour l'heure, SU2-ICE génère un fichier de sortie contenant les nouvelles coordonnées de la surface et exploitable par l'outil de déformation SU2-DEF. La déformation de maillage fonctionne mais reste cantonnée aux accrétions très régulières. Améliorer SU2-DEF pour traiter des accrétions fortement irrégulières permettrait de contribuer au succès de l'approche multicouches.

Finalement, les études de sensibilité menées dans cette thèse se concentraient sur la rugosité. Cependant, et comme testé dans la section 2.5.3.2, il est possible d'étudier la sensibilité d'une accrétion à d'autres paramètres comme par exemple les conditions atmosphériques. Poursuivre le travail au-delà de l'accrétion seule, avec par exemple le calcul de performance (portance, trainée, finesse, séparation…) d'une aile givrée pourrait permettre en bout de chaîne d'étudier la sensibilité des performances aérodynamiques aux conditions atmosphériques givrantes.

ANNEXE I

GRID CONVERGENCE STUDY MAIN RESULTS (CHAPITRE 3)

This appendix sums up the main results obtained during the mesh convergence study. Three meshes are used for a channel simulation (a coarse (1), a medium (2) and a fine (3)). The roughness parameters used are k = 0.5 mm and k_s = 1.55 mm. The mesh convergence methodology suggested by (Celik et al., 2008) is used to compute the convergence order p and the Grid Convergence Index (GCI). The flow quantities monitored are h_c at three locations: x = 0.16 m, x = 0.46 m and x = 0.80 m. The results are gathered in Table-A I-1.

Table-A I-1 Convergence orders and GCIs values

	h_c *(x=0.16m)*	h_c *(x=0.46m)*	h_c *(x=0.8 m)*
p	0.7	1.7	2.1
GCI^{21}	0.9%	0.2%	0.1%
GCI^{32}	1.4%	0.7%	0.5%

Table-A I-1 shows low GCIs, mainly below 1% except for one which is at 1.4%. For instance, for the monitored h_c at 0.8 m on the fine mesh, the interpretation of the GCI value is that the uncertainty on the monitored h_c due to the mesh refinement is 0.1%. Applying the same interpretation for each value denotes a satisfactory mesh convergence study. To be conservative and confident about the quality of the CFD results, even with the various roughness patterns planned to be run, the fine mesh is retained for the rest of the process.

ANNEXE II

VÉRIFICATION DE SU2-ICE POUR LES CAS DE GIVRE BLANC (RIME) ET LIQUIDE

En plus des cas de givre transparent (glaze ice), SU2-ICE est en capacité de simuler des accrétions de givre blanc (rime ice) à plus basse température sans film liquide et des films liquides ruisselants sans glace lorsque la température est plus haute que le point de congélation. Ces deux cas sont vérifiés ici. La configuration numérique utilisée est la même que celle décrite pour le givre transparent dans la section 4.6.1 et seules les conditions atmosphériques et d'exposition ont été modifiées. Le Tableau-A II-1 regroupe les conditions de ces cas test. Le cas NASA28 correspond à un cas documenté tandis que le cas liquide a été créé pour s'assurer que le film ruisselait de façon convenable. Le profil NACA0012 a été employé sans rugosité.

Tableau-A II-1 Conditions pour les cas de givre blanc et liquide

	NASA28 (givre blanc)	**Liquide**
Température ambiante	253.2 K	288.15 K
Pression ambiante	95 610 Pa	100 000 Pa
Corde du NACA0012	0.5334 m	0.5334 m
Angle d'attaque	4°	0°
Vitesse d'écoulement (Mach)	58.1 m/s (0.182)	102.8 m/s (0.302)
Contenu en eau liquide (LWC)	1.30 g/m^3	1.00 g/m^3
Diamètre median des gouttelettes (MVD)	20 µm	20 µm
Temps total d'exposition	480 s	2 s

La forme de glace obtenue dans le cas NASA28 est illustrée sur la Figure-A II-1. La comparaison y est effectuée avec l'accrétion expérimentale ainsi que les accrétions multicouches de la DRA (4 couches), de la NASA (2 couches) et de Özgen et Canibek (4 couches) (Özgen & Canıbek, 2008; Wright, Gent, et al., 1997). L'accrétion prédite par SU2-ICE est satisfaisante compte-tenu de la simulation monocouche. La simulation permet également d'obtenir une épaisseur de film liquide nulle en tout point du profil.

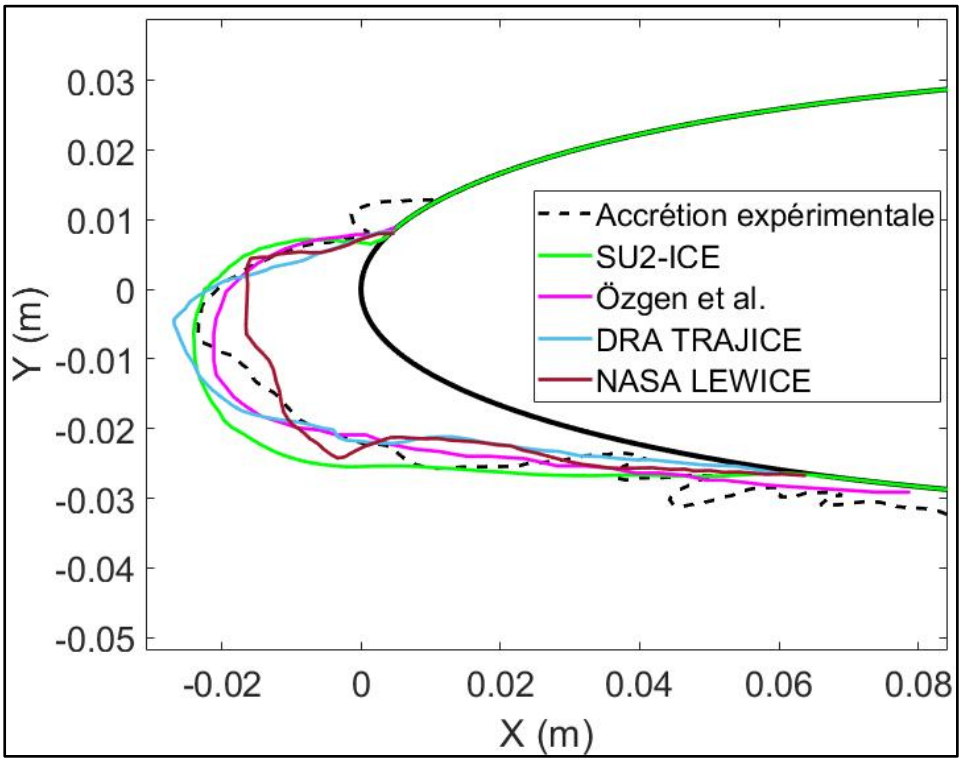

Figure-A II-1 Comparaison de l'accrétion SU2-ICE avec la littérature (cas NASA28)

Le cas liquide est l'étape importante permettant de vérifier le ruissellement sur la géométrie. La vérification est satisfaisante si le film ruisselle dans la bonne direction en sortant de la zone d'impact des gouttelettes. La Figure-A II-2 présente l'épaisseur de film liquide à différents instants (0.5 s, 1 s, 1.5 s et 2 s), ce qui permet de visualiser l'avancement du film dans le temps. L'efficacité de captation est également tracée pour montrer que le film sort bel et bien de la zone d'impact. Le comportement observé est conforme à ce qui est attendu avec un film qui

ruisselle graduellement dans la direction d'écoulement, vers le bord de fuite. Il n'y a aucune glace formée, ce qui est rassurant à 15°C.

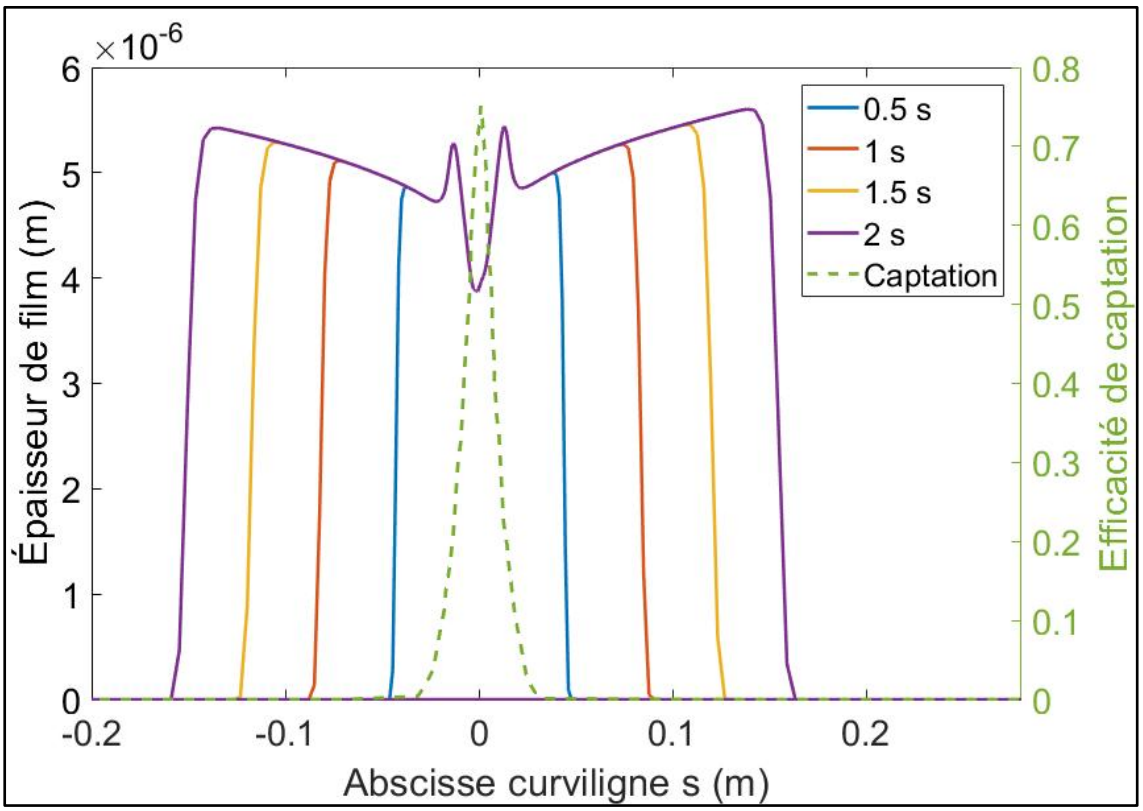

Figure-A II-2 Évolution du film liquide dans le temps (cas liquide)

ANNEXE III

ESSAIS DE CALIBRATIONS AVEC RUGOSITÉ NON UNIFORME (CAS NASA31)

Cette Annexe présente les accrétions de glace obtenues pour le cas NASA31 en utilisant différentes configurations de points de calibration, correspondant aux calibrations #5-1, #5-2, #5-3, #5-4 et #5-5 (voir CHAPITRE 5, Tableau 5.3). Les Figure-A III-1 à Figure-A III-5 montrent les formes de glaces, en incluant les erreurs RMS correspondantes.

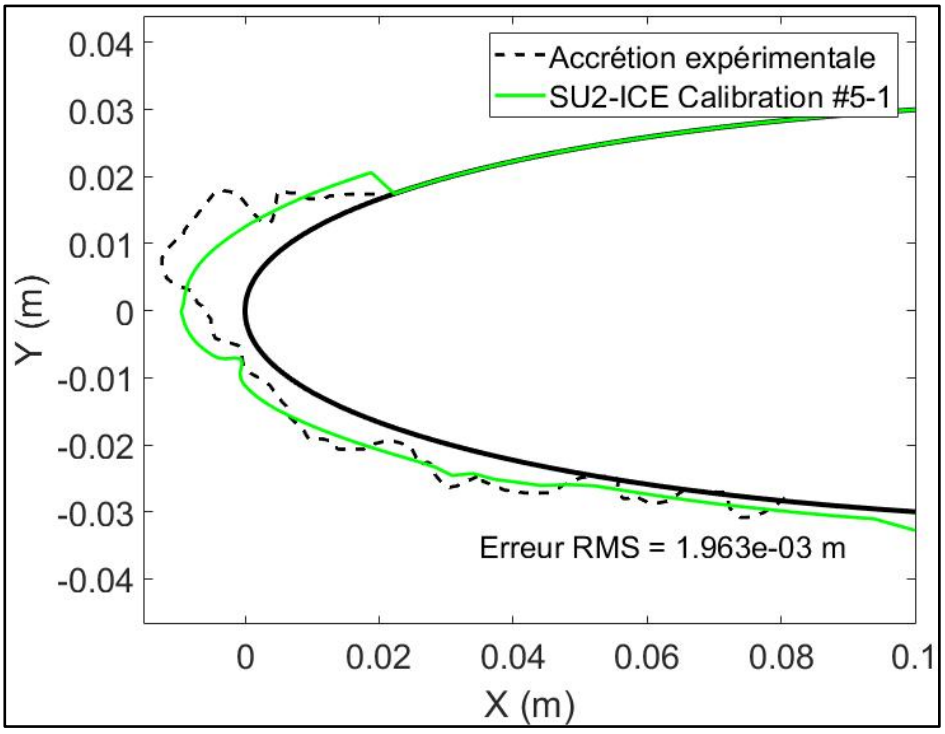

Figure-A III-1 Accrétion obtenue, calibration #5-1

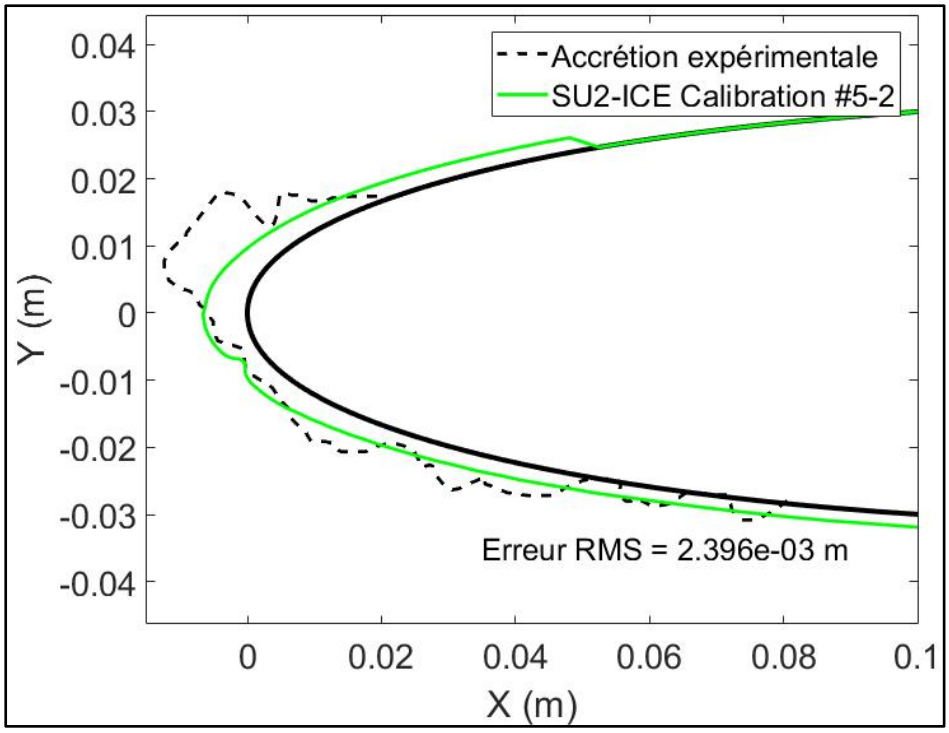

Figure-A III-2 Accrétion obtenue, calibration #5-2

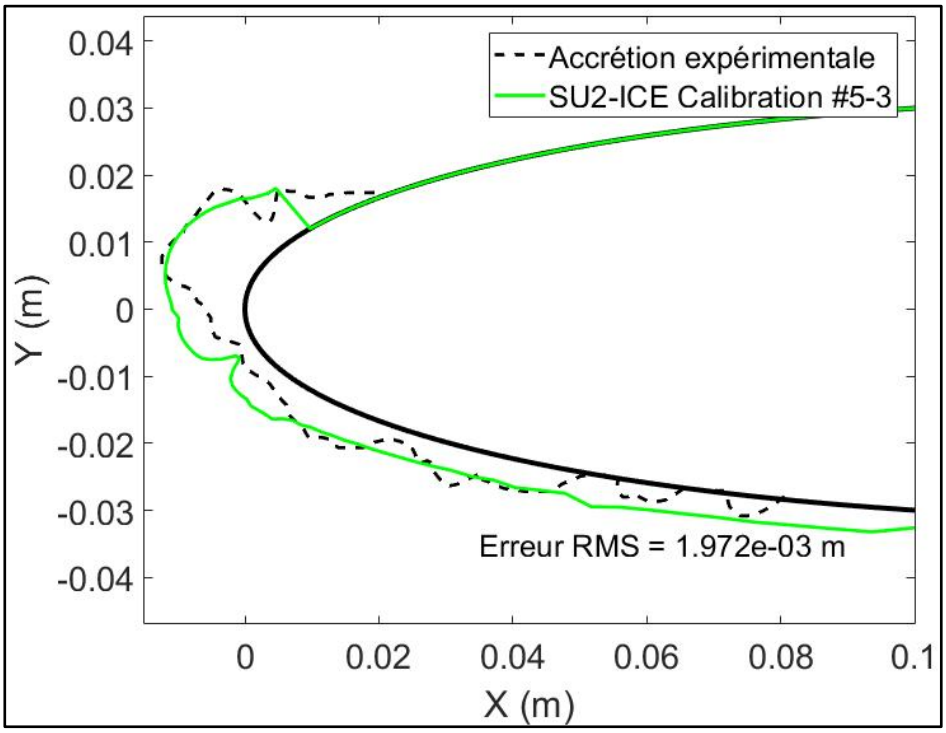

Figure-A III-3 Accrétion obtenue, calibration #5-3

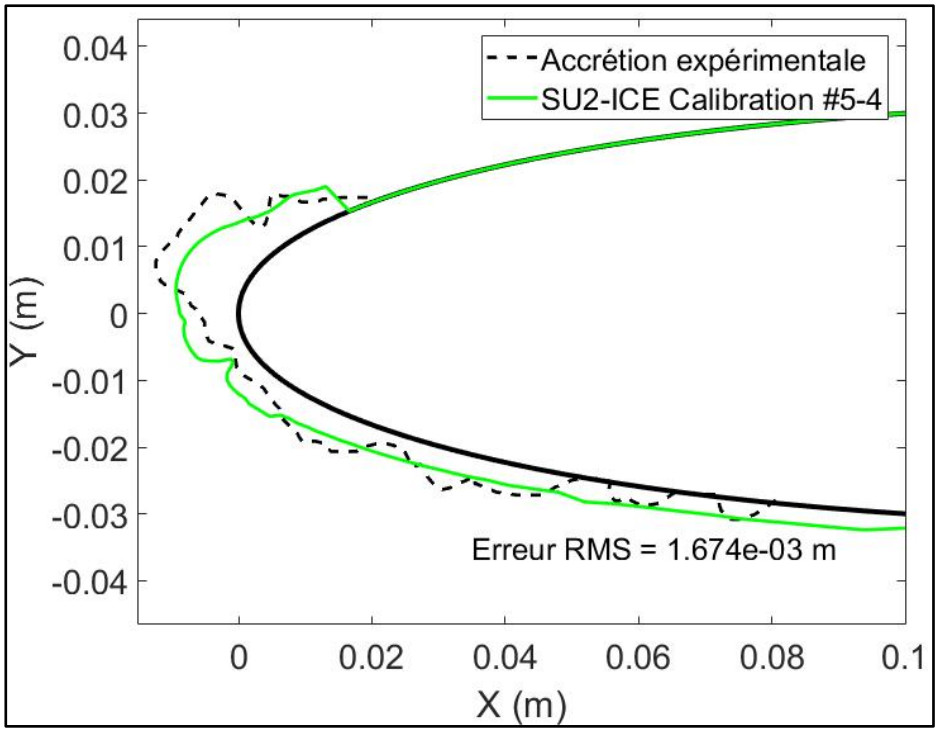

Figure-A III-4 Accrétion obtenue, calibration #5-4

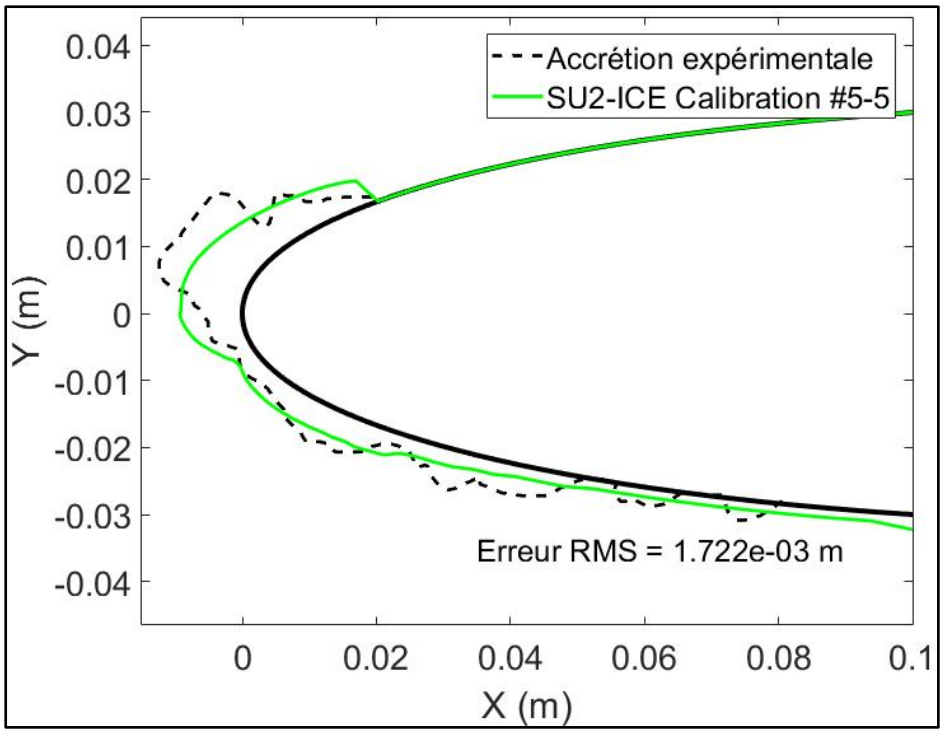

Figure-A III-5 Accrétion obtenue, calibration #5-5

LISTE DE RÉFÉRENCES BIBLIOGRAPHIQUES

Aghaei Jouybari, M., Junlin, Y., Brereton, G. J., & Murillo, M. S. (2021). Data-driven prediction of the equivalent sand-grain height in rough-wall turbulent flows. *Journal of Fluid Mechanics, 912*, A8 (23 pp.). doi: 10.1017/jfm.2020.1085. Repéré à http://dx.doi.org/10.1017/jfm.2020.1085

Akbal, O., Ayan, E., Murat, C., & Ozgen, S. (2023). *In Flight Ice Shape Prediction with Data Fit Surrogate Models*. doi: 10.4271/2023-01-1480. Repéré à https://doi.org/10.4271/2023-01-1480

Anderson, D., & Shin, J. (1997). *Characterization of ice roughness from simulated icing encounters* présentée à AIAA 35th Aerospace Sciences Meeting and Exhibit, Reno, NV. doi: 10.2514/6.1997-52. Repéré à https://arc.aiaa.org/doi/abs/10.2514/6.1997-52

Andersson, J., Oliveira, D. R., Yeginbayeva, I., Leer-Andersen, M., & Bensow, R. E. (2020). Review and comparison of methods to model ship hull roughness. *Applied Ocean Research, 99*, 102119. doi: 10.1016/j.apor.2020.102119. Repéré à https://www.sciencedirect.com/science/article/pii/S0141118719308946

Ansys. (2014). ANSYS FENSAP-ICE Capabilities: Ansys.

ANSYS. (2020). *ANSYS FENSAP-ICE User Manual*. Canonsburg, PA, USA.

Aupoix, B. (2015). Improved heat transfer predictions on rough surfaces. *International Journal of Heat and Fluid Flow, 56*(1), 160-171. doi: 10.1016/j.ijheatfluidflow.2015.07.007

Aupoix, B. (2016). Revisiting the Discrete Element Method for Predictions of Flows over Rough Surfaces. *Journal of Fluids Engineering, Transactions of the ASME, 138*(3). doi: 10.1115/1.4031558. Repéré à http://dx.doi.org/10.1115/1.4031558

Aupoix, B., & Spalart, P. R. (2003). Extensions of the Spalart–Allmaras turbulence model to account for wall roughness. *International Journal of Heat and Fluid Flow, 24*(4), 454-462. doi: 10.1016/S0142-727X(03)00043-2. Repéré à http://www.sciencedirect.com/science/article/pii/S0142727X03000432

Ayan, E., & Ozgen, S. (2017). *Modification of the Extended Messinger Model for Mixed Phase Icing and Industrial Applications with TAICE* présentée à 9th AIAA Atmospheric and Space Environments Conference.

Baghel, A. P., Sotomayor-Zakharov, D., Knop, I., & Ortwein, H.-P. (2023). *Detailed Study of Photogrammetry Technique as a Valid Ice Accretion Measurement Method*. doi: 10.4271/2023-01-1411. Repéré à https://doi.org/10.4271/2023-01-1411

Baker, N., Kelly, G., & O'Sullivan, P. D. (2020). A grid convergence index study of mesh style effect on the accuracy of the numerical results for an indoor airflow profile. *International Journal of Ventilation, 19*(4), 300-314. doi: 10.1080/14733315.2019.1667558. Repéré à https://doi.org/10.1080/14733315.2019.1667558

Baumert, A., Bansmer, S., Trontin, P., & Villedieu, P. (2018). Experimental and numerical investigations on aircraft icing at mixed phase conditions. *International Journal of Heat and Mass Transfer, 123*, 957-978. doi: https://doi.org/10.1016/j.ijheatmasstransfer.2018.02.008. Repéré à https://www.sciencedirect.com/science/article/pii/S0017931017332684

Beaugendre, H. (2003). *A PDE-based 3D approach to in-flight ice accretion* (McGill University, Montréal).

Beaugendre, H., Morency, F., Habashi, W. G., & Benquet, P. (2003). Roughness Implementation in FENSAP-ICE: Model Calibration and Influence on Ice Shapes. *Journal of Aircraft, 40*(6), 1212-1215. doi: 10.2514/2.7214. Repéré à https://arc.aiaa.org/doi/abs/10.2514/2.7214

Bennani, L., Trontin, P., Chauvin, R., & Villedieu, P. (2020). A non-overlapping optimized Schwarz method for the heat equation with non linear boundary conditions and with applications to de-icing. *Computers & Mathematics with Applications, 80*(6), 1500-1522. doi: https://doi.org/10.1016/j.camwa.2020.07.017. Repéré à https://www.sciencedirect.com/science/article/pii/S0898122120302832

Bennani, L., Villedieu, P., Salaun, M., & Trontin, P. (2014). Numerical simulation and modeling of ice shedding: Process initiation. *Computers & Structures, 142*, 15-27. doi: 10.1016/j.compstruc.2014.06.001. Repéré à http://www.sciencedirect.com/science/article/pii/S0045794914001333

Biswal, B. B., Sarkar, B. K., & Mahanta, P. (2020). *Advances in Mechanical Engineering: Select Proceedings of ICRIDME 2018*. Springer Nature Singapore. Repéré à https://books.google.ca/books?id=wtXKDwAAQBAJ

Blatman, G., & Sudret, B. (2010). An adaptive algorithm to build up sparse polynomial chaos expansions for stochastic finite element analysis. *Probabilistic Engineering Mechanics, 25*(2), 183-197. doi: https://doi.org/10.1016/j.probengmech.2009.10.003. Repéré à http://www.sciencedirect.com/science/article/pii/S0266892009000666

Blazek, J. (2005). *Computational Fluid Dynamics: Principles and Applications* (Second Edition éd.). Elsevier.

Bons, J. P. (2002). St and cf Augmentation for Real Turbine Roughness With Elevated Freestream Turbulence. *Journal of Turbomachinery, 124*(4), 632-644. doi: 10.1115/1.1505851. Repéré à https://doi.org/10.1115/1.1505851

Bons, J. P. (2010). A review of surface roughness effects in gas turbines. *Journal of Turbomachinery, 132*(2). doi: 10.1115/1.3066315. Repéré à http://dx.doi.org/10.1115/1.3066315

Botros, K. K. (2016). Experimental Investigation into the Relationship between the Roughness Height in Use with Nikuradse or Colebrook Roughness Functions and the Internal Wall Roughness Profile for Commercial Steel Pipes. *Journal of Fluids Engineering, Transactions of the ASME, 138*(8). doi: 10.1115/1.4032601. Repéré à http://dx.doi.org/10.1115/1.4032601

Bourgault-Cote, S., Docampo-Sánchez, J., & Laurendeau, E. (2018). *Multi-Layer Ice Accretion Simulations Using a Level-Set Method With B-Spline Representation* présentée à 2018 AIAA Aerospace Sciences Meeting. doi: 10.2514/6.2018-1835. Repéré à https://arc.aiaa.org/doi/abs/10.2514/6.2018-1835

Bourgault, Y., Beaugendre, H., & Habashi, W. G. (2000). Development of a Shallow-Water Icing Model in FENSAP-ICE. *Journal of Aircraft, 37*(4), 640-646. doi: 10.2514/2.2646

Bragg, M. B., Broeren, A. P., & Blumenthal, L. A. (2005). Iced-airfoil aerodynamics. *Progress in Aerospace Sciences, 41*(5), 323-362. doi: 10.1016/j.paerosci.2005.07.001

Brent, R. (2002). Algorithms For Minimization Without Derivatives. *Englewood Cliffs, Prentice Hall, 19*. doi: 10.2307/2005713

Caccia, F., & Guardone, A. (2023). Numerical simulations of ice accretion on wind turbine blades: are performance losses due to ice shape or surface roughness? *Wind Energy Science, 8*(3), 341-362. doi: 10.5194/wes-8-341-2023. Repéré à http://dx.doi.org/10.5194/wes-8-341-2023

Cao, Y., Ma, C., Zhang, Q., & Sheridan, J. (2012). Numerical simulation of ice accretions on an aircraft wing. *Aerospace Science and Technology, 23*(1), 296-304. doi: https://doi.org/10.1016/j.ast.2011.08.004. Repéré à http://www.sciencedirect.com/science/article/pii/S127096381100126X

Cao, Y., Tan, W., & Wu, Z. (2018a). Aircraft icing: An ongoing threat to aviation safety. *Aerospace Science and Technology, 75*, 353-385. doi: 10.1016/j.ast.2017.12.028. Repéré à https://www.sciencedirect.com/science/article/pii/S1270963817317601

Cao, Y., Tan, W., & Wu, Z. (2018b). *Aircraft icing: An ongoing threat to aviation safety* (Vol. 75). doi: 10.1016/j.ast.2017.12.028

Celik, I., Ghia, U., Roache, P. J., Freitas, C., Coloman, H., & Raad, P. (2008). Procedure of Estimation and Reporting of Uncertainty Due to Discretization in CFD Applications. *J. Fluids Eng., 130*, 078001. doi: 10.1115/1.2960953

Chan, K., Saltelli, A., & Tarantola, S. (1997). Sensitivity Analysis of Model Output: Variance-based Methods Make the Difference. Dans (pp. 261-268). doi: 10.1109/WSC.1997.640407

Chedevergne, F. (2018). Analytical wall function including roughness corrections. *International Journal of Heat and Fluid Flow, 73*, 258-269. doi: 10.1016/j.ijheatfluidflow.2018.08.001. Repéré à http://www.sciencedirect.com/science/article/pii/S0142727X17310391

Chedevergne, F. (2021). A double-averaged Navier-Stokes k -ω turbulence model for wall flows over rough surfaces with heat transfer. *Journal of Turbulence, 22*(11), 713-734. doi: 10.1080/14685248.2021.1973014. Repéré à http://dx.doi.org/10.1080/14685248.2021.1973014

Chedevergne, F. (2023). Modeling rough walls from surface topography to double averaged Navier-Stokes computation. *Journal of Turbulence, 24*(1-2), 36-56. doi: 10.1080/14685248.2023.2173760. Repéré à https://doi.org/10.1080/14685248.2023.2173760

Chen, W., & Jin, R. (2005). Analytical Variance-Based Global Sensitivity Analysis in Simulation-Based Design Under Uncertainty. *Journal of Mechanical Design, 127*(5). doi: 10.1115/1.1904642

Cinnella, P., Congedo, P. M., Parussini, L., & Pediroda, V. (2010). Quantification of Thermodynamic Uncertainties in Real Gas Flows. *International Journal of Engineering Systems Modelling and Simulation, 2*. doi: 10.1504/IJESMS.2010.031867

Cinquegrana, D., D'Aniello, F., de Rosa, D., Carozza, A., Catalano, P., & Mingione, G. (2023). *A CIRA 3D Ice Accretion Code for Multiple Cloud Conditions Simulations*. doi: 10.4271/2023-01-1461. Repéré à https://doi.org/10.4271/2023-01-1461

Colebrook, C. F., White, C. M., & Taylor, G. I. (1937). Experiments with fluid friction in roughened pipes. *Proceedings of the Royal Society of London. Series A - Mathematical and Physical Sciences, 161*(906), 367-381. doi: 10.1098/rspa.1937.0150. Repéré à https://royalsocietypublishing.org/doi/abs/10.1098/rspa.1937.0150

Committee, S. E. (2023). *Surface Texture*. SAE International. doi: 10.4271/J448_202302. Repéré à https://doi.org/10.4271/J448_202302

Conn, A. R., Gould, N. I. M., & Toint, P. (1991). A Globally Convergent Augmented Lagrangian Algorithm for Optimization with General Constraints and Simple Bounds. *SIAM Journal on Numerical Analysis, 28*(2), 545-572. doi: 10.1137/0728030. Repéré à https://epubs.siam.org/doi/abs/10.1137/0728030

Conversy, S., Chatty, S., Gaspard-Boulinc, H., & Vinot, J.-L. (2014, 2014-10-28). *The Accident of Flight AF447 Rio-Paris: a Case Study for HCI Research* présentée à IHM'14, 26e conférence francophone sur l'Interaction Homme-Machine, Lille, France.

Croce, G., Candido, E. D., Habashi, W., Aubé, M., & Baruzzi, G. (2009). *FENSAP-ICE: Numerical Prediction of In-flight Icing Roughness Evolution* présentée à 1st AIAA Atmospheric and Space Environments Conference, San Antonio, Texas. doi: 10.2514/6.2009-4126. Repéré à https://arc.aiaa.org/doi/abs/10.2514/6.2009-4126

Da Ronch, A., Panzeri, M., Drofelnik, J., & d'Ippolito, R. (2020). Sensitivity and calibration of turbulence model in the presence of epistemic uncertainties. *CEAS Aeronautical Journal, 11*(1), 33-47. doi: 10.1007/s13272-019-00389-y. Repéré à https://doi.org/10.1007/s13272-019-00389-y

Dai, H., Zhu, C., Zhao, H., & Liu, S. (2021). A New Ice Accretion Model for Aircraft Icing Based on Phase-Field Method. *Applied Sciences, 11*(12), 5693. Repéré à https://www.mdpi.com/2076-3417/11/12/5693

De Marchis, M. (2016). Large eddy simulations of roughened channel flows: Estimation of the energy losses using the slope of the roughness. *Computers & Fluids, 140*, 148-157. doi: 10.1016/j.compfluid.2016.09.021. Repéré à http://dx.doi.org/10.1016/j.compfluid.2016.09.021

de Rosa, D., Capizzano, F., & Cinquegrana, D. (2023). *Multi-step Ice Accretion by Immersed Boundaries*. doi: 10.4271/2023-01-1484. Repéré à https://doi.org/10.4271/2023-01-1484

DeGennaro, A. M., Rowley, C. W., & Martinelli, L. (2015). Uncertainty Quantification for Airfoil Icing Using Polynomial Chaos Expansions. *Journal of Aircraft, 52*(5), 1404-1411. doi: 10.2514/1.c032698. Repéré à https://arc.aiaa.org/doi/abs/10.2514/1.C032698

Dipprey, D. F., & Sabersky, R. H. (1963). Heat and momentum transfer in smooth and rough tubes at various prandtl numbers. *International Journal of Heat and Mass Transfer, 6*(5), 329-353. doi: 10.1016/0017-9310(63)90097-8. Repéré à https://www.sciencedirect.com/science/article/pii/0017931063900978

Dirling, R. (1973). *A method for computing roughwall heat transfer rates on reentry nosetips* présentée à 8th Thermophysics Conference. doi: 10.2514/6.1973-763. Repéré à https://arc.aiaa.org/doi/abs/10.2514/6.1973-763

Dukhan, N., Masiulaniec, K. C., Dewitt, K. J., & Fossen, G. J. V. (1999a). Acceleration Effect on the Stanton Number for Castings of Ice-Roughened Surfaces. *Journal of Aircraft, 36*(5), 896-898. doi: 10.2514/2.2527. Repéré à https://arc.aiaa.org/doi/abs/10.2514/2.2527

Dukhan, N., Masiulaniec, K. C., Dewitt, K. J., & Fossen, G. J. V. (1999b). Experimental Heat Transfer Coefficients from Ice-Roughened Surfaces for Aircraft Deicing Design. *Journal of Aircraft, 36*(6), 948-956. doi: 10.2514/2.2556. Repéré à https://arc.aiaa.org/doi/abs/10.2514/2.2556

Durbin, P. A., Medic, G., Seo, J. M., Eaton, J. K., & Song, S. (2001). Rough wall modification of two-layer k-ε. *Transactions of the ASME. Journal of Fluids Engineering, 123*(1), 16-21. doi: 10.1115/1.1343086. Repéré à http://dx.doi.org/10.1115/1.1343086

Economon, T. D., Palacios, F., Copeland, S. R., Lukaczyk, T. W., & Alonso, J. J. (2015). SU2: An Open-Source Suite for Multiphysics Simulation and Design. *AIAA Journal, 54*(3), 828-846. doi: 10.2514/1.J053813

Esmaeilifar, E., Raj, L., & Myong, R. S. (2022). Computational simulation of aircraft electrothermal de-icing using an unsteady formulation of phase change and runback water in a unified framework. *Aerospace Science and Technology, 130*, 107936. doi: 10.1016/j.ast.2022.107936. Repéré à https://www.sciencedirect.com/science/article/pii/S1270963822006101

FAA. (2006). Introduction to Icing Certification. Repéré à http://lessonslearned.faa.gov/AmericanEagle/Intro_to_Icing_Certification.pdf

FAA. (2007). *Advisory Circular : Certification of part 23 airplanes for flight in icing conditions*. (23.1419-2D). Repéré à https://www.faa.gov/documentLibrary/media/Advisory_Circular/AC_23.1419-2D_Incl_Chg_1.pdf.

FAA. (2016). Resulting Safety Initiatives. Repéré à http://lessonslearned.faa.gov/ll_main.cfm?TabID=3&LLID=37&LLTypeID=10

Flack, K. A., & Schultz, M. P. (2010). Review of Hydraulic Roughness Scales in the Fully Rough Regime. *Journal of Fluids Engineering, 132*(4). doi: 10.1115/1.4001492. Repéré à https://doi.org/10.1115/1.4001492

Forooghi, P., Stroh, A., Schlatter, P., & Frohnapfel, B. (2018). Direct numerical simulation of flow over dissimilar, randomly distributed roughness elements: a systematic study on the effect of surface morphology on turbulence. *Physical Review Fluids, 3*(4). doi: 10.1103/PhysRevFluids.3.044605. Repéré à http://dx.doi.org/10.1103/PhysRevFluids.3.044605

Fortin, G. (2019). *Equivalent Sand Grain Roughness Correlation for Aircraft Ice Shape Predictions*. doi: 10.4271/2019-01-1978. Repéré à https://doi.org/10.4271/2019-01-1978

Fortin, G., Laforte, J.-L., & Ilinca, A. (2006). Heat and mass transfer during ice accretion on aircraft wings with an improved roughness model. *International Journal of Thermal Sciences, 45*(6), 595-606. doi: 10.1016/j.ijthermalsci.2005.07.006. Repéré à https://www.sciencedirect.com/science/article/pii/S1290072905001754

Fossati, M., Khurram, R. A., & Habashi, W. G. (2012). An ALE mesh movement scheme for long-term in-flight ice accretion. *International Journal for Numerical Methods in Fluids, 68*(8), 958-976. doi: doi:10.1002/fld.2588. Repéré à https://onlinelibrary.wiley.com/doi/abs/10.1002/fld.2588

Fujiwara, G. E. C., Bragg, M. B., & Broeren, A. P. (2020). Comparison of Computational and Experimental Ice Accretions of Large Swept Wings. *Journal of Aircraft, 57*(2), 342-359. doi: 10.2514/1.c035631. Repéré à https://arc.aiaa.org/doi/abs/10.2514/1.C035631

Gallia, M., Bellosta, T., & Guardone, A. (2023). Automatic roughness characterization of simulated ice shapes. *Journal of Computational and Applied Mathematics, 427*, 115114. doi: https://doi.org/10.1016/j.cam.2023.115114. Repéré à https://www.sciencedirect.com/science/article/pii/S0377042723000584

Gao, H., Li, X., Nezhad, A. H., & Behshad, A. (2022). Numerical simulation of the flow in pipes with numerical models. *Structural Engineering and Mechanics, 81*(4), 523-527. doi: 10.12989/sem.2022.81.4.523. Repéré à http://dx.doi.org/10.12989/sem.2022.81.4.523

Gent, R., Markiewicz, R., & Cansdale, J. (1987). Further Studies of Helicopter Rotor Ice Accretion and Protection. *Vertica, 11*, 473-492.

Ghanadi, F., & Djenidi, L. (2022). Study of a rough-wall turbulent boundary layer under pressure gradient. *Journal of Fluid Mechanics, 938*. doi: 10.1017/jfm.2022.156. Repéré à http://dx.doi.org/10.1017/jfm.2022.156

Goldberg, D. E. (1989). *Genetic Algorithms in Search, Optimization and Machine Learning*. Addison-Wesley Longman Publishing Co., Inc.

Gori, G., Bellosta, T., & Guardone, A. (2023). Numerical Simulation of In-Flight Icing Under Uncertain Conditions. Dans W. G. Habashi (Éd.), *Handbook of Numerical Simulation of In-Flight Icing* (pp. 1-34). Cham: Springer International Publishing. doi: 10.1007/978-3-030-64725-4_31-1. Repéré à https://doi.org/10.1007/978-3-030-64725-4_31-1

Grigson, C. (1992). Drag Losses of New Ships Caused by Hull Finish. *Journal of Ship Research, 36*(02), 182-196. doi: 10.5957/jsr.1992.36.2.182. Repéré à https://doi.org/10.5957/jsr.1992.36.2.182

Guillas, S., Glover, N., & Malki-Epshtein, L. (2014). Bayesian calibration of the constants of the – turbulence model for a CFD model of street canyon flow. *Computer Methods in Applied Mechanics and Engineering, 279*. doi: 10.1016/j.cma.2014.06.008

Habashi, W., Tran, P., Baruzzi, G., & Benquet, M. (2003). *Design of Ice Protection Systems and Icing Certification Through the FENSAP-ICE System*.

Han, Y., & Palacios, J. (2014). *Transient Heat Transfer Measurements of Surface Roughness due to Ice Accretion* présentée à 6th AIAA Atmospheric and Space Environments Conference, Reston, VA, USA.

Han, Y., & Palacios, J. (2017). Surface Roughness and Heat Transfer Improved Predictions for Aircraft Ice-Accretion Modeling. *AIAA Journal, 55*(4), 1318-1331. doi: 10.2514/1.j055217. Repéré à https://arc.aiaa.org/doi/abs/10.2514/1.J055217

Hansman, R., Yamaguchi, K., Berkowitz, B., & Potapczuk, M. (1989). Modeling of Surface Roughness Effects on Glaze Ice Accretion. *Journal of Thermophysics and Heat Transfer, 5*(1). doi: 10.2514/3.226

Hanson, D. R., & Kinzel, M. P. (2016). Application of the discrete element roughness method to ice accretion geometries. Dans *46th AIAA Fluid Dynamics Conference, 2016, June 13, 2016 - June 17, 2016*. American Institute of Aeronautics and Astronautics Inc, AIAA.

Hanson, D. R., Kinzel, M. P., & McClain, S. T. (2019). Validation of the discrete element roughness method for predicting heat transfer on rough surfaces. *International Journal of Heat and Mass Transfer, 136*, 1217-1232. doi: 10.1016/j.ijheatmasstransfer.2019.03.062. Repéré à https://www.sciencedirect.com/science/article/pii/S0017931018331296

Harry, R., Radenac, E., Blanchard, G., & Villedieu, P. (2021). Heat transfer modeling by integral boundary-layer methods towards icing applications. Dans *AIAA Aviation 2021 Forum* (pp. AIAA 2021-2640). American Institute of Aeronautics and Astronautics. doi: 10.2514/6.2021-2640. Repéré à https://hal.archives-ouvertes.fr/hal-03327690

Heldt, E. (2006). Measurement of component surface roughness. *Qualitaet und Zuverlaessigkeit, 51*(5), 80-84.

Hellsten, A., & Laine, S. (1997). *Extension of the k-omega-SST turbulence model for flows over rough surfaces* présentée à AIAA 22nd Atmospheric Flight Mechanics Conference, New Orleans, LA.

Heng, L., Duo, W., & Hongyi, X. (2020). Improved Law-of-the-Wall Model for Turbulent Boundary Layer in Engineering. *AIAA Journal, 58*(8), 3308-3319. doi: 10.2514/1.J058464. Repéré à http://dx.doi.org/10.2514/1.J058464

Hosder, S., Walters, R., & Perez, R. (2006). A Non-Intrusive Polynomial Chaos Method For Uncertainty Propagation in CFD Simulations. Dans *44th AIAA Aerospace Sciences Meeting and Exhibit*. doi: 10.2514/6.2006-891. Repéré à https://arc.aiaa.org/doi/abs/10.2514/6.2006-891

Hosni, M. H., Coleman, H. W., Garner, J. W., & Taylor, R. P. (1993). Roughness element shape effects on heat transfer and skin friction in rough-wall turbulent boundary layers. *International Journal of Heat and Mass Transfer, 36*(1), 147-153. doi: 10.1016/0017-9310(93)80074-5. Repéré à http://www.sciencedirect.com/science/article/pii/0017931093800745

Howell, J., Forbes, D., Passmore, M., & Page, G. (2017). The Effect of a Sheared Crosswind Flow on Car Aerodynamics. *SAE International Journal of Passenger Cars - Mechanical Systems, 10*(1), 278-285. doi: 10.4271/2017-01-1536. Repéré à http://dx.doi.org/10.4271/2017-01-1536

Hussain, M. F., Barton, R. R., & Joshi, S. B. (2002). Metamodeling: Radial basis functions, versus polynomials. *European Journal of Operational Research, 138*(1), 142-154. doi: https://doi.org/10.1016/S0377-2217(01)00076-5. Repéré à https://www.sciencedirect.com/science/article/pii/S0377221701000765

I.A.T.A. (2016). *Safety Report 2015*. Montreal, Quebec: International Air Transport Association.

Ignatowicz, K., Beaugendre, H., & Morency, F. (2023). Numerical Simulation of In-Flight Iced Surface Roughness. Dans W. G. Habashi (Éd.), *Handbook of Numerical Simulation of In-Flight Icing* (pp. 1-48). Cham: Springer International Publishing. doi: 10.1007/978-3-030-64725-4_29-1. Repéré à https://doi.org/10.1007/978-3-030-64725-4_29-1

Ignatowicz, K., Morency, F., & Beaugendre, H. (2019a, May 14-16, 2019). *Numerical simulation of ice accretion using Messinger-based approach: effects of surface roughness* présentée à CASI AERO 2019, Laval, Québec, Canada.

Ignatowicz, K., Morency, F., & Beaugendre, H. (2019b). Simulations numériques de changement de phase appliquées au givrage en aéronautique. Dans CIFQ (Éd.), *XIVème Colloque International Franco-Québécois en énergie*.

Ignatowicz, K., Morency, F., & Beaugendre, H. (2021a). *Extension of SU2 CFD capabilities to 3D aircraft icing simulation* présentée à 29th Annual Conference of the Computational Fluid Dynamics Society of Canada (CFDSC2021), Online.

Ignatowicz, K., Morency, F., & Beaugendre, H. (2021b, April 12-14, 2021). *Sensitivity of the convective heat transfer coefficient to the uncertain surface roughness characteristics* présentée à 55th 3AF International Conference on Applied Aerodynamics : AERO2020, Poitiers, France, Online.

Ignatowicz, K., Morency, F., & Beaugendre, H. (2021c). Sensitivity Study of Ice Accretion Simulation to Roughness Thermal Correction Model. *Aerospace, 8*(3), 84. Repéré à https://www.mdpi.com/2226-4310/8/3/84

Ignatowicz, K., Morency, F., & Beaugendre, H. (2023a). *Data-driven Roughness Estimation for Glaze Ice Accretion Simulation*. doi: https://doi.org/10.4271/2023-01-1449. Repéré à https://doi.org/10.4271/2023-01-1449

Ignatowicz, K., Morency, F., & Beaugendre, H. (2023b). Surface Roughness in RANS Applied to Aircraft Ice Accretion Simulation: A Review. *Fluids, 8*(10), 278. Repéré à https://www.mdpi.com/2311-5521/8/10/278

Ignatowicz, K., Morency, F., Beaugendre, H., & Solaï, E. (2022, March 28-30, 2022). *Data-driven calibration of RANS heat transfer prediction on a curved rough surface* présentée à 3AF AERO2022, Toulouse, France.

Ignatowicz, K., Morency, F., & Lopez, P. (2019). Dynamic Moment Model for Numerical Simulation of a 6-DOF Plate Trajectory around an Aircraft. *Journal of Aerospace Engineering, 32*(5). doi: 10.1061/(ASCE)AS.1943-5525.0001059

Ignatowicz, K., Solaï, E., Morency, F., & Beaugendre, H. (2022). Data-Driven Calibration of Rough Heat Transfer Prediction Using Bayesian Inversion and Genetic Algorithm. *Energies, 15*(10), 3793. Repéré à https://www.mdpi.com/1996-1073/15/10/3793

Jafari, M., & Alipour, A. (2021). Review of approaches, opportunities, and future directions for improving aerodynamics of tall buildings with smart facades. *Sustainable Cities and Society, 72*. doi: 10.1016/j.scs.2021.102979. Repéré à http://dx.doi.org/10.1016/j.scs.2021.102979

Jameson, A. (2017). Origins and Further Development of the Jameson–Schmidt–Turkel Scheme. *AIAA Journal, 55*(5), 1487-1510. doi: 10.2514/1.j055493. Repéré à https://arc.aiaa.org/doi/abs/10.2514/1.J055493

Javanappa, S. K., & Narasimhamurthy, V. D. (2019). DNS of plane Couette flow with surface roughness. *International Journal of Advances in Engineering Sciences and Applied Mathematics, 11*(4), 288-300. doi: 10.1007/s12572-020-00260-y. Repéré à http://dx.doi.org/10.1007/s12572-020-00260-y

Jayabarathi, S. B., & Ratnam, M. M. (2022). Comparison of Correlation between 3D Surface Roughness and Laser Speckle Pattern for Experimental Setup Using He-Ne as Laser Source and Laser Pointer as Laser Source. *Sensors, 22*(16). doi: 10.3390/s22166003. Repéré à http://dx.doi.org/10.3390/s22166003

Jones, S. M., Reveley, M. S., Evans, J. K., & Barrientos, F. A. (2008). *Subsonic Aircraft Safety Icing Study* (nº NASA/TM--2008-215107, L-19435). Hampton, VA, United States: NASA.

Jung, S., Raj, L., Rahimi, A., Jeong, H., & Myong, R. S. (2020). Performance evaluation of electrothermal anti-icing systems for a rotorcraft engine air intake using a meta model. *Aerospace Science and Technology, 106*, 106174. doi: https://doi.org/10.1016/j.ast.2020.106174. Repéré à http://www.sciencedirect.com/science/article/pii/S1270963820308567

Kadivar, M., Tormey, D., & McGranaghan, G. (2021). A review on turbulent flow over rough surfaces: Fundamentals and theories. *International Journal of Thermofluids, 10*. doi: 10.1016/j.ijft.2021.100077. Repéré à http://dx.doi.org/10.1016/j.ijft.2021.100077

Kato, H., Ito, K., & Lepot, I. (2010). Sensitivity analysis based on high fidelity simulation: application to hypersonic variable-cycle engine intake design. *International Journal of Engineering Systems Modelling and Simulation, 2*. doi: 10.1504/IJESMS.2010.031869

Kaya, M. N., Kok, A. R., & Kurt, H. (2021). Comparison of aerodynamic performances of various airfoils from different airfoil families using CFD. *Wind and Structures, An International Journal, 32*(3), 239-248. doi: 10.12989/was.2021.32.3.239. Repéré à http://dx.doi.org/10.12989/was.2021.32.3.239

Kays, W. M., & Crawford, M. E. (1993). *Convective heat and mass transfer*.

Kennedy, M. C., & O'Hagan, A. (2001). Bayesian calibration of computer models. *Journal of the Royal Statistical Society: Series B (Statistical Methodology), 63*(3), 425-464. doi: https://doi.org/10.1111/1467-9868.00294. Repéré à https://rss.onlinelibrary.wiley.com/doi/abs/10.1111/1467-9868.00294

Khan, A. H., Islam, M. S., & Sazzad, I. U. (2021). Calibration of κ-ε turbulence model for thermal–hydraulic analyses in rib-roughened narrow rectangular channels using genetic algorithm. *SN Applied Sciences, 3*(6), 678. doi: 10.1007/s42452-021-04645-x. Repéré à https://doi.org/10.1007/s42452-021-04645-x

Knopp, T., Eisfeld, B., & Calvo, J. B. (2009). A new extension for k–ω turbulence models to account for wall roughness. *International Journal of Heat and Fluid Flow, 30*(1), 54-65. doi: 10.1016/j.ijheatfluidflow.2008.09.009. Repéré à https://www.sciencedirect.com/science/article/pii/S0142727X08001495

Kontogiannis, A., Prakash, A., Laurendeau, E., & Moens, F. (2018). *Sensitivity of Glaze Ice Accretion and Iced Aerodynamics Prediction to Roughness* présentée à 26th Annual Conference of the Computational Fluid Dynamics Society of Canada, Winnipeg, MB.

Kuwata, Y., Yamamoto, Y., Tabata, S., & Suga, K. (2023). Scaling of the roughness effects in turbulent flows over systematically-varied irregular rough surfaces. *International Journal of Heat and Fluid Flow, 101*. doi: 10.1016/j.ijheatfluidflow.2023.109130. Repéré à http://dx.doi.org/10.1016/j.ijheatfluidflow.2023.109130

Langelandsvik, L. I., Kunkel, G., & Smits, A. (2008). Flow in a commercial steel pipe. *Journal of Fluid Mechanics, 595*, 323-339. doi: 10.1017/S0022112007009305

Laurendeau, E., Bourgault-Cote, S., Ozcer, I. A., Hann, R., Radenac, E., & Pueyo, A. (2022). *Summary from the 1st AIAA Ice Prediction Workshop* présentée à AIAA AVIATION 2022 Forum, Chicago, IL. doi: 10.2514/6.2022-3398. Repéré à https://arc.aiaa.org/doi/abs/10.2514/6.2022-3398

Lavoie, P. (2017). *Modeling of Thin Water Films on Swept Wings in Icing Conditions* (Polytechnique Montréal, Montréal).

Lavoie, P., Pena, D., Hoarau, Y., & Laurendeau, E. (2018). Comparison of thermodynamic models for ice accretion on airfoils. *International Journal of Numerical Methods for Heat & Fluid Flow, 28*(5), 1004-1030. doi: 10.1108/HFF-08-2016-0297

Leach, R. (2013). *Characterisation of Areal Surface Texture* (1 éd.). Springer. doi: 10.1007/978-3-642-36458-7

Leach, R. (2013). Introduction to Surface Topography. Dans R. Leach (Éd.), *Characterisation of Areal Surface Texture* (pp. 1-13). Berlin, Heidelberg: Springer Berlin Heidelberg. doi: 10.1007/978-3-642-36458-7_1. Repéré à https://doi.org/10.1007/978-3-642-36458-7_1

Lee, Y. K., Mavris, D. N., Volovoi, V. V., & Yuan, M. (2011). A Bayesian method for calibrating computer models to test data. *Inverse Problems in Science and Engineering, 19*(3), 395-408. doi: 10.1080/17415977.2011.551930. Repéré à https://doi.org/10.1080/17415977.2011.551930

Li, S., & Paoli, R. (2019). Modeling of Ice Accretion over Aircraft Wings Using a Compressible OpenFOAM Solver. *International Journal of Aerospace Engineering, 2019*, 4864927. doi: 10.1155/2019/4864927. Repéré à https://doi.org/10.1155/2019/4864927

Ligrani, P. M., & Moffat, R. J. (1986). Structure of transitionally rough and fully rough turbulent boundary layers. *Journal of Fluid Mechanics, 162*, 69-98. doi: 10.1017/S0022112086001933. Repéré à https://www.cambridge.org/core/article/structure-of-transitionally-rough-and-fully-rough-turbulent-boundary-layers/6F23EDDA4246E10F3FC6E63C0A927F0C

Ligrani, P. M., Moffat, R. J., & Kays, W. M. (1979). *The thermal and hydrodynamic behavior of thick, rough-wall, turbulent boundary layers*. Stanford University.

Liu, Y., & Hu, H. (2018). An experimental investigation on the unsteady heat transfer process over an ice accreting airfoil surface. *International Journal of Heat and Mass Transfer, 122*(1), 707-718. doi: 10.1016/j.ijheatmasstransfer.2018.02.023. Repéré à http://www.sciencedirect.com/science/article/pii/S0017931017357125

Liu, Y., Zhang, K., Tian, W., & Hu, H. (2020). An experimental investigation on the dynamic ice accretion and unsteady heat transfer over an airfoil surface with embedded initial ice roughness. *International Journal of Heat and Mass Transfer, 146*, 118900. doi: 10.1016/j.ijheatmasstransfer.2019.118900. Repéré à http://www.sciencedirect.com/science/article/pii/S0017931019342814

MacArthur, C., Keller, J., & Luers, J. (1982). *Mathematical modeling of ice accretion on airfoils* présentée à 20th Aerospace Sciences Meeting. doi: 10.2514/6.1982-284. Repéré à https://arc.aiaa.org/doi/abs/10.2514/6.1982-284

Marelli, S., & Sudret, B. (2019). *UQLab user manual -- Polynomial chaos expansions*. Chair of Risk, Safety and Uncertainty Quantification, ETH Zurich, Switzerland

Marquet, O., Leontini, J. S., Zhao, J., & Thompson, M. C. (2022). Hysteresis of two-dimensional flows around a NACA0012 airfoil at Re=5000 and linear analyses of their mean flow. *International Journal of Heat and Fluid Flow, 94*. doi: 10.1016/j.ijheatfluidflow.2021.108920. Repéré à http://dx.doi.org/10.1016/j.ijheatfluidflow.2021.108920

Martini, F., Ibrahim, H., Contreras Montoya, L. T., Rizk, P., & Ilinca, A. (2022). Turbulence Modeling of Iced Wind Turbine Airfoils. *Energies, 15*(22), 8325. Repéré à https://www.mdpi.com/1996-1073/15/22/8325

McClain, S. T., Vargas, M., & Jen-Ching, T. (2016). *Characterization of Ice Roughness Variations in Scaled Glaze Icing Conditions* présentée à 8th AIAA Atmospheric and Space Environments Conference, 13-17 June 2016, Reston, VA, USA.

Mejia-Alvarez, R., & Christensen, K. T. (2013). Wall-parallel stereo particle-image velocimetry measurements in the roughness sublayer of turbulent flow overlying highly irregular roughness. *Physics of Fluids, 25*(11). doi: 10.1063/1.4832377. Repéré à http://dx.doi.org/10.1063/1.4832377

Menter, F. R. (1994). Two-equation eddy-viscosity turbulence models for engineering applications. *AIAA Journal, 32*(8), 1598-1605. doi: 10.2514/3.12149

Messinger, B. L. (1953). Equilibrium Temperature of an Unheated Icing Surface as a Function of Air Speed. *Journal of the Aeronautical Sciences, 20*(1), 29-42. doi: 10.2514/8.2520

Morency, F., & Beaugendre, H. (2020). Comparison of turbulent Prandtl number correction models for the Stanton evaluation over rough surfaces. *International Journal of Computational Fluid Dynamics*. doi: 10.1080/10618562.2020.1753712

Morita, Y., Rezaeiravesh, S., Tabatabaei, N., Vinuesa, R., Fukagata, K., & Schlatter, P. (2022). Applying Bayesian optimization with Gaussian process regression to computational fluid dynamics problems. *Journal of Computational Physics, 449*, 110788. doi: 10.1016/j.jcp.2021.110788. Repéré à https://www.sciencedirect.com/science/article/pii/S0021999121006835

Moshansky, V. P. (1992). *Commission of Inquiry Into The Air Ontario Crash At Dryden, Ontario* (nº CP32-55/1992E).

Muehleisen, R. T., & Bergerson, J. (2016). *Bayesian Calibration - What, Why And How* présentée à International High Performance Buildings Conference.

Myers, T. G. (2001). Extension to the Messinger Model for Aircraft Icing. *AIAA Journal, 39*(2), 211-218. doi: 10.2514/2.1312

Myers, T. G., Charpin, J. P. F., & Chapman, S. J. (2002). The flow and solidification of a thin fluid film on an arbitrary three-dimensional surface. *Physics of Fluids, 14*(8), 2788-2803. doi: 10.1063/1.1488599. Repéré à https://aip.scitation.org/doi/abs/10.1063/1.1488599

Najm, H. N. (2009). Uncertainty Quantification and Polynomial Chaos Techniques in Computational Fluid Dynamics. *Annual Review of Fluid Mechanics, 41*(1), 35-52. doi: 10.1146/annurev.fluid.010908.165248. Repéré à https://www.annualreviews.org/doi/abs/10.1146/annurev.fluid.010908.165248

NASA. (2013). Turbulence Modeling Resource. Repéré à https://turbmodels.larc.nasa.gov/naca0012_val.html

Newton, J., van Fossen, J. G., Poinsatte, P., & Dewitt, K. J. (1988, 1988). *Measurement of local convective heat transfer coefficients from a smooth and roughened NACA-0012 airfoil: Flight test data* présentée à 26th Aerospace Sciences Meeting, Reno, Nevada.

Nikuradse, J. (1933). Laws of flow in rough pipes. *VDI Forschungsheft, 4*(B), 63.

NTSB. (1997). *Aircraft Accident Report*. Washington, DC: National Transportation Safety Board.

Oh, J., & Chien, N. B. (2018). Optimization Design by Coupling Computational Fluid Dynamics and Genetic Algorithm. Dans IntechOpen (Éd.), *Computational Fluid Dynamics - Basic Instruments and Applications in Science*. doi: https://doi.org/10.5772/intechopen.72316

Omoware, W. D., Maheri, A., & Azimov, U. (2014). Aerodynamic analysis of flapping-pitching flat plates. Dans *3rd International Symposium on Environmental Friendly Energies and Applications (EFEA)* (pp. 1-5). doi: 10.1109/EFEA.2014.7059973

Orych, M., Werner, S., & Larsson, L. (2022). Roughness effect modelling for wall resolved RANS – Comparison of methods for marine hydrodynamics. *Ocean Engineering, 266*, 112778. doi: 10.1016/j.oceaneng.2022.112778. Repéré à https://www.sciencedirect.com/science/article/pii/S0029801822020613

Owen, P. R., & Thomson, W. R. (1963). Heat transfer across rough surfaces. *Journal of Fluid Mechanics, 15*(3), 321-334. doi: 10.1017/S0022112063000288. Repéré à https://www.cambridge.org/core/article/heat-transfer-across-rough-surfaces/CDB40085D75F5692423E01B3629F4BFC

Owoyele, O., Pal, P., Torreira, A., Probst, D., Shaxted, M., Wilde, M., & Senecal, P. (2021). *Application of an automated machine learning-genetic algorithm (AutoML-GA) approach coupled with computational fluid dynamics simulations for rapid engine design optimization*.

Ozcer, I. A., Baruzzi, G. S., Reid, T., Habashi, W. G., Fossati, M., & Croce, G. (2011). *FENSAP-ICE: Numerical Prediction of Ice Roughness Evolution, and its Effects on Ice Shapes*. doi: 10.4271/2011-38-0024. Repéré à https://doi.org/10.4271/2011-38-0024

Özgen, S., & Canıbek, M. (2008). Ice accretion simulation on multi-element airfoils using extended Messinger model. *Heat and Mass Transfer, 45*(3), 305. doi: 10.1007/s00231-008-0430-4

Patel, V. C., & Yoon, J. Y. (1995). Application of Turbulence Models to Separated Flow Over Rough Surfaces. *Journal of Fluids Engineering, 117*(2), 234-241. doi: 10.1115/1.2817135. Repéré à https://doi.org/10.1115/1.2817135

Pena, D., Hoarau, Y., & Laurendeau, E. (2016). A single step ice accretion model using Level-Set method. *Journal of Fluids and Structures, 65*, 278-294. doi: 10.1016/j.jfluidstructs.2016.06.001

Poinsatte, P., Van Fossen, J. G., & Dewitt, K. J. (1991). Roughness effects on heat transfer from a NACA 0012 airfoil. *Journal of Aircraft, 28*(12), 908-911. doi: 10.2514/3.46116. Repéré à https://arc.aiaa.org/doi/abs/10.2514/3.46116

Prince Raj, L., Yee, K., & Myong, R. S. (2020). Sensitivity of ice accretion and aerodynamic performance degradation to critical physical and modeling parameters affecting airfoil icing. *Aerospace Science and Technology, 98*, 105659. doi: https://doi.org/10.1016/j.ast.2019.105659. Repéré à https://www.sciencedirect.com/science/article/pii/S127096381931805X

Radenac, E., Bayeux, C., & Villedieu, P. (2020). Use of a Two-Dimensional Finite Volume Integral Boundary-Layer Method for Ice-Accretion Calculations. *AIAA Journal, 58*, 1-15. doi: 10.2514/1.J058701

Radenac, E., Gaible, H., Bezard, H., & Reulet, P. (2019). *IGLOO3D Computations of the Ice Accretion on Swept-Wings of the SUNSET2 Database* présentée à International Conference on Icing of Aircraft, Engines, and Structures, Minneapolis, USA. doi: 10.4271/2019-01-1935. Repéré à https://doi.org/10.4271/2019-01-1935

Radenac, E., Kontogiannis, A., Bayeux, C., & Villedieu, P. (2018). *An extended rough-wall model for an integral boundary layer model intended for ice accretion calculations* présentée à 2018 Atmospheric and Space Environments Conference, Atlanta, Georgia. doi: 10.2514/6.2018-2858

Raj, L., Yee, K., & Myong, R. S. (2020). Sensitivity of ice accretion and aerodynamic performance degradation to critical physical and modeling parameters affecting airfoil icing. *Aerospace Science and Technology, 98*(1). doi: https://doi.org/10.1016/j.ast.2019.105659. Repéré à http://www.sciencedirect.com/science/article/pii/S127096381931805X

Ranftl, S., & von der Linden, W. (2021). Bayesian Surrogate Analysis and Uncertainty Propagation. *Physical Sciences Forum, 3*(1), 6. Repéré à https://www.mdpi.com/2673-9984/3/1/6

Rao, V. N., Jefferson-Loveday, R., Tucker, P. G., & Lardeau, S. (2014). Large eddy simulations in turbines: influence of roughness and free-stream turbulence. *Flow, Turbulence and Combustion, 92*(1-2), 543-561. doi: 10.1007/s10494-013-9465-9. Repéré à http://dx.doi.org/10.1007/s10494-013-9465-9

Ravenna, R., Song, S., Shi, W., Sant, T., De marco muscat-fenech, C., Tezdogan, T., & Demirel, Y. K. (2022). CFD analysis of the effect of heterogeneous hull roughness on ship resistance. *Ocean Engineering*, 111733. doi: 10.1016/j.oceaneng.2022.111733. Repéré à http://dx.doi.org/10.1016/j.oceaneng.2022.111733

Reddy, T. A., Maor, I., & Panjapornpon, C. (2007). Calibrating Detailed Building Energy Simulation Programs with Measured Data—Part II: Application to Three Case Study Office Buildings (RP-1051). *HVAC&R Research, 13*(2), 243-265. doi: 10.1080/10789669.2007.10390953. Repéré à https://www.tandfonline.com/doi/abs/10.1080/10789669.2007.10390953

Reichardt, H. (1951). Vollständige Darstellung der turbulenten Geschwindigkeitsverteilung in glatten Leitungen. *ZAMM - Journal of Applied Mathematics and Mechanics / Zeitschrift für Angewandte Mathematik und Mechanik, 31*(7), 208-219. doi: 10.1002/zamm.19510310704. Repéré à https://onlinelibrary.wiley.com/doi/abs/10.1002/zamm.19510310704

Resmini, A., Peter, J., & Lucor, D. (2016). Sparse grids-based stochastic approximations with applications to aerodynamics sensitivity analysis. *International Journal for Numerical Methods in Engineering, 106*(1), 32-57. doi: 10.1002/nme.5005. Repéré à http://dx.doi.org/10.1002/nme.5005

RTO/NATO. (2001). *Ice Accretion Simulation Evaluation Test* (nº RTO-TR-038(AVT-006)). Neuilly sur Seine, France.

Ruff, G. A., & Berkowitz, B. M. (1990). *Users manual for the NASA Lewis ice accretion prediction code (LEWICE)* (nº NASA CR-185129.). Washington, DC: National Aeronautics and Space Administration.

Rumpfkeil, M. P., & Beran, P. S. (2020). Multifidelity Sparse Polynomial Chaos Surrogate Models Applied to Flutter Databases. *AIAA Journal, 58*(3), 1292-1303. doi: 10.2514/1.j058452. Repéré à https://arc.aiaa.org/doi/abs/10.2514/1.J058452

Saeed, F. (2002). State-of-the-Art Aircraft Icing and Anti-Icing Simulation. *ARA Journal, 2000-2002*.

Salehi, S., Raisee, M., Cervantes, M. J., & Nourbakhsh, A. (2017). Efficient uncertainty quantification of stochastic CFD problems using sparse polynomial chaos and compressed sensing. *Computers & Fluids, 154*, 296-321. doi: https://doi.org/10.1016/j.compfluid.2017.06.016. Repéré à https://www.sciencedirect.com/science/article/pii/S0045793017302281

Saltelli, A., Ratto, M., Andres, T., Campolongo, F., Cariboni, J., Gatelli, D., . . . Tarantola, S. (2008). *Global Sensitivity Analysis. The Primer* (Vol. 304). doi: 10.1002/9780470725184.ch6

Schaefer, J. A., Cary, A. W., Mani, M., & Spalart, P. R. (2017). Uncertainty Quantification and Sensitivity Analysis of SA Turbulence Model Coefficients in Two and Three Dimensions. Dans *55th AIAA Aerospace Sciences Meeting*. doi: 10.2514/6.2017-1710. Repéré à https://arc.aiaa.org/doi/abs/10.2514/6.2017-1710

Schaefer, J. A., Romero, V. J., Schafer, S. R., Leyde, B., & Denham, C. L. (2020). Approaches for Quantifying Uncertainties in Computational Modeling for Aerospace Applications. Dans *AIAA Scitech 2020 Forum*. doi: 10.2514/6.2020-1520. Repéré à https://arc.aiaa.org/doi/abs/10.2514/6.2020-1520

Schlichting, H. (1937). *Experimental investigation of the problem of surface roughness* (nº NACA-TM-823). National Advisory Commitee for Aeronautics.

Schlichting, H., & Gersten, K. (2017). *Boundary-Layer Theory* (9 éd.). Springer Berlin. doi: 10.1007/978-3-662-52919-5

Schultz, M. P., & Flack, K. A. (2007). The rough-wall turbulent boundary layer from the hydraulically smooth to the fully rough regime. *Journal of Fluid Mechanics, 580*, 381-405. doi: 10.1017/S0022112007005502. Repéré à https://www.cambridge.org/core/article/roughwall-turbulent-boundary-layer-from-the-hydraulically-smooth-to-the-fully-rough-regime/EFCC27E28F0A053DD0D62E4D67A1F516

Shahane, S., Aluru, N. R., & Vanka, S. P. (2019). Uncertainty quantification in three dimensional natural convection using polynomial chaos expansion and deep neural networks. *International Journal of Heat and Mass Transfer, 139*, 613-631. doi: https://doi.org/10.1016/j.ijheatmasstransfer.2019.05.014. Repéré à https://www.sciencedirect.com/science/article/pii/S0017931018363919

Shannon, T., & McClain, S. T. (2019). An Assessment of LEWICE Roughness and Convection Enhancement Models. *SAE International Journal of Advances and Current Practices in Mobility, 2*(1), 128-139. doi: 10.4271/2019-01-1977. Repéré à https://doi.org/10.4271/2019-01-1977

Shin, J. (1996). Characteristics of surface roughness associated with leading-edge ice accretion. *Journal of Aircraft, 33*(2), 316-321. doi: 10.2514/3.46940. Repéré à https://arc.aiaa.org/doi/abs/10.2514/3.46940

Shin, J., Berkowitz, B., Chen, H. H., & Cebeci, T. (1991). *Prediction of ice shapes and their effect on airfoil performance* présentée à AIAA 29th Aerospace Sciences Meeting, Reno, NV.

Shin, J., & H. Bond, T. (1992). *Results of an icing test on a NACA 0012 airfoil in the NASA Lewis Icing Research Tunnel*. doi: 10.2514/6.1992-647

Sigal, A., & Danberg, J. E. (1990). New correlation of roughness density effect on the turbulent boundary layer. *AIAA Journal, 28*(3), 554-556. doi: 10.2514/3.10427. Repéré à https://arc.aiaa.org/doi/abs/10.2514/3.10427

Solaï, E., Beaugendre, H., Congedo, P.-M., Daccord, R., & Guadagnini, M. (2019). Numerical Simulation of a Battery Thermal Management System Under Uncertainty for a Racing Electric Car. Dans *La simulation pour la mobilité électrique*. NAFEMS.

Son, C., Oh, S., & Yee, K. (2012). Quantitative analysis of a two-dimensional ice accretion on airfoils. *Journal of Mechanical Science and Technology, 26*(4), 1059-1071. doi: 10.1007/s12206-012-0223-z. Repéré à https://doi.org/10.1007/s12206-012-0223-z

Spalart, P., & Allmaras, S. (1992). A one-equation turbulence model for aerodynamic flows. Dans *30th Aerospace Sciences Meeting and Exhibit*. American Institute of Aeronautics and Astronautics. doi: 10.2514/6.1992-439

Stein, M. (1987). Large sample properties of simulations using latin hypercube sampling. *Technometrics, 29*(2), 143-151. doi: 10.2307/1269769

Sudret, B., Marelli, S., & Wiart, J. (2017). Surrogate models for uncertainty quantification: An overview. Dans *2017 11th European Conference on Antennas and Propagation (EUCAP)* (pp. 793-797). doi: 10.23919/EuCAP.2017.7928679

Suga, K., Craft, T. J., & Iacovides, H. (2006). An analytical wall-function for turbulent flows and heat transfer over rough walls. *International Journal of Heat and Fluid Flow, 27*(5), 852-866. doi: 10.1016/j.ijheatfluidflow.2006.03.011. Repéré à http://www.sciencedirect.com/science/article/pii/S0142727X06000804

Szilder, K., & Lozowski, E. P. (2018). Comparing Experimental Ice Accretions on a Swept Wing with 3D Morphogenetic Simulations. *Journal of Aircraft, 55*(6), 2546-2549. doi: 10.2514/1.c034879. Repéré à https://arc.aiaa.org/doi/abs/10.2514/1.C034879

Tabatabaei, N., Raisee, M., & Cervantes, M. J. (2019). Uncertainty Quantification of Aerodynamic Icing Losses in Wind Turbine With Polynomial Chaos Expansion. *Journal of Energy Resources Technology, 141*(5). doi: 10.1115/1.4042732. Repéré à https://doi.org/10.1115/1.4042732

Tagawa, G. d., Morency, F., & Beaugendre, H. (2018). CFD study of airfoil lift reduction caused by ice roughness. Dans *2018 Applied Aerodynamics Conference*. doi: 10.2514/6.2018-3010. Repéré à https://arc.aiaa.org/doi/abs/10.2514/6.2018-3010

Todhunter, L. D., Leach, R. K., Lawes, S. D. A., & Blateyron, F. (2017). Industrial survey of ISO surface texture parameters. *CIRP Journal of Manufacturing Science and Technology, 19*, 84-92. doi: 10.1016/j.cirpj.2017.06.001. Repéré à http://dx.doi.org/10.1016/j.cirpj.2017.06.001

Toulouse, M.-L., & Lewis, R. (2015). *A350XWB Icing Certification Overview* présentée à SAE 2015 International Conference on Icing of Aircraft, Engines, and Structures, Prague, The Czech Republic. doi: https://doi.org/10.4271/2015-01-2111. Repéré à https://doi.org/10.4271/2015-01-2111

Trontin, P., Kontogiannis, A., Blanchard, G., & Villedieu, P. (2017). *Description and assessment of the new ONERA 2D icing suite IGLOO2D*. doi: 10.2514/6.2017-3417

Turner, A. B., Hubbe-Walker, S. E., & Bayley, F. J. (2000). Fluid flow and heat transfer over straight and curved rough surfaces. *International Journal of Heat and Mass Transfer, 43*, 251-262. doi: 10.1016/S0017-9310(99)00128-3

van Leer, B. (1979). Towards the ultimate conservative difference scheme. V. A second-order sequel to Godunov's method. *Journal of Computational Physics, 32*(1), 101-136. doi: https://doi.org/10.1016/0021-9991(79)90145-1. Repéré à https://www.sciencedirect.com/science/article/pii/0021999179901451

van Rij , J. A., Belnap , B. J., & Ligrani, P. M. (2002). Analysis and Experiments on Three-Dimensional, Irregular Surface Roughness. *Journal of Fluids Engineering, 124*(3), 671-677. doi: 10.1115/1.1486222. Repéré à https://doi.org/10.1115/1.1486222

Venkatakrishnan, V. (1993). *On the accuracy of limiters and convergence to steady state solutions* présentée à 31st Aerospace Sciences Meeting. doi: 10.2514/6.1993-880. Repéré à https://arc.aiaa.org/doi/abs/10.2514/6.1993-880

Von Kármán, T. (1931). *Mechanical similitude and turbulence* (nº NACA-TM-611). Washington, DC, United States: National Advisory Committee for Aeronautics.

Wagner, P. R., Fahrni, R., Klippel, M., Frangi, A., & Sudret, B. (2019). Bayesian calibration and sensitivity analysis of heat transfer models for fire insulation panels. *Engineering Structures, 205*. doi: 10.1016/j.engstruct.2019.110063

Wagner, P. R., Nagel, J., Marelli, S., & Sudret, B. (2021). *UQLab user manual – Bayesian inference for model calibration and inverse problems*. Zurich, Switzerland: Chair of Risk, Safety and Uncertainty Quantification, ETH Zurich, Switzerland

Wang, Y., Zhang, Y., Wang, Y., Zhu, D., Zhao, N., & Zhu, C. (2022). Quantitative Measurement Method for Ice Roughness on an Aircraft Surface. *Aerospace, 9*(12), 739. Repéré à https://www.mdpi.com/2226-4310/9/12/739

Weissenbrunner, A., Fiebach, A., Schmelter, S., Bär, M., Thamsen, P. U., & Lederer, T. (2016). Simulation-based determination of systematic errors of flow meters due to uncertain inflow conditions. *Flow Measurement and Instrumentation, 52*, 25-39. doi: https://doi.org/10.1016/j.flowmeasinst.2016.07.011. Repéré à http://www.sciencedirect.com/science/article/pii/S0955598616300875

Wiener, N. (1938). The Homogeneous Chaos. *American Journal of Mathematics, 60*(4), 897-936. doi: 10.2307/2371268. Repéré à http://www.jstor.org/stable/2371268

Wilcox, D. C. (2006). *Turbulence Modeling for CFD*. DCW Industries. Repéré à https://books.google.ca/books?id=tFNNPgAACAAJ

Wright, W. B. (2008). User's manual for LEWICE version 3.2.

Wright, W. B., Al-Khalil, K., & Miller, D. (1997). Validation of NASA thermal ice protection computer codes. II - LEWICE/Thermal. Dans *35th Aerospace Sciences Meeting and Exhibit*. American Institute of Aeronautics and Astronautics. doi: doi:10.2514/6.1997-50
10.2514/6.1997-50. Repéré à https://doi.org/10.2514/6.1997-50

Wright, W. B., Gent, R. W., & Guffond, D. (1997). *DRA/NASA/ONERA Collaboration on Icing Research. Part II- Prediction of Airfoil Ice Accretion*.

Wright, W. B., Rigby, D., & Ozoroski, T. (2023). *Roughness Parameter Optimization of the McClain Model in GlennICE*. doi: 10.4271/2023-01-1468. Repéré à https://doi.org/10.4271/2023-01-1468

Wright, W. B., Struk, P., Bartkus, T., & Addy, G. (2015). *Recent Advances in the LEWICE Icing Model*. doi: https://doi.org/10.4271/2015-01-2094. Repéré à https://doi.org/10.4271/2015-01-2094

Yan, L., Chao, W., Shi-nan, C., & Du, C. (2011). Simulation of Ice Accretion Based on Roughness Distribution. *Procedia Engineering, 17*, 160-177. doi: 10.1016/j.proeng.2011.10.019. Repéré à https://www.sciencedirect.com/science/article/pii/S1877705811026981

Yang, X.-S. (2021). Chapter 6 - Genetic Algorithms. Dans X.-S. Yang (Éd.), *Nature-Inspired Optimization Algorithms (Second Edition)* (pp. 91-100). Academic Press. doi: https://doi.org/10.1016/B978-0-12-821986-7.00013-5. Repéré à https://www.sciencedirect.com/science/article/pii/B9780128219867000135

Yanxia, D., Yewei, G., Chunhua, X., & Xian, Y. (2010). Investigation on heat transfer characteristics of aircraft icing including runback water. *International Journal of Heat and Mass Transfer, 53*(19), 3702-3707. doi: https://doi.org/10.1016/j.ijheatmasstransfer.2010.04.021

Zhang, K., Li, J., Zeng, F., Wang, Q., & Yan, C. (2022). Uncertainty Analysis of Parameters in SST Turbulence Model for Shock Wave-Boundary Layer Interaction. *Aerospace, 9*(2), 55. Repéré à https://www.mdpi.com/2226-4310/9/2/55

Zhu, C., Fu, B., Sun, Z., & Zhu, C. (2012). 3D Ice Accretion Simulation For Complex Configuration Basing On Improved Messinger Model. *International Journal of Modern Physics: Conference Series, 19*, 341-350. doi: 10.1142/s2010194512008938

Zhu, P., Yan, Y., Song, L., Li, J., & Feng, Z. (2016). Uncertainty Quantification of Heat Transfer for a Highly Loaded Gas Turbine Blade Endwall Using Polynomial Chaos. Dans *ASME Turbo Expo 2016: Turbomachinery Technical Conference and Exposition* (Vol. Volume 2C: Turbomachinery). V02CT45A008. doi: 10.1115/gt2016-56575. Repéré à https://doi.org/10.1115/GT2016-56575

Zocca, M., Gori, G., & Guardone, A. (2017). Blockage and Three-Dimensional Effects in Wind-Tunnel Testing of Ice Accretion over Wings. *Journal of Aircraft, 54*(2), 759-767. doi: 10.2514/1.c033750. Repéré à https://arc.aiaa.org/doi/abs/10.2514/1.C033750